REPORT DOCUMENTATION PAGE

1. Recipient's Reference	2. Originator's Reference	3. Further Reference	4. Security Classification of Document
	AGARD-LS-137	ISBN 92-835-1477-7	UNCLASSIFIED

5. Originator	Advisory Group for Aerospace Research and Development North Atlantic Treaty Organization 7 rue Ancelle, 92200 Neuilly sur Seine, France

6. Title	PROCESS MODELING APPLIED TO METAL FORMING AND THERMOMECHANICAL PROCESSING

7. Presented at a Lecture Series under the sponsorship of the Structures and Materials Panel and the Consultant and Exchange programme of AGARD on 15—16 October 1984 in Oslo, Norway, on 18—19 October 1984 in Paris, France and 22—23 October 1984 in Lisbon, Portugal

8. Author(s)/Editor(s)	9. Date
Various	September 1984

10. Author's/Editor's Address	11. Pages
Various	164

12. Distribution Statement	This document is distributed in accordance with AGARD policies and regulations, which are outlined on the Outside Back Covers of all AGARD publications.

13. Keywords/Descriptors

Metal working   Mathematical models

14. Abstract

This Lecture Series considers process modeling which provides a new perspective to advance metal forming and thermo-mechanical processing.

Working and forming processes are viewed as systems which integrate component behaviour such as workpiece flow, heat flow and friction at the workpiece — tooling interface, and microstructural evolution. These are combined to form a system process model using deformation mechanics.

The Lecture Series covers extrusion, forging, rolling, and sheet forming processes. It will provide specific results for light metals, steels and superalloys and introduce finite element methods and related aspects of computer-aided process design.

The Lecture Series was sponsored by the Structures and Materials Panel and organized by the Consultant and Exchange Program of AGARD.

AGARD-LS-137

AGARD-LS-137

AGARD

ADVISORY GROUP FOR AEROSPACE RESEARCH & DEVELOPMENT

7 RUE ANCELLE 92200 NEUILLY SUR SEINE FRANCE

AGARD LECTURE SERIES No.137

Process Modeling Applied to Metal Forming and Thermomechanical Processing

NORTH ATLANTIC TREATY ORGANIZATION

**DISTRIBUTION AND AVAILABILITY
ON BACK COVER**

NORTH ATLANTIC TREATY ORGANIZATION

ADVISORY GROUP FOR AEROSPACE RESEARCH AND DEVELOPMENT

(ORGANISATION DU TRAITE DE L'ATLANTIQUE NORD)

AGARD Lecture Series No.137

PROCESS MODELING APPLIED TO METAL

FORMING AND THERMOMECHANICAL PROCESSING

The material in this publication was assembled to support a Lecture Series under the sponsorship of the Structures and Materials Panel and the Consultant and Exchange Programme of AGARD presented on 15—16 October 1984 in Oslo, Norway, 18—19 October 1984 in Paris, France and 22-23 October 1984 in Lisbon, Portugal.

THE MISSION OF AGARD

The mission of AGARD is to bring together the leading personalities of the NATO nations in the fields of science and technology relating to aerospace for the following purposes:

— Exchanging of scientific and technical information;

— Continuously stimulating advances in the aerospace sciences relevant to strengthening the common defence posture;

— Improving the co-operation among member nations in aerospace research and development;

— Providing scientific and technical advice and assistance to the North Atlantic Military Committee in the field of aerospace research and development;

— Rendering scientific and technical assistance, as requested, to other NATO bodies and to member nations in connection with research and development problems in the aerospace field;

— Providing assistance to member nations for the purpose of increasing their scientific and technical potential;

— Recommending effective ways for the member nations to use their research and development capabilities for the common benefit of the NATO community.

The highest authority within AGARD is the National Delegates Board consisting of officially appointed senior representatives from each member nation. The mission of AGARD is carried out through the Panels which are composed of experts appointed by the National Delegates, the Consultant and Exchange Programme and the Aerospace Applications Studies Programme. The results of AGARD work are reported to the member nations and the NATO Authorities through the AGARD series of publications of which this is one.

Participation in AGARD activities is by invitation only and is normally limited to citizens of the NATO nations.

LIST OF SPEAKERS

Lecture Series Director: Dr Joseph F.Thomas, Jr
Wright State University
School of Engineering
Dayton, Ohio 45435
USA

SPEAKERS

Dr B.Andersson
Central Institute for
    Industrial Research
Forskningsveien, 1
P.B. 350 Blindern
Oslo 3
Norway

Dr B.Baudelet
Institut National Polytechnique
    de Grenoble
ENSIEG
B.P. 46
38402 Saint Martin d'Hères Cedex
France

Dr H.L.Gegel
AFWAL/MLLM
Materials Laboratory
Wright-Patterson AFB
Ohio 45433
USA

Dr J-P.A.Immarigeon
Structures & Materials Laboratory
National Aeronautical Establishment
National Research Council
Montreal Road
Ottawa, Ontario K1A 0R6
Canada

Dr N.Rebelo
Department of Mechanical
Engineering, University of Oporto
Rua dos Bragas
4099 Oporto
Portugal

Dr C.M.Sellars
Department of Metallurgy
University of Sheffield
Mappin Street
Sheffield S1-3JD
UK

CONTENTS

FLOW-BASED ANALYSES OF METAL DEFORMATION PROCESSES: AN OVERVIEW

by
Joseph F. Thomas, Jr.
Materials Science and Engineering
Wright State University
Dayton, Ohio 45435 USA

SUMMARY

Flow-based analysis of metal deformation processing provides a new design perspective to assess optimum process variables and workpiece material behavior. Components of flow-based analysis include finite element computation of process mechanics, realistic constitutive equations for workpiece plastic flow, and analytical models for workability during processing. Process requirements such as press loads and maximum limiting strains can be determined in terms of process variables such as temperature and preform design. In principle the strain history of each element in the workpiece can be determined and used to predict the distribution of properties within the product. The material characterization necessary to implement flow-based analysis will be illustrated for the hot forging behavior of the high strength aerospace titanium alloy, Ti-6242.

INTRODUCTION

Over the past several years there has been a widespread interest in advancing the technology of metals deformation processing. This interest has ranged from scientific questions such as the effect of workpiece microstructure on formability to interdisciplinary engineering developments such as computer-aided design. The basic approach adopted in much of this research has been to consider the forming process as a system which integrates the behavior of components such as the workpiece, tooling, lubrication, and equipment. Each component of the system can then be studied separately with the objective of developing a model based on identified input and output variables. These component models are then combined into an overall simulation model for the process based upon one of several deformation mechanics formulations.

The workpiece material model is the most fundamental component of a process model, providing multi-faceted relationships among the quantitative measures of mechanical behavior and microstructural response under deformation processing conditions. The scope of the workpiece model is necessarily tailored to the process, but always includes a plastic flow law expressing the dependence of flow stress on strain, strain rate, and temperature. In some cases, the flow stress is also functionally related to structure parameters, such as percent recrystallization, which evolve with accumulated strain. In addition, since deformation processes usually involve multi-axial stresses, a yield function which describes the dependence of plastic yield on stress state, and thereby provides a definition of effective stress, is also required. Either singly or in combination, these functions which describe the flow stress behavior are referred to as constitutive equations.

These constitutive equations enter the forming analysis in several distinct ways. In the first place, an accurate flow stress model is needed to predict the required press load and energy. Furthermore, for a sufficiently detailed process model such as can be provided by the finite-element method (FEM), realistic constitutive equations allow prediction of the strain-strain rate-temperature path for each element of the deformation zone as a function of process variables such as temperature, deformation rate, and preform shape. It is this capability, to whatever extent it is actually achieved, that is referred to as flow-based analysis. The term is used to distinguish the current approach from earlier analyses which were purely geometrical, invoked only nominal strains, and ignored metallurgical features other than reference to an average flow stress.

In principle then, a successful flow-based analysis implies that the microstructure and properties of each element of the final product can be determined. In primary processes, such as rolling, the perspective would be thermomechanical processing of the material to achieve a desirable final microstructure. In shaping processes, such as hot forging, product integrity would be a key objective. Overall final properties are still important, but, in addition, nonuniform deformation is unavoidable in shaping processes and must be analyzed to assure that strains do not localize to the extent that defects are likely to occur.

This leads to the concept of workability. Constitutive equations of the type described above can be used to determine workability or formability indices, such as strain rate sensitivity, which are needed for input to models which predict the maximum strains that the workpiece can undergo without failure for specified process conditions. In general, there are two types of workability limits, plastic instability and fracture. For the former, limiting strains are determined from the plastic flow law and process conditions such as friction factors. For fracture processes, microstructural features such as the distribution of second phase particles will enter an analytical model. Of course, if temperature effects are to be included in these calculations, a model for deformation heating and heat flow out of the workpiece, primarily into the tooling, must be combined with the process mechanics.

The importance of flow-based analyses in understanding the nature of a deformation process and the structure of the final product is illustrated in Fig. 1. These results are taken from a rigid-plastic FEM calculation of the forging of a turbine blade by Rebelo et al. [1]. The grid distortions and iso-strain contours in Fig. 1 demonstrate that local strain may vary within the workpice by more than a factor of 10. In fact, since this calculation was isothermal, neglecting any temperature variation, the gradients shown may be the minimum to be expected. For example, in a conventional warm forging process, die chilling may lead to temperature variations of several hundred degrees celsius. In such a case, the chilled surface layer further resists deformation leading to even greater strain inhomogeneity.
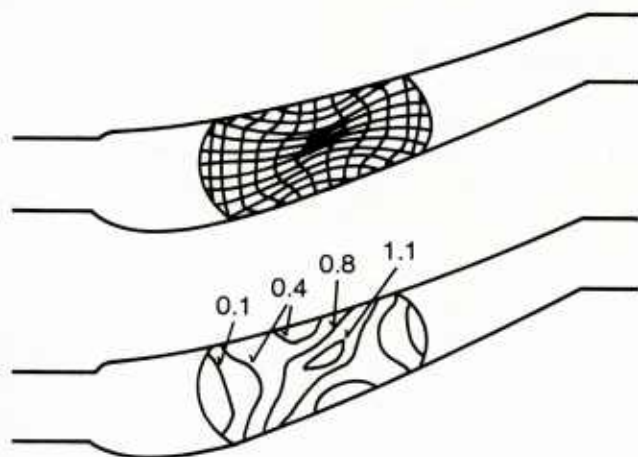
Fig. 1. Calculated grid distortions (top) and effective strain distributions (bottom) during simulated forging of a turbine blade. From [1].

In this overview of flow-based analyses of deformation processes, some of the fundamental considerations important in the determination of realistic constitutive equations for workpiece flow will be summarized. The features of the plastic flow rule which are useful to predict the formability of sheet and the workability in bulk processes will be highlighted. To illustrate these concepts, the determination and application of constitutive equations for the hot forging behavior of the high temperature titanium alloy, Ti-6242, will be described, and some deformation induced microstructures will be discussed. Finally, a hierarchy of process mechanics formulations will be discussed so as to emphasize the relaton between model sophistication and predictive capability.

CONSTITUTIVE EQUATIONS

Plastic Flow Law

A general expression for the constitutive equation expressing the functional dependence of the true flow stress is

$$\sigma = \sigma\ (S,\ \dot{\varepsilon},\ T) \tag{1}$$

where S is a structure parameter, $\dot{\varepsilon}$ is the true strain rate, and T is the absolute temperature. In Eq. (1), the parameter S is intended to represent those features of the microstructure which determine the current flow stress of the material. The variable S is an evolutionary parameter in that it evolves with the thermomechanical history of the workpiece. Its current value represents the net structure. In order to focus the discussion, it is helpful to think of S as a parameter with functional dependences similar to those of the yield stress. Thus, S increases with accumulated strain for a material that work hardens and decreases during periods of annealing that lead to recovery or recrystallization. During hot-working, S may be relatively constant if strain hardening or thermal softening are nearly in balance. To apply Eq. (1) in the most general way, both the strain and temperature-time dependence of S would have to be modeled analytically. Phenomena such as strain-induced transformations, which couple strain and thermal variables, would complicate the task further. Modeling at this level is a goal, but certainly not a current reality.

The most common approximation of Eq. (1) is to replace S by the current value of the accumulated plastic strain ε,

$$\sigma = \sigma\ (\varepsilon,\ \dot{\varepsilon},\ T) \tag{2}$$

a constitutive equation form originally proposed by Zener and Holloman [2]. This approximation, of course, limits the consideration of microstructural efforts to those directly caused by strain hardening, eliminating time-dependent effects such as static recovery. However, even for pure strain hardening, there is a fundamental difficulty. This arises because the current flow stress of a material is not a unique functon of accumulated plastic strain, since it may depend on the strain rate and temperature history while the strain was being accumulated. In other words, strain is a path variable, not a state variable, as implied by Eq. (2). However, since the plastic strain is a nearly unavoidable path variable in the description of metalforming processes, a constitutive equation of the form shown in Eq. (2) can be very useful in a practical sense as long as the fundamental limitations are recognized.

Eq. (2) is usually considered in differential form,

$$d\ \ln\ \sigma = \gamma\ d\ \varepsilon\ +\ \nu\ d\ \ln\ \dot{\varepsilon}\ +\ \phi\ dT \tag{3}$$

where the coefficients of strain, strain rate, and temperature increments are given by the respective partial derivatives

$$\gamma\ =\ \frac{\partial \ln \sigma}{\partial\ \varepsilon}\ \bigg|\ \dot{\varepsilon}, T \tag{4}$$

$$\nu = \left.\frac{\partial \ln \sigma}{\partial \ln \dot{\varepsilon}}\right|_{\varepsilon, T} \qquad (5)$$

$$\emptyset = \left.\frac{\partial \ln \sigma}{\partial T}\right|_{\varepsilon, \dot{\varepsilon}} \qquad (6)$$

It is these derivatives which usually enter analytical models for workability, particularly when plastic instability is involved. If the strain, strain rate, and temperature increments in Eq. (3) are thought of as spatial variations within the workpiece, it is seen that the derivatives in question control the tendency for hardening or softening locally and, hence, the tendency to retard or accelerate strain inhomogeniety. Some features of the physical behavior, and analytical modeling of these coefficients will now be discussed in turn.

Strain Dependence

In considering deformation processing over a wide temperature range, one encounters both strain hardening and strain softening behavior. Strain hardening is prevalent for most cold and warm-working processes but is also encountered in some hot-working processes particularly at low strains, say $\varepsilon < 0.3$. As the temperature increases for a work hardening material, thermal softening processes such as dynamic recovery can come into play, and a nearly flat flow curve, with flow stress independent of strain may be obtained. This is frequently referred to as perfectly plastic behavior. For some materials at hot working temperatures, actual flow softening is observed which can have many origins [3]. In single phase materials such as austenitic steel, it is generally due to dynamic recrystallization processes [4]. In materials with two or more phases, such as pearlitic steel or titanium alloys, other processes such as phase transformations, texture softening, or solute redistribution can contribute [5]. In addition to microstructural softening mechanisms, deformation heating can also lead to a reduction in work-hardening rate of actual flow softening.

When strain hardening occurs, it is important to describe it analytically in order to be able to calculate press loads. In addition, for flow-based analyses, since strain hardening partially determines overall strain distribution in a part, an analytical description is important in predicting flow patterns during forming and formability/workability limits related to strain localization. The effect of strain hardening on strain distribution is particularly important in sheet metal formability calculations [6].

In order to model strain hardening, the strain dependence of the flow stress is usually described by empirical equations such as those suggested by Hollomon [7],

$$\sigma = k\varepsilon^n \qquad (7)$$

or Swift [8],

$$\sigma = k(\varepsilon_0 + \varepsilon)^n \qquad (8)$$

The Hollomon equation, though oversimplified for many applications, is the one most frequently invoked. The Hollomon strain hardening exponent n has become a nearly ubiquitous factor in metalforming calculations which include the effect of strain hardening. The Swift equation, which includes three adjustable parameters, is somewhat more flexible in describing work-hardening behavior. The Swift ε_0 can be interpreted in some cases as a prestrain and accounts for a finite yield stress, $k\,\varepsilon_0^n$, at zero plastic strain.

The adjustable parameters in empirical stress-strain laws such as Eqs. (7) and (8) are usually determined by numerical regression on stress-strain data. A convenient way to assess the appropriateness and potential accuracy of a particular regression procedure is to examine a plot of some stress derivative versus either stress or strain [9]. An example is shown in Fig. 2 which illustrates an empirical fit of the tensile stress-strain behavior of 2024-O aluminum sheet at 163°C (325°F) using the Swift equation. For the Swift equation, the derivative γ is related to stress as

$$\gamma = n(\sigma/k)^{-1/n} . \qquad (9)$$

Hence, a plot of log γ vs. log σ should result in a straight line of slope $(-1/n)$ if the Swift equation is an appropriate description. The insert in Fig. 2 shows approximately linear behavior at either high or low stress (or strain) with the break coming at about $\varepsilon = 0.05$. Since the interest in the work referenced (9) was in sheet formability, the Swift parameters were determined to fit the higher strain portion of the stress-strain curve. The excellent fit obtained explicitly for the higher strain regime increases the chance that some extrapolation beyond the strains achieved in the tensile test will be meaningful for metalforming calculations.

For flow softening behavior observed under hot-working conditions, less work has been done in terms of strictly analytical modeling. For single phase materials, where softening is usually due to dynamic recrystallization, the
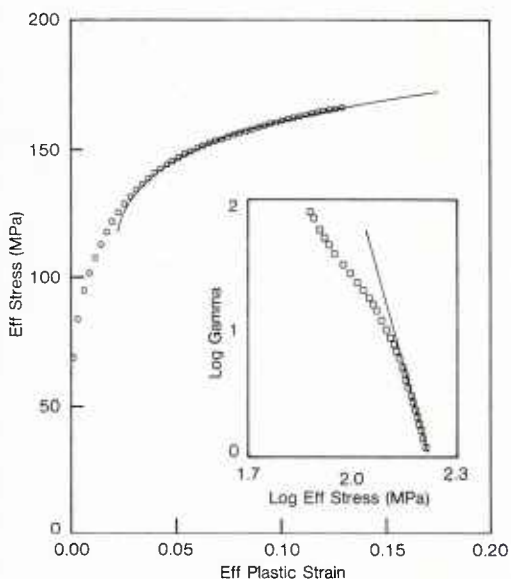

Fig. 2. Effective true stress - strain and workhardening - stress (insert) plots for 2024-O aluminum sheet at 163°C. From [9].

behavior is described in terms of the critical strain to initiate recrystallization, the peak true stress, and the steady state stress [10]. These parameters are, of course, functions of strain rate and temperature. At low strain rates, the flow stress often oscillates due to repeated cycles of dynamic recrystallization. Under these conditions, a steady state stress is difficult to determine.

For multi-phase alloys, it has been found that the strain rate and temperature dependence of the flow softening is similar for a variety of alloys with quite different microstructural features [11,12,13]. This general behavior is shown in Fig. 3 [14,15]. It is seen that the flow softening rate is largest at the lower temperatures in the hot working range and at higher strain rates. Presumably at higher temperature and lower strain rates, the microstructural changes leading to softening occur at rates more in balance with the deformation rate, and the higher stress levels are never reached. For one example of the type of softening behavior shown in Fig. 3, namely for the titanium alloy Ti-6242, an analytical description of the flow softening has been determined in a form suitable for computer modeling of the forging process [13]. This will be discussed in more detail below.
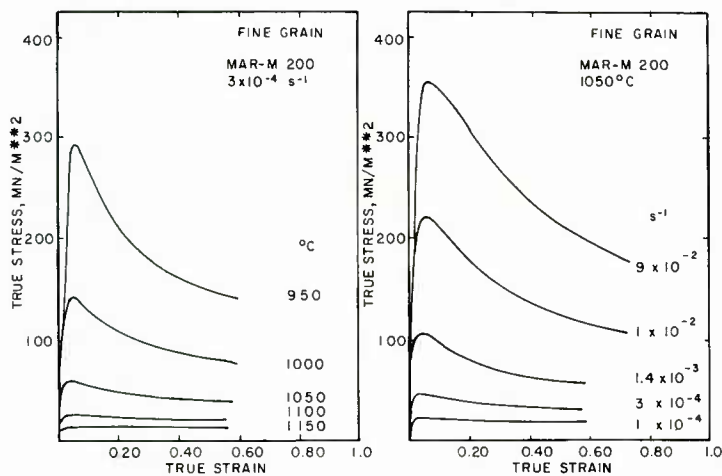

Fig. 3 True stress true strain curves for MAR M200 compacts illustrating effects of temperature (left) and strain-rate (right) on flow softening. From [14].

Strain Rate Dependence

For modeling of flow stress behavior under hot-working conditions, the strain rate dependence of the flow stress is of equal if not greater importance than the strain dependence. When strain hardening and recovery mechanisms are in balance to produce nearly perfectly plastic behavior, constitutive equations are frequently written to represent the strain rate (and temperature) dependence of the flow stress only. The most common example is

$$\sigma = K\dot{\varepsilon}^m \qquad (10)$$

where K is a temperature dependent strength parameter. In this case, the strain rate sensitivity ν, defined by Eq. (5), is simply $\nu = m$ = constant. More generally, of course, the strain rate sensitivity, at constant strain ε, is a function of strain rate and temperature.

Under hot working conditions, the strain rate sensitivity can be quite large, on the order of m = 0.1 to 0.5. For m = 0.3, which is accepted as the minimum m-value for superplastic behavior, a decade increase in strain rate corresponds to a factor of 2 increase in flow stress. At lower temperatures, the strain rate sensitivity is smaller, say m = 0.001 to 0.05. For these m-values, strain rate has a negligible influence on the magnitude of the flow stress. However, even for m-values in this range, strain rate sensitivity can have a large effect on strain localization and the development of instabilities. Both incipient necking and constrained flow, as occurs for example near a die-workpiece contact surface due to friction, lead to strain rate gradients. In regions of increasing strain rate, the strain rate sensitivity leads to strengthening which retards the strain localization process. Thus, strain rate hardening acts like strain hardening to promote uniform strain distribution but only after strain rate gradients develop.

A phenomenological constitutive equation which describes the strain rate dependence of the strain rate sensitivity over a wide range of temperatures has been developed by Hart [16,17,18]. The result is most easily presented in terms of the material behavior at high and low temperature limits. At high temperature, above about one-third the absolute melting temperature,

$$\ln(\sigma^*/\sigma) = (\dot{\varepsilon}^*/\dot{\varepsilon})^\lambda \ . \qquad (11)$$

In this equation, σ^* is an evolutionary parameter equivalent to the parameter S in Eq. (1). The parameter $\dot{\varepsilon}^*$ is functionally related to σ^* and temperature, and λ is a material constant. From Eq. (11), the strain rate sensitivity is

$$\nu = \lambda \ \ln(\sigma^*/\sigma) \qquad (12)$$

which shows that ν decreases as the strain rate and, hence, the flow stress, increases. Below about one-third the melting point, the flow stress is given by

$$\sigma = \sigma^* + \sigma_0 (\frac{\dot{\epsilon}}{\dot{\epsilon}_0})^{1/M} \tag{13}$$

where M is a material constant. In this case, the strain rate sensitivity is

$$\nu = \frac{1}{M} (1 - \frac{\sigma^*}{\sigma}) \tag{14}$$

and, hence, increases as the strain rate and flow stress increase.

The general trends for strain rate dependence described in these equations have been verified for a number of materials [17], and are illustrated here for the titanium alloy Ti-6Al-4V [19] in Fig. 4. This shows the strain rate dependence of the flow stress at three temperatures, as determined by stress relaxation, and presented as a plot of log flow stress vs. log strain rate. The strain rate sensitivity at a particular temperature and strain rate is given by the slope of these curves. It is seen that the strain rate sensitivity increases with strain rate at lower temperatures and decreases with increasing strain rates at higher temperatures, as predicted. There is an intermediate temperature, approximately one-third the melting point, at which the strain rate sensitivity is very small for all strain rates. In general, the strain rate sensitivity is higher for higher temperatures, but this increase may be quite small for high strain rate processes [20].

Temperature Dependence

In general, the flow stress of structural alloys decreases with temperature. It is well accepted that the homologous temperature, the ratio of the absolute temperature to the absolute melting temperature, can be used to define effective temperature regimes for the temperature dependence. For example, hot-working temperatures are restricted to homologous temperatures above 0.5 with 0.6 being a practical lower limit for hot deformation processes. The discussion here will be restricted to the temperature dependence in the hot-working regime.


Fig. 4. Log stress vs. log strain-rate curves for Ti-6Al4V illustrating effect of temperature and strain-rate on strain-rate sensitivity. From [19].

In its simplest form, the description of the temperature dependence of hot deformation assumes thermally-assisted mechanisms such that the strain rate depends on temperature through an Arrhenius factor

$$\dot{\epsilon} = f(\sigma) \exp(-Q/RT) \tag{15}$$

where Q is an apparent activation energy, R is the universal gas constant, and T is the absolute temperature. Eq. (15) is most useful when Q is constant, independent of stress and temperature [21]. Rearranging Eq. (15), we obtain

$$f(\sigma) = \dot{\epsilon} \exp(Q/RT) \cong Z \tag{16}$$

where Z is known as the Zener-Hollomon parameter [22] and can be interpreted as a temperature-compensated strain rate. When Eq. (16) holds, the flow stress temperature coefficient ϕ, defined by Eq. (6), is related to Q as

$$\phi = - \nu Q/RT^2 \tag{17}$$

This provides for an alternate representation for the increment in flow stress with temperature at constant strain and strain rate,

$$d \ln \sigma = \nu Q d(1/RT). \tag{18}$$

The applicability of this equation will be discussed below in relation to the hot-working of Ti-6242 [13,23].

According to Eq. (16), the flow stress is uniquely dependent on the parameter Z, independent of prior deformation history. Conceptually, this implies that for a greater Z, produced by a lower temperature or a higher strain rate (hence, a shorter time), the contribution of thermally activated processes to flow softening will be smaller and a higher value for the instantaneous flow stress will be predicted. While this is a reasonable description, the usefulness of Eq. (16) depends on identifying an activation energy Q which is constant over a sufficiently broad temperature range. For simple alloy systems, predominantly single phase, where a single hot deformation mechanism such as dynamic recovery or recrystallization may govern the deformation behavior, the association of the prevalent mechanism with a constant activation energy Q is a possibility [24]. However, for most structural alloys, the
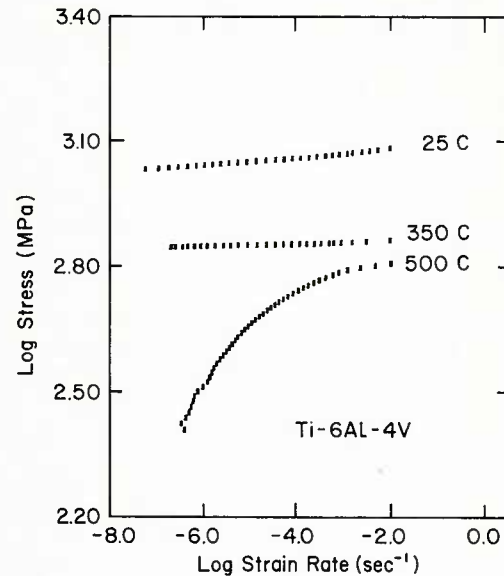
condition of a constant activation energy deformation process usually is not observed over a sufficiently large temperature and strain rate regime. Because of this, the range of application of this formulation is somewhat limited [25].

WORKABILITY

The term workability refers to the maximum amount of strain which a workpiece can provide without failure. This may be difficult to determine, since the strains are rarely uniform during forming operations or even under testing conditions, and it is important to know the approximate value of the local strain at the failure site. Measurement of the local strain is usually complicated by the fact that the failure may initiate in a region of very large strain gradients.

Failure modes can be classified in two broad categories, strain localization by plastic instability and fracture. In addition, fracture mechanisms are quite diverse and depend upon microstructural features such as grain boundary configurations and the existence of second phase particles in addition to process variables such as stress state. In the general case, a failure path may involve both plastic instability and fracture with strain localization due to instability leading to microstructural conditions such as void coalescence which initiate final fracture.

Tensile Instability

The most common failure is localization in a visible neck in a uniaxial tensile test, and it is instructive to consider the relation of necking instability to mechanical properties. In a tensile test, the strain is uniform throughout the gauge section up to the point of maximum load. The load maximum is evidence that a diffuse neck is beginning to develop and corresponds to the condition at which the incremental increase in cross-sectional area becomes greater than the increase in flow stress due to work hardening.

For a strain rate insensitive material, the occurence of a load maximum in the tensile test is equivalent to the strain hardening coefficient γ reducing to the value $\gamma = 1$. This is simply the well-known Considere condition. The influence of strain rate sensitivity on initiation of a diffuse neck was treated originally by Hart [26]. For the common case of a constant extension rate test, the result is that diffuse necking initiates at a slightly larger strain value at which the strain hardening exponent is $\gamma = 1-m$, where m is the strain rate exponent in Eq. (10). Physically, this is due to the gradual decrease of the strain rate tensile test, the Considere condition would remain unchanged. Since m is usually quite small (m = 0.01), and since the beginning of a diffuse neck is difficult to detect, rate sensitivity is of negligible importance in the initiation of necking instability.

On the other hand, rate sensitivity is of critical importance in regard to the growth of a necking instability. If one assumes, for simplicity, that strain hardening has essentially saturated such that $\gamma = 0$, then Hart [26] has shown that the growth of an area defect δA from an original value δA_0 over a period during which A_0 reduces to A is given by

$$\delta A / \delta A_0 = (A_0/A)^{\frac{1}{m} - 1}.$$ (19)

Thus, for small values of m, the localization rate is very large and localized necking follows initiation of a diffuse neck rapidly. On the other hand, for larger m values, a quasi-stable flow can procede for a large strain increment past the point of maximum load. To summarize the situation for instability in tension, strain hardening capacity (γ or n) determines the initiation of localization whereas the strain rate sensitivity determines the rate of growth of the localization. In other words, the strain at the point of maximum load depends on the n value whereas the post-uniform elongation depends on the rate sensitivity m. This has been documented very clearly for both simulated and experimental tests by Ghosh [27]. This description of tensile instability is emphasized here because it illustrates the important complementary features of strain and strain rate hardening.

Biaxial Instability

The analysis of diffuse necking stability was extended from uniaxial to biaxial stress states for application to sheet metal formability studies by Swift [8]. Swift showed that diffuse necking in a biaxially stretched sheet begins when the strain hardening coefficient reduces to a critical value, $0 < \gamma < 1$, which depends on the ratio $\varepsilon_2/\varepsilon_1$, of the principal strains in the plane of the sheet. This treatment was restricted to rate insensitive materials.

As for a tensile specimen, the onset of diffuse necking in a sheet is not readily observable, and, hence, is not equated to failure in a sheet forming process. Plastic instability leads to failure only when a localized neck forms. The condition for a localized neck in a thin sheet was presented by Hill [28]. The neck develops as the result of a localized shear zone which forms along a direction of zero length change. The Hill criterion for the formulation of a localized neck is

$$\gamma \leq (\frac{\partial f}{\partial \sigma_1} + \frac{\partial f}{\partial \sigma_2})/\frac{\partial f}{\partial \bar{\sigma}}$$ (20)

where f is a yield function which accounts for plastic anisotropy, σ_1 and σ_2 are principal stresses in the plane of the sheet, and $\bar{\sigma}$ is the effective stress. From Eq. (20) a general result (29) is that

$$\varepsilon_1 + \varepsilon_2 = \gamma \bar{\varepsilon}$$ (21)

where ε_1 and ε_2 are the principal limit strains and the critical γ and $\bar{\varepsilon}$ depend on ε_1 and ε_2

through the definition of $\bar{\epsilon}$. If constitutive equation and anisotropic yield function parameters are known, Eq. (21) represents a specific forming limit curve (FLC) which can be plotted to illustrate the separation of safe strain states from those for which failure by localized necking is expected. For the Hill model, the FLC is restricted to negative minor strains, $\epsilon_2<0$, since no directions of zero length change exist in the plane of the sheet for biaxial tension.

A typical FLC for 2024-0 aluminum [9] is shown in Fig. 5 and is compared to experimentally determined forming limits (the forming limit diagram or FLD) obtained by measuring local strain values on electrochemically gridded sheets which had been stretched to failure. The agreement between the calculated FLC and experimental FLD is good for in-plane (tensile) tests which correspond to the geometry used for the Hill calculation. The higher limit strains obtained by punch stretching are not, at present, well understood [6]. It is also important to note that no way has been found to include strain rate effects explicitly in the Hill theory. Thus, comparisons of the Hill theory with experiment should be limited to materials such as 2024 aluminum at room temperature for which the strain rate sensitivity is very small.
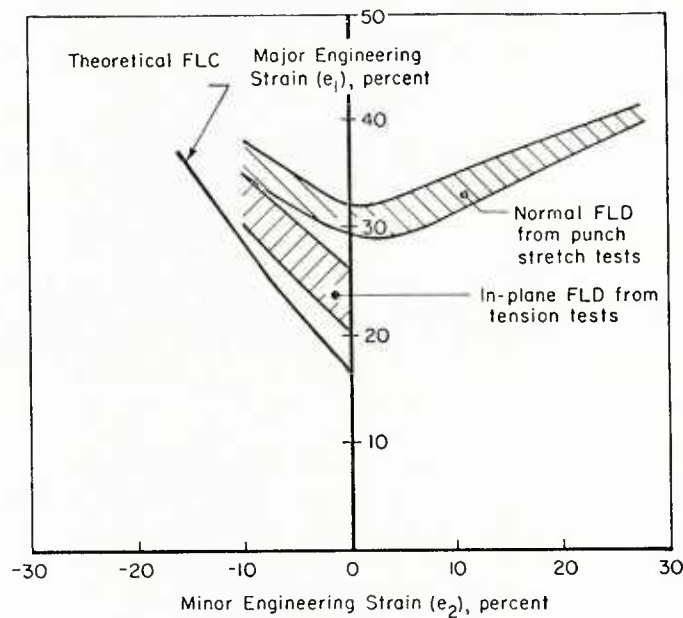
Fig. 5. Theoretical forming limit curve calculated from Hill theory compared to experimental forming limits for 2024-0 aluminum. From [9].

In order to extend plastic instability failure models for sheet formability to positive minor strains and to include the effects of rate sensitivity, a different failure criterion is needed. The most successful has been one developed by Marciniak and co-workers (30,31) who postulated the localization of strain to a pre-existing defect, generally pictured as a thickness groove across the plane of the sheet. The defect severity is defined in terms of a parameter f (not to be confused with the f in Eq. (20)) which is taken as the ratio of the sheet thickness in the groove to that outside the groove,

$$f = 1 - t_{og}/t_o \, . \tag{22}$$

Similar results for forming limits can be obtained if the defect is described in terms of a localized metallurgical weakness.

Details of the Marciniak calculation have been reviewed elsewhere recently [6] and will not be described here. To apply the theory, one needs to model strain hardening behavior, $\gamma(\epsilon)$, strain rate sensitivity, and select a yield function which also accounts for plastic anisotropy. A particularly difficult question is identification and justification of an appropriate defect severity f. It may be that this must remain an arbitrary parameter to be fit to experimental forming limit data. One interesting comparison is that, under certain conditions for negative minor strains, the Hill theory can be thought of as the f=0, m=0 limit of the Marciniak theory. This has recently been pursued quite successfully by Chan et al. [32]. Otherwise, the overall appropriateness and success of the Marciniak theory is still being evaluated.

Compressive Instability

The discussion to this point has been primarily concerned with formability under conditions of imposed tensile stress. For workability in processes and tests which involve imposed compressive stresses, several different modes of failure must be considered. These include shear bands [33], free surface fractures [34], and internal grain boundary and triple point cracks [35]. Again, the initiation and growth or propagation of these defects can be related to material constitutive relation parameters and their dependence on process variables such as temperature and strain rate.

An important defect in hot forging is the shear band. A shear band is a region of highly localized deformation with a planar geometry and a width which extends across many grains. While the term shear band is sometimes used to refer to microscopic inhomogeneities related to local dislocation or twin

distributions, it is used here to refer to a macroscopic phenomenon which can clearly be observed by microetching. An example, for an isothermally sidepressed cylinder of the titanium alloy Ti-6242, is shown in Fig. 6.

Shear bands develop during deformation along interfaces between adjacent regions of discontinuous deformation such as the dead zone near a compression die and a central region of high strain. The dead metal zone at the die surface can result from either a frictional constraint due to poor lubrication or, for non-isothermal conditions, from die chilling which markedly increase the local flow stress. Once initiated, a shear band is likely to become self-propagating because the large strains in the band promote softening due to deformation heating and, in some cases, strain-induced microstructural softening. Clearly the large localized strains lead to microstructural changes which may produce defects such as potential sites for crack initiation.

For hot forging, the incidence of shear bands can be related to a specific set of material properties. These can be identified by extending the analysis for tensile instabilities discussed above. Hart's analysis [26] of tensile instability has been applied to compressive deformation by Jonas et al. [36]. They postulated a local areal bulge as the analogy to a tensile neck. However, the local increase in area due to a bulge is a stabilizing influence as compared to the destabilizing influence of a tensile neck. Hence, local bulging will only lead to gross instability if a destabilizing influence such as flow softening predominates.

Using the fact that the load on any cross-sectional area must be constant along the forging axis, $\delta F = 0$, and representing variation of the stress in terms of corresponding variations in strain, strain rate, and temperature as in Eq. [3], the following relation is obtained:

$$\delta A/A + \gamma\delta\epsilon + \nu\delta\ln\dot{\epsilon} + \phi\ \delta T = 0 \qquad (23)$$

Here, γ, ν, and ϕ are the flow parameters defined in Eqs. (4-6), and it is emphasized that the differentials in Eq. (23) such as $\delta\epsilon$ correspond to variations along the forging axis. Strain localization is defined in terms of an increase in compressive strain rate with an increment of compressive strain by the parameter

$$\alpha = -\delta\ln\dot{\epsilon}/\delta\epsilon\ . \qquad (24)$$

The negative sign is included so that α will be positive for compressive localization considering the usual sign convention that strain, strain rate, and their increments are all taken to be negative. Combining Eqs. [23] and [24], the rate of localization α is given by

$$\alpha = (-1 + \gamma + \phi\delta T/\delta\epsilon)/\nu\ . \qquad (25)$$

For initially isothermal conditions and assuming no deformation heating ($\delta T = 0$), the expression for the localization parameter reduces to

$$\alpha = (\gamma-1)/\nu \qquad (26)$$

Since α must be positive for localization to occur, localization is initiated at $\gamma = 1$. For the usual convention that compressive stress as well as strain and their increments are negative, γ is positive for strain softening and negative for strain hardening. Hence, for isothermal conditions, instability will only be initiated if strain-induced microstructural softening occurs. Once initiated, the rate of localization is determined largely by the strain rate sensitivity ν which is always positive. Since the strain rate sensitivity decreases with increasing strain rate, the rate of instability will be more rapid for high strain rate deformation.

The term in Eq. (25) which is proportional to δT decribes deformation heating or die chilling. The influence of deformation heating was first treated by Dadras and Thomas (37). By noting that

$$\delta T/\delta\epsilon = \eta\sigma/\rho c, \qquad (27)$$

temperature variations due to deformation heating can be included in the expression for α as

$$\alpha = \left(-1 + \gamma + \eta\frac{\partial\sigma}{\partial T}/\rho c\right)/\nu \qquad (28)$$

In these equations ρ is the density, c is the heat capacity, and η is a factor which accounts for the fraction of deformation work which is effective in increasing the workpiece temperature. For this analysis, it is convenient to define

$$\gamma' = \gamma + \eta\frac{\partial\sigma}{\partial T}/\rho c \qquad (29)$$

so that the instability condition becomes

$$\alpha = (\gamma'-1)/\nu\ . \qquad (30)$$

Since the temperature derivative of the flow stress is positive for compression (the flow stress becomes less negative with increasing temperature), the second term in Eq. (29) is positive, and the effect of deformation heating is to promote the initiation and rate of localization. In addition to the tendency for localization to be promoted by increasing strain rate due to a lower rate sensitivity, the second term in the expression for γ' also increases with strain rate due to the combined effects of higher flow stress and larger η. One convenience of the parameter γ' is that it describes the strain rate dependence of the flow stress in constant true strain rate compression tests.

While this analysis is qualitatively applicable, none of these expressions apply directly to shear bands, since these are best observed under plane strain rather than axisymmetric conditions. Shear bands occur along directions of zero length change and, correspondingly, no change in area. Semiatin and Lahoti (38) pointed out that for these conditions one expects $\delta\sigma = 0$ along the forging axis. The result is that Eq. (30) becomes

$$\alpha = \gamma'/\nu . \tag{31}$$

Hence, because of the geometrical influence of plane strain, instability can initiate at $\gamma' = 0$ instead of $\gamma'=1$. For a given γ' and ν, α will be larger and shear band formation more likely and more rapid. When gross instabilities corresponding to shear bands are observed under initially axisymmetric conditions, a change in strain state toward plane strain will have occurred.

For non-isothermal forging which is the conventional situation, the forging dies are up to several hundred degrees celsius cooler than the workpiece and severe die chilling can occur. If one assumes no microstructural hardening or softening ($\gamma = 0$) and plane strain conditions, then Eq. (23) can be written as

$$\delta\ln\dot\varepsilon = -\phi\delta T/\nu . \tag{32}$$

It is convenient to emphasize the fact that the variations are spatial by writing

$$\delta\ln\dot\varepsilon/\delta x = -(\phi/\nu)\delta T/\delta x . \tag{33}$$

Here it is seen that the tendency toward localization is driven by the temperature gradients which depend upon temperature differences, thermal conductivities, and the time available for temperature gradients to develop. As for the deformation heating effect, localization increases with the temperature dependence of the flow stress and is inversely proportional to the strain rate sensitivity.

Based on this discussion, it is possible to summarize the material flow parameters which influence shear band formation. Strain softening γ, strain rate sensitivity ν, and flow stress temperature dependence ϕ are of primary importance. Equally important is the dependence of these parameters on strain rate and temperature. For non-isothermal conditions, thermal conductivity of both workpiece and die and the conductance of the lubricant also play important roles.

MODELING OF TI-6242

A recent example of process modeling and flow-based analysis for hot-working focused on the design of the forging process for a Ti-6Al-2Sn-4Zr-2Mo(0.1Si) turbine engine compressor disk [39]. Ti-6242 is a near alpha, alpha-beta titanium alloy which is a candidate material for intermediate temperature (500°C) applications in compressor disks, blades, and other critically stressed components in high performance jet engines. For this type of titanium alloy, two preform microstructures are most common. A microstructure of equiaxed alpha phase in a matrix of transformed beta phase is provided by hot working and subsequent heat treatment below the beta transus temperature (990°C for Ti-6242). This microstructure is termed $\alpha + \beta$ and is known to produce good high temperature fatigue properties. Hot-working and heat treatment above the beta transus temperature results, upon cooling, in a Widmanstatten alpha of basketweave microstructure. This will be termed the transformed β or, simply, β microstructure and is known to have good high temperature creep properties. These microstructures are shown in Fig. 7. Several studies have been completed of both the mechanical behavior under hot forging conditions [13,38] and the deformation microstructures induced by hot forging for Ti-6242 [23]. These results have also been used to analyze the workability of this material with respect to the occurrence of shear bands [40,41]. The work to be summarized here is primarily related to the development of analytical constitutive equations for Ti-6242 [13] and their relation to deformation induced microstructures [23].

A factor of considerable importance in understanding the deformation behavior of this alloy is the relative stability of the two basic microstructures just described. From a morphological standpoint, the $\alpha + \beta$ microstructure is essentially stable whereas the β microstructure, produced during nonequilibrium cooling, is metastable at subtransus temperatures. Hence, during hot working below the transus, a β preform microstructure evolves toward the $\alpha + \beta$ microstructure, and the nature and extent of this transformation depend upon temperature, strain, and, to a lesser extent, the strain rate. This allows the possibility of controlling the final microstructure and property distribution in a Ti-6242 forging by control of preform geometry, which determines the strain distribution, and hot-forging process variables. The goal of the work discussed and referenced here is the design of a Ti-6242 turbine engine compressor disk with a gradient in properties from the bore to the rim [39].

Flow Behavior of Ti-6242

Upset compression tests were used to determine the flow stress of Ti-6242 as a function of strain and strain rate over a temperature range of 816°C to 1010°C. Results to be discussed are for tests conducted at strain rates of 10^{-3}, 10^{-2}, and 10^{-1} s^{-1}, but other investigations covered higher strain rates [23,42].

Representative plots of true stress vs. true plastic strain are shown in Fig. 8. In general, deformation induced flow softening was observed under most test conditions for both $\alpha + \beta$ and β specimens. For the $\alpha + \beta$ specimens, the observed softening is attributed primarily to deformation heating. For example, the 10^{-3} s^{-1} strain rate test shown in Fig. 8 is at a sufficiently slow strain rate that it is assumed to be isothermal, and it is seen that the flow stress is essentially constant. For the $\alpha + \beta$ test at 10^{-1} s^{-1}, a deformation heating correction of the flow curve also leads to a nearly constant flow stress. However, for the β microstructure, a deformation heating correction is a much smaller fraction of the observed softening, and true microstructural softening is the dominant feature. An explanation of this fact is thought to be related to the observation that the flow curves at corresponding
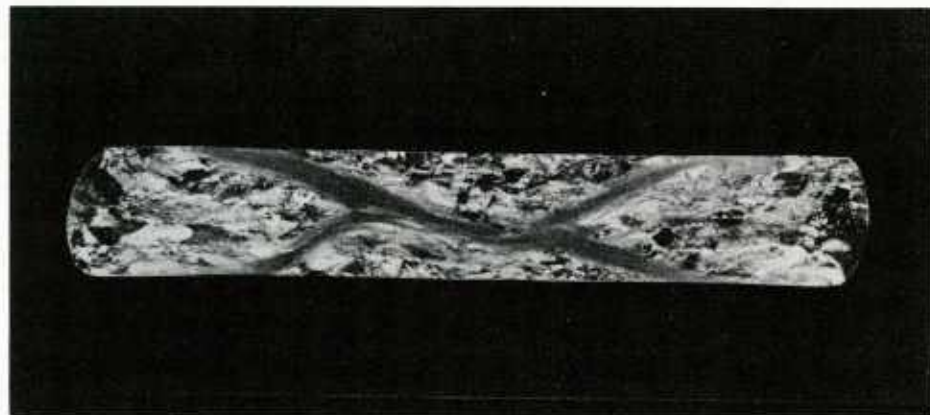
Fig. 6. Transverse section of an isothermally sidepressed cylinder of Ti-6242 illustrating macroscopic shear bands. Width of the section is approximately 1 inch (25 mm). From [33].


(a)

50μm

(b)
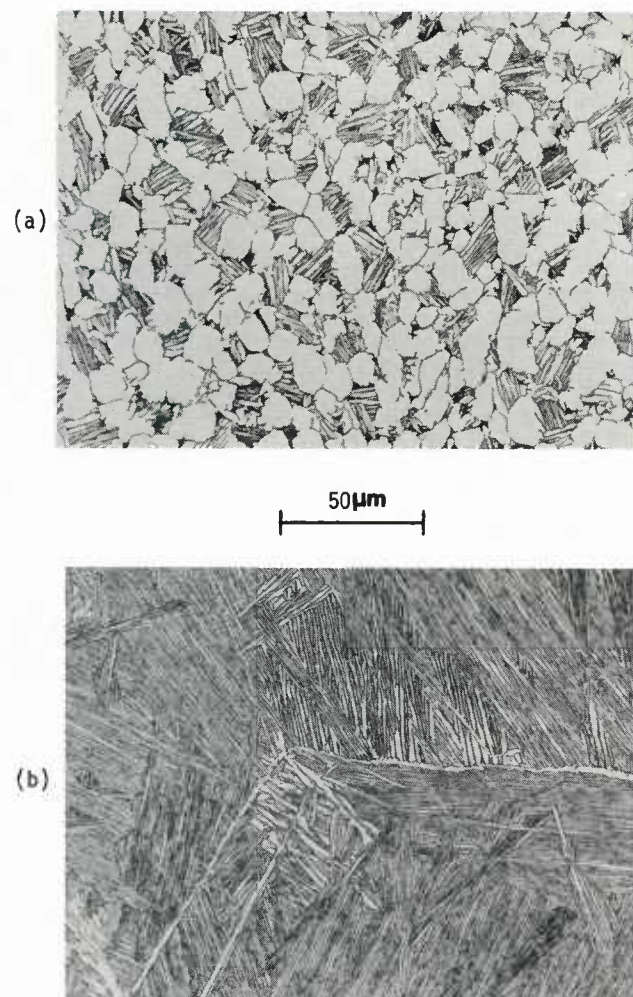
Fig. 7. Optical micrographs of (a) equilibrium alpha + beta and (b) metastable transformed beta microstructures of Ti-6242.

temperatures and strain rates for the α + β and β specimens gradually approach each other as seen for the two test conditions in Fig. 8. At a true strain of ε = 0.6 the flow stress levels become nearly the same for any temperature and strain rate in the regime investigated. This is taken as evidence that, during hot deformation, the metastable β microstructure is evolving toward the equilibrium α + β microstructure.
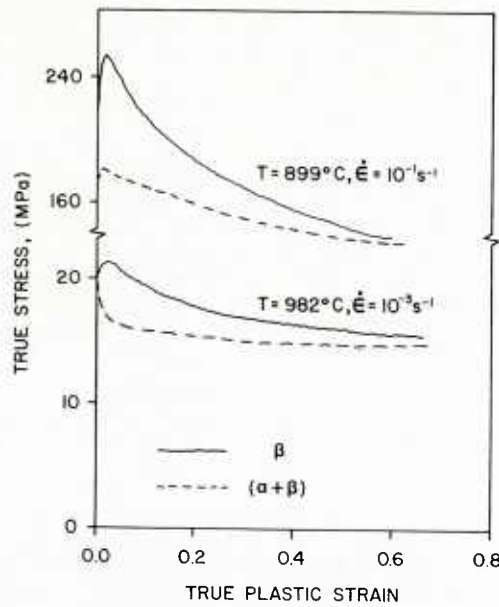

Fig. 8. True stress vs. true strain flow curves for (α + β) and (β) microstructures of Ti-6242. From [13].

Temperature and Strain Rate Dependence

A revealing description of the temperature dependence of the flow stress of Ti-6242 can be obtained by plotting log flow stress vs. inverse absolute temperature for the early stages of deformation for tests conducted at various strain rates as shown in Fig. 9. The data in this figure at strain rates of 2 and 10 s⁻¹ are taken from reference [42]. These plots result in a series of straight lines for which the slopes are proportional to the product νQ (see Eq. (18)). It is seen that, for both preform microstructures, the slopes are independent of strain rate. For the α + β microstructure, Fig. 9(a), an overall linear behavior is observed; for the β microstructure, Fig. 9(b), a more complicated bilinear behavior results which separates the temperature dependence into "high" and "low" temperature regimes. It will be seen that these regimes correlate with distinct deformation-induced microstructures.
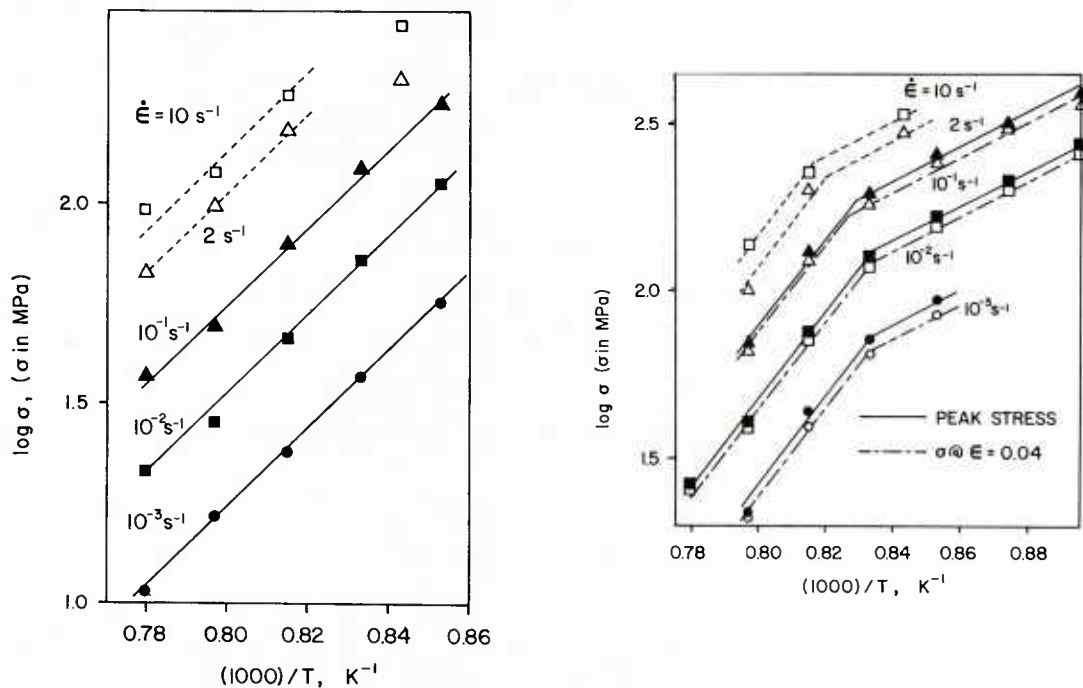

Fig. 9. Plots of log σ vs. 1/T for (o) (α + β) microstructure and (b) (β) microstructure for the early stages of deformation. From [13].

In conjunction with the temperature dependence, it is important to examine the strain rate dependence of the flow stress. It is found that this rate dependence is qualitatively similar to that shown for Ti-6Al-4V at 500°C in Fig. 4, that is, the strain rate sensitivity ν increases with decreasing strain rate [13]. The important point is that the strain rate sensitivity of Ti-6242 is not a constant but varies by a factor of two or more with strain rate over the strain rates and temperatures investigated. Since ν depends significantly on strain rate, it is surprising that the log σ vs. 1/T slopes do appear to be independent of strain rate. Since ν is not constant, neither is Q, and the Zener-Hollomon description (Eq. (16) breaks down. If it was forced, by using an average value of Q, the description would be very approximate.

Deformation-Induced Microstructures

The plot of the temperature dependence of the flow stress for the β microstructure (Fig. 9(b)) shows that the temperature separating the high and low temperature regimes is approximately 930°C at the lower strain rates and increases slightly with temperature. The deformation-induced microstructures which occur in the low temperature regime are illustrated for deformation at 899°C (1650°F) and a strain rate of 2×10^{-3} s^{-1} in Fig. 10(a). The microstructure shows very nonuniform deformation as characterized by two distinct features: (1) the occurrence of regions of intense localized shear which result in sharp curvature of the α and β platelets in the Widmanstatten structure and the grain boundary α and (2) a localized breakup and spheroidization of the α and β platelets in the Widmanstatten structure [23]. The first feature begins to appear at a strain of approximately $\varepsilon = 0.2$ while the second appears at somewhat higher strains and is still incomplete at a strain $\varepsilon = 1$. It is thought that the first feature essentially preceeds the second, with the regions of intense shear providing a high enough stored energy density to initiate the spheroidization. The observation of curved platelets after deformation at lower strain is evidence that the β microstructure morphology is thermally stable with the spheroidization occuring during deformation.

Deformation-induced microstructures typical of the high temperature regime are illustrated in Fig. 10(b). In this temperature regime the deformation is more uniform with a general trend toward thicker α plates and an overall coarsening of the structure, features which are also developed by heat treatment alone. This suggests that the observed homogeneity is at least partly related to microstructure developed during preheating prior to deformation (23). The microstructures observed following deformation in the high temperature regime are much less dependent on strain than those which occur in the low temperature regime.

The as-deformed β microstructures show no clearly visible indication of evolving toward the equilibrium $\alpha + \beta$ microstructure as suggested by the flow behavior in Fig. 8. This evolution does, however, become apparent after post-deformation heat treatment. The microstructure of a specimen deformed at 899°C and, subsequently, heat treated at 954°C is shown in Fig. 11(a) and can be compared to an $\alpha + \beta$ specimen heat treated for two hours at the same temperature, Fig. 11(b). It is clear that the highly deformed regions have now recrystallized, and these regions appear similar to the equilibrium $\alpha + \beta$ microstructure. Thus, in a deformation process, the evolution of microstructure from a creep-resistant transformed β structure to the more fatigue-resistant $\alpha + \beta$ structure can be controlled by controlling the strain distribution in the product.

Analytical Flow Laws

In order to avoid both extensive die chilling and gross plastic instabilities which are likely at very high strain rates, Ti-6242 is usually forged isothermally at strain rates on the order of $\dot{\varepsilon} = 10^{-2}$ s^{-1}. Hence, in order to describe the flow behavior of Ti-6242 in a manner appropriate for input to computer-based forging process models, it is sufficient to model the flow stress over a strain rate range of 10^{-3} s^{-1} to 10^{-1} s^{-1}. Similarly, microstructural considerations suggest that a temperature range of 982°C > T > 871°C is sufficient. The modeling scheme will be to account for the temperature and strain rate dependence of the initial flow stress and, separately, the flow softening observed for the β microstructure. The equilibrium $\alpha + \beta$ microstructure will be considered perfectly plastic, with flow stress independent of strain, over the flow regime considered. This analysis was first presented in reference [13].

For the regimes to be considered, the temperature and strain rate dependence of the initial flow stress shown in Fig. 9 can be described by the following equations:

$$\log \sigma = 9850/T - A \text{ for } (\alpha + \beta) @ 1283K \geq T \geq 1144K \tag{34}$$

$$\log \sigma = 13100/T - B \text{ for } (\beta) @ 1283K \geq T \geq T' \tag{35}$$

$$\log \sigma = 5230/T - C \text{ for } (\beta) @ T' \geq T \geq 1144K \tag{36}$$

where T' is the transition temperature separating the two β miscrostructural regimes and the intercepts A, B, and C are given by

$$A = 0.0350X^2 - 0.1090X + 5.992 \tag{37}$$

$$B = 0.0180X^2 - 0.1710X + 8.398 \tag{38}$$

$$C = 0.0345X^2 - 0.0765X + 1.956 \tag{39}$$

with $X = \log \dot{\varepsilon}$. The very exact linear or bilinear behavior seen in Fig. 9 guarantees that this representation will be quite accurate. A maximum discrepancy of 7 percent has been determined.

These equations can be used to determine the strain rate dependence of the transition temperature T' which separates the high and low temperature regimes. The calculated values of T' vary from 924° C to
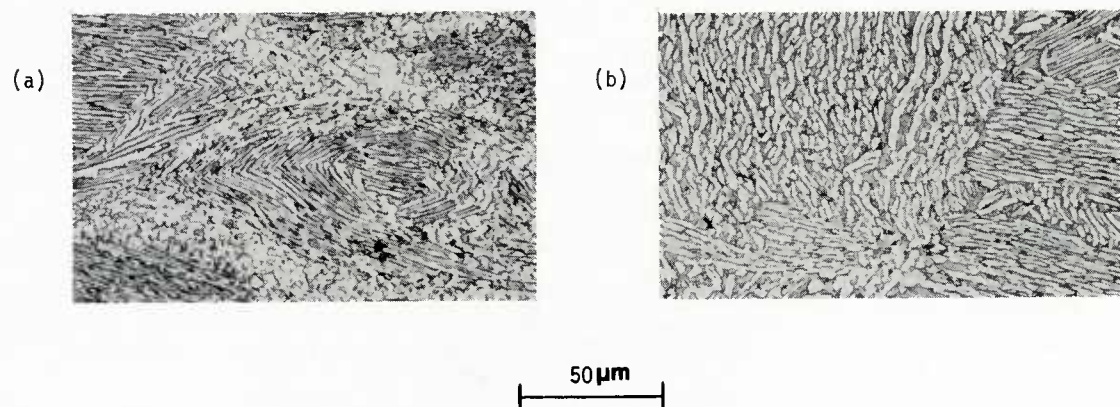
Fig. 10. Microstructure of transformed beta Ti-6242 deformed to a strain of 1.0 and a temperature (a) T = 899°C and (b) T = 954°C. The lower temperature deformation results in distinct, nonuniform microstructural features. From [23].
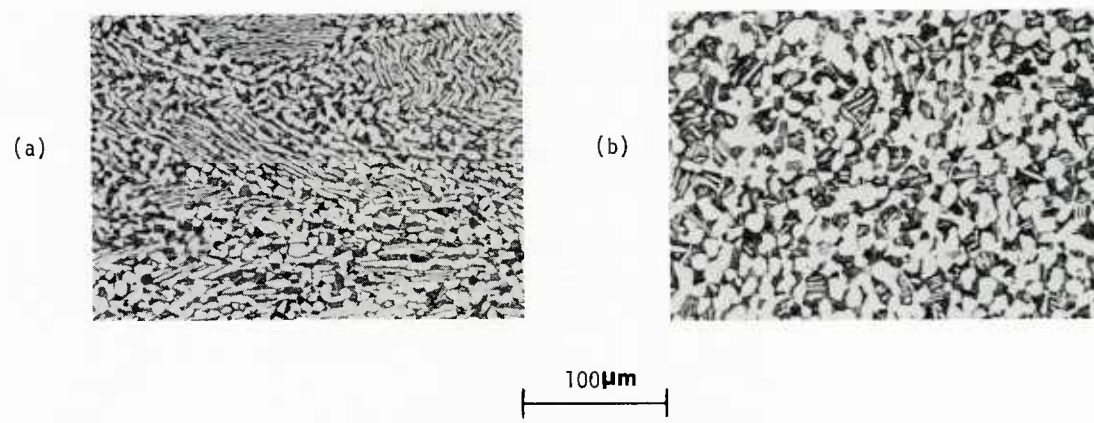

Fig. 11. (a) Microstructure of transformed beta Ti-6242 deformed at T = 899°C to a strain of 1.0 and heat-treated for four hours at T = 954°C compared to (b) microstructure of equilibrium alpha + beta Ti-6242 heat-treated for two hours at T = 954°C. From [23].

970°C as the strain rate increases from 10^{-3} s^{-1} to 10 s^{-1}. This was found to be consistent with the maximum temperature at which the inhomogenious deformation – induced microstructures, illustrated in Fig. 10(a), were observed for deformation at various strain rates, even though the higher strain rate requires an extrapolation outside the modeling range considered.

The remaining task is to model the flow softening behavior of the β microstructure. Recall that the strain dependence of the flow stress measured in a constant true strain rate compression test is given by the parameter γ' defined in Eq. (29). The parameter γ' has been determined from the Ti-6242 flow curves by differentiating digital stress-strain data numerically. By superimposing plots of γ' vs. strain as shown in Fig. 12(a), it is noticed that a unique pattern of behavior, idealized in Fig. 12(b) is obtained. The irregularities in Fig. 12(a) are due to serrations in the flow curves, and Fig. 12(b) shows the smoothed behavior.

Based on this figure, the following expressions are obtained:

$$\gamma' = ae^3 + be^2 + ce + f \quad \text{for } 0 \le e \le e_s,$$

$$= (e_0-e)s/e_0 \text{ for } e_s \le e \le e_0 \tag{40}$$

Several of the parameters in this equation are defined in Fig. 12(b) whereas the constants a, b, and c are determined from the boundary conditions at $e = e_s$, namely the continuity of γ' and its first and second derivatives with respect to e. The latter, of course, vanishes due to the linear segment from e_s to e_0. Substituting for a, b, and c, in Eq. (40) and integrating, the result is
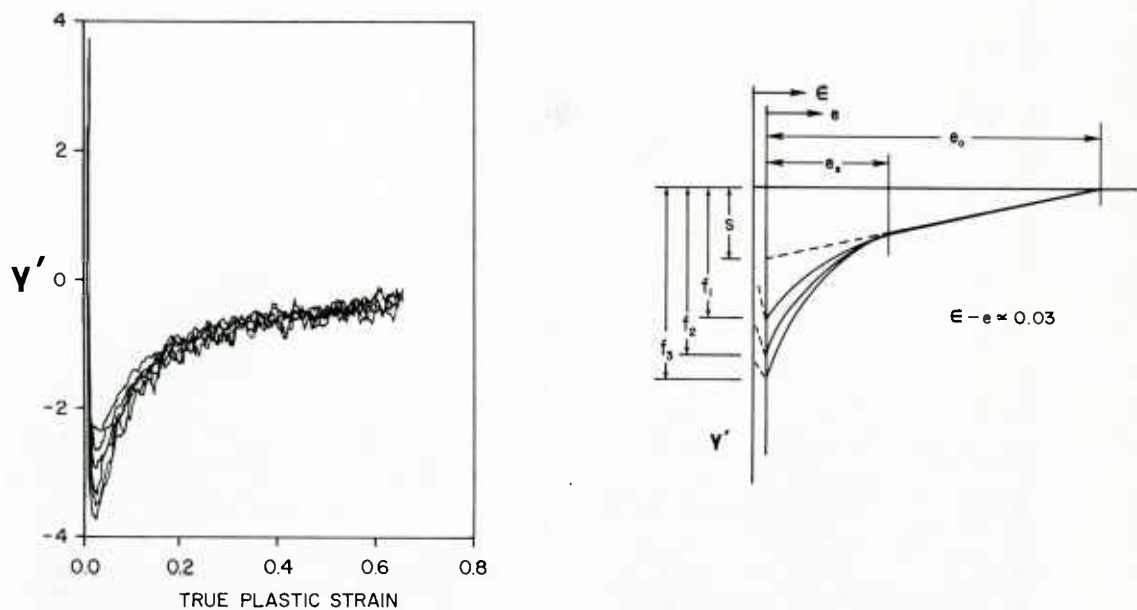

Fig. 12. Plots of γ' vs. strain ε for the (β) microstructure. (b) is an idealized representation of (a) and defines model parameters. For convenience, compressive stress has been taken as positive reversing the model sign of γ'. From [13].

$$\ln \sigma = -\frac{(f-s)}{4e_s^3} e^4 + \frac{(f-s)}{e_s^2} e^3 - \frac{s}{2e_0} e^2 - \frac{3(f-s)}{2e_s} e^2 + fe + c_1 \quad \text{for } 0 \le e \le e_s,$$

$$= se - \frac{se^2}{2e_0} + c_2 \text{ for } e_s \le e \le e_0. \tag{41}$$

At $e = 0$, $\sigma \cong \sigma_p$, the peak stress. Also, at $e = e_s$, the governing flow stress equations for the two strain intervals should yield the same σ. It follows that $c_1 = \ln \sigma_p$ and $c_2 = \ln \sigma_p + (f-s) e_s/4$. For Ti-6242 with the β microstructure, $s = -1.07$, $e_s = 0.34$, and $e_0 = 1.00$. Consequently, only two parameters, namely σ_p and f, are needed in order to obtain a complete description of the flow curves. The peak stress σ_p is determined from Eqs. (34-39) for the given values of temperature and strain rate, and the parameter f is obtained from,

$$f = -1 - [17.456 - 0.044(\log \dot{\varepsilon})^5]X/(25 + X^2), \tag{42}$$

where $X = 0.1(984-T)$ with T in °C.

The predicted flow curves, for three combinations of temperature and strain rate, are shown in Fig. 13. It is seen that the analytical description describes the flow softening behavior of this alloy very accurately. This is important since flow softening is the primary material (as opposed to process) variable which controls the initiation of plastic instability, and an accurate description of flow softening is needed for subsequent process models.
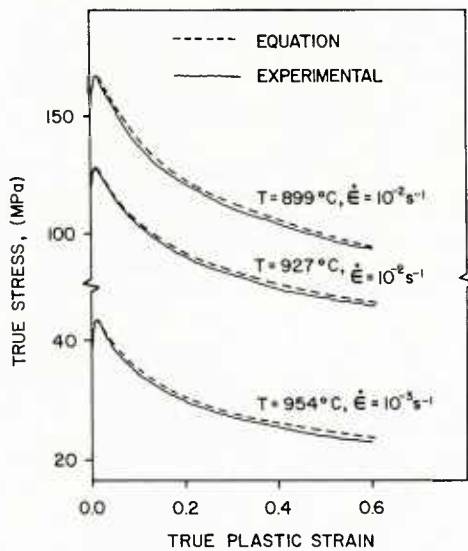
Fig. 13. Comparison of predicted and measured flow curves for the (β) microstructure. From [13].

PROCESS MODELS

In most deformation processes, geometrical and frictional constraints lead to very complicated, non-uniform distributions of stress and strain within the product. In fact, even for highly symmetrical geometries such as axisymmetry or plane strain, the situation is sufficiently complicated that analytical solutions for stress, strain and strain rate distributions are usually only possible under assumptions which turn out to be highly restrictive and prevent the consideration of realistic material behavior models. A further complication results when it is necessary to consider coupled stress - temperature effects in order to account for deformation heating or die chilling.

The usual attempts at an analytical solution involve either the slab method or the upper bound method. The slab method (43) is a stress analysis approach which is based on solutions of the force equilibrium equations using a yield criterion and a constitutive law for stress-strain dependence. The equilibrium equations are written for typical geometrical elements of the deforming body, and the deformation is usually considered homogeneous. In spite of these assumptions, the slab method is still considered useful, but principally for calculating average or integrated process variables such as press load.

In the upper bound method, the analysis is based on velocity field equations describing material point movements during deformation. The velocity field must be kinematically admissable, which implies that velocities and their derivatives must be continuous inside each deformation zone, and that the normal component of velocity across any zone boundaries must also be continuous. Additionally, incompressibility and boundary conditions must be satisfied. The upper-bound solutions are not exact, as the resulting stress components need not satisfy the equilibrium equations. The development of successful upper-bound solutions requires an understanding of the key features of a process so that an optimum model can be obtained.

Some of the limitations of the slab and upper bound methods have recently been overcome by extensions of these techniques developed for the problem of axisymmetric upsetting. A new method [44,45] based upon force equilibrium eliminates the simplifying assumptions of the slab method and provides a more accurate solution based on assumed, but realistic, stress distribution functions. For upset forging, this method allows calculation of the boundary of the elastic (or dead) zone in contact with the die, the shape of the side-surface bulge, and the distribution of stresses within the forged billet. A limitation is specialization to a specific geometry.

A method has also been developed to extend the upper-bound method. Existing upper-bound calculations do not provide information on nonuniform deformation patterns and localized stresses and strains, even for the case of axisymmetric upsetting of interest here. In order to provide such information, an analysis based on flow pattern observations has been developed [46]. For the cylindrical billet being upset, a four zone deformation pattern is assumed and realistic, admissable velocity fields are proposed. The solution allows the calculation of deformed grid patterns, localized stresses and strains, and side-surface foldover in close agreement with experimental observations and more sophisticated finite-element calculations.

In spite of these improvements in the more traditional process analysis, numerical techniques such as the finite-element method (FEM) are still needed for detailed, localized calculations of stress and strain distributions which are generally required to realize the full potential of flow-based analysis for deformation processes. A recent, important advance which greatly enhances the efficiency of the FEM for metalforming calculations is the development of the matrix method program ALPID (Analysis of Large Plastic Incremental Deformation)[47]. The increased efficiency of ALPID is due, in part, to the use of advanced elements with quadratic or cubic displacement functions. Also, the program is set up to use rigid-viscoplastic constitutive relations, as elastic deformation is of negligible importance in most metalforming applications. In addition, the program can be applied to a wide variety of workpiece-die geometries. While the program ALPID has been applied to a variety of calculations related to the hot

forging of Ti-6242, one of particular interest and related to the thrust of this paper involves the modeling of strain localization in isothermal sidepressing of Ti-6242 cylinders [48]. In this work, ALPID was applied to calculate the strain rate distribution for cylinders of both the α + β and transformed β microstructures. The only major difference in the modeling for these two cases is the extensive flow softening which characterizes the β microstructure. The results of this calculation can be described in terms of several features of the strain rate distribution at 50 percent reduction in height. For the α + β microstructure, strain rate contours do not show large gradients over the cross-section. In contrast, the β microstructure does show large strain rate gradients over the cross-section. The strain rate gradients and contours provide a clear indication of shear band initiation in the process simulation. The important point is that this occurs as a natural consequence of material properties and geometry, that is flow softening and plane strain. This calculation provides an excellent example of the progress that has been made in flow-based analysis of deformation processing.

ACKNOWLEDGEMENTS

REFERENCES

1. N. Rebelo, H. Rydstad, and G. Schroder, "Simulation of Material Flow in Closed-Die Forging by Model Techniques and Rigid Plastic FEM," in NUMERICAL METHODS IN INDUSTRIAL FORMING PROCESSES, ED. BY J.F. Pittman Pineridge Press, Swansea UK. 1982, pp. 237-246.

2. C. Zener and J. H. Hollomon, "Problems in Non-Elastic Deformation of Metals," J. Appl. Physics, Vol. 17, 1946, pp. 69-82.

3. J.J. Jonas and M.J. Luton, "Flow Softening at Elevated Temperatures," in ADVANCES IN DEFORMATION PROCESSING, ed. by J.J. Burke and V. Weiss, Plenum Publishing Co., 1978, pp. 215-243.

4. C. Rossard, Metaux Corros. Inds., Vol. 35, 1960, pp. 102-115, 140-153, and 190-205.

5. S.L. Semiatin and G.D. Lahoti, "Deformation and Unstable Flow in Hot Forging of Ti-6Al-2Sn-4Zr-2Mo-0.1Si," Met. Trans. A, Vol. 12A, 1981, pp. 1705-1717.

6. J.F. Thomas, Jr. and P. Dadras, "Modeling of Sheet Forming Processes - An Overview," in EXPERIMENTAL VERIFICATION OF PROCESS MODELS, American Society for Metals, Metals Park, OH, 1983.

7. J.H. Hollomon, "Tensile Deformation," Trans. AIME, Vol. 112, 1945, pp. 268-290.

8. H.W. Swift, "Plastic Instability Under Plane Stress," J. Mech. Phys. Solids, Vol. 1, pp. 1-18.

9. V. Nagpal, B.S. Shabel, J.F. Thomas, Jr., and H.L. Gegel, "Formability Models for 2024-0 Aluminum Alloy Sheet Material," in PROCEEDINGS NAMRC VII, Society of Manufacturing Engineers, Dearborn, MI, 1979, pp. 172-179.

10. H.J. McQueen and J.J. Jonas, "Recovery and Recrystallization during High Temperature Deformation," in TREATISE ON MATERIALS SCIENCE AND TECHNOLOGY, vol. 6, PLASTIC DEFORMATION OF MATERIALS, ed. by R.J. Arsenault, Academic Press, New York, 1975, pp. 393-493.

11. J-P. A. Immarigeon and P.H. Floyd, "Microstructural Instabilities during Superplastic Forging of a Nickel-Base Superalloy Compact," Met. Trans. A, Vol. 12A, 1981, pp. 1177-1186.

12. J.J. Jonas, B. Heritier, and M.J. Luton, "Anneal Hardening and Flow Softening in Beta Zirconium-Niobium Alloys," Met. Trans. A, Vol. 10A, 1979, pp. 611-620.

13. P. Dadras and J.F. Thomas, Jr., "Characterization and Modeling for Forging Deformation of Ti-6Al-2Sn-4Zr-2Mo-0.1Si," Met. Trans. A, Vol. 12A, 1981, pp. 1867-1876.

14. R.L. Hewitt, J.-P.A. Immarigeon, W. Wallace, A. Kaudeil, and M.C. deMalherbe, "Isothermal Forging of the National Aeronautical Establishment," DME/NAE QUARTERLY BULLETIN, Vol. 4, 1978, National Research Council Canada, Ottawa, pp. 1-23.

15. A.Y. Kandeil, J.-P.A. Immarigeon, W. Wallace, and M.C. deMalherbe, "Flow Behavior of Mar M200 Powder Compacts During Isothermal Forging," Met. Sci., Vol. 14, 1980, pp. 493-499.

16. E.W. Hart, "A Phenomenological Theory for Plastic Deformation of Polycrystalline Metals," Acta Met., Vol. 18, 1970, pp. 599-610.

17. E.W. Hart, C.Y. Li, H. Yamada, and G.L. Wire, "Phenomenological Theory: A Guide to Constitutive Relations and Fundamental Deformation Properties," in CONSTITUTIVE EQUATIONS IN PLASTICITY, ed. by A.S. Argon, MIT Press, Cambridge, MA, 1975, pp. 149-197.

18. E.W. Hart, "Constitutive Equations for the Non-Elastic Deformation of Metals," ASME J. of Engr. Mater. and Technol., Vol. 98, 1976, pp. 193-202.

19. J.F. Thomas, Jr., S.I. Oh, and H.L. Gegel, "Sheet Forming of Titanium Alloys," in ADVANCED PROCESSING METHODS FOR TITANIUM, ed. by D. F. Hasson and C.H. Hamilton, The Metallurgical Society - AIME, Warrendale, PA, 1982, pp. 81-100.

20. J.F. Thomas, Jr., B.S. Shabel, V. Nagpal, and H.L. Gegel, "Elevated Temperature Formability of Some Aluminum Aerospace Alloy Sheet Materials," in PROCEEDINGS NAMRC-VIII, Society of Manufacturing Engineers, Dearborn, MI, 1980, pp. 223-228.

21. U.F. Kocks, A.S. Argon, and M.F. Ashby, "Thermodynamics and Kinetics of Slip," in PROGRESS IN MATERIALS SCIENCE, vol. 19, ed. by B. Chalmers, J.W. Christian, and T.B. Massalski, Pergamon Press, 1975.

22. C. Zener and J.H. Hollomon, "Effect of Strain Rate upon Plastic Flow of Steel," J. Appl. Physics, Vol. 15, 1944, pp. 22-32.

23. S.L. Semiatin, J.F. Thomas, Jr., and P. Dadras, "Processing Microstructure Relationships for Ti-6Al-2Sn-4Zr-2Mo-0.1Si," Met. Trans. A., Vol. 14A, 1983, pp 2363-2374.

24. W.J. McG. Tegart, "The Role of Ductility in Hot Working," in DUCTILITY, American Society for Metals, Metals Park, OH, 1968, pp. 133-177.

25. H.J. McQueen, "Deformation Mechanisms in Hot Working," J. of Metals, Vol. 20, 1968, pp. 31-38.

26. E.W. Hart, "Theory of the Tensile Test," Acta. Met., Vol. 15, 1967, pp. 351-355.

27. A.K. Ghosh, "A Numerical Analysis of the Tensile Test for Sheet Metals," Met. Trans. A, Vol. 8A, 1977, pp 1221-1232.

28. R. Hill, "On Discontinuous Plastic States With Special Reference to Localized Necking in Thin Sheets," J. Mech. Phys. Solids, Vol. 1, 1952, pp. 19-30.

29. J.F. Thomas, Jr., H.L. Gegel, and L.J. Teutonico, "Analytical Simulation of Material Behavior for Sheet Metal Forming," Proceedings NAMRC-V, Society of Manufacturing Engineers, Dearborn, MI, 1977, pp. 147-151.

30. Z. Marciniak and K. Kuczyaski, "Limit Strains in the Processes of Stretch-Forming Sheet Metal," Int. J. Mech. Sci., Vol. 9, 1967, pp. 609-620.

31. Z. Marciniak, K. Kuczinski, and T. Pokora, "Influence of the Plastic Properties of a Material on the Forming Limit Diagram for Sheet Metal in Tension," Int. J. Mech. Sci., Vol. 15, 1973. pp. 789-805.

32. K.S. Chan, D.A. Koss, and A.K. Ghosh, "Localized Necking of Sheet at Negative Minor Strains," Met. Trans. A, Vol. 15A, 1984, pp. 323-329.

33. S.L. Semiatin, G.D. Lahoti, and S.I. Oh, "The Occurrence of Shear Bands in Metalworking," in MATERIAL BEHAVIOR UNDER HIGH STRESS AND ULTRAHIGH LOADING RATES, 29th Sagamore Army Materials Research Conference, 1982.

34. P.W. Lee and H. Kuhn, "Fracture in Cold Upset Forging - A Criterion and Model," Met. Trans., Vol. 4, 1973, p. 969.

35. P.C. Koeller and R. Raj, "Diffusional Relaxation of Stress Concentration at Second Phase Particles," Acta Met., Vol. 26, 1978, p. 1551.

36. J.J. Jonas, R.A. Holt, and C.E. Coleman, "Plastic Stability In Tension and Compression," Acta Met., Vol. 24, 1976, p. 911.

37. P. Dadras and J.F. Thomas, Jr., "Compressive Plastic Instability and Flow Localization in Ti-6242,' Res. Mech. Letters, Vol. 1, 1981, pp. 97-103.

38. S.L. Semiatin and G.D. Lahoti, "Deformation and Unstable Flow in Hot Forging of Ti-6Al-2Sn-4Zr-2Mo-0.2Si," Met. Trans. A, Vol. 12A, 1981, pp. 1705-1717.

39. G.D. Lahoti and T. Altan, "Research to Develop Process Models for Producing a Dual Property Titanium Alloy Compressor Disk, AFML TR-79-4156, AFWAL Materials Laboratory, Wright-Patterson AFB, Ohio, 1979.

40. S.L. Semiatin and G.D. Lahoti, "The Occurrence of Shear Bands in Nonisothermal, Hot Forging of Ti-6Al-2Sn-4Zr-2Mo-0.1Si," Met. Trans., A. Vol. 14A, 1983, pp. 105-115.

41. S.L. Semiatin and G.D. Lahoti, "The Effect of Shear Bands on Service Properties of Ti-6Al-2Sn-4Zr-2Mo-0.1Si Forgings," Met. Trans. A, Vol. 14A, 1983, pp. 743-750.

42. S.L. Semiatin, G.D. Lahoti, and T. Altan, "Determination and Analysis of Flow Stress Data for Ti-6242 at Hot Working Temperatures," in PROCESS MODELING: FUNDAMENTALS AND APPLICATIONS TO METALS, ed. by T. Altan et al., American Society for Metals, Metals Park, Ohio, 1980, pp. 387-408.

43. G.E. Dieter, MECHANICAL METALLURGY, 2nd Edition, McGraw-Hill, New York, 1976, p. 565.

44. P. Dadras, "A Semi-Empirical Solution to Upset Forging," Trans. ASME: J. Engr. for Ind., Vol. 103, 1981, p. 478-483.

45. P. Dadras and J.F. Thomas, Jr., "Deformation Inhomogeneities in Upset Forging," in COMPRESSION TESTING OF HOMOGENIOUS MATERIALS AND COMPOSITES, ASTM STP-808, 1983, p. 24.

46. P. Dadras and J.F. Thomas, Jr., "Analysis of Axisymmetric Upsetting Based on Flow Pattern Observations," Int. J. Mech. Sci., Vol. 25, 1982, p. 421-427.

47. S.I. Oh, "Finite Element Analysis of Metal Forming Processes With Arbitrarily Shaped Dies," Int. J. Mech. Sci., Vol. 24, 1982.

48. S.L. Semiatin and G.D. Lahoti, "The Occurrence of Shear Bands in Isothermal, Hot Forging," Met. Trans. A., Vol. 13A, 1982, pp. 275-288.

MICROSTRUCTURE, TEXTURE AND FORMABILITY OF THIN ALUMINIUM SHEETS

Björn Andersson and J.E. Tibballs

Central Institute for Industrial Research
Blindern, Oslo 3, Norway

ABSTRACT

The processing of thin aluminium sheet includes casting, hotrolling and various coldrolling and interannealing sequences. The task considered here is to model the microstructural changes at each production stage and to link the models corresponding to given process routes. In this work we have concentrated on contineous casting of commercial aluminium and of AlMn(Mg). To predict microstructural parameters from processvariables we had to depend on systematical characterization of the alloys but general trends expected from the theory of solidification were helpful in the formulations. The kinetics of the precipitation reactions followed reaction rate theory provided that correct precipitation reactions and nucleation mechanism were used. Also the coarsening followed established theory well but the density of nucei could not be predicted. During coldrolling we were mainly concerned with the texture development which followed the general trends outlined in the Taylor model. A numerical evaluation was, however, necessary. The development of the deformation structure is to a large extent known in principle but the knowledge is insufficient to explain the macroscopic properties of these materials. Special attention was given to the annealing stage as for instance texture, grainsize and precipitation is greatly influenced. The texture is found to follow simple mathematical expressions very well and parameters for the rate of increase and the level of the texture strength could be related to the structure. However, direct comparison to the relevant structure parameters have not yet been done. The grainsize depended on primary particles and precipitation reaction as expected from theory. Consequently, the necessary relations can be formulated.

Finally, models incorporating these theories or empirical relations have been linked in order to predict earing,strength and formability in typical processroutes. By combining the numerical descriptions on each step, it is possible to predict the earing with a reasonnable accuracy for given alloy type and homogenization. Special attention had to be given to the coherency between the models due to step-like variations when connecting the models together. Furthermore, the numerical expressions are suitable for generalizations. The other properties are not so dependant on the process route and in that way simpler. Numerical descriptions could therefore be made less complex than in the texture case. The main difficulty is that the initial values on the distribution of dispersoids which can not be determined from processvariables but must depend on experimental data. With that limitation the results are found acceptable. Another problem is that the structure-property models are too crudely for instance for the prediction of stretch formability.

1. INTRODUCTION

Computer simulation is already well established in the Norwegian aluminium industry for modelling the mechanical and thermodynamic aspects of strip and D.C. casting and of extrusion. The task we shall consider here is the modelling of the microstructural changes occurring in several steps in the production of thin aluminium sheet that is to be used mainly for food and drink containers. The aim of our work is to describe the microstructural changes that result from altering controllable process variables. The models for each production stage are then linked to correspond to the process route in order to predict final product properties. Process control in an integrated sense is the ultimate aim, so that the work can be applied to the important tasks of alloy development and optimalization. The basic problem is that a change in one process variable has an impact on several structural parameters and other process variables so that even qualitative evaluations or rules of thumb are difficult to make. While the principles governing the effect of each process stage on the individual elements of the microstructure of aluminium are largely understood, the whole network of interrelations makes for an exacting calculation. Texture control is a good example of this. One adds to the complexity when one wishes to consider a spectrum of product properties rather than a single property.

Traditionally, production has been tuned to a satisfactory routine through much trial processing and production experience. Alterations in the established procedures are therefore hard to make. In order to cut down on expensive trials, to make production more flexible and new product development easier, Norwegian aluminium producers, sponsored by the NTNF, have defined a research program some of whose first results we now

report.

The first task in developing a useful model has been to establish mathematical descriptions of the individual metallurgical processes. Frequently, these involve quantities such as activation energies, equilibrium solubilities, etc., that must be determined in order to specify the dependence of the microstructure on temperature, time and degree of deformation. A number of experimental studies have been undertaken to supplement literature estimates of such quantities.

The second requirement for a numerical model is to link the various stages so as to describe the microstructure at the final stage. Relationships between microstructure and macroscopic mechanical properties are then available, although they are frequently of an empirical nature. By determining these relationships for the alloy compositions of interest we aim to build up a model by which relevant mechanical properties can be estimated from processing variables.

The starting material for the thermomechanical processing of aluminium sheet is determined by the composition of the charge and by method of casting and breaking down, so, ideally, these factors need to be included in a complete description of the production sequence.

The main body of our work has been on two economically important aluminium systems: commercial pure aluminium and AlMn(Mg) alloys. To a large extent we have limited the model to the relatively straightforward strip-casting process in which hot rolling is unnecessary. The usual semi-finished product is sheet in the thickness range 0.25 - 0.5 mm in soft or deformation-hardened condition. The process stages are given in Table 1 together with the process variables and the microstructural parameters considered in the model.

Processing of a given alloy may, for example, involve only some of these processes; homogenisation, for example, is not always necessary. Furthermore, cold rolling and annealing are frequently repeated so as to produce the desired final temper. Computer simulation therefore usefully can be divided into routines describing each process that can be combined as necessary. For instance, to produce sheets in H14 condition (final reduction 33%) from strip-cast pure aluminium, the route is 1-2-(4)-5-6-5-6-5. In this case, the degree of cold reduction before the first annealing can freely chosen to optimise the anisotropy of the sheet, while the second must be undertaken at 1.5 times the final thickness. To produce stronger materials the route is simpler: 1-2-(4)-5-6-5 where the annealing position is adjusted so as to give the required temper.

Table 1: <u>Process variables and microstructural parameters
for modelling the production of aluminium sheet</u>

Production Stage	Process Variables	Metallurgy	Microstructral Parameters
1. Charge	Alloying elements Impurities		Total concentrations
2. Casting	Solidification rate (DC - 10-20 K/s, sc - 200-500 K/s)	Solidification	Primary phases, solute concentrations, dendrite and eutectoid morphology, texture and grain size.
3. Hot rolling	Reduction, exit temperature	Dynamic recovery	Primary phase distribution, subgrain structure, texture
4. Homogenisation	Heating and cooling rates, Hold-time and temperature	Dissolution, nucleation, precipitation, Ostwald growth	Primary and secondary particle distribution, solute concentration
5. Cold rolling	Cold reduction	Dislocation-particle interaction	Dislocation structure, texture
6. Annealing	Heating and cooling rates, Hold-time and temperature	Recrystalliz-ation, recovery, precipitation	Grain size, precipitate distribution, texture

The properties we are seeking to control or predict by means of modelling are those relevant to forming: strength, earing, bendability, stretchability (including deformation hardening), springback, softening. Fortunately, the description of the microstructure

need not be particularly detailed for this purpose. The existing theories relating these properties to the microstructure depend to a large extent on a few structural parameters that are evaluated as averages. The microstructure parameters we need to consider are the size and spatial distribution of i) coarse particles and ii) dispersoids, iii) the concentration of elements dissolved in the Al matrix, iv) the dislocation structure and, determined by these, v) texture and vi) grain size.

In the following, we discuss the theories we have used to model changes in the structural parameters at each production stage. The model has to date been assembled using empirical results where the metallurgical processes, e.g., nucleation, are particularly difficult to model ab initio. In these circumstances, quantitative characterization of the results of the process, (e.g.,the particle distribution in the case of nucleation) can provide the necessary parameters. It is emphasized that in each case the parameters or properties are related to controllable process variables. Finally, ideas for developing the model further are discussed.

2. STRUCTURE MODEL

2.1 SOLIDIFICATION

Solidification determines the initial values of most of the relevant structure parameters. The features of the as-cast structure are the compositions and the spatial and size distributions of the primary, precipitated phases, and the solute content and preferred orientation of the Al matrix. These parameters determine the nucleation of recrystallization and the supply of solutes to sustain precipitation reactions during subsequent annealing and homogenisation.

A typical example of the cast structure is shown in Fig. 1. It is characterized by cells or grains each with a core (the nucleation site) and a long tail of secondary dendrites extended normal to the solidification front. The size of the grains depends on the amount of effective titanium-boride particles added in the melt. The modelling of the grain-refining is a seperate item which we have not yet included (Hellawell, 1979; Sigworth, 1984). The importance of the secondary dendrite spacing is that it determines the initial distribution of intermetallic particles and the thickness of the eutectic colonies. It is reported to depend mainly on the local cooling rate (Bower, 1966) and to some extent also on alloying (Miki et al., 1975). The spacing in m is very well described by the following expression:

$$SDS = A \cdot T'^{-B}, \tag{1}$$

where T' is the cooling rate in K/s and the coefficients A and B are approximately equal to 33 and 0.33, respectively.

The morphology of the eutectic volume between the dendrites is normally characterized by a lamellar structure which, in section, appears more irregular than in a eutectic alloy. Its regularity becomes apparent, however, when the particles are viewed in their full three-dimensional complexity. By the dissolving the Al matrix in a suitable alcohol, the morphology of the intermetallic phases can be revealed (Simensen et al., 1984) (Fig. 2). As a guideline it is useful to consider the factors determining the minimum lamella spacing, , for a eutectic (Porter, 1981).

$$\lambda^* = \frac{2 \cdot \gamma \, T_E}{H \cdot T_o} \qquad\qquad \lambda^* = \frac{2\gamma \, T_E}{\Delta H \cdot \Delta T_o} \tag{2}$$

The enthalpy, ΔH, and the phase boundary energy, γ, depend on the phase precipitated whereas the undercooling ΔT depends on cooling conditions and the position in the metastable phase diagram. T_E is the equilibrium eutectic temperature. The problem of predicting the precipitating phases is nonetheless a major hurdle for a model based on fundamental principles so we will outline some means of skirting it.

A measure of the coarseness and the spread in the dimensions of the eutectic structure or,ideally, the lamella structure is needed for the prediction of properties. We shall see that it is a feasible with modern characterizing methods to chart how such parameters depend on, for instance, alloying elements and cooling rate and hence obtain an empirical link.

The prediction of the type and amount of each phase is an obvious difficulty. We know that the cooling rate determines the metastable phase diagram and therefore the order in which phases nucleate and grow. An example can be found in the competition between Al_3Fe and Al_6Fe where Al_3Fe is the equilibrium phase which forms when undercooling is small. With increasing cooling rate, the undercooling increases more rapidly for this phase than for Al_6Fe leading to a preference for the latter for cooling rates above 10 deg/min (see Figure 17 in Bäckerud, 1968). The same argument is probably valid for the precipitation of Al_mFe above 100 deg/min. One needs also to consider the temperature gradient (Adam et

al., 1972).

Having set up the sequence in which the phases are likely to precipitate, the relative proportions are governed by the availability of the necessay solute elements. We have used this type of analysis for the AlMn(Mg) where the number of possible phases is limited and empirical limits on the range of substitution of Fe for Mn in Al_6Mn and $\alpha-Al_{12}(Mn,Fe)_3Si$ are known (Mondolfo, 1978). Furthermore, in this case, the average compositions of the primary phases were available from TEM studies (Dons, 1984).

If we now turn to the problem of predicting the solute concentrations in the Al matrix, we get less help from the fundamental principles and have to rely on experimental findings. For the Al-Fe system, these can,to a large extent, be systemized. Using the data of Miki et al. (1975), we find to a good approximation that the amount of iron remaining in solution on cooling to room temperature, S'_{Fe}, is given by:

$$S'_{Fe} = C_{Fe} \cdot \log(T') \tag{3}$$

where C_{Fe} is the total concentration of Fe and T' is the cooling rate. It is less clear, however, to what degree precipitation of Fe is accelerated by the presence of Si or Mn.

The solubility of silicon in AlFeSi and AlMn(Mg) alloys is not available in the literature. By analysing the concentration in the alcohol used to dissolve the matrix around the intermetallic particles, however, one obtains a useful estimate of this quantity. It appears to be governed by the phases formed and cooling rate. The concentration, S'_{Si}, remaining in solution after cooling to room temperature decreases slowly with cooling rate from about 0.12 wt% at $T' = 300$ deg/s. Initial concentrations of Si above this provide a driving force for the precipitation of Si and it can be shown (Fig. 4) that the Si concentration in the intermetallics, M_{Si}, is proportional to this excess, i.e.,

$$f \cdot M_{Si} = (C_{Si} - S'_{Si}). \tag{4}$$

where $S'_{Si} = k_1 + k_2 \cdot \log(T')$ and f is the volume fraction of particles.

The final structure parameter to be considered here is the texture. The formation of preferred orientations during solidification is relatively straightforward since crystals grow fastest in the (200) directions. The texture is then determined by the orientation of the solidification front which for the Hunter-casting process is inclined at about 30 deg to the casting direction in the bulk of the sheet. The resulting texture is a (100) fibre type about the normal to the front but cyclic due to the sheet symmetry (Fig. 4).

In concluding this subsection, we can note that the prediction of the microstructural variables is imperfect because we lack systematic information about the metastable phase diagrams for the cooling rates found in strip casting. From a extensive, systematic characterization of a few standard alloys, it has been possible to establish an empirical, numerical description of the local cooling conditions, and factors governing phase-selection, morphology and solublity for a specific casting process. Extension of these analyses to related alloys and to other casting processes in order to establish the necessary phase diagrams will place this stage of the process model on a more secure foundation.

2.2 HOMOGENIZATION

For some products, the metastable primary particles make the sheet poorly suited for the subsequent processing. They give rise to unacceptable galling, large grain size, poor formability, extreme earing, etc. In order to improve these properties the sheet is subjected to relatively long-term heating at temperatures between 550 and 640 deg C. During this process the primary particles change in shape and size, the less stable phases transform, secondary particles precipitate and the solute content is redistributed. This is well illustrated by the result of Theler & Bichsel (1967) shown schematically in Fig. 5.

The geometrical changes in the primary particles are not easily quantified. We have found it most useful to quantify their distribution after rolling (see Sec. 2.3) particularly because it is to the nucleation of recrystallization at that stage of processing that they are most relevant.

Al-Fe-Si. As mentioned in the previous section, the commercial Al system is in fact one of the most complicated alloy systems with several elemental, binary and ternary phases occurring (Westengen, 1982). In strip-cast materials with higher cooling ratesadditional metastable phases occur (Andersson, 1980). On heating, the metastable Al_6Fe and Al_mFe phases transform to the equilibrium Al_3Fe with kinetics determined by Kosuge and Takada (1978). Other phases may, however, be stabilized by traces of other elements. An example is Mn which is often present in recycled aluminium and which stabilizes the cubic phase, $\alpha-Al_{12}(Fe,Mn)_3Si_x$.

Al-Mn-(Mg). The stabilization of the α-phase by Mn is one reason for the intermetallic

flora" being somewhat simpler in this system. There are essentially just two competing secondary phases, Al_6Mn (isomorphous with Al_6Fe) and the α-phase. When Si is present and available, the dominant second phase has the α-$Al_{12}Mn_3Si_x$ structure where x equals 1 for low Si contents and 2 for higher concentrations. The crystal structures are closely related; the second Si atom lowers the b.c.c. symmetry of the x = 1 structure to s.c. for x = 2. The availability or activity is reduced by the other elements notably Mg (Watanabe et al, 1984)

The distribution characteristics of the second phase particles appear to determine the plastic properties such as ductility that are relevant to forming (Mathiesen et al,1983). The development of this distribution occurs in three stages form the supersaturated Al matrix. Semicoherent discs of the -phase nucleate (Hausch et al, 1978), most readily in cold-worked material. After recovery and recrystallisation have removed favourable nucleation sites, supercritical nuclei continue to grow by precipitation. Finally, the larger particles grow at the expense of the smaller because of their more favourable surface-to-free energy ratio (Ostwald ripening). At temperatures of commercial interest, nucleation and recrystallisation are complete within seconds, precipitation within minutes so the processes are difficult to follow even with small laboratory samples. Modelling of the precipitation of secondary particles must take into account i) the density of nuclei which depends on the availablity of nucleation sites formed during casting or subsequent cold rolling, ii) supersaturation, iii) solutes released through phase transformations, iv) the phases being precipitated.

In order to establish the mechanisms involved in the precipitation and ripening stages, we have examined the response to isothermal heat treatment of the strip-cast AlMn(Mg) alloy, Norsk Hydro 303,. The treatments were performed on the cast sheet and on sheet cold rolled 75% and 90%. The precipitation was followed by electrical conductivity measurements, the recrystallisation by Vickers hardness, HV_3, and the forming properties by tensile testing and punch stretching. From the conductivity data (Fig. 6), especially for the shorter heat treatments at low temperatures, we were able to establish the order, n, of the reaction (see Walas (1959), p29ff) to be 3. The expected differential rate equation is:

$$\frac{dS_{Mn}}{dt} = -kS_{Mn}^3 \cdot S_{Si}^x \qquad (5)$$

The value of 3 for n indicates that S_{Si} is not a rate determining factor for the precipitation. That is, that the factor S_{Si}^x can be included in the constant, k. Furthermore, the fact that the reaction rather than diffusion determine the precipitation rate means that k will also depend on the area of the phase boundary, which, in turn, is proportional to the number of particles nucleated. Subgrain boundaries appear to be the favoured nucleation sites, so recrystallization stops nucleation. Since recrystallization and nucleation have different activation energies, heating rates must be considered in a model that is to describe the distribution of precipitates.

For n > 1, integrating (5) and establishing the boundary conditions from the initial and equilibrium values, gives an equation for S_{Mn} as a function of time:

$$(S_{Mn}-S_{Mn}(eq))^{-2} - (S'_{Mn}(0)-S_{Mn}(eq))^{-2} = 2.k'.(t-t_o) \qquad (6)$$

where t_o is the time that precipitation is initiated.
The constant, k', in (6) includes the temperature dependence of the reaction constant k which is expected to be of the form $k_o.exp(-H/RT)$, where H, the activation energy for the reaction, was found to be approximately 35 kcal/mol.

The third stage in the development of the secondary particle distribution involves coarsening via one of several transport mechanisms. The average particle diameter increases as the elapsed time raised to a power of 1/m where m = 2,3,4 or 5 according to limiting transport mechanism. For NH 303, a value m equals 3 was found, indicating that bulk diffusion controls the rate of coarsening. An activation energy appropriate to Mn diffusion explained the increase in the growth rate from 1 nm^3/s at 435 deg C to 75 nm^3/s at 550 deg C.

Although the work and theories mentioned above refer to high temperature homogenization treatments, they are also valid for the development of the particle size distribution and precipitation during annealing at lower temperatures.

Changes in the texture during homogenisation have little direct bearing on the texture in the final sheet but changes in the concentration of iron in solution, in the small dispersoids and in the distribution of coarse particles will have a profound influence. This topic will be treated in subsection 2.4 on the annealing process.

2.3 COLD-ROLLING

The microstructural changes during cold rolling with which we need to be concerned are
i) the development of texture both in the bulk of the sheet and in the surface and mid thickness layers which undergo hetrogeneous deformation,
ii) the breaking up of the eutectic structure into single particles, and

iii) the strengthening mechanisms operating in deformed materials.

The theory of texture development is based on the work of Taylor (1938). Several sophisticated computer programs have been developed (Aernondt,1978) to predict textures for given strains and strain ratios. The calculated textures are sharper than in reality and they are to some extent displaced (Dillamore & Katoh, 1974a) but they provide a qualitatively correct picture. The Taylor model is therefore accepted as a useful tool for understanding of texture development.

The detailed evolution of the main texture components can be followed by measuring the Orientation Distribution Function, a three-dimensional presentation of the preferred orientations (Hirsch et al.,1982; Ebslöh, 1984). The orientational changes which occur during rolling are important for an understanding of the recrystallized texture. According to the views of Dillamore and Katoh (1974b), some mechanisms of recrystallisation such as subgrain growth and nucleation at grain boundaries, tend to reproduce existing texture components. Heterogenities can be formed during rolling in the following way. A crystal may break up in such a way that one part follows one path (in Euler space) to a stable orientation whereas a neighbouring part rotates to a different orientation. The highly deformed regions in the transition zone between them becomes a very potent site for nucleation. The cube texture which can dominate in annealed aluminium, probably nucleates on such sites. As we shall see, precipitation and segregation at high or low-angle boundaries can critically change the balance between the texture components in the annealed microstructure.

Our main purpose in studying textures in sheet aluminium is to predict earing. For this, a numerical description of the variation of stable deformation textures and the cube texture is required. Since the former are nearly equivalent to each other in their consequences for earing, no distinction need be made between them. Accordingly the texture strength may be characterized by the intensity of the main maxima in (111) pole figures. The cube texture is similarly measured by the intensity of the characteristic peaks in the pole figures.

Except for a small effect of the rolling practice and a tendency for variation to be less at high strains (above $\varepsilon = 2.5$), the intensity, R, of the rolling texture increases linearly with strain in those parts of the sheet that experience plane strain.

$$R = k.\varepsilon \tag{7}$$

This agrees well with observations on the earing behaviour in the strain-hardened condition.

The effect of rolling on the cube texture component is more complex. It is most easily described as a rotation about the rolling direction towards an {hk0}<001> orientation (Takahashi et al., 1978). The rotation increases with deformation but the migration towards the stable orientations is slow. The variation in the strength can be described as an exponential decay. The rotated texture component gives less strength parallel to the rolling direction than at 90 deg to it. Denoting here the change in the intensity of the fibrous cube peak by C, we can express the effect of cold rolling by:

$$C = C(0).\exp(-a.\varepsilon) \tag{8}$$

Consideration must also be given to the inhomogeneous deformation that occurs with rolling. Near the surface there is an increased deformation which includes a shear component. The extra deformation gives stronger textures, while the shear leads to weaker textures or even new texture components (Dillamore & Katoh, 1974a). We have found that textures are only slightly stronger in the surface, showing that the effect of any shear component is weak. A slight acceleration in the texture development that is observed when using a four-high mill (for which inhomogeneous deformation is larger) compared with a two-high mill needs attention, however.

The size of the primary particles is important for the prediction of several properties. The quantification of the morphology of the eutectic particles in the casting was difficult because of their complex shapes. During deformation these particles are broken up into simpler pieces whose size distributions are found to follow a log-normal curve. The distribution is therefore described by three parameters: the volume fraction of the particles, the mean diameter and the width of the size distribution (the standard deviation in logarthmic coordinates). Since some of the particles are rod shaped, a fourth parameter, the thickness-to-length ratio, is sometimes needed. Any other parameters that enter into relationships of interest may be derived from these.

The volume fraction of binary particles is reasonably well determined from a knowledge of the approximate phase composition. The particle size is governed mainly by the dendrite spacing. There are however differences from alloy to alloy, such as the systematic decrease in the average size with the Fe/Si ratio observed in the D.C., the VAW and the Hunter casting methods (Fig. 7a). This can be understood as a shift towards less favourable phases at greater undercooling.

Systematic trends have also been found in the width of the particle-size distributions. Here, the Si content (C_{Si}) appears to be responsible (Fig. 7b). The reason is not clear but the rapid decrease in the solidus temperature with Si enrichment may play a role. In a similar way the effect of homogenization on particle distribution can be mapped.

The spatial distribution of particles can be quite inhomogeneous in continuously cast sheet because it is subject to much less deformation than D.C. slabs undergo during breaking down. Since grain size, bendability and stretchability are all influenced by this inhomogeneity, a statistical characterization of it is an important feature to be incorporated in the model.

Finally, the increase in flow stress that occurs during rolling reflects an rapid increase in the stored dislocation density (Sheppard and Zaidi, 1982). The applications with which we are most concerned do not depend critically on differences in yield strength from one alloy to the next within the Al-Fe-Si alloy system. The dislocation behaviour is of more concern in the prediction of work-hardening amd ductility properties and recrystallization. For other applications, notably in connection with finite element methods (Ayres, 1983) and MATMOD (Schmidt and Miller,1982) great efforts have been made to establish general constitutive equations for the microstructural dependence of the stress-strain curve. The observations and calculations that we have performed have indicated that consideration of solute content, particle size and texture allow a description of the yield properties.

2.4 ANNEALING

As mentioned in the introduction, annealing can be introduced into the cold rolling sequence at virtually any sheet thickness in order to adjust the temper of the final sheet. This means that the microstructural parameters at the start of annealing will vary. Generally, however, the metallurgical processes will be the same: the precipitation and growth of second phases, the recovery and recrystallization of cold work and the development of preferred orientations. All these are interrelated.

The kinetics and mechanism of the recovery and recrystallization processes are determined by retardation effects which in our case means drag forces due to small dispersoids or segregation on grain boundaries, and by acceleration aided by large particles and increased deformation energy or dislocation density. The retarding effect of small particles has been clearly demonstrated by Doherty & Martin (1976). The nucleation rate for recrystallization, as measured by the final grain size, rapidly becomes sluggish with decreasing interparticle spacing. The drag forces determining these effects can be expressed as (see Martin, 1980)

$$F = 3\alpha_B f/r \quad \text{for grain boundaries,} \qquad (9a)$$

and

$$F = 3\alpha_{SB} Lf/8r^2 \quad \text{for sub-boundaries} \qquad (9b)$$

where α_B and α_{SB} are the specific boundary energies for grains and subgrains, respectively, and L is the subgrain size.

The parameters needed for the calculation of the drag forces exerted by dispersoids are then the dispersion ratio f/r and particle size r (or the related parameters such as interparticle spacing). Empirical data is available for a numerical description, but an aim of the calculations referred to in subsection 2.2 is to estimate these quantities.

Of the factors which accelerate recovery and recrystallization, the stored deformation energy increases with the work hardening and flow stress. Some factors which relate these quantities are covered briefly in the next section and otherwise thoroughly in the literature on strengthening mechanisms (e.g., Kelly and Nicholson, 1971).

The other important which enters into predictions of recrystallized grain sizes (Nes, 1976; Sandström, 1980) is the density of particles larger than a given size. The statistical description given in subsection 2.3 yields all necessary information. The spatial inhomogeneity typical of continous cast material is that particles tend to be found in layers from which recrystallization starts (Langsrud, 1983). The spatial distribution therefore also needs to be incorporated in the modelling.

It may seem difficult to make any numerical calculations, but to illustrate that reasonable results can be obtained using very simple concepts, an example can be given. We assume that acceleration is due solely to the density of particles larger than 1.2 μm (chosen arbitrarily, but gives correct alloy dependency) and retardation solely to the amount of secondary precipitation of iron. These parameters are calculated according to the prescriptions given previously. From Fig. 8 it is seen that the systematic variations are given surprisingly well in a plot like this - especially in view of the neglect of variations in deformation energy, spatial distribution, etc.

Predicting the textures at the first interannealing position is of major importance for

the determination of the final texture (Naess & Andersson, 1984). The texture development at this stage has been extensively been studied in a joint Norwegian-German project on the control of texture. This project has shown that strengths of the two dominating texture types - the retained rolling textures and the cube texture - change systematically with deformation, alloy composition, homogenization and rolling practice. This is best illustrated by an example. We have chosen to present some results on materials cast with the VAW continous casting machine (Moritz,1969) basically because these materials are the least complicated thanks to their nearly random starting texture. The development in the strength of the retained rolling textures as measured by the peak intensities of the main maxima in the (111) pole figure is shown in Fig 9. From plots like these it is clear that the texture strength increases progressively with the strain and a suitable description at this stage is:

$$R = R_o \cdot \exp(k \cdot \varepsilon) \qquad (10)$$

Furthermore, these coefficients should bear a relation to the structure parameters. This texture component depends on drag forces, like iron in solution and dispersoids and on the occurrence of large particles. The analysis has not proceeded far enough to allow a formulation to be made. We have therefore looked directly at the alloy composition to find an empirical parameter that reflects the overall variation in the structure parameters. For this purpose the ratio $r = C_{Si}^{1/2}/C_{Fe}$ was selected. Plotting the inclination k and level R_0 against this parameter (Fig 10), relationships can be found:

$$R_0 = A \cdot \exp(-B \cdot r) \qquad (11)$$

$$k = D + E \cdot r + F \cdot C_{Si}/C_{Fe} \qquad (12)$$

where A, B, D, E and F are coefficients which depend on the casting method and the homogenisation conditions.

According to the ideas of Dillamore and Katoh (1974b), the cube texture is expected to increase in strength but, as shown by Ridha and Hutchinson (1982), recrystallization nuclei can be destroyed so that a maximum intensity is found as the cold deformation is increased. It is not clear whether this mechanism operates here but, by plotting the texture strength against the cold reduction, a maximum is found in the cube intensity. Furthermore, on a logarithmic scale, the curves are hyperbolae so a suitable mathematical expression is:

$$C_2 = C_{max} \cdot \exp(- ((\varepsilon - \varepsilon_m)^2 + B^2) \qquad (13)$$

where C_{max} is the cube strength maximum at strain ε_m and B determines the width of the maximum.

By means of expressions (7) to (13), the texture can be described analytically as a function of cold reduction. In the next section we shall see how by combining the results for cold rolling and annealing the texture of the final sheet may be predicted.

In the AlMn(Mg) system, the strength of the various components is strongly affected by the average dispersoid diameter and to the extent to which the primary particles have dissolved. For small dispersoid diameters (underaged), grain boundaries are strongly pinned to the extent that the texture remains very similar to that of the casting and the mechanical properties are highly anisotropic. For dispersoid radii greater than approximately 50 nm, normal recrystallization occurs giving more isotropic mechanical properties.

3. FINAL STRUCTURE

So far, we have tried to model the microstructural changes occurring during each process step. We shall now give an example of how these calculations are combined to describe the structure in the semi-fabricated product. The selection of structure parameters has been made by considering the controlling factors for a variety of interesting properties. Many structural parameters could be chosen; we have chosen one of particular interest to us at the Central Institute and to our aluminium industry.

3.1 Texture

The texture at the first interannealing position (denoted by I) has been treated subsection 2.4. In order to use that result the influence of previous orientations must be ascertained. It is most pronouced after hot rolling slab-cast materials because a large number of potent cube-oriented nuclei are present if the finishing or exit temperature is below the recrystallization temperature. This also occurs to some extent in Hunter-cast materials. The modification that we need to make to the model has to take into account that cube nuclei are very effective at small cold reductions but gradually lose their importance at large reductions. Numerically, it is sufficient to include an extra term

$$C_1(I) = C_o \cdot \exp(-a \cdot \varepsilon) . \qquad (14)$$

The term in equation (13) is then denoted $C_2(I)$ and the texture strength of the cube at the first annealing position is the sum of these contributions. If the processing is to produce deformation-hardened sheet, then the effect of the final reduction is simply described by equations (7) and (8). The linearly increasing deformation texture can be added to the partially destroyed cube texture:

$$R = R(II) + k.\varepsilon \qquad (15)$$

and

$$C = C(I).\exp(-a.\varepsilon) \qquad (16)$$

To obtain the H14 or the soft condition, intermediate cold rolling and an extra annealing is necessary. In this case the cube texture prior to the cold rolling is that resulting from the first annealing, i.e., C_o in equation (14) is given by

$$C_o = C_1(I) + C_2(I) \qquad (17)$$

since the cube-oriented grains may serve as nuclei in the same way as in the previous stage of processing.

At low deformations, nucleation can be slow and the resulting grain sizes are then large. In this situation, the cube texture dominates over the retained rolling textures in the case of unhomogenized continuously cast sheet. Numerically, we express this effect as a multiplicative factor k_m depending on the fraction of large primary particles. For homogenized or DC-materials the factor differs little from 1 as is also the case for higher alloyed materials. It should be noted that the drag forces which would increase this factor are substantially lowered by the previous annealing. The size of the primary particles, however, has not increased, so unhomogenised materials will still have a low nucleation rate. Furthermore, a second contribution to the cube component develops in the same way as $C_2(I)$. In particular it seems to depend on the same microstructural parameters.

The main texture components after the second interannealing can now be described by :

$$C(II) = k_m(N_v, \varepsilon).(C(I) + C_2(I)) + C_2(II) \qquad (18)$$

$$R(II) = k_m(-N_v, \varepsilon).R(I) \qquad (19)$$

where N_v is the density of large particles and the strain implicit in the expression is the cold reduction between first and second interannealing.

These final texture changes are not significant in the case of materials in H14 condition.

The description given above could be made more complete. At present we use different sets of coefficients in equations (14) to (19) depending on the casting method or the degree of homogenization. By establishing the functional dependence of these coefficients on the structural parameters which are altered in these process steps, we would obtain a model that covered the complete processing sequence.

4. STRUCTURE-PROPERTY RELATIONSHIPS

It has been shown that it is possible to set up a complete system to describe texture in the semi-fabricated sheet product following any common process route for the commercial aluminium alloys discussed. We now consider how these results can be related to the properties of the sheet and its behaviour during fabrication of the final product.

4.1 EARING

Having determined the texture strength at the final product thickness, the relation to earing for any given geometry must be found. This problem is treated in some detail by Bate and Rodrigues (1984). For a given deep drawing product we have found it possible to simply relate the strength of the texture components directly to earing values with a linear expression, the coefficients of which could be determined by linear least square method. Using the set of equations described above it has been possible to calculate the percentage earing to an accuracy of about 1%.

4.2 STRENGTH

The strength of non-hardnenable aluminium alloys depends on several of the structure parameters we have been concerned about like small particles, solute content, grain size and texture. Theories on their effects are well known (see Martin, 1980). The strength increase due to impenetrable particles follows the Orowan equation where the important parameter is the interparticle distance. The solid solution contribution due to the strain

field around foreign atoms varies as the square root of the solute content (Kelly,1971). The effect of grain size follows the Hall-Petch relation in the general case. The strength differences due to textural anisotropy can be described in terms of the Taylor model. It is not clear how these strength contributions should be added but normally one chooses to add the square roots of each contribution and then square the sum. In the present program an adequate correspondence between observed and calculated initial flow stresses is found for commercial pure aluminium (Fig. 11) using the procedure above but neglecting the Orowan mechanism.

The stress-strain relationship follows approximately the simple Holloman equation but - especially for large-strain deformation of aluminium - a better equation is a modified Voce type (Lloyd & Kenny,1982). The coefficients must then be related to the structure parameters. For the important case of Mg-bearing alloys for instance, numerical relations have been measured (Lloyd & Kenny, 1982 and Kohara & Katsuta, 1978). The interpretation of these relations are qualitative at this stage (Lloyd et al. (1978).

4.3 STRETCH-FORMING

The stretch forming properties of sheet are governed by so many factors that involve the interaction of the work piece and the tooling that a microstructural description of the sheet can only partially describe the performance of a given alloy. Two important characteristics are the work hardening capacity, especially at low strains, and the plastic anisotropy ratio which describes the resistance of the sheet to thinning.

The work-hardening index measured by tensile testing cold-rolled and annealed AlMn(Mg) sheet was found to increase with the duration of the homogenization treatment up to a limiting value of 0.22. This improvement was accompanied by an increase in the radii of the dispersoids from 30 to 150 nm, both as a result of Ostwald ripening and by the reprecipitation of solute elements from the dissolution of the metastable primary phases. The increase in this index reflected the importance of dispersoids with radii larger than approximately 65 nm in creating dense dislocation tangles in deformed material. Smaller particles appeared from TEM studies to play no role in the development of the dislocation subcells that were found in samples deformed 10 to 20%. This observation led us to relate the maximum density of dislocations, and hence the tensile strength, to the dimension of the subcells which, in turn, was determined by the average spacing between particles greater than 65 nm (Mathiesen et al., 1983). The work-hardening index, w, was found to be described by

$$w = 0.2 - 0.05 \log(\lambda_{65}) \qquad\qquad (20)$$

where λ_{65} is the spacing between particles larger than 65 nm. Using this, a relationship between the homogenization treatment and the ductility of the annealed sheet could be developed.

CONCLUSIONS

Since solidification determines the initial values of most of the relevant structure parameters, a knowledge on how these depend on cooling conditions and alloying elements is necessary. The phase-selection, the morphology and the solubility have at this stage to be determined from simple governing rules and with the help of extensive, systematical characterization. The description of the important secondary dendrite structure is, however, satisfactory.

During homogenization the kinetics follows very well the reaction rate theory but it is imperative to know the ongoing reactions and the nucleation mechanism. The theory of predicting the density of nuclei need to be developed. The coarsening of the particles follows a normal power law with an exponent of 3 which indicate that bulk diffusion is the rate controlling process.

The microstructural changes occurring during coldrolling is qualitatively well understood. The general texture development and possible texture components can be predicted by means of for instance the Taylor model. Such information needs to be quantified, however. The mechanisms of deformation are also relatively well understood in terms of interaction between dislocation with other dislocation and with particles but at large strains the behaviour is too complex. The stress-strain relationships are well known but there is a lack of knowledge on the structural interpretation of the parameters in these relations. Finally, the rolling has the important effect of breaking up the eutectic colonies into single particles but in this case we must depend on an emperical relation.

The description of precipitation during annealing follows closely what was referred to under the homogenization process. The recovery and recrystallization seem to be well understood in terms of dragforces on subcells and grain boundaries due to precipitates and segregations and of acceleration due to large primary particles. For model applications the relative importance of these factors must be evaluated and the parameters determined. The annealing determines to a large extent the texture which is of

applications the relative importance of these factors must be evaluated and the parameters determined. The annealing determines to a large extent the texture which is of major concern in these thin aluminium sheets. The texture development and its relation to the structure is presently essentially emperical. The description is found adequate for a prediction and control of the main texture components. A more fundamental interpretation of the mathematical expressions and more direct relations to relevant structure parameters is needed.

Earing, strength and stretchability were chosen as examples of how the calculations can be combined to describe the structure and thereby the properties in the semi-fabricated products. For specific alloy systems these properties were calculated to an acceptable degree of accuracy. The most complex case dealt with in the present context is the prediction of earing and also most of the effort have been put into that problem. It is therefore satisfactory to have a modell that works sufficiently well. However,a lot of work remains to be done on the generalization of the model and on the detailed understanding of the functional behaviour and structural dependencies.

Clearly there are a large number of properties depending on the structure parameters considered here. A lot of information of qualitative and semiquantitative nature and calculation models for a number of properties based on related structure parameters can be found in the literature. An effort must therefore be put into the quantification of such relations or models in order to obtain realistic models able to describe the effect of processing on the structure as well as to predict a number of useful properties.

ACKNOWLEDGEMENTS

REFERENCES

Adam, C.Mcl. and Hogan, L.M. (1972) J.Aust. Inst. Metals, 17, 437.

Aernoudt, E. (1978) in Proc. Int. Conf. on Texture of Materials; G. Gottstein and K. Lücke (ed.), Springer Verlag, Heidelberg, p45.

Andersson, B. (1980) SI-report 800203-2, "Microstructure of strip-cast Al-Fe-Si alloys"(in Norwegian)

Ayres, R.A. (1983) Met. Trans., 14A, 2269-75.

Bäckerud, L. (1968) Jernkont. Ann., 152, 109.

Bower, T.F., Brody, H.D., and Fleming, M.C. (1966) Trans. Met. Soc. AIME, 236,624.

Dillamore, I.L. and Katoh, H. (1974a) Metal Sci., 8,21.;(1974b) ibid.,73.

Doherty, R.D. and Martin, J.W. (1962-3) J.Inst.Metals, 91, 332.

Dons, A.-L. (1984) Scand. J. Metall., 13, 137-43.

Ebsläh, H. (1984) in 7th Int. Conf. on Textures of Materials, 17-21 Sept., Nordwijkerhout.

Hausch, G., Furrer, P. and Warlimont, H. (1978) Z. Metallkde, 69, 174.

Hellawell,A.(1979) in Proc. Int. Conf. on Solidification and Casting of Metals; The Metals Society, London, p161.

Hirsch, J., Virnich, K.H. and Lücke, K. (1982) in Proc. Int. Conf. on Texture of Materials, The Iron and Steel Institute of Japan, Tokyo, 375.

Kelly, A. and Nicholson, R.B. (1971) "Strengthening Methods in Crystals", Applied Science Publishers, London

Kelly,P.M. (1971) J.Aust.Inst.Metals, 16, 104.

Kohara, S. and Katsuta, M. (1978) J.Jap.Inst.Light.Met., 28, 277.

Kosuge, H. and Takada, H. (1979) J.Jap.Inst.Light Met., 29, 64.

Lloyd, D.J., Sang, H., Embury, J.D., Wycliffe, P. and Leroy, G. (1978) Mat.Sci. and Eng., 36, 35.

Lloyd, D.J. and Kenny, D. (1982) Met.Trans.A, 13A, 1445.

Mathiesen, H., Tibballs, J.E., and Andersson, B. (1983) in "Deformation of Multi-phase and Particle Containing Materials" ; J.B. Bilde-Sørensen, N. Hansen, A. Horsewell, T.Leffers and H. Lilholt (ed.) Risö, p429-34.

Martin, J.W. (1980) "Micromechanisms in particle-hardened alloys"; Cambridge University Press, Cambridge, England, p156.

Miki, I., Kosuge, H. and Nagahama, K. (1975) J.Jap.Inst.Light Met., 25, 1.

Mondolfo, L.F. (1978) "Manganese in Aluminium Alloys"; The Manganese Centre, Neuilly sur Seine, p7.

Moritz, G. (1969) Z.Metallkde, 60, 694.

Naess, S.E. and Andersson, B. (1984) TMS-AIME Fall Meeting, 16-20 sept., Detroit

Nes, E. (1976) Acta Met., 25, 1323.

Porter, D.A. and Easterling, K.E. (1981) "Phase Transformation in Metals and Alloys", Van Nostrand Reinhold, Oxford, p255.

Ridha, A.A. and Hutchinson, W.B. (1982) Acta Metall., 30, 1929.

Rodrigues, P.M.B. and Bate, P.S. (1984) TMS-AIME Fall Meeting, 16-20 sept., Detroit

Sandström, R. (1980) Z.Metallkde., 71, 681.

Schmidt, C.G. and Miller, A.K. (1982) Acta Metall., 30, 615.

Sheppard, T. and Zaida, M.A. (1982) Met.Techn., 9, 52.

Sigworth, G.K. (1984) Metall. Trans., 15A, 277-82.

Simensen, C.J., Fartum, P. and Andersen, A. (1984) Frezenius Z.Anal.Chemie (in press)

Takahashi, T., Mwakam, T. and Nguyen, C.D. (1978) J.Jap.Inst. of Light Met., 28, 35.

Taylor, G.I. (1938) J..Inst.Met., 62, 307.

Theler, J.J. and Bichsel, H. (1967) Metall., 21, 195.

Walas, S.M. (1959) "Reaction kinetics for Chemical Engineers", McGraw-Hill, New York, p29.

Watanabe, H., Ohori, K. and Takeuchi, Y. (1984) Aluminium, 60, 373-6.

Westengen, H. (1982) Z.Metallkde, 73, 360.
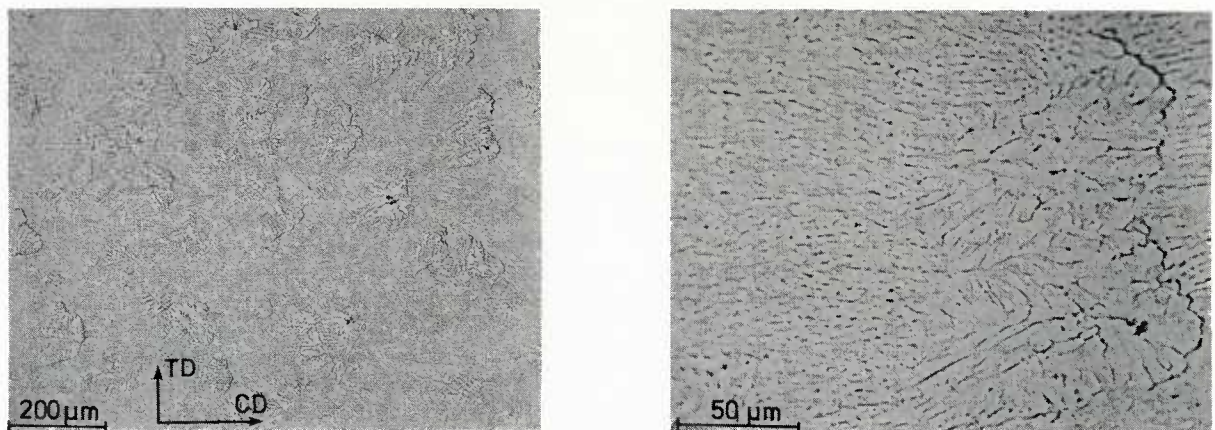
Optical micrograph of the casting structure of AlFeSi as cast with a Hunter machine. The structure is characterized by a cells or grains each with a core and a long tail of secondary dendrites normal to the solidification front.

Fig. 2
Scanning electron micrograph of the intermetallic phases as residue on a filter after dissolving the aluminium matrix.

Fig. 3
Comparison between the observed fraction of silicon in the intermetallic particles and the theoretical value from equation 4.
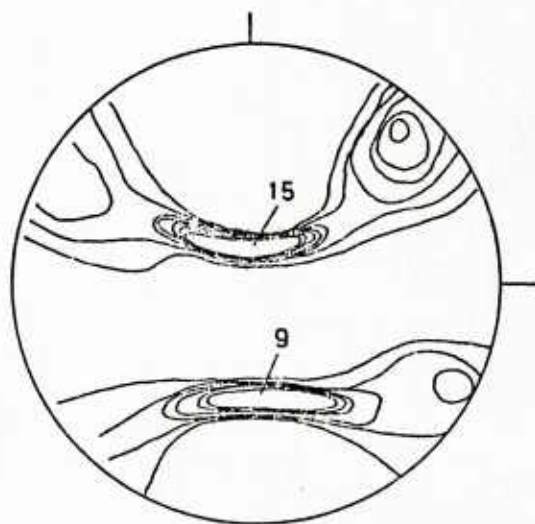
Fig. 4
A (111)-pole figure from a Hunter-cast coarse-grained material 25% below the surface. The texture is a (100)-fibre type with fibre axis normal to the solidification front. Due to the sheet symmetry the texture components are centered around 111   112 .
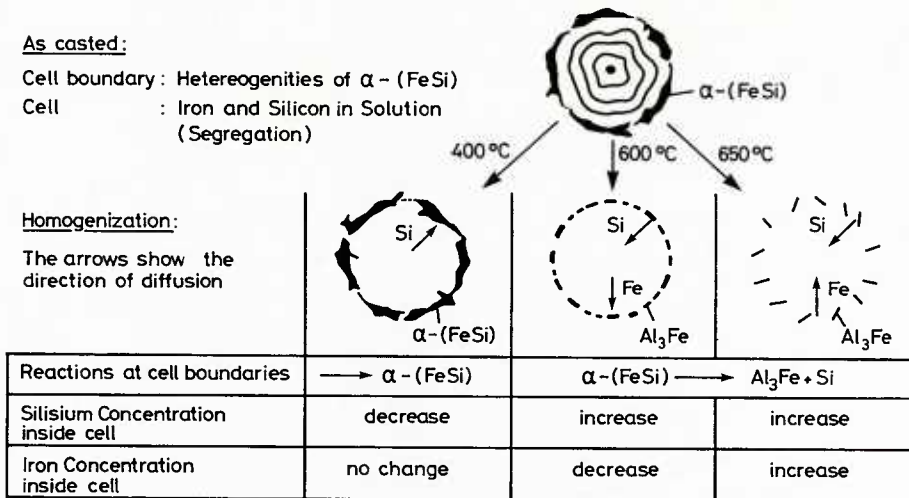
Fig. 5
The influence of homogenization on the phases and solute concentration in 99% Al shown schematically (after Theler & Bichsel,1967).
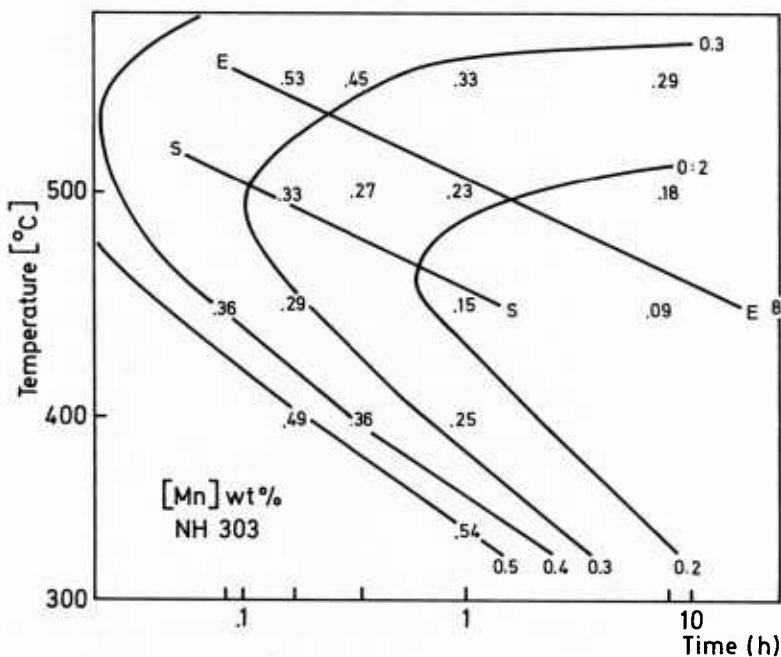
Fig. 6
TTT diagram for the precipitation of Mn in the AlMn(Mg) alloy, NH 303. The figures denote the weight percentage of Mn in solution. The C-curves are calculated using the rate equation (5). The straight lines marked S and E indicate the start and end, respectively, of recrystallization.
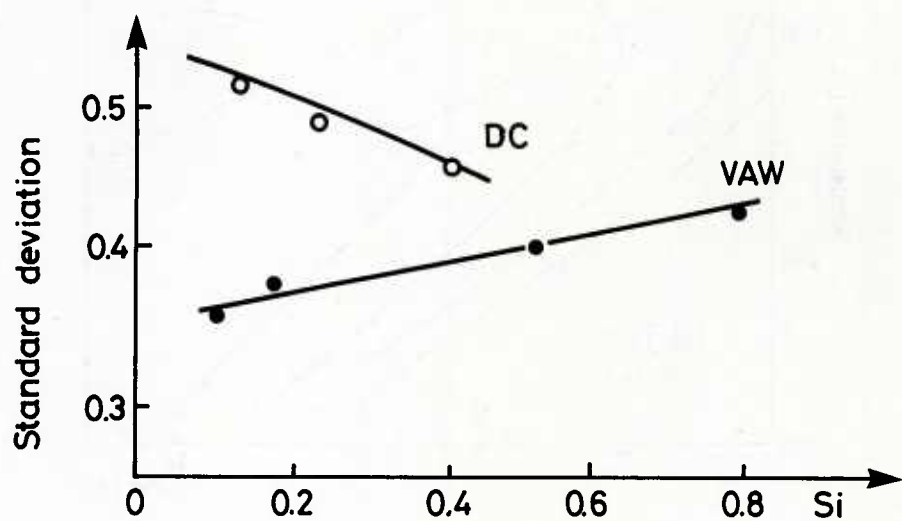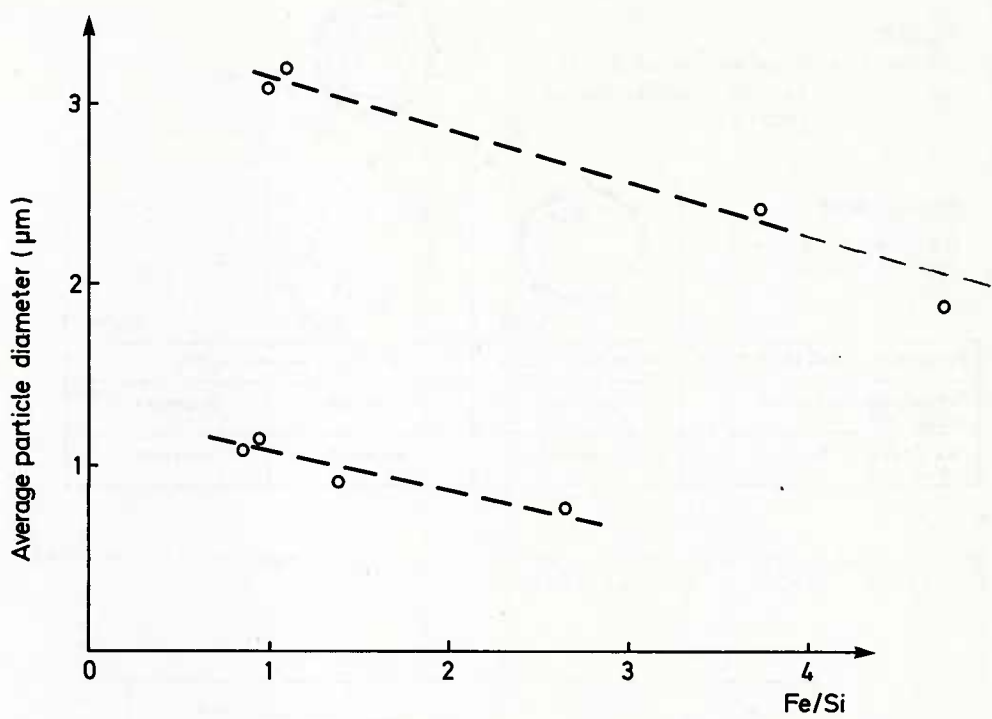
Fig. 7
Changes in the log-normal distribution parameters: a)mean value <u>versus</u> the Fe/Si ratio
and b) standard deviation <u>versus</u> the Si-content as observed for <u>commercial</u> aluminium.
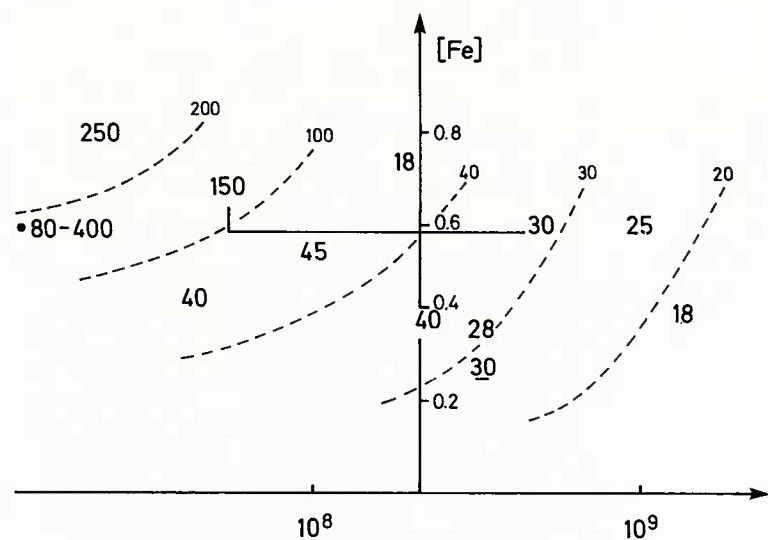
Fig. 8
The observed grain size at ε = 2.5 for a number of Al-alloys plotted as function of the density of particles > 1.2 μm and the estimated content of iron in solution. The arrow indicates the shift in these values from the middle to the surface region in Hunter cast sheet illustrating the expected gradient in the grain size.
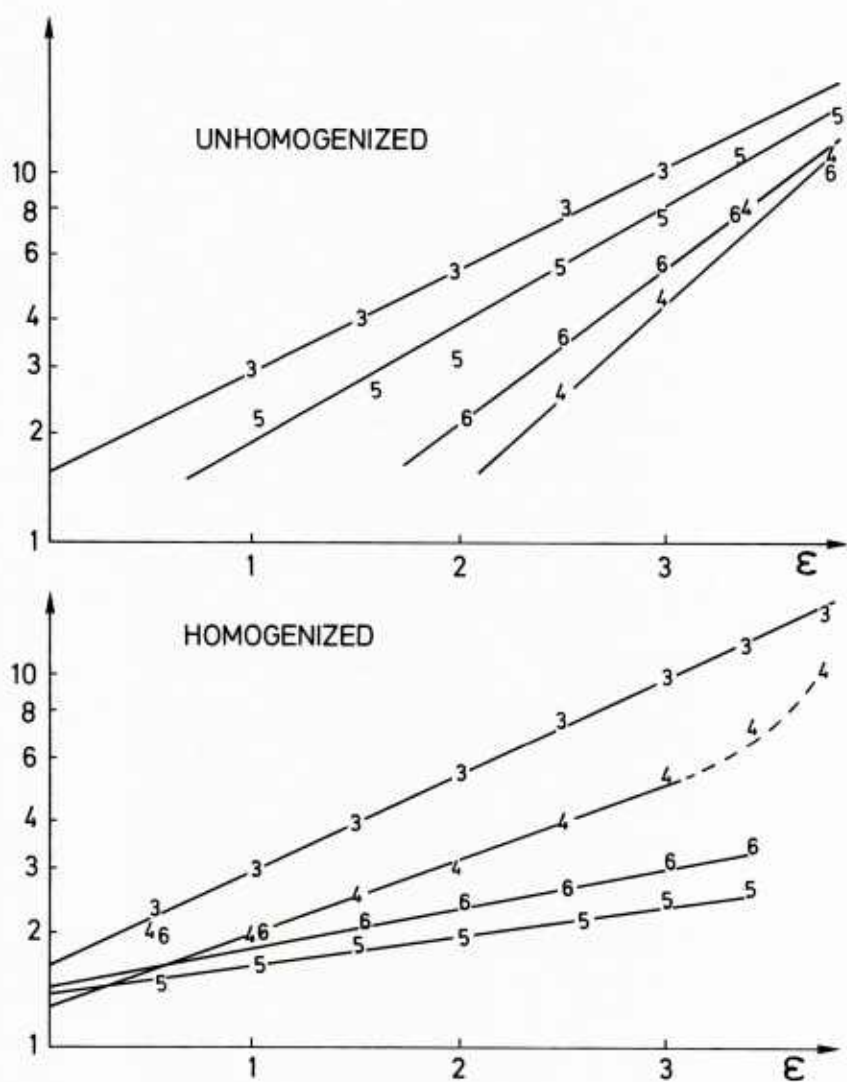
Fig. 9
Texture strength of the retained rolling texture as function of the cold deformation before annealing for different alloys as indicated by numbers 3 - 6.
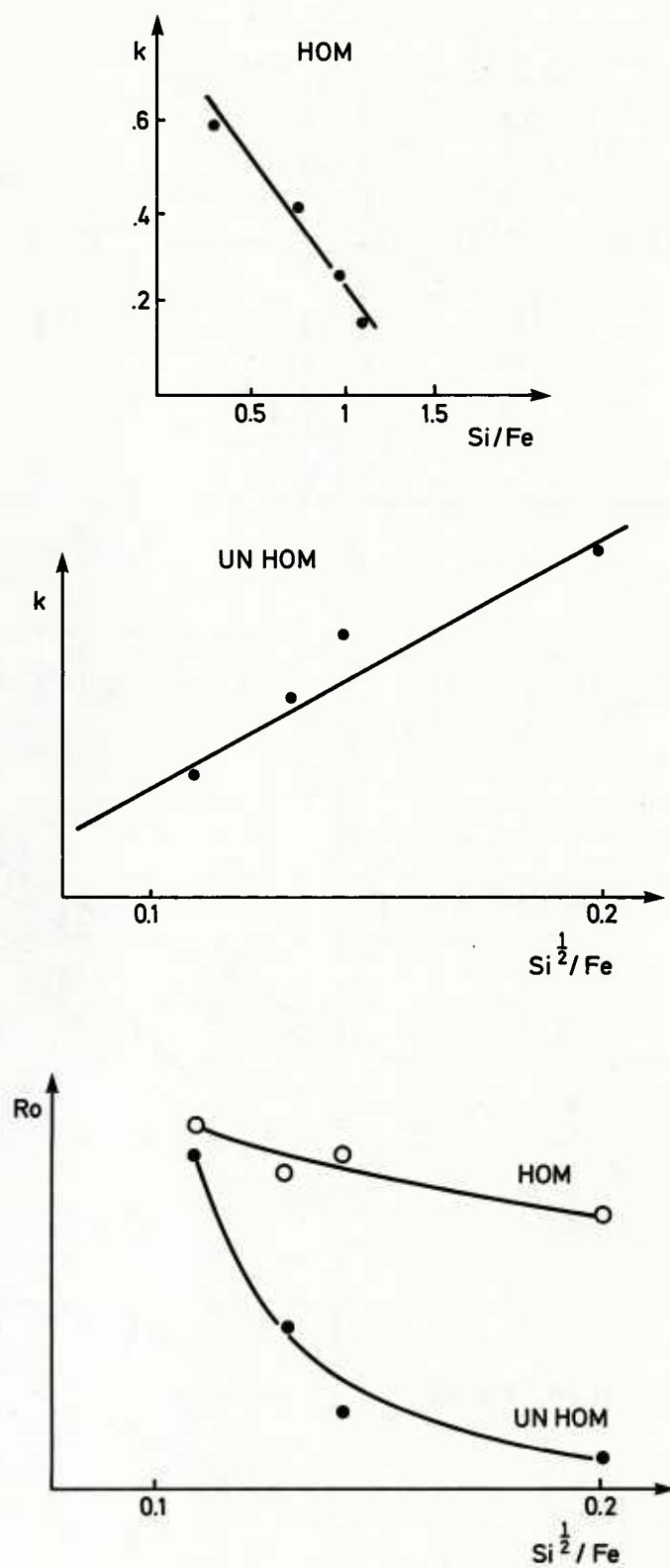
Fig. 10
The variation in a) R_o and b) k (see eq. 10) as function of the ratios $Si^{1/2}/Fe$ and Si/Fe.
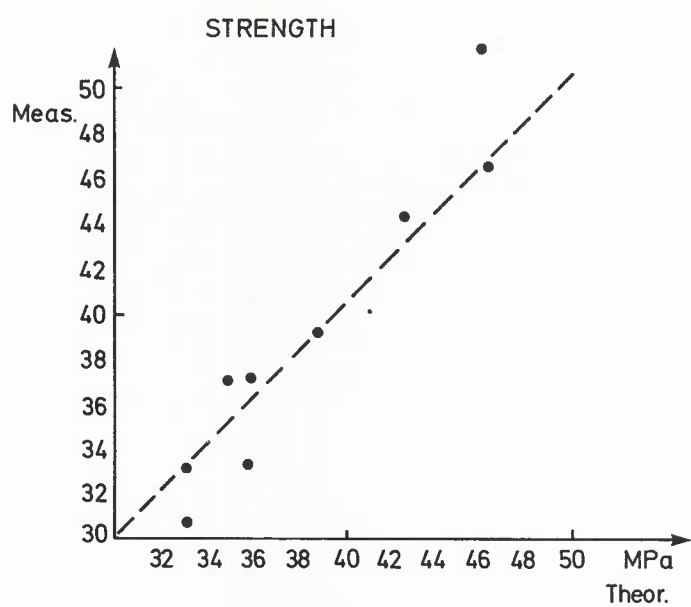
Fig. 11
Comparison between the observed and calculated initial flow stress for a series of AlFeSi alloys in the unhomogenized condition.

PREDICTION OF FORMING LIMIT DIAGRAMS FOR DEEP DRAWING

B. BAUDELET

Génie Physique et Mécanique des Matériaux
Unité Associée au CNRS N° 793
Institut National Polytechnique de Grenoble
I.E.G. - Domaine Universitaire - B.P. 46

38402 - SAINT MARTIN D'HERES CEDEX - France

.=.=.=.=.=.

Abstract

The use of steels of increasing strength and decreasing thickness is associated with different forming problems such as spring-back, surface deflexions, low forming limit. There is therefore a need for accurate optimization of the use of these materials through carefull modelling of sheet metal forming.

This paper presents different theoritical approaches to the determination of the forming limit diagrams at necking and rupture taking into account the influence of the constitutive law, surface defects and evolution of volume damage. The theory is compared with experiments.

I. Introduction

Sheet metal forming is and industrial process strongly dependent on numerous interactive variables : material behaviour, die design, press speed, loading conditions, hold down pressure, lubrication, etc. The basic objective is to increase the stability of press performance by a correct choice of the press shop variables. The deformation bahaviour of sheet metal is one of the most sensitive parameters in press forming operations. Characterization of sheet metal formability is therefore a subject of major importance in sheet metal forming analysis, providing technical means for increasing the performance in the press shop.

The formability of sheet metal is often evaluated from strain analyses using the concept of forming limit diagrams (FLD), introduced by KEELER and GOODWIN (1,2). Forming limit diagrams, which represent the relationship between limiting major and minor principal strains in the plane of the strained sheet, have found increased usage in sheet metal forming analyses.

Many attempts have been made to predict the FLDs on the basis of the theory of plasticity, material parameters, and instability conditions.

The limit strains for the diffuse necking condition have been derived by SWIFT (3), assuming that plastic instability occurs at a load maximum for proportional loading. In industrial stampings, the maximum allowable strain levels are not determined by diffuse but by localized necking and therefore diffuse necking limit curves have little practical interest.

HILL (4,5) first describes localized necking in thin sheet under plane stress states. HILL's analysis predicts localized plastic deformation in the characteristic directions of zero extension, for the stress states where one of the surface strains is negative. However, localized necking can be observed experimentally in biaxial stretched sheets, and several methods have been proposed to compute the entire FLDs.

MARCINIAK and KUCZYNSKI (6-8) have developed a theory (the M-K theory) based on the assumption that necking develops from local regions of initial heterogeneity. Assuming the initial heterogeneity in the form of a narrow band across the sheet, and incorporating the "J_2" flow theory of plasticity, MARCINIAK et al. (6-8) derived a system of equations which enabled a complete description of the necking process under various plane stress conditions.

The M-K theory has been later developed by HUTCHINSON and NEALE (9,10) and extended using a "J_2" deformation theory.

A number of authors (11,12) have given a different approach to sheet necking description, valid for homogeneous materials, incorporating a "J_2" deformation theory into a bifurcation analysis, that predicts the entire FLD.

Theoretical and experimental FLDs are determined for proportional strains paths, i.e., the ratio ρ of major to minor strain is constant at any stage of deformation .

During one step forming operations, the strain path is often linear in the first stages of deformation, but as straining progresses, the strain path gradually curves towards plane strain (13-15).

Industrial stampings of complex shapes, often involve multiple stage forming operations, and linear strain paths can no longer be observed. The evolution of the strain ratio in certain points of the workpiece is generally quite complex and abrupt changes can take place (14-16) as shown in Fig. 1.

Numerous experimental works (17-24) have shown that formability of sheet metals strongly depends on strain path and strain "history". Premature instabilities are observed for strain paths consisting of prior balanced biaxial prestrain followed by uniaxial tension. Conserversly, uniaxial prestrain followed by balanced biaxial stretching considerably increases limit strains at onset of necking. In addition, a change in strain path towards plane strain, results in a significant loss of plastic stability.

Under such conditions, the forming limit diagrams referred to linear strain paths cannot be used to estimate the safety margin of the forming operations. The effect of the strain path on the formability of sheet metals is often assessed using FLDs for complex strain paths. From these diagrams, it is possible to understand the behaviour of the material under complex strain paths, to estimate the severity of the strain paths imposed to the workpiece, and to optimize the shape of the dies to avoid the occurrence of necking (18).

MUSCHENBORN and SONNE (25) proposed two empirical methods to determine the FLDs for complex strain paths, assuming that instability occurs at critical values of the effective strain (or thickness strain), determined by the strain increment ratio in the final stage of deformation.

Several authors (26-28) have studied the effect of strain path on the SWIFT-HILL limit strains. However, localized necking in biaxial stretching cannot be predicted using such theories.

Recently, FLDs were determined (29,30), assuming time-independent material behaviour, using the M-K theory.

Considering the M-K theory, the present paper examines for an isotropic material, the effects on the forming limit diagrams of the characteristic parameters involves in :

- the constitutive law : $\sigma_c = K\ (\bar{\varepsilon} + E_0)^N\ \dot{\bar{\varepsilon}}^M$
- the deformation paths, simple on complex
- the initial geometrical defect F_0 (appendix A)
- the defect due to volume damage (appendices B and C)

Furthermore, this paper presents for an anisotropic material, the effects on the forming limit diagrams of the parameters of the consititutive law and of the deformation paths.

All these results were obtained in my laboratory by Augusto BARATA DA ROCHA, Frédéric BARLAT and Jean-Michel JALINIER (31-35).
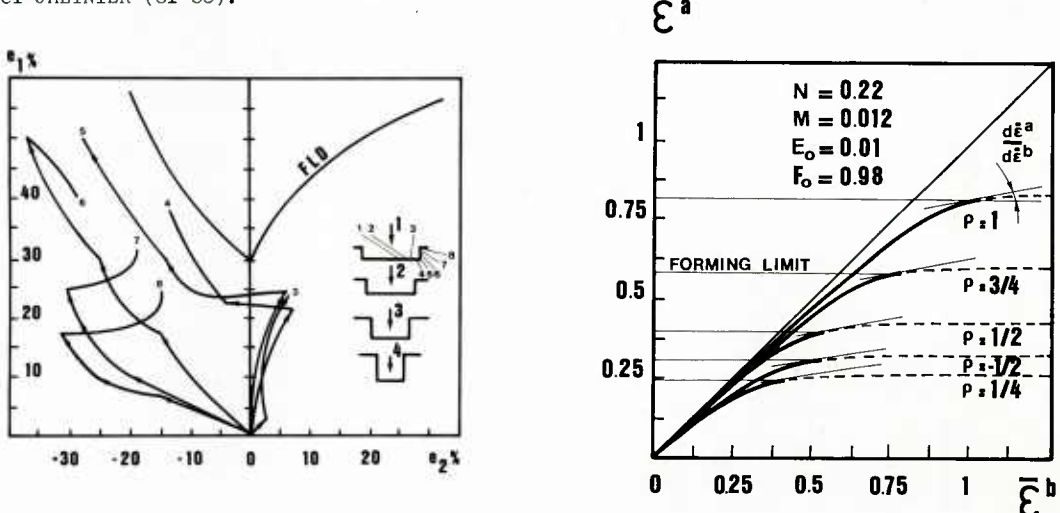

Fig.1 – Deformation paths of different points of the workpiece during multiple stage forming operations (from Ref.14).

Fig.2 – Strain localization process during linear incremental deformation.

II. Theoretical Analysis of the Forming Limit Diagrams for Isotropic Materials

II.1 – Prediction of the FLDs in Simple Deformation Paths for Isotropic Materials with an Initial Geometrical Defect.

To proceed with the simulation, a linear incremental strain path is imposed to region "a" (Fig.A.1). As straining progresses, region "b" will undergo more plastic deformation than the rest of the sheet (Fig.2). From the boundary condition (Eq.A.8), the strain in the "t" direction is equal for both regions "a" and "b". Therefore, as both "$\bar{\varepsilon}$" and "ε_{nn}" strains are more important in region "b", it results a change in the strain path in this region which tends to approach plane strain. Figure 3 shows the evolution of the strain path in the two regions, computed using the M-K model. It can be noticed that, because of the neck orientation, the "ε_2" strain is always the same in regions "a" and "b" during straining for the cases : $\varepsilon_2 \geqslant 0$.

Instability occurs when the ratio of strain rates reaches a critical value (Fig. 2).

$$\frac{d\bar{\varepsilon}^a}{d\bar{\varepsilon}^b} = constant$$

The computed limit strains depend on the initial orientation of the groove band (Fig 4). The curves of Fig.5 indicate that the initial band orientation greatly influences the limit strains for negative strain ratios. In contrast, for positive strain ratios, this effect gradually vanishes as balanced biaxial tension is reached. The value of the initial angle "Ψ_0" which leads to final necking at the lowest level of deformation " Ψ_0^*", defines the actual condition of the necking process. For positive strain ratios, necking always occurs for neck orientations parallel to the minor principal strain direction ($\Psi_0 = 0$), and therefore

the current band orientation remains constant. For balanced biaxial stretching, limit strains are independent of the initial orientation of the necking band, since in this case, for an isotropic material, the principal strain directions in the plane of the sheet are not determined.

The forming limit diagram is obtained for a range of imposed strain ratios from uniaxial tension ($\rho = -1/2$) to equibiaxial tension ($\rho = 1$) (Fig.3).
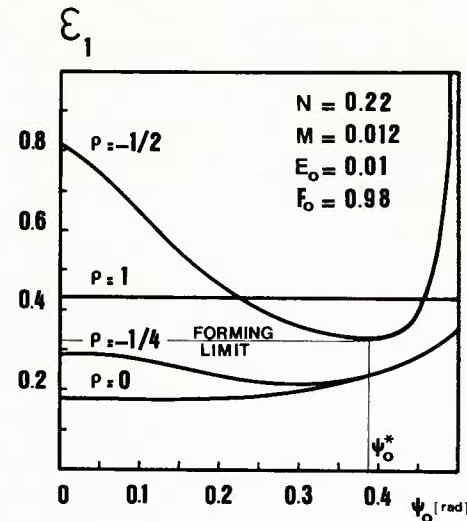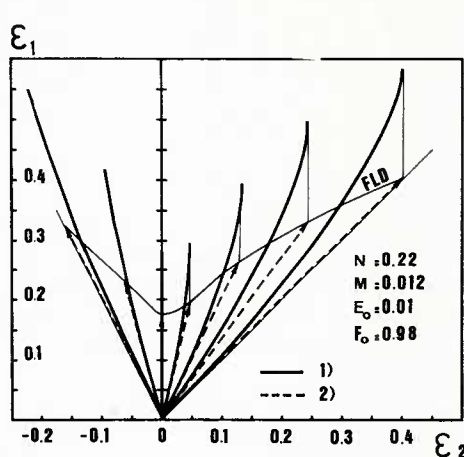

Fig.3 - 1) : Strain path in the necking region
2) : Strain path in the homogeneous region
Strain paths obtained in the necking region if proportional straining is imposed to region "a".

Fig.4 - Dependence of the computed limit strain on the initial orientation of the necking band for several linear strain paths.

II.2 - Prediction of the FLDs in Complex Deformation Paths for Isotropic Materials with an Initial Geometrical Defect.

The behaviour of sheet metal under complex strain paths is often examined by means of different linear deformation path combinations. Two different types of complex FLDs can be used to determine the effect of strain path changes on the formability of the material :

- One preliminary deformation followed by proportional straining at different strain ratios.
- One linear prestrain up to different deformation levels and subsequent straining at a fixed strain ratio.

Examples of such experimental curves are shown on Fig.5(a) and (b).
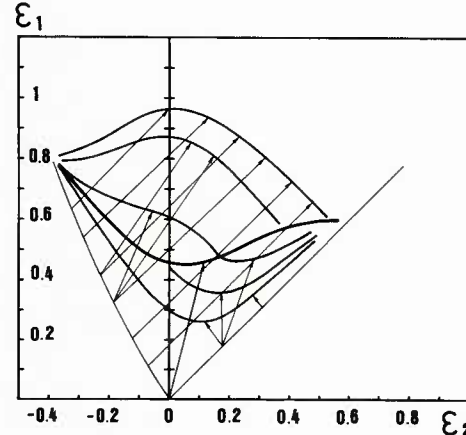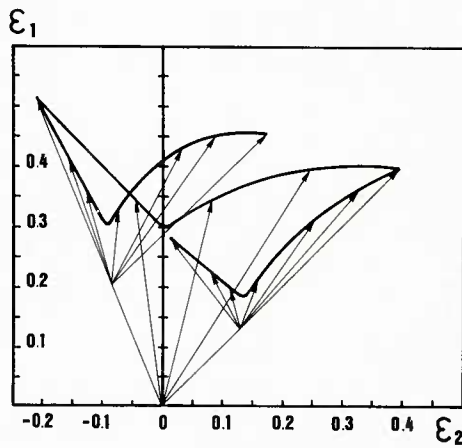
Fig.5(a) - Experimental FLDs of ARMCO Iron in simple and complex strain paths. Preliminary deformation in uniaxial and equibiaxial stretching, followed by proportional straining at different strain ratios (from Ref.17).

Fig.5(b) - Experimental FLDs of steel in simple and complex strain paths. Uniaxial or equibiaxial prestrain up to different deformation levels and subsequent straining at a fixed strain ratio (from Nakazima et al.61).

In order to predict these curves, forming limit diagrams are computed for a preliminary constant strain ratio ($\rho = \rho_1$) in the bulk up to a certain amount of prestrain, followed by an abrupt change in the strain path ($\rho = \rho_2$). Knowing the strain paths followed by the homogenous region, it is possible to compute the principal stain increments in the necking region :

$$de_1^b = \frac{d\varepsilon_1^a \sin^2 \psi + d\varepsilon_2^a \cos^2 \psi + d\varepsilon_3^b \cos^2 \psi}{\sin^2 \psi - \cos^2 \psi}$$

$$d\varepsilon_2^b = - d\varepsilon_3^b - d\varepsilon_1^b \tag{1}$$

The principal strains are calculated by integrating the strain increments along the corresponding strain paths :

$$\varepsilon_1^b = \int_{\rho_b} d\varepsilon_1^b \quad ; \quad \varepsilon_2^b = \int_{\rho_b} d\varepsilon_2^b$$

$$\varepsilon_2^a = \int_{\rho_a} d\varepsilon_2^a \quad ; \quad \varepsilon_1^a = \int_{\rho_a} d\varepsilon_1^a \tag{2}$$

The results shown in Fig. 4 indicate that the initial critical angle which minimizes the limit strains depends on the strain path. However, we are now dealing with a two stage deformation path, and the choice of the critical angle may be discussed. In fact, a critical value of the initial band orientation corresponds to each linear strain path.

The first approach to solve the problem is to consider that the current band orientation may suffer an abrupt change as the strain path changes. A critical band orientation is selected to minimize the final limit strains for each strain path. From a physical viewpoint, this assumption means that the strain gradient at the end of the prestrain is not sufficiently strong to impose the subsequent necking direction. Another interpretation is to consider a distribution of geometrical defects due to internal damage instead of only one single groove.

On the contrary, it can be considered that the amount of prestrain is large enough to develop high directional strain gradients and therefore to impose the neck orientation for any subsequent deformation. The computation in this case is carried out using the value of the current groove orientation at the end of the prestrain as the initial value of the groove orientation for the second strain path.

It is interesting to note that both approaches give the same results for two stage deformation paths involving balanced biaxial tension, since in this case limit strains are independent of the necking band orientation.

In the following, our computations are carried out using the second approach for different strain path combinations. The initial value of the groove orientation in the second strain path is therefore imposed to be equal to the value of the current band orientation at the end of the prestrain.

The value of the initial critical band orientation which leads to final necking at the lowest level of deformation can be found from the curves of principal strain vs. initial band orientation as in the case of linear strain paths.

As described previously for the case of proportional straining, the limit strains can be derived from the evolution of the effective strain in the two regions. Figure 6 shows the evolution of the computed effective strains for two typical strain path combinations. It can be seen that an abrupt change in the strain path dramatically modifies the evolution of these strains in comparison with the case of proportional straining. Furthermore, a change from balanced biaxial to uniaxial tension considerably accelerates the instability process, while a change from uniaxial to equibiaxial stretching greatly increases the stability of the deformation.
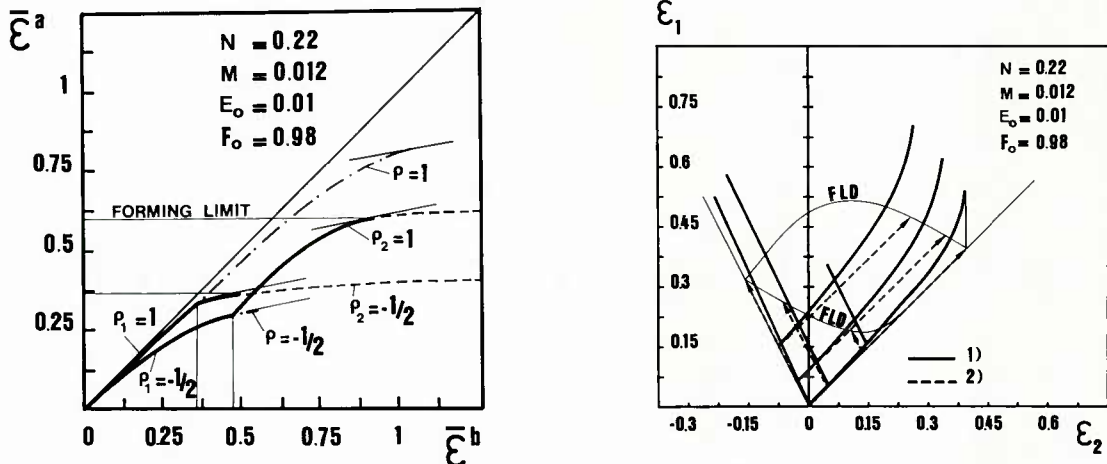

Fig.6 - Strain localization process for two typical complex strain paths.

Fig.7 - 1) Strain path in the necking region
2) Strain path in the homogeneous region
Strain paths obtained in the necking region if a complex strain path is imposed to region "a".

The limit strains can be calculated using the criterion defined for the case of proportional straining, which is based on the analysis of a critical strain rate ratio.

The strain path in the neck obtained imposing the above mentioned strain path combinations is presented in Fig.7. As expected, as necking develops, the strain path in the neck turns towards plane strain, for the cases where the current band orientation is approximatively parallel to the minor strain.

The influence of the initial band orientation on the computed limit strain is presented on Fig.8 for the case of uniaxial prestrain followed by balanced biaxial stretching. These curves indicate that the limit strains are rather insensitive to the initial band orientation for low amounts of prestrain, and that this sensitivity increases with increasing uniaxial prestrain.
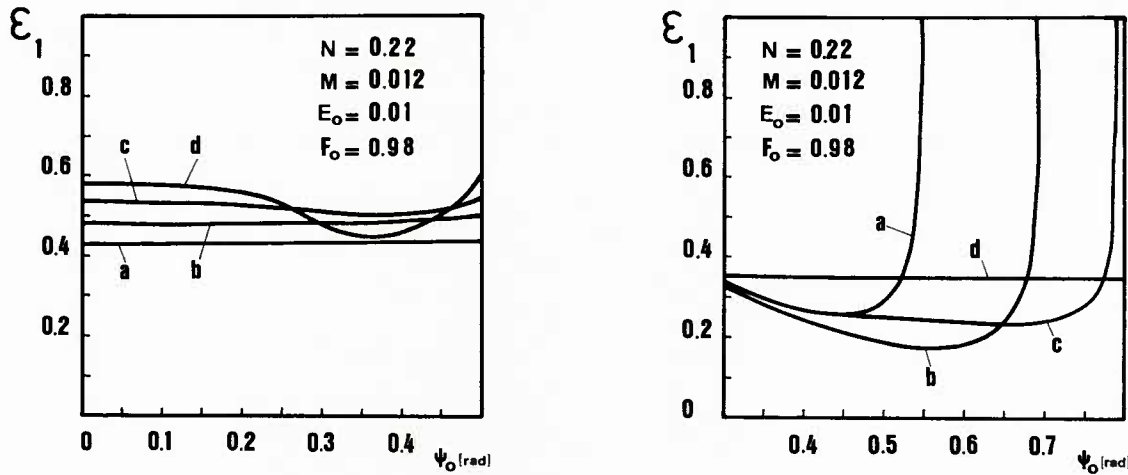
Fig.8 — a: Uniaxial prestrain up to ε_1 = 0.05
        b: Uniaxial prestrain up to ε_1 = 0.15
        c: Uniaxial prestrain up to ε_1 = 0.25
        d: Uniaxial prestrain up to ε_1 = 0.32
        Dependence of the computed limit strain on the initial orientation of the necking band for the case of uniaxial prestrain followed by balanced biaxial stretching.

Fig.9 — a: Equibiaxial prestrain up to ε_1 = 0.05
        b: Equibiaxial prestrain up to ε_1 = 0.15
        c: Equibiaxial prestrain up to ε_1 = 0.25
        d: Equibiaxial prestrain up to ε_1 = 0.35
        Dependence of the computed limit strain on the initial orientation of the necking band for the case of equibiaxial prestrain followed by uniaxial tension.

Figure 9 illustrates the dependence of the computed limit strain on the initial orientation of the necking band for the case of equibiaxial prestrain followed by uniaxial tension. A strong resemblance is evident with the case of linear uniaxial tension. A strong resemblance is evident with the case of linear uniaxial tension. In fact, the computation is independent of the initial band orientation for the first stage of deformation (equibiaxial straining) and the computed limit strains only depend on the current band orientation during the second stage of deformation for isotropic materials.

Contrary to the previous behaviour for the case of uniaxial prestrain followed by balanced biaxial stretching, here , the effect of the initial band orientation decreases with increasing prestrain until it vanishes for the cases where no subsequent uniaxial straining is possible.

The effect of different strain paths on the FLDs is presented in Figs. 10 (a) and (b). It can be seen that uniaxial tension followed by balanced biaxial stretching results in a significant increase of the limit strains. Conversely, uniaxial or biaxial prestrains followed by plane strain greatly reduced the forming limit strains.

In all cases, the highest forming limit curve is obtained for uniaxial prestrain followed by balanced biaxial stretching. One the other hand, for the range of strain paths considered, the lowest limit curve is found under the combined strain paths of primary uniaxial or balanced biaxial stretching and subsequent plane strain stretching. These results are in perfect accordance with previous experimental investigations (18-25). A more important observation is that a change in strain path to plane strain is more detrimental for the case of primary balanced biaxial stretching than for the case of primary uniaxial tension. This fact can explain the excessive levels of the predicted limit strains using the M-K theroy in the case of proportional biaxial stretching, since a slight curvature in the strain path will significantly reduce the limit strains. Here again a good agreement is obtained between these results and those obtained experimentally by KOBAYASHI et al. (18).

Equibiaxial prestraining enhances the subsequent uniaxial tension limit strains for small amounts of prestrain. However, with increasing prestrain this effect is reversed and premature instability will occur. According to this result, it is possible to define regions, in the principal strain space, attainable after balanced biaxial prestrain which are not attainable with a linear strain path. Conversely, strain regions which are attainable in a single-step operation are no longer attainable after the biaxial prestrain.

This theoretical result is in perfect agreement with those obtained experimentally by different authors (18,23,36).
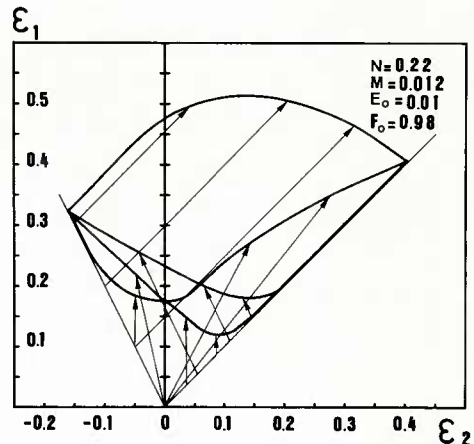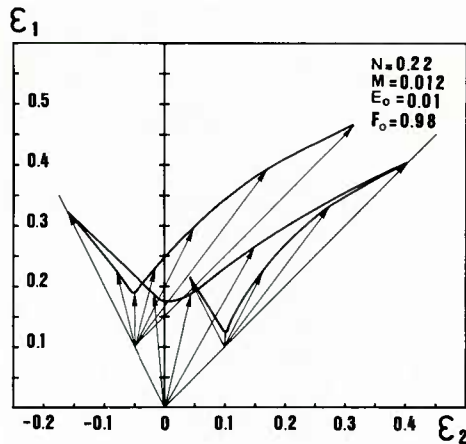
Fig.10(a) - Computed FLD's in simple and complex strain paths.
          - preliminary deformation in uniaxial and equibiaxial stretching followed by proportional straining at different strain ratios.

Fig.10(b) - Computed FLDs in simple and complex strain paths.
          - uniaxial or biaxial prestrain up to different deformation levels and subsequent straining at a fixed strain ratio.

It should be noted here that the direction of the strain increment has an increasingly strong effect on the plastic instability as the deformation progresses.

The forming limit curves obtained for the case of primary equibiaxial stretching and subsequent uniaxial or plane strain stretching, partially coincide with the linear balanced biaxial strain path. Therefore, in this region, a change in the strain path towards negative strain ratios will dramatically increase the strain rate in the necking region, and immediate plastic instability occurs, preventing any subsequent deformation.

Conversely, for uniaxial prestraining and subsequent biaxial stretching, enhanced stability is observed and premature instability does not occur. In this case, further uniaxial straining would lead to excessive strain rates in the necking region, while a change to biaxial stretching will considerably stabilize the deformation process. In other words, further uniaxial straining results in instability while biaxial stretching leads to a high level of the limit strains as expected from the results of Fig.6. The instability condition is not irreversible since it is based on a strain rate criterion. Therefore, further straining is possible, if the strain rate in the necking region decreases after the abrupt change in the strain path.

The forming limit diagrams obtained with such criterion will therefore present straight lines for high values of biaxial prestrain and for the case of uniaxial prestrain up to the limit strains in proportional loading.

This type of behaviour may be interpreted as a metastable plastic state in which the residual formability depends on the current direction of the strain increment.

II.3 - Prediction of the FLDs in Simple and Complex Strain Paths for Isotropic Material with Differents N and M values and Different Initial Geometrical Defect F_O.

In Fig.11, the dependence of limit strains on the strain hardening exponent is illustrated for several strain path combinations. The effect of increasing "N" is essentially to increase the level of the FLDs. However, this effect is the more pronounced for the cases of negative linear strain ratios, and large uniaxial prestrain followed by biaxial stretching.

The effect of material strain rate dependence on forming limit diagrams is depicted in Fig.12. The predicted limit strains for proportional loading substantially increase with increasing strain rate sensitivity. This effect is greater for negative strain ratios. Metastable plastic states are considerably reduced for high levels of strain rate sensitivity. Residual formability is always reduced by increasing prestrain. For biaxial prestrain, this reduction is more rapid for low values of strain rate sensitivity. Thus, while large biaxial prestraining followed by uniaxial stretching of a rate independent material results in immediate instability, this effect becomes progressively smaller with increased strain rate sensitivity.

In contrast, for large amounts of primary uniaxial tension the residual formability in equibiaxial streching decreases as the strain rate sensitivity increases.

Figure 13 shows the theoretical influence of the imperfection size on the forming limit diagrams. It can be seen from these curves that the predicted limit strains are very sensitive to variations in the initial heterogeneity. Large initial defects are more detrimental for both linear positive strain ratios and uniaxial followed by biaxial stretching.

Some experimental works (37-39) have shown that strain and strain rate hardening behaviour vary with both increasing biaxiality and increasing effective strain.
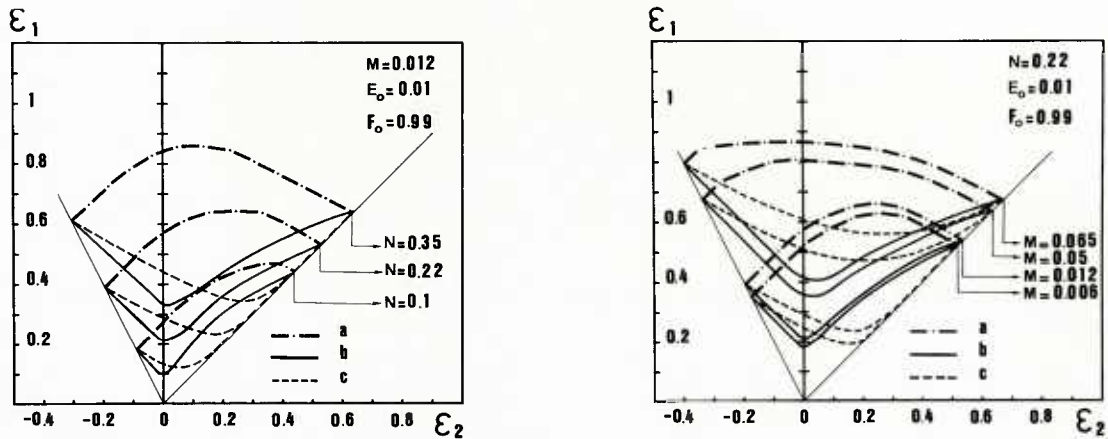
Fig.11 - a: Uniaxial prestrain followed by balanced biaxial stretching
         b: Linear strain paths
         c: Equibiaxial prestrain followed by uniaxial tension
         Effect of strain hardening exponent on the FLDs under simple and complex strain paths.

Fig.12 - a: Uniaxial prestrain followed by balanced biaxial stretching
         b: Linear strain paths
         c: Equibiaxial prestrain followed by uniaxial tension.
         Effect of strain rate sensitivity on the FLDs under simple and complex strain paths.
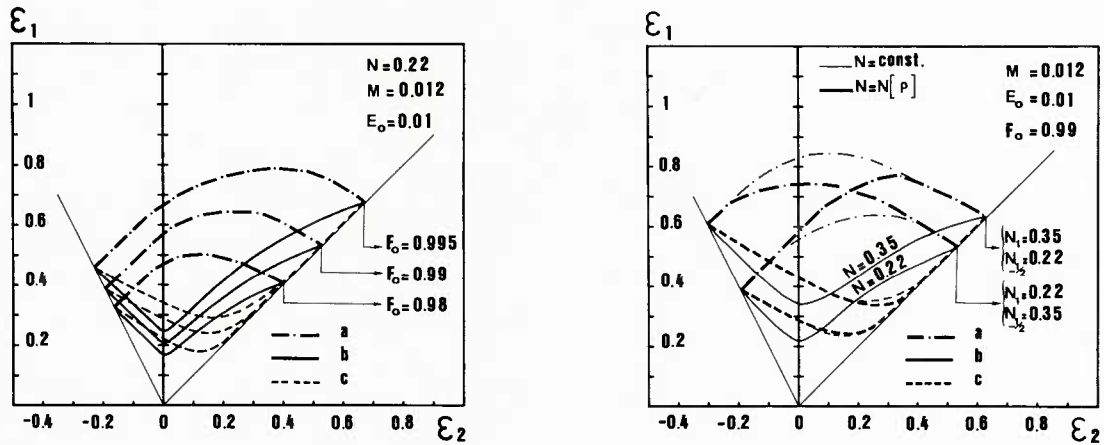
Fig.13 - a: Uniaxial prestrain followed by balanced biaxial stretching
         b: Linear strain paths
         c: Equibiaxial prestrain followed by uniaxial tension.
         Effect of the imperfection level on the FLDs under simple and complex strain paths.

Fig.14 - a: Uniaxial prestrain followed by balanced biaxial stretching
         b: Linear strain paths
         c: Equibiaxial prestrain followed by uniaxial tension.
         Effect of the evolution of the rheological parameter "N" during deformation, on the FLDs
         under complex strain paths.

Accurate predictions of FLDs require an exact characterization of the material behaviour. Therefore, predictive models of localized necking must incorporate such effects either by using more accurate constitutive equations or by correcting the rheological parameters of an approximate law.

Figure 14 shows the predicted FLDs for a strain path dependent n-value :

$$N = N (\rho) \tag{3}$$

for two schematic cases. Strain paths consisting of balanced biaxial tension followed by uniaxial tension generally lead to low formability and therefore no significant influence of the strain-hardening can be observed. On the other hand, strain paths consisting of uniaxial tension followed by biaxial stretching induce large plastic strains. An increase or decrease of the strain hardening exponent at the change in strain path will greatly influence the further deformation. Specially, the metastable state is widely increased when the strain hardening is increased and on the contrary is reduced when the strain hardening value drops.

II.4 – Prediction of the FLD's in Simple and Complex Deformation Paths for Isotropic Materials with Volume Damage.

Plastic instability phenomena are considered through a macroscopic description of the material as well as a microstructural parameter, the volume damage. This parameter describes the appearance and growth of microscopic cavities arising from material discontinuities whose origin in industrial materials is frequently associated with the presence of inclusions, precipitates and a second phase. Very often, a number of these particles are either needed in sheet production or required for particular mechanical and metallurgical properties. However, they provide favorable sites for cavity formation which gives rise to a progressive deterioration of the material.

In particular, it is well known that ductile fracture results from the nucleation, growth and coalescence of cavities. In figure 15 which shows this type of fracture, one recognizes traces of the cavity coalescence during the last deformation stages.

If volume damage is one of the factors leading to fracture, it must have an effect leading to unstable material behavior from the earliest deformation stages. This underscores its importance with respect to plastic instability phenomena.

C.C. CHU (40) analyzed different factors giving rise to high deformation gradients during the stamping of an axially symmetric sheet using a circular die. A finite element method was used to examine the effects of friction and boundary conditions. Volume damage was introduced through GURSON's (41) plastic flow criterion for porous materials as well as the flow laws associated with this criterion.

C.C. CHU shows that the presence of cavities reduces the deformability of the material. However, in order to have reasonable results, he must introduce initial values of cavity volume fractions values of 0.01 to 0.03 and these evolve to values of 5 to 10 % for stages just preceding the striction. It seems that these values are much too high as compared to those usually measured for metal sheets : (10^{-3} to 5.10^{-3} (42)).

For the basic model of MARCINIAK, NEEDLEMAN and TRIANTAFYLLIDIS (43) have shown that one can consider the following defect types : thickness heterogeneity between the homogeneous portion and the defect, deformation heterogeneity, different flow stress. They also studied the heterogeneity due to a greater volume fraction of cavities near the defect. The calculation for the biaxial case supposes the localisation band is perpendicular to the least of the principal stresses. The constitutive equations for porous materials of GURSON were introduced. To obtain theoretical forming limit curves in agreement with experimental results, they had to use initial volume fraction values of the order of 10^{-2} . As in the study of C.C. CHU, these appear to be unreasonably high. Nevertheless, the authors conclude that the difference in the forming limit curves may be attributed to the growth of cavities.

Furthermore, CHU and NEEDLEMAN (44) analyzed the influence of cavity nucleation on the forming limit calculated as in the preceding investigations (40-43). Various nucleation criteria were introduced in the equations and in particular, a criterion based on a critical equivalent strain. It is assumed that cavities appear at strains normally distributed around the critical deformation. It was shown that when the standard deviation of this normal law is small (almost all of the cavities appear at the same strain), all the cavities are created in the defect and not in the less deformed homogeneous portion. This explains why the influence of nucleation in this case is very destabilizing and it leads to rather low forming limit curves.

MELANDER (37,45,46) developped a theory in which the geometrical model is identical to that of MARCINIAK-KUCZINSKI or HUTCHINSON-NEALE. It supposes, however, that the heterogeneity is a region of the material where the volume fraction of inclusions is greater than the mean value. It is a region whose thickness is not necessarily different from that of the homogeneous portion. MELANDER assumes the volume fraction of cavities to be a function of that of inclusions and of the accumulated strain in each of the two regions of the material This function may be identified by quantitative microscopy. As in the preceding studies, he introduced the volume fraction of cavities in the equations of his model using GURSON's criterion. For numerical applications, he used experimental values of strain-hardening, strain rate sensitivity, anisotropy (r) and mean initial inclusion concentration. The only unknown is the inclusion concentration in the defect. He uses this as an adjustable parameter for the agreement of theoretical and experimental curves. This leads him to conclude that the purer the material, the more concentrated must the inclusions be in the defect in order for the theory to be satisfactorily applicable to different materials.

Damage is introduced in a different manner by JALINIER and SCHMITT (38,47). They consider that the volume dilatation is negligible and that the constitutive laws of incompressible plasticity are appreciable. Damage is introduced through a statistical study in which it is shown that plane sections in the material cut a great number of cavities. These sections will then have a smaller area that the average section. This section defect is then assumed to be equivalent to a thickness defect which enables them to identify the model to be that of MARCINIAK. However, they add to the defect increase due to heterogeneous plastic flow, a defect increase due to cavity growth. Through this method, physical parameters based on quantitative microscopic observations can be introduced. The forming limit curves obtained are in good agreement with experimental curves. Furthermore, their theory explains why thinner sheets give rise to less satisfactory deformation and this is a well known experimental observation (25,48,49). This approach gives a physical description of damage and uses a simple mechanical model for the analysis of plastic instability phenomena.

Another purely statistic method, was proposed by VAN MINH, SOWERBY and DUNCAN (50) to explain the distribution of experimentalloy observed deformation limits for a given material and a given operation (51). This study is based on the hypothesis that MARCINIAK's theory holds for an elementary surface of a sheet in which a certain cavity distribution exists. The defect amplitude is given by the largest cavity in this element. After a probability calculation, it is possible to associate to a given stamping operation, a forming limit obeying a statistical distribution law. The authors show that the mean deformation limit decreases as the cavity mean size increases or as the sheet thickness decreases. However, this statistical investigation introduces very arbitrary parameters to describe cavities.
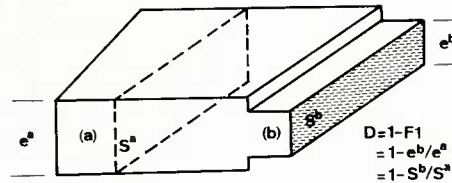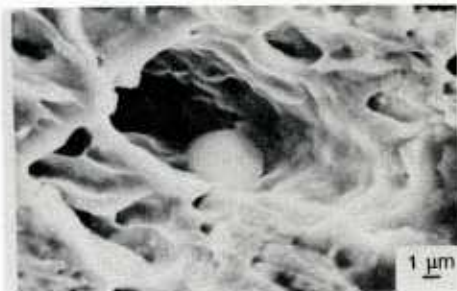
Fig.15 – Fracture surface of Nb microalloyed steel. One finds in a cusp an inclusion of aluminium oxide.

Fig.16 – Equivalence between a thickness defect and a section defect.

MARCINIAK's model(6-8) uses a macroscopic description of the material. He assumes that after a certain amount of deformation, flow becomes localized on a defect represented by a narrow linear band initially present in the material. One supposes that the material has properties in this band different from those in the homogeneous portion and this difference is modelized by a smaller thickess or section area at the band. Equilibrium equations show that the stress is higher at the zone "b" and, hence, plastic flow in the two zones differ from each other.

A physical explanation can be given to the section defect from the concept of damage . For a certain distribution of cavities, there exist sections, normal to the sheet plane, which intercept more cavities than other sections (Fig.16). For a random distribution of cavities in a material, a statistical study shows the existence of these sections.

This determination, developped in Appendix B, is divided into two parts:

– the first consists of calculation for a point on the sheet, the probability of finding a point defect, due to the superposition of one or several cavities, along a line passing through the point and normal to the sheet plane. This calculation was already done for the cases of one class of cavities (42) or of two classes of cavities (59).
– the second considers a local defect distribution and calculates a linear defect F_1 equivalent to the defect of the plastic instability model using the M-K theory.

The evolution of the statistic defect due to the growth of cavities during the deformation is described in Appendix C.

When damage is not taken into account in the analysis, the defect values increase (F_1 decreases) only by heterogeneous plastic flow of the material of two zones. If the cavity evolution is to be accounted for, one must, at each step of the calculation, add to the defect, an increment due to cavity growth.

The influence of cavity growth becomes evident through the following two simulations.

The initial statistical defect is calculated for a material containing one class of spherical cavities of concentration $C_{vo} = 10^{-3}$. The parameter v is equal to 350 and this corresponds, for example, to a sheet having a thickness of 0.7 mm. and containing cavities whose initial radius is 1 µm. For the first case (a), one neglects the incremental defect due to cavity growth while the second case (b) takes the cavity growth into account (Fig.17).

The difference between the curves obtained for linear strain paths is considerable, in particular, for the equibiaxial case. The forming limit curves are also shown for complex strain paths consisting of two linear branches :
. uniaxial tension followed by equibiaxial expansion (TE)
. equibiaxial expansion followed by uniaxial tension (ET)

The influence of cavity growth on the TE curves level is very appreciable. The loss of formability may attain 20%. The difference between the curves shown in figure 17 could be explained by the evolution of damage, i.e., much less cavity growth in tension than in equibiaxial expansion.

The effect of the initial volume fraction of cavities can be seen for one class of initially spherical cavities in a sheet of a given thickness (Fig.18). In other words, the number of cavities per unit volume is the only variable parameter. Calculations were made for cavity concentration values observable in cold rolled materials ($C_{vo} = 5.10^{-4}$, 10^{-3}) and for a reasonable limit value ($C_{vo} = 5.10^{-3}$).

As noted previously, the influence of damage is greater for complex TE strain paths. Furthermore, one must emphasize the appreciable influence of the initial cavity concentration on the forming limit level. Reducing this concentration is therefore very useful.
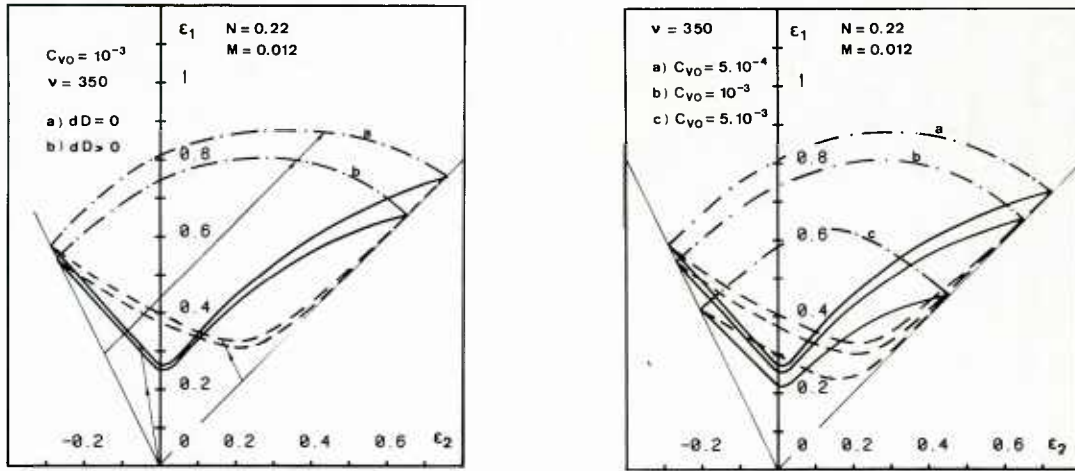
Fig.17 - Influence of damage evolution on the FLD
a) the cavity growth is neglected
b) the cavity growth is taken into account.
Solid lines : linear strain paths
Dashed lines: expansion - tension E.T.
Mixed lines : tension - expansion T.E.

Fig.18 - Influence of the cavity volume fraction on the FLD level.

The parameter ν which remains constant during the deformation is defined as the ratio of the initial thickness of the sheet to the cavity diameter. For a given initial concentration of cavities, figure 19 shows that as the value of ν increases, the higher the curve level is. This result may have two interpretations :

. for an initial thickness of the sheet, ν is inversely proportional to the cavity diameter. It is therefore preferable for a given volume fraction to have a large number of small cavities rather than a small number of large cavities.

. For a given cavity size, ν is proportional to the thickness of the sheet. Thus, for a given material, the forming limit curve level is higher when the sheet is thicker. This result is in agreement with many experimental results (25,48,49).

Most often, the cavity size of industrial materials is not constant. As a first approach, two classes of cavities which differ in size (A and B) are considered. Simulations were done with the following parameters (Fig.20) :

- large cavities (class A) R_{OA} = 5 µm (initial radius)
- small cavities (class B) R_{OB} = 1 µm (initial radius)
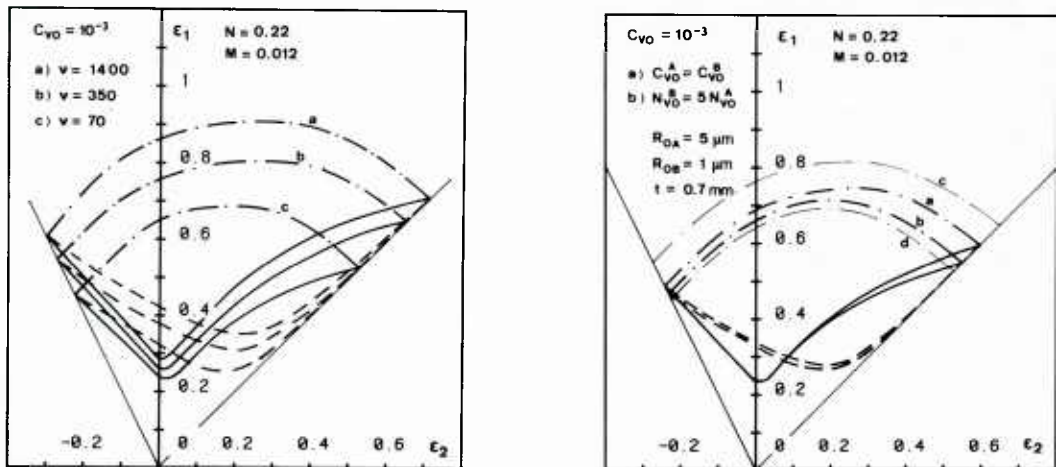
Fig.19 - Influence of the parameter ν on the FLD level

Fig.20 - Effect of two cavity sizes for a given total cavity volume fraction.
a) the two classes of cavities have equal volume fraction
b) the number of smaller cavities per unit volume is 5 times greater than that of larger cavities.
c and d) limiting cases for just one class of cavities.

The total volume fraction of cavities is imposed to be 10^{-3}. The variable parameter is the relative volume fraction of each class. The extreme curves are obtained by assuming just one class of cavities (curves c and d for the path TE). Two intermediate cases are considered :

- the two classes have the same relative concentrations (curve a)
- the number of small cavities per unit volume is 5 times greater than that of large cavities (curve b).

These curves show that the main influence of damage is due to the presence of large cavities. In most cases, and in a first approximation, the influence of small cavities can be neglected.

III. Theoretical Analysis of the Forming Limit Diagrams for Anisotropic Materials in Simple and Complex Deformation Paths with an Initial Geometrical Defects.

In most anisotropic materials, the defect inclination which leads to the minimum value for expansion deformation limits, does not coincide with the direction angle $\Psi = 0$ (Fig.A.1). Hence, plastic anisotropy can control the striction orientation.

A very representative case can explain this phenomenon by ascribing the value unity to r_0 and r_{90} and by using r_{45} as a variable parameter (r_0, r_{90} and r_{45} are defined in the Appendix A). Figure 21 shows the influence of the defect orientation on the deformation limits calculated in equibiaxial expansion ($\varepsilon_1 = \varepsilon_2$). In the isotropic case ($r_{45} = 1$, curve b) the deformation limits are independent of the initial orientation of the band. For values of r_{45} less than unity (curve a), the deformation limits depend on Ψ_0 and the minimum of these curves correspond to an initial inclination of the band perpendicular to either the rolling direction or to the transversal direction (0° or 90°). Therefore, the forming limit in expansion ($\rho = 1$) is equal to that of the isotropic case.

It is interesting to note that stampers characterize sheet anisotropy in terms of r and Δr :

$$r = (r_0 + r_{90} + 2r_{45})/4$$

$$\Delta r = (r_0 + r_{90} - 2r_{45})/4$$

In the present case, the value of r_{45} less than unity is equivalent to positive values of Δr. For values of r_{45} greater than unity ($\Delta r < 0$), curves (c) and (d) show a minimum for values of the angle Ψ_0 different from 0 ; this does not agree with the assumption of an initial defect perpendicular to the direction 1. It therefore appears that the value of r_{45} (or Δr) plays a very important role in this case since it controls the advent of plastic instability in expansion and can considerably lower the forming limit curve level (Fig.22). Furthermore, the curves in figure 21 meet for values of the angle Ψ_0 equal to 0° and 90° and this proves that for these values, the instability calculation is independent of r_{45}.

In fact, studies for the theoretical determination of forming limit curves for anisotropic materials under linear strain paths in expansion, have imposed the wrong hypothesis of a defect orientation normal to the direction of the largest principal stress (53-55). This hypothesis was inferred from results obtained in isotropic materials.
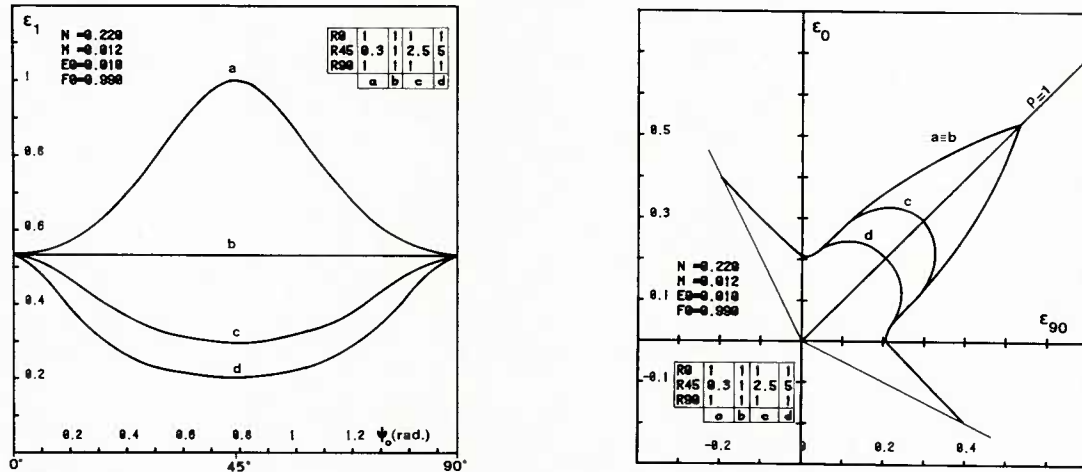

Fig.21 – Forming strain limits as a function of the defect orientation for a sheet under equibiaxial loading ($\alpha = 1$ and $\rho = 1$).

Fig.22 – Influence of r_{45} on the FLD level for linear strain paths. ε_0 and ε_{90} represent strains in the rolling and the transverse directions respectively.

For the most general case of anisotropic materials ($r_0 \neq r_{45} \neq r_{90}$), figure 23 shows that the forming limit curves are also very dependent on r_{45}. In this figure, the continuous solid line represents striction instabiity limit for linear paths. In the expansion region (ε_0 and ε_{90} positives) the dashed line represents this limit under the assumption of an initial defect perpendicular to one of the principal stress directions. In fact, the defect orientation minimizing the deformation limits for biaxial states passes continuously from 0° to 90°, i.e., from plane deformation in the rolling direction ($\varepsilon_{90} = 0$) to plane deformation in the transverse direction ($\varepsilon_0 = 0$).

This theoretical analysis which predicts striction directions neither colinear to the rolling nor to the transverse directions, is compatible to experimental observations of fracture orientations in sheets deformed in expansion (56,57).

The anisotropic character of the material leads to sheet behavior for uniaxial tension along the rolling direction different from that along the transverse direction. This property of only deforming slightly along the thickness direction is reflected by a high coefficient of anisotropy. This explains the higher level of the plastic instability limit along the rolling direction as compared to that along the transverse direction (r_{90} =1) (Fig.23). This lack of symmetry requires the representation of the forming limit curves in the material axes, defined by the rolling and transverse directions.

It is interesting to note that there exist regions where the principal stress axes are rotated by $\pi/2$ with respect to those of the principal deformations. The largest principal stress direction coincides with the direction of the least principal deformation. This region lies between the linear paths corresponding to ρ and α equal to unity.

The success of a stamping operation depends on the orientation of the flange with respect to the loading axes, i.e., with respect to the tool positions. The choice of this orientation is generally based on the stampers experience and on preliminary tests. A theoretical explanation may be given to this phenomenon by the superposition of the forming limit half-curves of an anisotropic material : from the uniaxial tension along the rolling direction to the expansion and from the uniaxial tension along the transverse direction to the expansion (Fig.24).
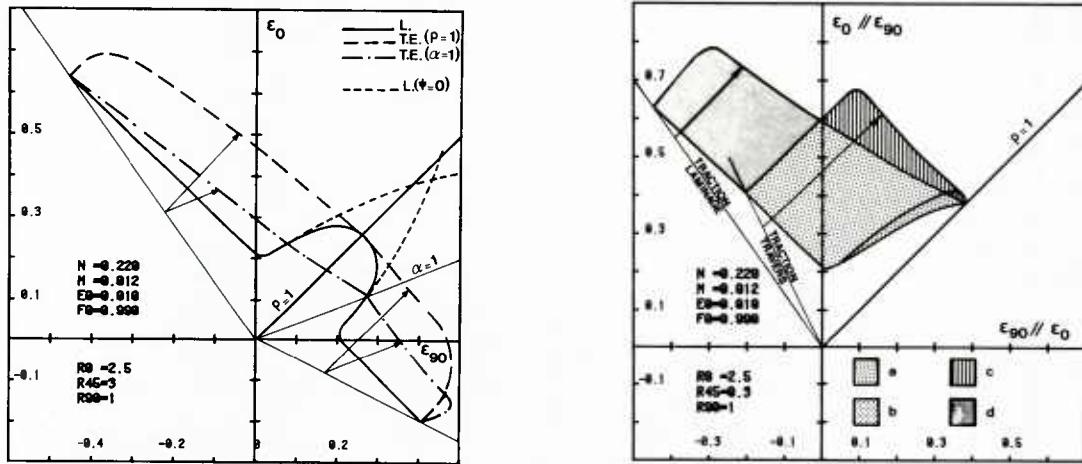

Fig.23 - Forming Limit Diagrams
       L   : linear paths
       TE (ρ = 1) : tension-expansion for ρ = 1
       TE (α = 1) : tension-expansion for α = 1
       L (Ψ = 0) : linear paths ; defect normal to one the principal stress directions.

Fig.24 - Importance of the flange orientation in a stamping operation.

For a given strain path, one can verify that certain zones can only be attained for a favorable orientation of the flange. It can be seen that for the tension expansion sequence, the deformation zone (d) can only be reached if the tensile predeformation is performed along the rolling direction. On the other hand, the region (b) can be attained in this sequence by either one of the flange orientations considered.

IV. Conclusions.

Forming limit diagrams in complex deformation paths are determined using the M-K theory. The theoretical analysis developed in this work can predict the plastic behaviour of sheet metal under complex strain paths. In this analysis :

- . the strain path is shown to be the most important industrial parameter controlling plastic instability in multiple stage forming operations. In particular, it is shown, with the help of different combinations of two stage linear strain paths, how premature instability can occur because of the strain path imposed to the material. Maximum limit strains are obtained for the case of uniaxial prestrain followed by equibiaxial stretching. The lowest FLD under complex strain path is obtained when the second stage of deformation consists of plane strain, and it is therefore possible to predict three different regions in the principal strain space. The first region is upper bounded by the minimum FLD and the strains inside this region can always be achieved without instability for any strain path combination. The second region lies between the maximum and minimum FLD, and the strains inside this region can only be achieved if a correct strain path is imposed to the material. Finally, the third region is lower bounded by the maximum FLD, which represents the ultimate limit strains and the strains inside this region can never be achieved with the two stage linear strain path combination considered.

- . the influence of the rheological parameters on the limit strains under complex strain paths is studied and it is shown the importance of the strain rate sensitivity on the shape of the forming limit curves.

. the model can be extended to actual complex strain paths of industrial stampings, either by dividing the real strain path in several linear strain increments or by a correct fit of an analytical function in order to predict the severity of the forming operation.

. the influence of the strain path on the formability of the material, and the general form of the complex FLDs is explained in terms of the strain rate of the necking region, and the concept of metastable plastic states is introduced.

. the direction of the strain increment at the last stages of deformation is shown to be an important parameter controlling plastic instability.

. the evolution of the strain hardening exponent during deformation is simulated and it is shown that complete objective comparisons with experimental results need accurate constitutive equations.

. volume damage was modelized and It was shown than small cavities lead to better formability.

. for anisotropic materials, the theoretical analysis look into account three anisotropic coefficients. It was shown that the value of the coefficient at 45° of the rolling direction has a greater influence on formability.

A successful correlation is obtained between the form of the experimental FLDs and the computed strain limits in this analysis.

APPENDIX A

PLASTIC INSTABILITY CALCULATION FOR AN ANISOTROPIC MATERIAL

The model of MARCINIAK and KUCZINSKI (6-8) reconsidered and improved by HUTCHINSON and NEALE (9) and recently by BARATA DA ROCHA and JALINIER (31) is based on the existence of a defect in the material. In this defect, represented by a local sub-thickness of the sheet (Fig.A.1) , plastic flow is localized upon reaching a certain amount of strain in the homogeneous portion under a plane state of uniform stresses (σ_1 , σ_2 on figure A.1). The plastic instability equations are developed in this study are based on the same principle, i.e., the search for the moment when all the deformation concentrates in zone "b" at the expense of zone "a". Two main differences lead however to a system of equations different from those obtained before: the first is the introduction of anisotropy described by three coefficients r_0, r_{45} and r_{90} equal to the ratio $d\varepsilon_2/d\varepsilon_3$ in a tensile test with the tensile axis at 0°, 45° and 90° respectively with respect to the rolling direction ; the second is the incremental expression of all the equations in order to simulate non linear strain paths.
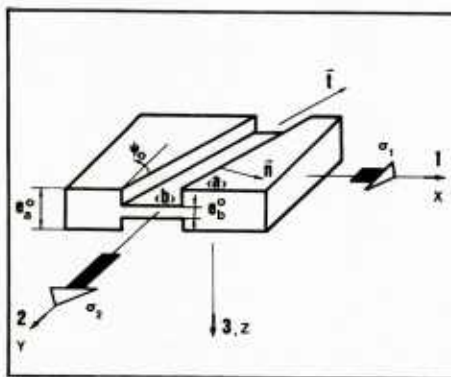

Fig. A.1 - Geometric configuration for the two zone plastic instability model.

A-1. Geometry of the model :

A plane state of stresses is applied to the homogeneous region (zone a). The directions 1 , 2 represent the principal loading axes and are superposed to the directions X,Y of the principal anisotropy reference axes. The defect is inclined with an angle Ψ with respect to direction 2. It is characterized by:

$$F_1 = e^b/e^a \qquad\qquad (A.1)$$

whose usual value is obtainable as a function of the initial defect :

$$F_1 = e^b/e^a = (e_0^b/e_0^a)(\exp(\varepsilon_3^b)/\exp(\varepsilon_3^a)) = F_0 \exp(\varepsilon_3^b - \varepsilon_3^a)$$

Differenciation of the preceding equation gives : $dF_1 = F_1 (d\varepsilon_3^b - d\varepsilon_3^a)$ $\qquad (A.2)$

where $d\varepsilon_3^a$ and $d\varepsilon_3^b$ are respectively the deformation increments in the thickness direction for the zones a and b of the model.

The rotation $d\psi$ of the band between time t and $t+dt$ is given by :

$$tg(\psi)=l_1/l_2$$

$$tg(\psi+d\psi)=tg(\psi)(1+d\varepsilon_1^a)/(1+d\varepsilon_2^a)$$

(A.3)

$d\varepsilon_1^a$ and $d\varepsilon_2^a$ are the principal strain increments of the homogeneous region in the sheet plane.

A-2. Equilibrium equations :

In the n,t,z reference axes defined in figure A.1, the components of the stress tensor are written as σ_{nn}, σ_{tt}, σ_{nt}. The equilibrium condition leads to the following equations :

$$\sigma_{nn}^a\, e_a = \sigma_{nn}^b\, e^b$$

(A.4)

$$\sigma_{nt}^a\, e^a = \sigma_{nt}^b\, e^b$$

(A.5)

where the superscripts a or b indicate that the variable is of the homogeneous zone a or of the defect b. Combining with equation A1, one finds:

$$\sigma_{nn}^a/\sigma_{nn}^b = e^b/e^a = F_1$$

Using a behavior law of the type :

$$\sigma_e = K(\bar{\varepsilon}+E_0)^N \dot{\bar{\varepsilon}}^M$$

one obtains:

$$\frac{(\sigma_{nn}^a/\sigma_e^a)}{(\sigma_{nn}^b/\sigma_e^b)} = F_1 \left(\frac{E_0+\varepsilon^b}{E_0+\varepsilon^a}\right)^N \left(\frac{d\varepsilon^b}{d\varepsilon^a}\right)^M$$

The behavior law used is intended to represent the material for all strain paths. This limiting hypothesis is generally not verified experimentally. Nonetheless,it has the advantage of simplifying calculations. In equation A.6, the main difficulty lies in the expression of σ_{nn}^a/σ_e^a and σ_{nn}^b/σ_e^b as a function of $d\bar{\varepsilon}^a$ and $d\bar{\varepsilon}^b$.

A-3. Calculation of σ_{nn}^a/σ_e^a and the strain increments in the zone a :

After writing σ_{nn}^a in the reference axes 1,2,3, it is possible to calculate σ_e^a from the anisotropic plastic flow criterion of HILL expressed in terms of plane stresses and identified through a tensile test along the x-direction :

$$\sigma_e^2 = \sigma_{xx}^2 + (F + H)\, \sigma_{yy}^2 - 2H\, \sigma_{xx}\, \sigma_{yy} + 2P\, \sigma_{xy}^2$$

we find : $\sigma_{nn}^a/\sigma_e^a = A_1/A_2$

with   : $A1=(\cos^2\psi+\alpha\sin^2\psi)$

$$A2=(1+(F+H)\alpha^2-2H\alpha)^{1/2}$$

The stress-strain relations give the strain increment values in zone a.

$$d\varepsilon_3^a = A4\, d\bar{\varepsilon}^a$$

$$d\varepsilon_2^a = A5\, d\bar{\varepsilon}^a$$

$$d\varepsilon_1^a = A6\, d\bar{\varepsilon}^a$$

with : $\alpha = \sigma_2/\sigma_1$ and $\rho = \varepsilon_2/\varepsilon_1$

(A.7)

$$A4=-(1-H+F\alpha)/A2$$

$$A5=((F+H)\alpha-H)/A2$$

$$A6=(1-H\alpha)/A2$$

A-4. Calculation of $\sigma_{nn}{}^b/\sigma_e{}^b$:

In order for the stress-strain relations to be uniquely used in the principal anisotropy axes, $\sigma_{nn}{}^b$ and $\sigma_e{}^b$ will always be expressed in this system :

$$\sigma_{nn}{}^b = \sigma_{xx}{}^b \cos^2\psi + \sigma_{yy}{}^b \sin^2\psi + 2\sigma_{xy}{}^b \cos\psi \sin\psi$$

$$\sigma_e{}^b = ((\sigma_{xx}{}^b)^2 + (F+H)(\sigma_{yy}{}^b)^2 - 2H\sigma_{xx}{}^b\sigma_{yy}{}^b + 2P(\sigma_{xy}{}^b)^2)^{1/2}$$

Since supplementary unknowns are introduced ($\sigma_{xx}{}^b$, $\sigma_{yy}{}^b$, $\sigma_{xy}{}^b$, one requires other equations ; the equilibrium equations A.4 and A.5 give :

$$\sigma_{nt}{}^b = (\sigma_{nt}{}^a/\sigma_{nn}{}^a)\sigma_{nn}{}^b$$

Transferring these terms in the principal anisotropy system, one gets

$$\sigma_{nt}{}^a/\sigma_{nt}{}^a = K0 = (\alpha-1)\cos\psi\sin\psi/A1$$

and considering

$$x = \sigma_{yy}{}^b/\sigma_{xx}{}^b$$
$$y = \sigma_{xy}{}^b/\sigma_{xx}{}^b$$

one obtains

$$(x-1)\cos\psi\sin\psi + y(\cos^2\psi - \sin^2\psi) = K0(\cos^2\psi + x\sin^2\psi + 2y\cos\psi\sin\psi)$$

A compatibility equation can reflect the identity between the strain along the direction t for the homogeneous zone to that for the defect.

$$d\varepsilon_{tt}{}^a = d\varepsilon_{tt}{}^b \tag{A.8}$$

Expressing the latter in the principal anisotropy system, one obtains

$$A3 d\varepsilon^a = d\varepsilon^b (\sigma_{xx}{}^b/\sigma_e{}^b)((\sin^2\psi - H\cos^2\psi) + x((F+H)\cos^2\psi - H\sin^2\psi) - 2Py\cos\psi\sin\psi)$$

with :

$$A3 = (1-H\alpha)\sin^2\psi/A2 + ((F+H)\alpha - H)\cos^2\psi/A2$$

Hence, four equations are available to calculate $\sigma_{xx}{}^b/\sigma_e{}^b$ as a function of $d\bar\varepsilon^a/d\bar\varepsilon^b$

1) Expression for $\sigma_e{}^b$:

$$\sigma_e{}^b = \sigma_{xx}{}^b (1 + (F+H)x^2 - 2Hx + 2Py^2)^{1/2} \tag{A.9}$$

2) Expression for $\sigma_{nn}{}^b$:

$$\sigma_{nn}{}^b = \sigma_{xx}{}^b (\cos^2\psi + x\sin^2\psi + 2y\cos\psi\sin\psi) \tag{A.10}$$

3) Equilibrium equation :

$$(x-1)\cos\psi\sin\psi + y(\cos^2\psi - \sin^2\psi) = K0(\cos^2\psi + x\sin^2\psi + 2y\cos\psi\sin\psi) \tag{A.11}$$

4) Compatibility equation :

$$A3(d\bar\varepsilon^a/d\bar\varepsilon^b) = (\sigma_{xx}{}^b/\sigma_e{}^b)((\sin^2\psi - H\cos^2\psi) + x((F+H)\cos^2\psi - H\sin^2\psi) - 2Py\cos\psi\sin\psi) \tag{A.12}$$

Equation A.10 gives :

$$y = K1x + K2$$

with : $K1 = -\cos\psi\sin\psi/(\cos^2\psi - \alpha\sin^2\psi)$

$$K2 = -\alpha K1$$

$d\bar{\varepsilon}^a/d\bar{\varepsilon}^b$ being considered as a parameter, equations A.9, A.11 and A.12 form a system of 3 equations with 3 unknowns x, y, σ_{xx}^b/σ_e^b. This system can theoretically be resolved ; the values of x and y would lead to an expression of σ_{xx}^b/σ_e^b as a function of $d\bar{\varepsilon}^a/d\bar{\varepsilon}^b$ using equations A.9 and A.10. In reality, the system is not resolved in this manner since x is the solution of a second degree equation which cannot be determined uniquely. Another method consists of writing two second degree equations with x as a variable :

$$p_1 x^2 + p_2 x + 1 = 0 \qquad (A.13)$$

$$q_1 x^2 + q_2 x + 1 = 0 \qquad (A.14)$$

Since equation A.11 is a linear equation in x and y, equation A.12 is obtained by a combination of expressions A.9 and A.10 ; the coefficients p_1 and p_2 are parametrized through σ_{nn}^b/σ_e^b. Equation A.14 comes from A.8 and A.11 and the coefficients q_1 and q_2 are parametrized through $d\bar{\varepsilon}^a/d\bar{\varepsilon}^b$ since this is the same mechanical problem, the value of x ($\sigma_{yy}^b/\sigma_{xx}^b$) is always unique. Equations A.13 and A.14 are equivalent and the following condition must be satisfied : $p_1 = q_1$

(the relation $p_2 = q_2$ must also be valide and this is numerically verified in the simulations). With this condition one can then express σ_{nn}^b/σ_e^b as a function of $d\bar{\varepsilon}^a/d\bar{\varepsilon}^b$. Practically, one obtains

$$p_1 = (A3^2 B6(d\bar{\varepsilon}^a/d\bar{\varepsilon}^b)^2 - B7^2)/(A3^2 B8(d\bar{\varepsilon}^a/d\bar{\varepsilon}^b)^2 - B9^2)$$

with :

$$B6 = F + H + 2PK1^2$$

$$B7 = (F+H)\cos^2\psi - H\sin^2\psi - 2PK1\cos\psi\sin\psi$$

$$B8 = 1 + 2\alpha PK1^2$$

and

$$B9 = \sin^2\psi - H\cos^2\psi + 2\alpha PK1\cos\psi\sin\psi$$

$$q_1 = (B6(\sigma_{nn}^b/\sigma_e^b)^2 - B4)/(B8(\sigma_{nn}^b/\sigma_e^b)^2 - B5)$$

with :

$$B4 = (\sin^2\psi + 2K1\cos\psi\sin\psi)^2$$

$$B5 = (\cos^2\psi - 2\alpha K1\cos\psi\sin\psi)^2$$

The equality of p_1 and q_1 gives the expression for $(\sigma_{nn}^b/\sigma_e^b)^2$:

$$(\sigma_{nn}^b/\sigma_e^b)^2 = (B1(d\bar{\varepsilon}^a/d\bar{\varepsilon}^b)^2 + B2)/B3$$

with :

$$B1 = A3^2(B4B8 - B5B6)$$

$$B2 = B5B7^2 - B4B9^2$$

$$B3 = B8B7^2 - B6B9^2$$

A-5. Calculation of $d\varepsilon_3^b$:

The value of $d\varepsilon_3^b/d\bar{\varepsilon}^b$ can be obtained from the stress-strain relations. These are expressed in the principal anisotropy axes using σ_{xx}^b, σ_{yy}^b, σ_{xy}^b. By a change of axes, $d\varepsilon_3^b/d\bar{\varepsilon}^b$ can be written as a function of σ_{nn}^b, σ_{tt}^b, σ_{nt}^b. The equilibrium equations can eliminate an unknown and give a relation between σ_{nt}^b and σ_{nn}^b. A relation between σ_{tt}^b and σ_{nn}^b can be obtained from the compatibility equation.

Finally, it is possible to express $d\varepsilon_n^b/d\bar{\varepsilon}^b$ as a function of σ_{nn}^b/σ_e^b and $d\bar{\varepsilon}^a/d\bar{\varepsilon}^b$.

$$d\varepsilon_3^b/d\bar{\varepsilon}^b = -(H6(\sigma_{nn}^b/\sigma_e^b) + H7(d\bar{\varepsilon}^a/d\bar{\varepsilon}^b)) \qquad (A.16)$$

with : $H7=((1-H)\sin^2\psi+F\cos^2\psi)A3/H5$

$H6=(1-H)(\cos^2\psi-2KO\cos\psi\sin\psi)+F(\sin^2\psi+2KO\cos\psi\sin\psi)-(G\sin^2\psi+F\cos^2\psi)H4/H5$

$H5=H1\sin^2\psi+H2\cos^2\psi-H3\cos\psi\sin\psi$

$H4=H1(\cos^2\psi-2KO\cos\psi\sin\psi)+H2(\sin^2\psi+2KO\cos\psi\sin\psi)+H3(\cos\psi\sin\psi+KO(\cos^2\psi-\sin^2\psi))$

$H3=-2P\cos\psi\sin\psi$

$H2=(F+H)\cos^2\psi-H\sin^2\psi$

$H1=\sin^2\psi-H\cos^2\psi$

A-6. Simulation procedure

The equations A.6, A.2, A.16, A.7 can be written as functions of different coefficients introduced in this analysis

$$A1/A2 = F_1 ((E_0+\bar\varepsilon^b)/(E_0+\bar\varepsilon^a))^N (d\bar\varepsilon^b/d\bar\varepsilon^a)^M (B1(d\bar\varepsilon^a/d\bar\varepsilon^b)^2+B2)/B3)^{1/2} \qquad (A.6)$$

$$dF=F(d\varepsilon_3^b-d\varepsilon_3^a) \qquad (A.2)$$

$$d\varepsilon_3^b = -(H6 (B1(d\bar\varepsilon^a/d\bar\varepsilon^b)^2+B2)/B3)^{1/2} + H7(d\bar\varepsilon^a/d\bar\varepsilon^b)) d\bar\varepsilon^b \qquad (A.16)$$

$$d\varepsilon_3^a=A4d\bar\varepsilon^a \qquad (A.7)$$

All the coefficients B1, B2, B3, A1, A2, A3, A4, H6, H7, can be determined at all instants. The usual values for the defect F_1 and the accumulated strains $\bar\varepsilon^a$ and $\bar\varepsilon^b$ are obtained by summing the corresponding increments.

The numerical resolution of the system is done step by step by imposing an incremental strain $d\bar\varepsilon^b$ in the defect. At each instant, all the coefficients of the system can be determined since they are only dependent on the model geometry (Ψ) and of the loading path (α), the latter being also imposed. The numerical resolution of equation A.6 by the Runge-Kutta method of the order 4 gives the value of $d\bar\varepsilon^a/d\bar\varepsilon^b$. The simulation is stopped when $d\bar\varepsilon^a/d\bar\varepsilon^b$ reaches a critical value which corresponds to negligeable deformations in the homogeneous zone ($d\bar\varepsilon^a/d\bar\varepsilon^b$ less than 0.1). The forming limit is then attained.

APPENDIX B

STATISTIC DEFECT CALCULATION

B-1. Defect for one class of cavities :

A material is supposed to contain one class of equiaxed cavities modelized by a parallelopiped of dimensions D_1, D_2, D_3 (Fig. B.1) (47).

Figure B.1 is a section of the sheet thickness. Each cavity can occupy any position in one of the ν slices of the material.

$\nu = t/D_3$

The length of each slice is imposed by the cavity volume fraction of the material.

$Cv = D_1/L$

If one supposes that the cavity occupies discrete positions and separated by the distance dh, then the probability that the slice of width dh will intercept one cavity in a given slice is:

$p = (D_1/dh)(L/dh) = C_v$

The local defect D_p, corresponding to the alignment of x cavities along a line through point P and normal to the sheet plane, is expressed as an elementary surface of width dh and defined by:

$D_p=1-F_p=xD_3/t=x/\nu$

The values of D_p = 0 or F_p = 1 correspond to the case where there are no defects. The probability that a defect D_p exists is given by the binomial law (58) :

$$p(x \text{ cavities})=\binom{\nu}{x}C_v^x(1-C_v)^{\nu-x} \qquad (B.1)$$

Knowing this probability, it is then possible to represent a plane of the sheet (Fig. B.2). The unshaded squares correspond to points without defects. The shaded squares represent points for which a line normal to the sheet plane and passing through them intercepts one or several cavities. The defect which leads to striction will start at sections containing the maximum number of local defects. In order for the mechanical plastic instability model to apply, it will be assumed that the defect is quasi-linear (Fig. B.2). Also, in order for the band to be continuous, this must pass through zones without defects.

Various representations identical to that of figure B.2 have been simulated by varying the probability p of the existence of a point defect at the point P of the sheet. The non-zero probability p^h of finding a local defect in the quasi-linear band was calculated as a function of p:

$$\begin{cases} p^h = -4p^2 + 4p & \text{if} \quad 0 < p < 0.5 \\ p^h = 1 & \text{if} \quad 0.5 < p < 1 \end{cases}$$

The linear defect F_1 can be defined as the sum of the average of the local defects affected by the probability p^h and of 1 (points without defects) affected by the probability $1 - p^h$:

$$F1 = \left(\frac{\sum_1^{\nu} p(x=k)(1-k/\nu)}{\sum_1^{\nu} p(x=k)} \right) p^h + 1 \cdot (1-p^h) \tag{B.2}$$

One can write :

$$\sum_1^{\nu} p(x=k) = 1-p(x=0) = 1-(1-C_\nu)^\nu \tag{B.3}$$

the term :

$$\sum_1^{\nu} p(x=k)(1-k/\nu) = A$$

can be divided as a sum of two terms :

$$A = A_1 - A_2 = \sum_1^{\nu} p(x=k) - 1/\nu \left(\sum_1^{\nu} k\, p(x=k) \right)$$

The term A1 is known (equation B.3). A2 can be expressed as :

$$A_2 = 1/\nu \left(\sum_1^{\nu} k\, p(x=k) \right) = 1/\nu (1-C_\nu)^{\nu-1} C_\nu \left(\sum_1^{\nu} \binom{\nu}{k} k \left(\frac{C_\nu}{1-C_\nu} \right)^{k-1} \right)$$

By adopting the change of variables :

$$u = C_\nu/(1-C_\nu) \qquad u + 1 = 1(1-C_\nu)$$

one obtains :

$$A_2 = g(C_\nu)\, h(u)$$

where g and h are two functions which can be written in the form :

$$g(C_\nu) = 1/\nu (1-C_\nu)^{\nu-1} C_\nu$$

$$h(u) = \sum_1^{\nu} \binom{\nu}{k} k\, u^{k-1}$$

Integration leads to :

$$h(u) = \sum_1^{\nu} \binom{\nu}{k} u^k$$

which represents the development of $(1+u) - 1$, from which :

$$h(u) = (1+u)^\nu - 1$$

Differentiation leads to:

$$A_2 = C_\nu$$

$$A = A_1 - A_2 = 1 - (1-C_\nu)^\nu - C_\nu$$

and finally the value for the defect is :

$$F = \left(1 - \frac{C_\nu}{1-(1-C_\nu)^\nu} \right) p^h + 1 - p^h \tag{B.4}$$

B-2. Defect for two classes of cavities :

The analysis consists of two simultaneous calculations, one for each class of cavities. The material contains cavities of type A with concentration C_{vA} and cavities of type B with concentration C_{vB} such that $C_v = C_{vA} + C_{vB}$. For the analysis, it is necessary to separate the two types of cavities. In this case, one can consider two sheets A and B, having thicknesses t_A and t_B respectively, divided respectively into ν_a and ν_b slices respectively.

It is then possible to perform two identical calculations using the procedure adopted for one class of cavities. Hence,

$$F=\left[1-\frac{C_v}{1-(1-C_v)^{\nu_a+\nu_b}}\right]p^h+(1-p^h) \tag{B.5}$$
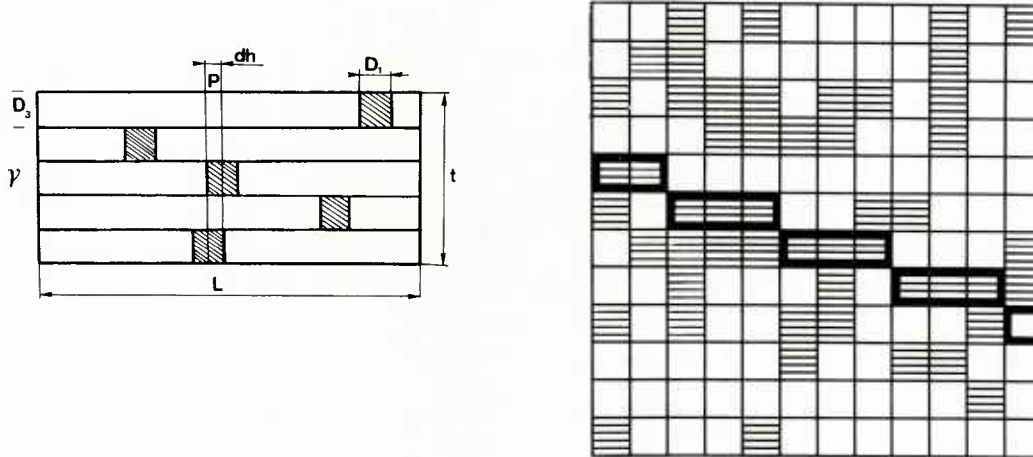
Fig.B.1 - Modelization of the sheet thickness

Fig.B.2 - Schematic description of the sheet plane : shaded elementary surfaces represent local points with one or more cavities under these points.

APPENDIX C

STATISTICAL DEFECT EVOLUTION DUE TO CAVITY GROWTH DURING DEFORMATION

C-1. Cavity growth :

For an isotropic material, damage growth is taken into account through the growth model of RICE and TRACEY (59). The evolution of an initially spherical cavity obeys the following law :

$$\dot{R}_i/R_i = C\dot{\varepsilon}_i + S\dot{\bar{\varepsilon}} \tag{C.1}$$

$\dot{R}_i$ represents the growth rate of the radius in the direction i
$C\dot{\varepsilon}_i$ is a term representing the cavity form evolution without volume change
$S\dot{\bar{\varepsilon}}$ is a term representing the volume change without cavity form variation
C is a factor which varies from 1.5 to 2 for the case of weak stress triaxiality which exists in thin sheets. The authors recommend the value C = 5/3.

In the case of a non-hardening material, D can have the form :

$$D = 0.558 \; sh((3/4)^{1/2}\sigma_m/\tau_o) + 0.008 \; \gamma \; ch((3/4)^{1/2}\sigma_m/\tau_o)$$

where σ_m is the mean hydrostatic pressure applied to the material,
τ_o is the shear flow stress. For a material obeying VON-MISES criterion, this stress is given by :

$$\tau_o = \sigma_e/3^{1/2}$$

$$\gamma = -3\dot{\varepsilon}_{II}/(\dot{\varepsilon}_I - \dot{\varepsilon}_{III})$$

where $\dot{\varepsilon}_I > \dot{\varepsilon}_{II} > \dot{\varepsilon}_{III}$

JALINIER (42) linearized these equations to facilitate their use.

In this study, we consider any strain path characterized by :

$$\rho = d\varepsilon_2/d\varepsilon_1$$

If one assumes that the strain path always lies in the region between uniaxial tension and equibiaxial expansion ($-0.5 < \rho < 1$), then γ can have the form :

$$\gamma = -3\rho/(2 + \rho)$$

For a plane stress state, the ratio α between the minimal and maximal principal stresses is expressed as a function of ρ.

$$\alpha = \sigma_2/\sigma_1 = (2\rho+1)/(\rho+2)$$

Under these conditions, the ratio σ_m/τ_o becomes :

$$\sigma_m/\tau_o = (\rho+1)/(1+\rho+\rho^2)^{1/2}$$

The accumulated strain for an isotropic material is written :

$$d\bar{\varepsilon} = (2/3 \ d\varepsilon_{ij} d\varepsilon_{ij})^{1/2}$$

By introducing the volume conservation during plastic deformation, one obtains:

$$d\bar{\varepsilon} = -d\varepsilon_3 (4/3)^{1/2} (1+\rho+\rho^2)^{1/2}/(1+\rho)$$

It is therefore possible to express the factor S of the cavity growth law in the form:

$$S = 0.558 \ \text{sh}(d\varepsilon_3/d\bar{\varepsilon}) - (0.024\rho/(2+\rho)) \ \text{ch}(d\varepsilon_3/d\bar{\varepsilon})$$

In figure C.1, the values of S can be written as a function of $d\varepsilon_3/d\bar{\varepsilon}$ for values of ρ between -0.5 and 1. A good linear approximation can be obtained, thus :

$$S = -K d\varepsilon_3/d\bar{\varepsilon} \qquad \text{with K = 0.64}$$

Equation C.1 which expresses cavity growth in the direction i, can take another form:

$$dR_i/R_i = C d\varepsilon_i - K d\varepsilon_3 \qquad\qquad (C.2)$$

This equation can be integrated easily. This expression is simple and hence easily used. We assume that it applies to hardening materials. This hypothesis seems to be valid for the case of thin sheets where stress triaxiality is weak (31).

C-2. Evolution of the statistical defect :

The statistical defect depends on two damage parameters: C_v and ν. One must therefore know the evolution of these parameters during plastic deformation. The ratio of the volume fractions of initially spherical cavities, after and before deformation is :

$$C_v = R_1 R_2 R_3/R_0^2$$

Differentiation gives :

$$dC_v/C_v = dR_1/R_1 + dR_2/R_2 + dR_3/R_3$$

Using the equation C.2 for cavity growth in the direction i, one gets :

$$dC_v/C_v = -3K d\varepsilon_3$$

The evolution of the cavity volume fraction is obtained by integration.

$$C_v = C_{v0} \exp(-3K\varepsilon_3)$$

This analysis predicts that the cavity volume fraction is uniquely dependent on ε_3 which is in good agreement with experimental measurements of relative density changes (60).

Furthermore, in the plane of the principal strains ε_1, ε_2, the cavity iso-volume-fraction curves are thickness iso-strain straight lines parallel to the lines defined by:

$$\varepsilon_1 + \varepsilon_2 = cte = -\varepsilon_3$$

One notes that another theoretical study (40) using plastic laws for porous materials, the iso-volume-fraction curves are also uniquely dependent on ε_3.

The parameter ν is equal to :

$$\nu = t/2R_3 = \frac{t_0 \exp(\varepsilon_3)}{2R_0 \exp(C\varepsilon_3 - K\varepsilon_3)}$$

with the following numerical values : $C = 5/3$ and $K = 0.64$; one can consider ν to be quasi-independent of ε_3 :

$$\nu = \nu_0 = t_0/2R_0$$

Figure C.2 shows the defect evolution as a function of plastic deformation with the cavity volume fraction taken into account. Several cases, with either the cavity size (R_0) or the volume fraction (C_{vo}) as parameters, are represented. It seems that for a given volume fraction, the initial defect is essentially constant but its growth is faster as its size is greater. On the other hand, for a given cavity size, the initial defect becomes larger as the initial cavity concentration increases.
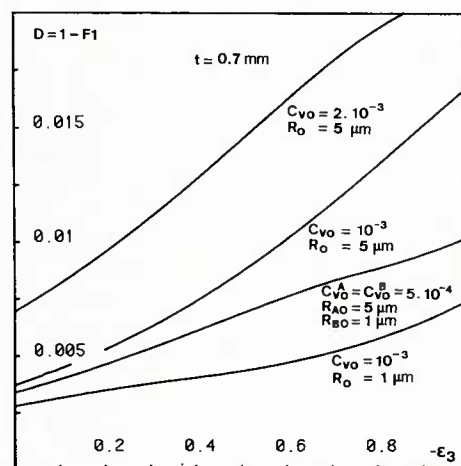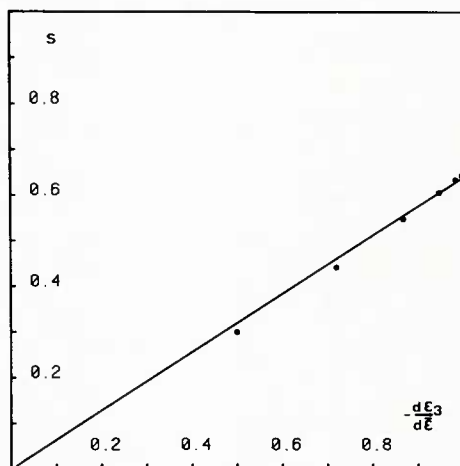
Fig.C.1 – Values for the spherical factor in the cavity growth law as a function of the ratio $d\varepsilon_3/d\bar{\varepsilon}$. A good linear approximation can be obtained.

Fig.C.2 – Evolution of the statistical defect due to cavity growth during deformation.

REFERENCES

1) S.P. KEELER – Sheet Metal Ind., **42** (1965), 683.
2) G.M. GODDWIN – La Metallurgica Italiana **8** (1968), 767.
3) H.W. SWIFT – J.Mech.Phys.Solids, **1** (1952), 1.
4) R. HILL – J.Mech.Phys.Solids, **1** (1952), 19.
5) R. HILL – The Mathematical Theory of Plasticity, Oxford University Press, London, (1950), 317.
6) Z. MARCINIAK and K. KUCZYNSKI – Int'l.J.Mech. Sci., **9** (1967), 609.
7) Z. MARCINIAK and K. KUCZYNSKI – Int'l.J.Mech. Sci., **15** (1973),789.
8) Z. MARCINIAK – Mechanics of Sheet Metal Forming, Plenum Press, New York, London, (1978), 215.
9) J.W. HUTCHINSON and K.W. NEALE – Mechanics of Sheet Metal Forming, Plenum Press, New York London, (1978), 127.
10) J.W. HUTCHINSON and K.W. NEALE – Proceedings of the IUTAM Symposium on Finite Elasticity, ed. by Lehigh University, Penn., (1980), 238.
11) S. STOREN and J.R. RICE – J.Mech.Phys.Solids, **23** (1975).
12) R. HILL and J.W. HUTCHINSON – J.Mech.Phys.Solids, **23** (1975), 239.
13) S.S. HECKER – Proceedings of 7th IDDRG Congress, International Deep Drawing Research Group, Hoogovens IJmuiden BV, Holland, (1972), 5.1.
14) M.M. FOURDAIN, H. JOSSELIN and R.EL HAIK – Proceedings of 7th IDDRG Congress, International Deep Drawing Research Group, Hoogovens IJmuiden BV, Holland, (1972), 15.1.
15) C. LEFEVRE, R. EL HAIK, E. LEVREZ and M.BOURGEON – Proceedings of the 12th IDDRG Congress, International Deep Drawing Research Group (WG2),ed.by the Associazione Italiana Metallurgia, Italy, (1982),129.
16) I. AOKI and T. HORITA – Mem.Sci.Rev.Met., **4** (1980), 553.
17) J.GRONOSTAJSKI, A. DOLNY and T. SOBIS – Proceedings of the 12th IDDRG Congress, International Deep Drawing Research Group (WG1),ed.by the Associazione Italiana Metallurgia, Italy (1982), 39.
18) T.KOBAYASHI, H.ISHIGAKI and T. ABE – Proceedings of the 7th IDDRG Congress, International Deep Drawing Research Group, Hoogovens IJmuiden BV, Holland, (1972) 8.1.
19) A. RANTA-ESKOLA – Mem.Sci.Rev.Met., **4** (1980), 543.
20) H. SANG and D.J. LLOYD – Met.Trans. A, **10A** (1979), 1773.

21) D.J. LLOYD and H. SANG – Met.Trans. A, **10A** (1979), 1767.
22) W.B. HUTCHINSON and R. ARTHEY – Script.Met., **10** (1976), 673.
23) J.V. LAUKONIS and A.K. GHOSH – Met.Trans. A, **9A** (1978), 1849.
24) R. ARRIEUX, C. BEDRIN and M. BOIVIN – Proceedings of the 12th IDDRG Congress, International Deep Drawing Research Group (WG1), ed.by the Associazione Italiana Metallurgia, Italy (1982), 61.
25) W. MUSCHENBORN and H. SONNE – Arch. Eisenhüttenw., **46** (1975), 597.
26) M.J. HILLIER – J.Appl. Mech., **33** (1966), 282.
27) F. NEGRONI, S. KOBAYASHI and E.G. THOMSEN – J.Eng.for Industry, **90** (1968) 387.
28) A.S. KORHONEN – J.Eng. Mat.and Tech.,**100** (1978), 303.
29) S.H. LEE and S.KOBAYASHI – Proceedings of 3rd North American Metal Working Research Conference, Carnegie Press, Pittsburgh, (1975), 277.
30) S.N. RASMUSSEN – Proceedings of 12th IDDRG Congress, International Deep Drawing Research Group (WG1), ed.by the Associazione Italinana Metallurgia, Italy, (1982), 83.
31) A. BARATA DA ROCHA and J.M. JALINIER – Trans. of the Iron and Steel Institute of Japan, **24**, (1984), 132.
32) F. BARLAT – Thesis de Docteur Ingénieur (1984)
33) A. BARATA DA ROCHA, F. BARLAT and J.M. JALINIER – 13th IDDRG Congress Melbourne (1984).
34) A. BARATA DA ROCHA, F. BARLAT and J.M. JALINIER – Accepted for publication in Mat.Sc.and Eng.
35) F. BARLAT, A. BARATA DA ROCHA and J.M. JALINIER – Accepted for publication in J.Mat.Science.
36) T. KIKUMA and K. NAKAZIMA – Trans. ISIJ, **11** (1971), 827.
37) A. MELANDER – Proceedings of the 12th IDDRG Congress, International Deep Drawing Research Group, (WG1), Italy, (1982), 129.
38) J.H. SCHMITT and J.M. JALINIER – Acta Met., **30** (1982), 1789.
39) K. YOSHIDA and K. MIYAUCHI – Mechanics of Sheet Metal Forming, Plenum Press, New York London(1978), 19.
40) C.C. CHU – Int.J.Sol.Struct. **16**, (1980), 913
41) A.L. GURSON – J.Eng.Mat.Tech., **99**, (1977), 2
42) J.M. JALINIER – Thesis of Docteur ès Sciences, University of Metz, (1981).
43) A. NEEDLEMAN, N. TRIANTAFYLLIDIS – J.Eng.Mat.Tech., **100**, (1978), 164
44) C.C. CHU, A. NEEDLEMAN – J.Eng.Mat.Techn., **102**, (1980), 249.
45) A. MELANDER – Mat.Sci.Eng., **58**, (1983), 63.
46) A. MELANDER – A. THUVANDER – Scand.J.Met., **12**, (1983), 217.
47) J.M. JALINIER, J.H. SCHMITT – Acta Met., **30**, (1982), 1799.
48) M.J. PAINTER, R.PEARCE – IDDRG, Dvsseldorf RFA, (1975), document WGIII/30H/75.
49) E. BOCCALARI, R. DAGLIO, W. IRMICI, G. MONTANO – Proc. 12th IDDRG Congress S.Margherita Ligure, Italie, may 1982, 21.
50) H. VAN MINH, R.SOWERBY, J.L. DUNCAN – Int.J.Mech.Sci., **17**, (1975), 339.
51) H. VAN MINH, R.SOWERBY, J.L. DUNCAN – Int.J.Mech.Sci., **16**, (1974), 31.
52) J.H. SCHMITT – Thesis de Docteur Ingénieur, University of Metz, (1981).
53) Z. MARCINIAK, K. KUCZINSKI, T. POKORA – Int.J.Mech.Sci., **15** (1973), 789.
54) J.L. BASSANI, J.W. HUTCHINSON, K.W. NEALE – Proc. IUTAM Symp. "Metal Forming Plasticity" Tutzin Germany, (1978), Springer-Verlag, Berlin 1.
55) Z. MARCINIAK, H. IKE – IDDRG, (WGII/6), Helsinki (1983).
56) D.V. WILSON, W.T. ROBERTS, P.M.B. RODRIGUES – Met.Trans. A, **12** (1981) 1595
57) D.V. WILSON, W.T. ROBERTS, P.M.B. RODRIGUES – Met.Trans. A, **12** (1981) 1603
58) M. MOREAU, A. MATHIEU – "STATISTIQUE APPLIQUEE A L'EXPERIMENTATION" Eyrolles Paris 1979.
59) J.R. RICE and D.M. TRACEY – J.Mech.Phys.Solids, **17**, (1969), 201.
60) A. PARMAR, P.B. MELLOR – Int.J.Mech.Sci., **22**, (1980), 133.
61) T. KIKUMA, K. NAKAZIMA – Transactions of the Iron and Steel Institute of Japan, **11** (1971), 827.

THE ROLE OF MICROSTRUCTURE IN THE MODELLING OF PLASTIC FLOW IN P/M SUPERALLOYS AT FORGING TEMPERATURES AND STRAIN RATE

by

J-P. IMMARIGEON
Structures and Materials Laboratory
National Aeronautical Establishment
NRCC, Ottawa, Ontario, Canada, K1A 0R6

SUMMARY

Interest has grown lately in the application of computer-aided plasticity analysis to model the deformation of alloys during forging with a view to optimizing the microstructure in forged components. In P/M superalloy disc forgings, the final grain size and therefore the mechanical properties are either directly or indirectly affected by several factors which make up the forging deformation history, such as preform and die shapes, preform microstructure, forging temperature and strain rate. By controlling these factors different regions of a disc can be made to experience different deformation histories. In this way, different grain sizes can be produced in the rim and the bore regions which may lead to improved disc performance.

Relying on finite element modelling techniques and a methodology for predicting local changes in grain size as a function of local deformation history, it should be possible to predict the final grain sizes in the rim and the bore regions of a disc via process modelling and therefore determine the processing conditions under which an optimum microstructure is produced. To this end, extensive work has been done at NAE to study the effects of thermomechanical history on the evolution of microstructure in P/M superalloys under isothermal forging conditions and to formulate physically realistic constitutive relations for plastic flow that are capable of quantifying the effects of the microstructural evolution, thereby allowing the prediction of final microstructure in forgings.

Using constant true strain rate uniaxial compression tests, microstructure-flow property data have been generated at isothermal forging temperatures and strain rates for a number of compacts, including P/M IN100, P/M MAR M200 and P/M 713LC. These data will be analyzed and discussed in the context of deformation modelling for microstructural control. It will be shown that the rate of change of grain size is an important parameter which governs changes in flow strength and must therefore be considered in the formulation of constitutive relations for compacts both in a coarse grained and in a fine grained superplastic condition. A deformation model for grain size and rate sensitive P/M superalloys will be introduced and a methodology that can be applied to predict grain size distributions in forgings will be presented.

INTRODUCTION

There has been growing interest in the application of finite element techniques to model bulk forming processes for predicting forming stresses and flow patterns in formed components[1]. The benefits offered by process modelling include a substantial reduction in conventional process development costs, generally incurred by experimenting with expensive die material, equipment and preforms. Several workers[2-7] have attempted to model isothermal forging, a process which is becoming increasingly important in the aerospace industry for forming high strength nickel and titanium alloys for use in gas turbine engines[8]. One potential application involves the selection of forging conditions to optimize metal flow and microstructure in compressor and turbine disc forgings for improving disc performance beyond current limits[9,10].

During service turbine discs, are exposed to severe radial stress and temperature gradients. The stresses are highest near the bore while the temperature is highest at the rim. Consequently, property requirements differ from bore to rim. For optimum performance, the rim and bore microstructures must be tailored to local design requirements. This means coarse grains in the rim for creep strength and fine grains in the bore for tensile strength and fatigue resistance, Figure 1. A disc with these features is commonly known as a dual property disc.

Strong interest has recently emerged in technology developments for the production of such components[9-11]. For superalloy discs, several fabrication techniques have been explored[10] including the use of selective thermomechanical treatments, an approach which relies on control of the deformation history introduced locally in the disc during its forging[12,13]. It will be recognized that different parts of a complex forging will normally undergo varying amounts and rates of deformation during forging. Since the grain size in wrought superalloys is strongly influenced by deformation conditions one can therefore expect some variation in grain size throughout a disc forging. On that basis it was suggested[14,15] that it might be possible to optimize the forging preform and die shapes, the preform microstructure and the forging conditions such that adequate amounts and rates of deformation are introduced locally in the rim and the bore regions of the disc to produce the dual property microstructure. This approach has since been demonstrated by Carlson[12] who showed that with proper die design and a hot isostatically pressed preform of the type shown in Figure 2, it was possible to selectively hot work the bore region of the preform and improve its tensile properties while leaving the rim area unreduced thereby maintaining as HIP creep properties in that region[12]. In this work, fine tuning of the die geometry was found to be crucial in avoiding cracking. No details were given, however, concerning the microstructural changes responsible for the improvements in tensile properties of the bore or concerning the extent by which microstructure could be controlled by forging. With conventional process developments, these are issues that would be addressed normally by experimenting with processing conditions. An alternative approach might be to rely on computers for process simulation. This would require a suitable computational procedure and a reliable constitutive relation for describing flow and microstructural changes during forging.

Several computational procedures have been developed to predict forming stresses and flow patterns in metalworking operations. Simulation can provide an estimate of local strains, in a given forging and these can be correlated in turn with properties of the forging based on property versus deformation data. The more complex and more powerful of these procedures, that rely on the finite element method[4-7], can provide a very accurate description of material flow within a forging if a reliable constitutive relation for flow and suitable material data are available. This is one of the major difficulties and limitations, in any of these analyses. In general, material flow data is not available for alloys of interest and much that is published is often incomplete for modelling purposes. The data are often given in terms of flow stress versus strain rate at various temperatures, usually in the form of a power law equation[3-5]. This may be quite inadequate since the flow stresses of complex industrial alloys may show a considerable sensitivity to microstructure and the microstructure may change substantially during forging. In superalloys, for instance, this can reduce resistance to flow markedly. For successful modelling, this occurence (or the occurence of flow hardening where applicable) should be taken into consideration. While some of the constitutive relations used in recent isothermal forging analyses do allow for the occurance of flow softening[7,16] none directly

PROPERTY REQUIREMENTS IN TURBINE DISCS

CREEP	YIELD STRENGTH
STRENGTH	LCF – HCF

COARSE
GRAINS

FINE
GRAINS

MICROSTRUCTURAL REQUIREMENTS

Forging
preform

Forging
die
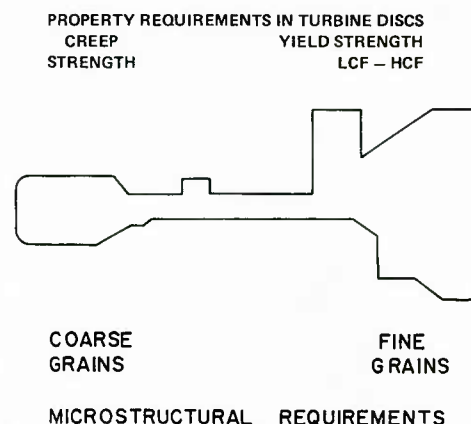
FIG 1   Half cross section of typical turbine disc showing microstructural requirements in the rim and bore regions for best meeting disc design requirements.
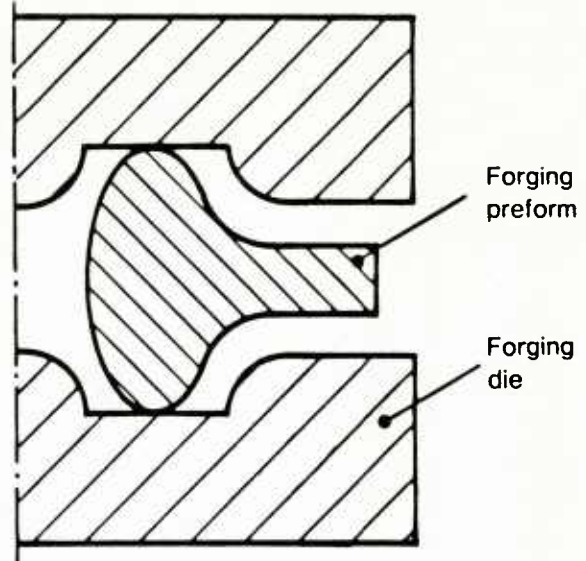
FIG 2   Schematic of optimized tooling and preform shape for producing dual property rotor disc forgings, after Carlson[12].

FINE GRAINED
+
COLD WORKED

A

FINE
GRAINED

B

NECKLACE

C

COARSE
GRAINED

D

YIELD STRENGTH

A
B
C
D

500   1000
TEMPERATURE

Log N_f in LCF

A
B
C
D

500   1000
TEMPERATURE
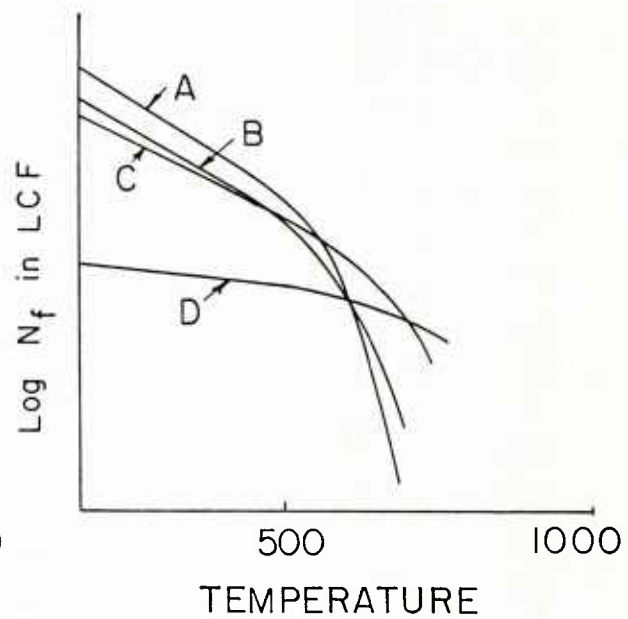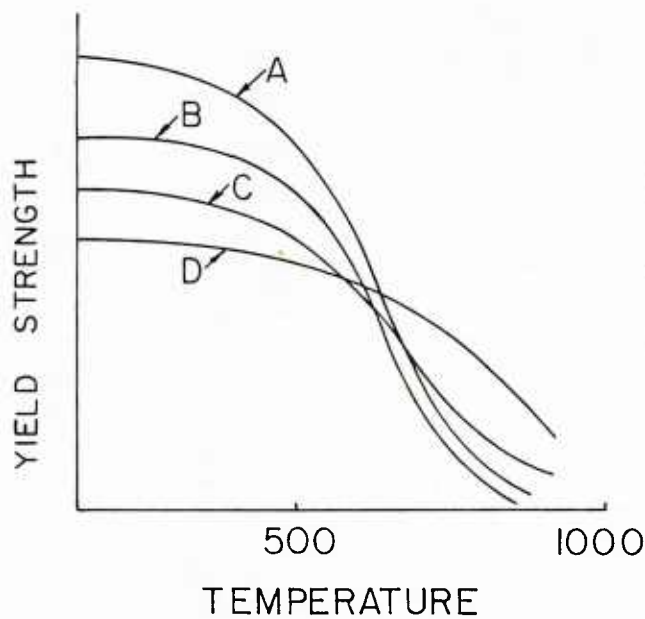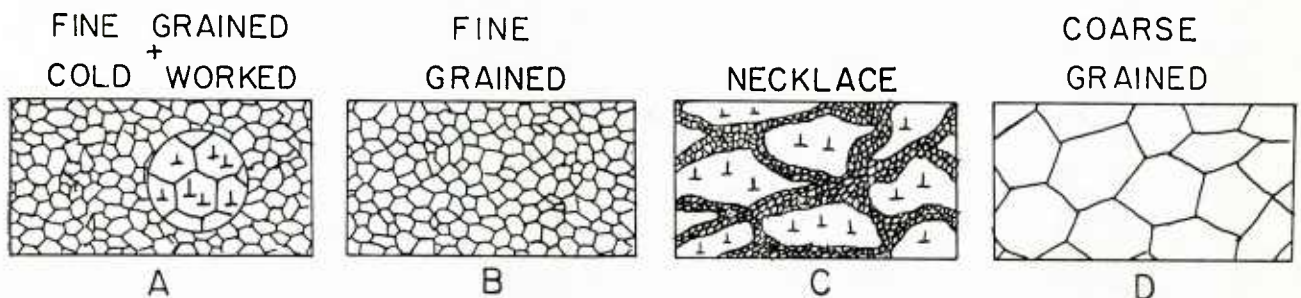
FIG 3   Effects of microstructure on mechanical properties of superalloys, after Gessinger and Singer[26].

consider the microstructural evolution as a dynamic variable of the forging process. Furthermore, most remain of a highly empirical nature[17]. In general, flow strength is related to the forging temperature, the strain rate and the strain which is in keeping with a practice common in the mechanical deformation literature[18]. This may not be suitable however at hot working temperatures when changes in microstructure are strain rate rather than strain dependent at constant temperature as appears to be the case for metals and alloys in general[19].

An analyses that could accurately predict as forged grain sizes directly would be most useful in the context of dual property disc production. This would require that the constitutive relation allows changes in microstructure to be predicted as a function of deformation history. Another requirement would be that the well established finite element techniques for bulk forming analyses are modified accordingly. How this might be done has already been suggested[15] and methodologies for modelling flow at constant temperature, both in fine grained and coarse grained P/M superalloys, have been developed that allow designers to incorporate the effects of structure in the analysis, and to predict grain sizes in isothermally forged parts[15,20]. It is the purpose of this paper to review this work and expand on the subject.

Extensive work has been done at NAE to study the behaviour of superalloy powder compacts under isothermal forging conditions[13,15,21-24]. Several powder processed versions of normally cast alloys including P/M IN100, P/M Mar M200 and P/M 713LC have been studied. Using P/M 713LC as a model material, a good phenomenological understanding of the hot working behaviour of this class of alloys has now been developed[15,20,25]. The extent by which grain size can be controlled during forging has also been demonstrated and the potential offered for control of the microstructure in superalloy disc forgings has been discussed[13]. In this paper these results are reviewed and the role of microstructure in the modelling of deformation in P/M superalloys is also discussed. A physically realistic constitutive relation, that can be used with the finite element method to predict the evolution of flow strength and microstructure in forgings of these materials is then introduced. To put the proposed methodology into perspective, the metallurgical characteristics of P/M superalloys are first briefly discussed and their processing into discs is also outlined.

2.0 METALLURGY OF P/M SUPERALLOYS

Powder processed superalloys have been developed for use in gas turbine engines for highly stressed hot section components such as compressor or turbine discs. In general, the chemistry of powder processed alloys is derived from that of high strength normally cast alloys and therefore their overall metallurgy is similar to that of cast alloys. However, they have some unique characteristics which can be related either directly or indirectly to the higher cooling rates experienced by powders during atomization as compared to castings. As a result of the high cooling rates, microsegregation is reduced and grain size is finer and this confers to compacts superior mechanical properties for disc applications.

Whether in the cast, wrought or powder processed forms, nickel-base superalloys are metallurgically complex materials. They derive their high strength primarily from the precipitation of an intermetallic ordered phase, the γ' phase which forms in the grain interiors, and from the precipitation of this phase and carbides along the grain boundaries. While γ' inhibits slip in the grain interiors, the carbides inhibit grain boundary sliding at high service temperatures. Additional strengthening of the γ austenitic matrix phase is derived from substitutional solutes. The mechanical properties of these alloys are strongly dependent on microstructure and this is in turn strongly affected by processing conditions. Heat treatments are carefully adjusted to achieve an adequate balance between intragranular strength and grain boundary strength. This is controlled by the volume fractions, the sizes, the shapes, and the morphologies of the γ' and carbides. Grain size is another important microstructural parameter which affects creep rupture properties and fatigue resistance, Figure 3[26]. Increasing the grain size generally improves creep resistance (high temperature strength, Figure 3). This is because the grain boundary surface area available for sliding is reduced and diffusional flow is suppressed. By contrast, decreasing the grain size generally improves tensile and low cycle fatigue resistance for optimum service performance at intermediate temperatures (low to intermediate temperatures, Figure 3).

The powder processed alloys are highly susceptible to contamination during processing. This is because of the fine powder size and the high surface to volume ratio of the material before compaction. Brittle foreign inclusions can be easily introduced during fabrication. Also powder surface boundaries can act as sites for the segregation of impurities and trace elements and for the nucleation of carbides. This may result in embrittlement of these boundaries and loss of toughness, ductility and fatigue resistance[21,27,28]. Reasons for the preferential precipitation of carbides along prior particle boundaries (PPB's) are not entirely clear. There is strong evidence that it occurs primarily as a result of solute segregation and particle surface contamination by oxygen[27-29]. The severity of precipitation appears very sensitive to a number of variables such as powder production technique, mesh size, powder handling, canning procedures and consolidation conditions. It can be minimized in a number of ways which are discussed at length in a recent critical review of the problem[30].

Typical microstructures for a powder processed alloy (hot isostatically pressed 713LC) are shown in Figure 4 for compacts in either the as-consolidated condition or after heat treatment, as indicated. In the heat-treated condition, Figure 4a, the intermetallic phase is present as small cuboidal particles ($< 0.5\,\mu$m) and as fine spheroids which can only be resolved within the matrix through electron optics techniques. The grain boundaries contain discrete carbide particles and these are enveloped in a thin continuous film of γ'. By contrast, in the as-hipped condition the γ' is in a coarse overaged condition mostly in the form of large angular particles (~ 2 to $5\,\mu$m) located along the grain boundaries and also within the grains. A finer spheroidal γ' ($< 0.5\,\mu$m) is also present within some of the larger grains. A problem with fine grained compacts is that often grain boundaries cannot be easily revealed by etching. However, a suitable grain boundary etch can normally be found (c.f. Figure 13a for the same alloy), and the γ grain size was found to vary from 8 to 12 μm. This fine grain size confers some degree of superplasticity to an otherwise unworkable alloy.

The fine grained superplastic condition in superalloy compacts is obtained by either extruding or hot isostatic pressing prealloyed powders at temperatures below the γ' solvus temperature of the alloy[8]. The presence of the γ' during compaction stabilizes the fine grains produced during extrusion or prevents coarsening of the fine as-atomized grains in compacts prepared by hot isostatic pressing. The condition of low strength and high ductility obtained in this way allows stronger normally cast alloys to be forged and this allows the production of discs capable of higher service temperatures and or higher rotational speeds than is normally possible with conventional wrought alloys.

2.1 POWDER PROCESSING OF TURBINE DISCS

There are several ways to produce a disc from powders[8]. With the first major process developed at Pratt and Whitney (USA), known as Gatorizing[31], the powder is first consolidated by hot extrusion and the superplastic compact is processed into disc shapes by slow strain rate isothermal forging. In this type of forging, the tooling is heated and kept at the forging temperature. Because of the absence of die chilling of the workpiece, slower forging rates can be used to take full advantage of the higher superplasticity exhibited by fine grained superplastic compacts
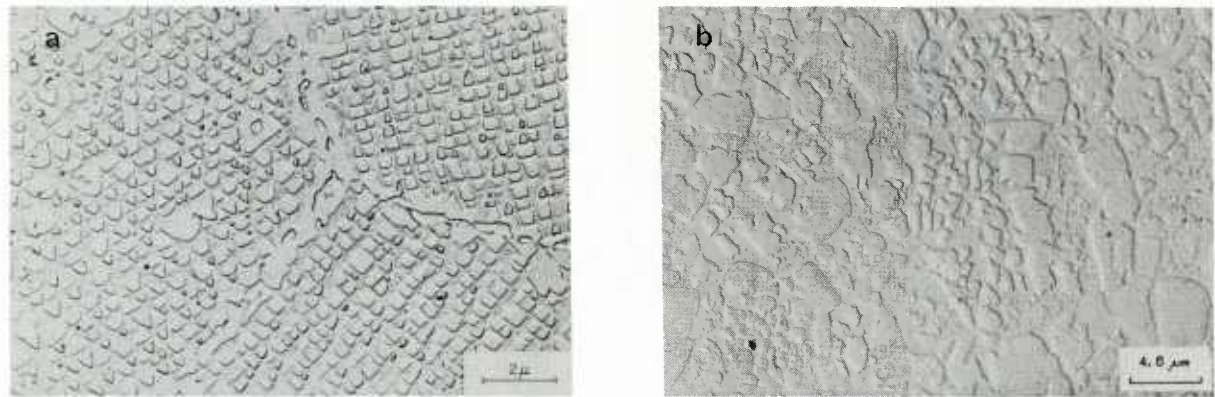
FIG 4   Microstructures in HIP processed (980°C/4hrs + 1175°C/2hrs/100MPa) 713LC compacts:

    a)   after solutioning, aging and stabilizing (1260°C/4hrs WQ; 980°C/30hr AC; 760°C/24hr AC);

   b)   in the as-hipped condition.
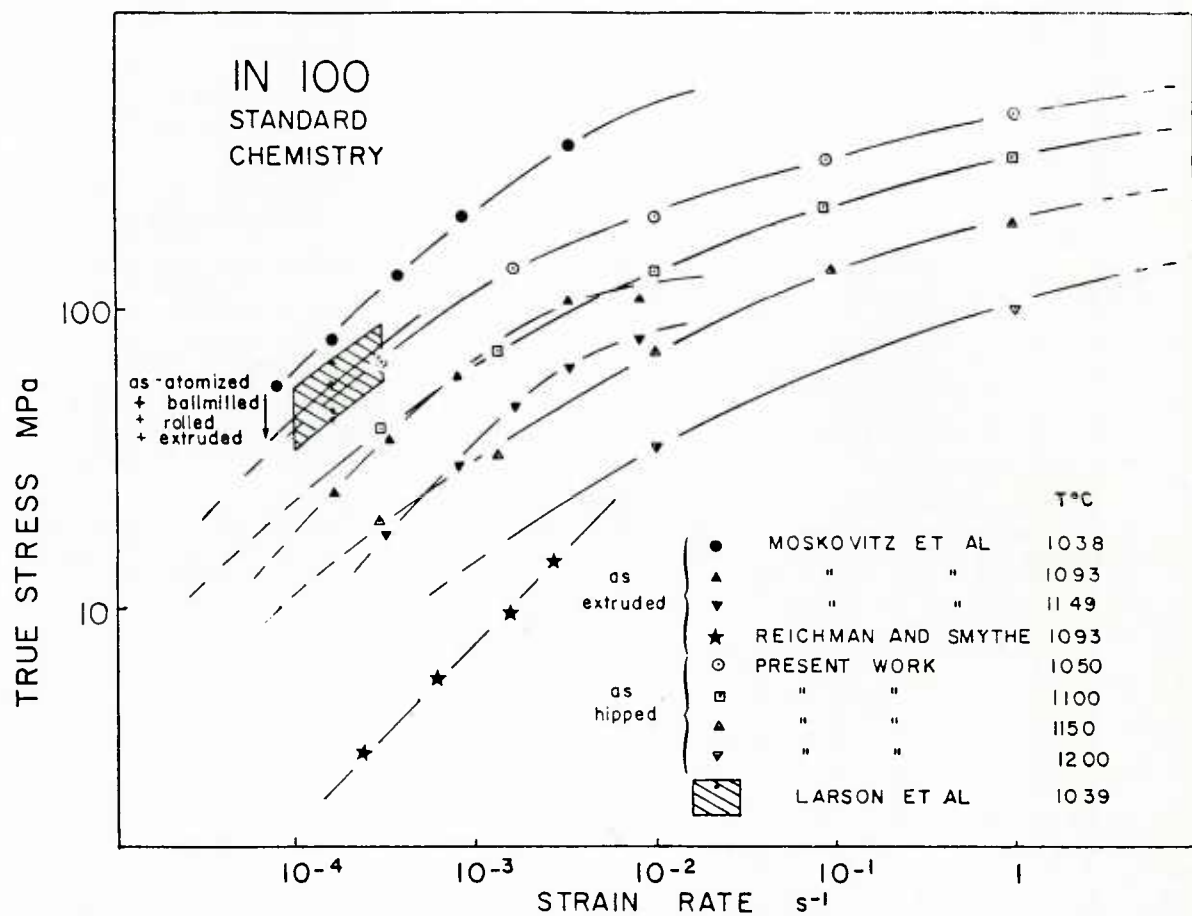
FIG 5   Effects of strain rate and temperature on flow strength in several powder processed alloys of standard IN 100 chemistry. Differences in flow resistance under identical forming conditions are due primarily to differences in grai size. The processing conditions for each set of data are:

    - Moskovitz et al[35]:
        as extruded (20:1 reduction at 1175°C) 8 µm grain size.

    - Reichman and Smythe[34]:
        as extruded (10:1 reduction at 1040°C) unresolvable grain size probably of the order of 1 to
        4 µm.

    - Larson et al[36]:
        hot pressed at 1038°C as atomized 70 µm, ball milled 60 µm, rolled 3 µm, attrited 1 µm grain sizes.

    - Present work:
        hot isostatically pressed 980°C/4hrs + 1175°C/2hrs/100MPa.

at slower forming rates[32]. Alternatively, the powder may be consolidated directly into near net shapes by hot isostatic pressing (HIP). With this process, the powder is encapulated into an evacuated and sealed container in the shape of the disc. The container is then exposed simultaneously to high gaseous pressures and high temperatures (Hipping)[33]. Still, with another process, the powder is consolidated by HIP and the compact is processed into disc shapes by conventional or slow strain rate isothermal forging.

Finer grain sizes and therefore higher degrees of superplasticity can be achieved by extrusion. This is shown in Figure 5 which compares the flow properties of several early powder processed compacts of IN100 produced by extrusion[34,35], hot isostatic pressing and hot closed die forging[36]. The flow strength of extruded IN100 can be more than one order of magnitude lower than that of hot isostatically pressed IN100 under the same testing conditions. This advantage may be lost when the extrusion temperature is the same as the HIP temperature, as indicated by Moskovitz et al's data[34]. In spite of the highest of all extrusion ratio used in this case, the flow resistance of the extrudate is not much different than that of the compacts prepared by hot isostatic pressing (present work). The data in Figure 5 also demonstrate that minimal reductions in flow resistance are achieved by cold working the powder prior to compaction[36] as compared to the gains that can be derived from low temperature extrusion.

Compared to extrusion, however, more complex shapes can be produced by HIP. This can provide the needed flexibility in producing the complex preform shapes which may be required to optimize microstructures in forgings by selective forging. As complex a shape as might be needed can be produced simply by HIP by encapsulating the powder in a container with the required shape.

Once the disc has been forged, the fine grain superplastic condition can be eliminated by solution treatment to induce grain growth and thus recover the desired coarse grain size for high temperature strength in service. Solution treatments well above the solvus temperatures of precipitating phases (γ', carbides) are used when coarse grains and optimum creep-rupture properties are required. Alternatively, solution treatments at or just below the solvus temperatures of the precipitating phases can be used to obtain a fine grain size for best tensile strength and LCF resistance.

Superalloy powder processing technologies are by now relatively well established. Powder processed parts are being used in some of the most advanced aircraft power plants. Meanwhile, interest is growing in the development of new technologies for improving disc performance beyond current limits. In this regard the use of selective forging to produce dual property discs in the manner described earlier has been attracting some attention. Detailed studies were undertaken at NAE to explore the potential of this technique and to develop the materials data required from modelling purposes and process optimization. Some of the earlier results of this and other relevant work on interdependence between strength and structure at forging temperatures in P/M superalloys are summarized below.

2.2 FORGING BEHAVIOUR OF P/M SUPERALLOYS

All the powder compacts examined came from earlier NAE studies. All were prepared from commercial prealloyed powders of high strength normally cast alloys either by hot isostating pressing[22,37,38] or by hot extrusion[39]. One of the compacts[38] was studied in greater depth. Details concerning this particular material and the results obtained will be discussed in later sections. The results of all studies concurred on one point: grain size has a strong effect on flow strength in these materials.

In an early study of the effects of consolidation temperature on flow strength in Hipped Mar M200 compacts[22], it was found that compacts pressed below the γ' solvus exhibited superplastic characteristics with a much reduced flow strength at forging temperatures compared to compacts pressed above the solvus, Figure 6. Furthermore, of the two compacts pressed below the γ' solvus, the one pressed at the lowest temperature gave the lowest flow strength. This was found to be due to differences in grain size from 5 to 10 μm in material pressed below the γ' solvus to 50 to 200 μm in material pressed above the γ' solvus, Figure 7. The flow curves for these compacts obtained by compression testing at 1050°C and 3×10^{-4} s^{-1} are compared in Figure 8. Under these testing conditions, peak flow strength in the compact with the finest grain size is reduced by a factor of six relative to peak strength in the coarsest grained material.

All compacts exhibited softening during flow. The degree of softening tended to decrease with a decrease in strain rate and/or an increase in temperature[22-24]. However, it was far more pronounced in the coarsest grained compacts under all testing conditions. This softening was attributed to a gradual refinement of the grains and redistribution of the major phases into a microduplex structure of γ and γ' grains, typified by the microstructures shown in Figure 9. The transformation is the result of a deformation induced recrystallization which starts at or near the grain boundaries of the original grains, Figure 9a and b and proceeds by nucleation and growth of new grains at the interface between transformed and untransformed regions[22]. As deformation progresses, the volume fraction of fine grained material also increases. The growth of new grains in this transformation appears to be limited to a few microns only, probably because the grains are prevented to grow due to the presence of the γ'. The redistribution of this phase occurs by mechanisms as yet not entirely understood but probably involving dissolution and reprecipitation of the γ' through mass transport and accelerated diffusion of γ' forming elements along the grain boundaries and the core of dislocations introduced during deformation.

The transformed microstructure, Figure 9a and b, is similar in scale and in morphology to the microstructure of the fine grained compact after testing under the same conditions, Figure 9c and d. In both cases, it is equiaxed microduplex with γ and γ' grains of the order of 2 to 5 μm in size. Since, the conditions for superplasticity in nickel base superalloys is a fine grain size of 10 μm or less[22], the transformed regions, like the fine grained compacts, are superplastic, and their resistance to deformation is much lower than that of the original untransformed material. Therefore, as the volume fraction of transformed material increases, the flow strength of the compact also decreases, as observed experimentally, Figure 8. For the same reason, flow tends to become localized within the fine grained regions. From the evidence provided (c.f Figures 8 and 9) it appears that quite large strains (>> 1) may be required before the original coarse grained structure is entirely replaced by the fine grained transformation product.

The development of the "necklace" structure (c.f Figure 9a), as it is often described in the literature, seems to be characteristic of deformation in coarse grained superalloys at forging temperatures, particularly in high γ'content alloys. It is also believed to be the main source of softening during flow in these alloys, including powder processed alloys. Examples of "necklace" structures at different stages of their evolution are shown in Figure 10 for two compacts (Mar M200 and 713LC). Both compacts were initially coarse grained and both were deformed at temperatures less than their respective γ' solvuses.

In a recent study undertaken to evaluate the effects of processing conditions on necklace formation in a 713LC compact[13], the extent of the transformation was found to vary with forming rate and temperature as well as with the amount of straining. It was also found that the transformation did not spread uniformly throughout the subscale cylindrical forging billet used, being in general more complete near its geometric centre, as shown in Figure 11. By contrast, the regions near the outer rim of the billet appeared less transformed. This was in spite of the large nominal strain introduced and was probably due to the large strain gradients developed under triaxial flow conditions as a result of poor lubrication at the tooling/testpiece interfaces. The presence and shape of the large dead metal zones near the end faces of the pancake, Figure 11, is consistent with this view.
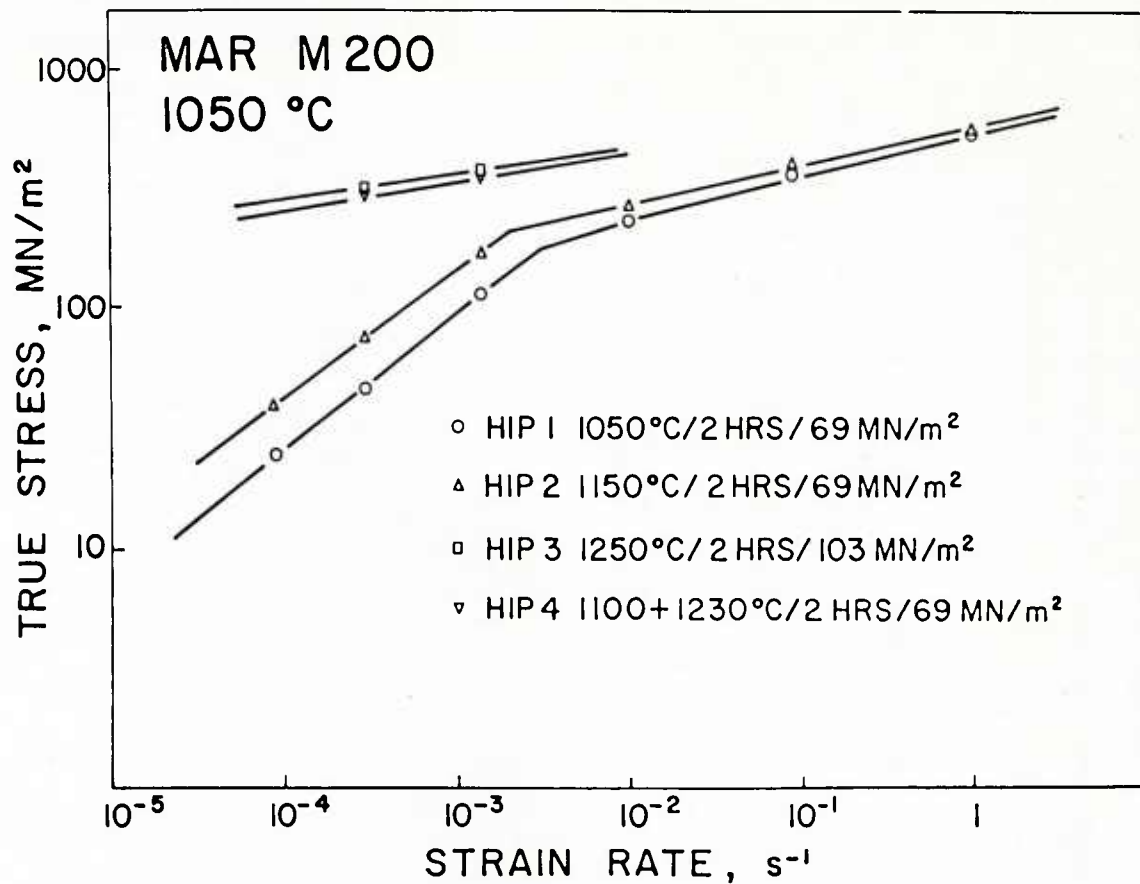
FIG 6   Effects of consolidation conditions on peak flow stress in low carbon P/M Mar M200.

a)   1050°C/2hrs/69 MN/m² (HIP 1)   b)   1250°C/2hrs/103 MN/m² (HIP 3)
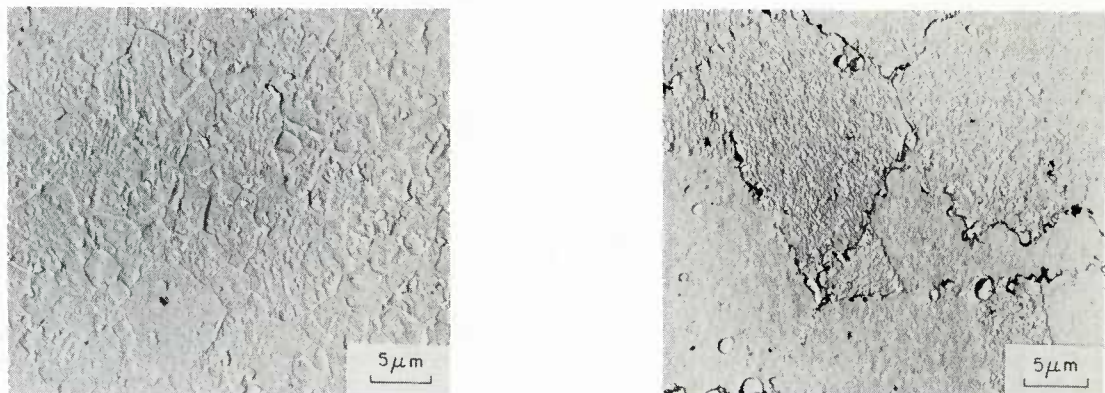
FIG 7   Effects of hot isostatic pressing conditions on grain size in powder processed low carbon MAR M200:
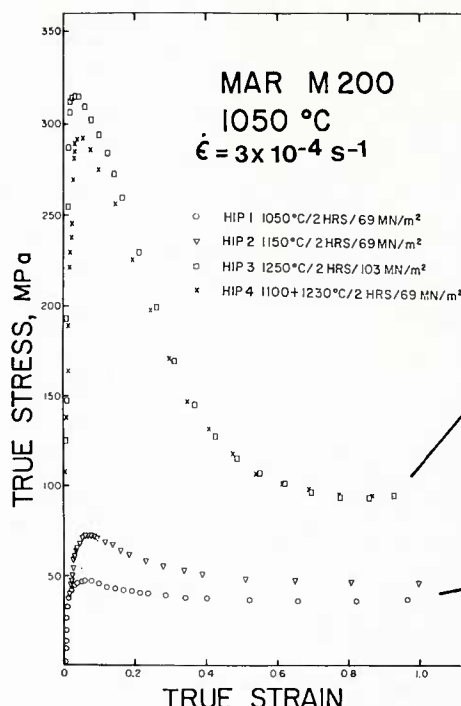
FIG 8   Effects of consolidation conditions on flow curves in low carbon P/M MAR M200 under typical forging conditions.
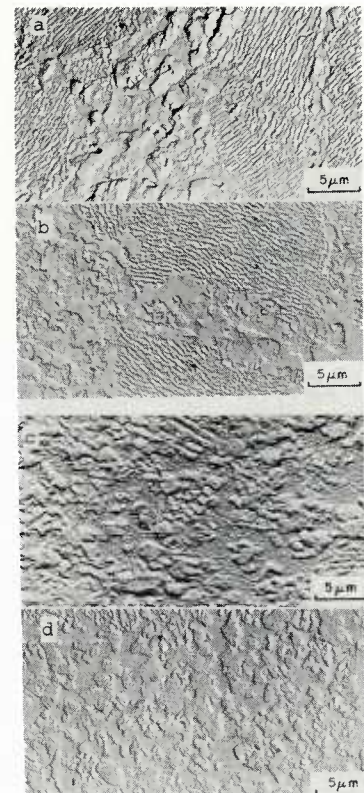
FIG 9   Effects of forging on microstructure in coarse (a,b) and fine (c,d) grained low carbon P/M MAR M200 (for consolidation conditions HIP 1 and HIP 3, see Fig 8).

a)   HIP 3   Marbles etch
           10 gm $CuSO_4$, 50 ml HCl, 50 ml H_2O.

b)   HIP 3   Inco etch
           50 ml HCl, 25 ml HNO_2, 2 gm $CuCl_2$, 200 ml H_2O.

c)   HIP 1   Marbles etch

d)   HIP 1   Inco etch

FIG 10   Necklace microstructures in a) low carbon P/M MAR M200 and b) P/M 713 LC, deformed under typical isothermal forging conditions.

This particular study demonstrated quite clearly that the growth of the necklace structure is strongly dependent on the amount of strain imparted. In a complex forging, different locations will experience different amounts of deformation and therefore the transformation will not progress everywhere to the same extent. This might be applied for producing dual property discs, using coarse grained preform and closed die forging equipment of the kind shown in Figure 12. With this equipment, and a preform shape as shown, the rim region would be constrained triaxially while the material in the bore would be forced to flow outwardly under the action of the ram, first radially and then transversely into suitably shaped recessed cavities. In this way, the original coarse grain size would be preserved in the rim while the microstructure in the bore would be refined. The procedure is essentially that adopted by Carlson earlier[12] (c.f Figure 2) except that in the present case, it would be possible to introduce larger strains as may be required to complete the transformation in the bore region of the disc. In addition the large hydrostatic pressure which would be generated in the constrained rim region would prevent radial cracking which might otherwise occur[12].

The results of all studies reported in this section concurred on two points: grain size has a strong influence on flow strength in P/M superalloy at forging temperatures <u>and</u> also grain size can change substantially in this class of alloys during mechanical working. In order to model deformation under such conditions, a clear understanding of the interdependence between evolving grain size and flow strength is required. A more detailed study of structure-property relationships in P/M superalloys at forging temperatures was therefore undertaken. The results and conclusions reached in that study form the basis of the rest of this paper.

3.0 EXPERIMENTAL MODEL MATERIAL

The model material selected was a compact from earlier studies[38] prepared from a -60 mesh argon atomized powder of 713LC. Details concerning powder chemistry and mesh size distribution are given elsewhere[25]. The powder was consolidated in evacuated and sealed mild steel containers by hot isostatic pressing, using a two step HIP cycle designed to minimize carbide formation at prior particle boundaries[39]. The nominal pressing conditions were 980°C/4 hrs/105 MPa + 1175°C/2 hrs/105 MPa. The maximum HIP temperature was kept below the γ' solvus temperature (~ 1180°C) and therefore the compact retained the fine as-atomized grains of the powder particles. This was found to confer superplasticity to the compact as expected[25].

The flow behaviour of this material was evaluated in the fine grained superplastic condition as well as in a grain coarsened condition. This was obtained using material hot isostatically pressed above the γ' solvus (see footnote below)* as well as by preheating fine-grained material above the γ' solvus prior to testing. This was done in situ, in the testing apparatus and was followed by cooling directly to the test temperature[13].

The microstructure of the as-hipped material has already been described in conjunction with Figure 4b. Actual microstructures prior to commencing a test were evaluated by quenching the as-hipped or grain coarsened material after holding at each test temperature for a period corresponding to the hold time in the apparatus prior to testing. After holding the fine grained as-hipped material for 30 minutes at 1050°C, for instance, the microduplex nature of the material was retained, although the overall volume fraction of γ' was reduced. In particular the fine cooling γ' formed during slow cooling in the hipper was not formed in this case, Figure 13a. The microstructure shown was typical of that present prior to forging at all test temperatures. However, there were minor differences in each case with a slightly lower γ' volume fraction at 1150°C compared to that present at 1050 and 1100°C[13], and with the intragranular γ' being more affected as expected, at a temperature close to the γ' solvus temperature. The grain boundary γ' size was in the range from 4 to 8 μm which was one quarter to one half of the γ grain size. The latter was found to remain stable at all test temperatures. Grain coarsening data, Figure 14 indicated that not until γ' goes into solution at approximately 1175°C, does the grain size of the as-hipped material grow significantly. This demonstrates the stabilizing effect of the precipitate phase on grain size at temperatures below 1175°C.

After the grain coarsening treatment (2 hours at 1220°C) the grain size was of the order of 50 μm consistent with the data from Figure 14. Upon cooling to the test temperatures, the γ' reformed along grain boundaries and in the grain interiors in quantities which varied with the test temperature. After holding for 30 minutes at 1050°C the microstructure was as shown in Figure 13b. There was little change in γ' volume fraction or morphology for larger hold times at any of the test temperatures. However, the γ' volume fraction tended to be slightly lower at the highest test temperature as one may have expected[13].

4.0 EXPERIMENTAL PROCEDURE
4.1 Testing Apparatus

Several laboratory test methods can be used for the study of metal flow under forming conditions. These methods and their relative usefulness have already been assessed and compression testing identified as the most suitable method for the simulation of forging operations[40]. Compared to other test methods, the stress state in compression is closer to that found in forging. Compression tests are also quite simple to perform and their analysis is relatively straight forward, providing flow is homogeneous and frictional effects at the tool/specimen interfaces can be neglected. In addition, the evolution of microstructure within the test piece is more representative of that observed in forged components. This makes compression testing more appropriate for collecting information concerning the relationship between flow strength and structure at forging temperatures. This, it will be recalled, is the main undertaking in this work and therefore compression testing was selected for this study.

The flow behaviour of the model compact was evaluated by means of carefully controlled uniaxial compression tests using a testing facility developed and built at NAE for this purpose[41]. The facility which is shown in Figure 15 consists of a servo-controlled hydraulic testing machine equipped with induction heated compression tooling and modified for constant true strain rate deformation. A schematic cross section of the tooling and its protective enclosure is shown in Figure 16. Details concerning the design of the equipment, the means of controlling the temperature and strain rate and the performance evaluation of the equipment can be found elsewhere[41].

* Two cans of the same alloy powder with different mesh size ranges were prepared which ended up with different as-hipped microstructures. The model material used in this investigation had the finest grain size. The other can exhibited a much coarser grain size, of ~ 40-60 μm versus ~ 8-12 μm for the model material. This difference was probaby the result of a temperature gradient in the hipper during pressing. Judging from the volume fraction of coarse γ' in the model material, it would seem that its actual pressing temperature may have been somewhat lower than the nominal pressing temperature of 1175°C. Conversely the actual pressing for the other can must have been very close or perhaps slightly above the γ' solvus (measured experimentally at ~ 1180°C).

Only under such conditions would the grains have been allowed to grow. Alternatively the γ' solvus may have differed for the two batches of powders, perhaps due to contamination during canning or to differences in mesh size distributions. However, experimental evidence supports the first interpretation. The availability of a coarse-grained compact provided an opportunity to evaluate the behaviour of the P/M 713LC in the coarse grained as well as the fine grained condition.
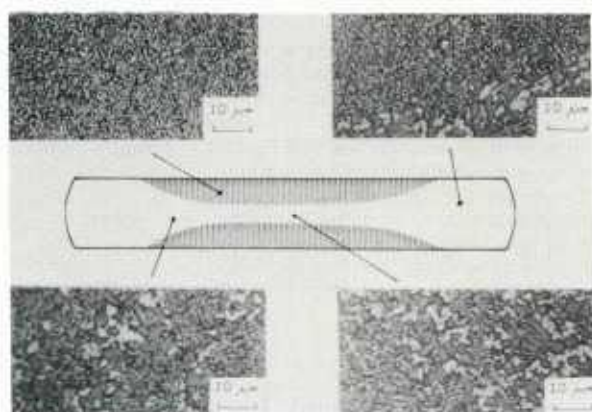
FIG 11   Section through deformed compression test piece showing non uniform distribution of necklace structure development at 1100°C in coarse grained 713 LC compacts.
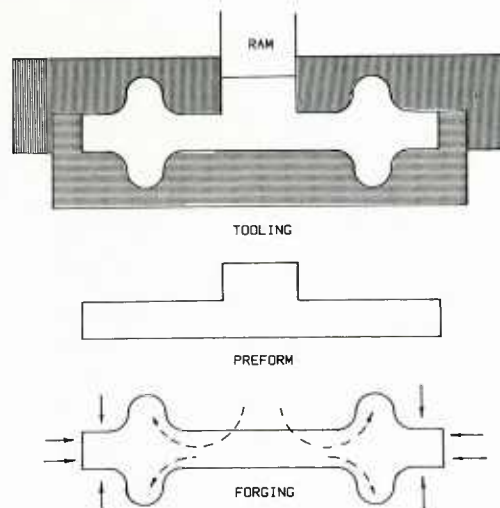

FIG 12   Close die forging equipment for producing dual property disc (not optimized as shown).
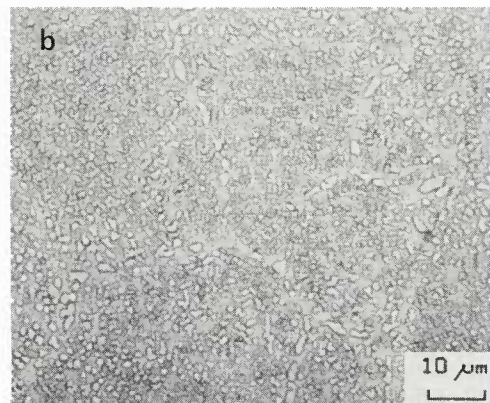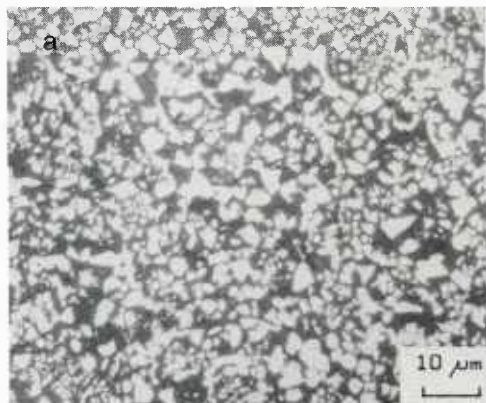

FIG 13   Microstructure of model material (Hipped 713 LC) prior to testing.

a)   after holding for 30 minutes at 1050°C followed by quenching;

b)   after grain coarsening treatment of 2 hours at 1220°C followed by slow cooling to 1050°C, holding for 30 minutes and quenching.
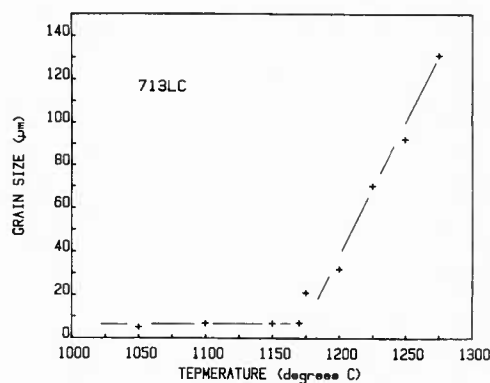
FIG 14   Grain coarsening characteristics of fine grained 713 LC compacts (2 hour exposures at temperatures). The γ' stabilizes the grain size below 1175°C.
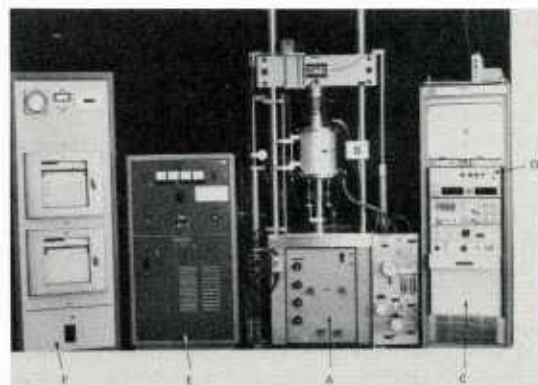
FIG 15   Constant true strain rate isothermal compression testing facility showing:

a)   MTS load frame
b)   environmental chamber and tooling
c)   MTS controller
d)   exponential function generator for strain rate control
e)   induction generator and
f)   temperature controller and recorders

The tests were done using small cylindrical specimens with a height to diameter ratio of ~ 1.5 (typically 12 mm high by 8 mm in diameter) at constant temperatures and strain rates. Temperatures were kept constant to within $^{+}_{-}$ 5°C and the strain rate to within 2% of selected values. The specimens were preheated for 30 minutes unless otherwise noted and then deformed between flat silicon nitride dies, under a flowing argon atmosphere. During the test, the developed load and reduction in height of the test piece were continuously monitored using a load cell and a high temperature axial displacement transducer designed to follow the relative displacement of the two compression dies[41], respectively. The true stress - true strain curves were calculated from the load -height data assuming constancy of volume and homogeneity of flow within the entire specimen (see Appendix I). For this reason, it was important to ensure that plastic flow remained as nearly homogeneous as possible during testing. To this end special considerations were given to loading conditions and specimen geometry as well as to specimen lubrication and deformation. Frictional effects at the die-specimen interfaces were minimized by using a molten glass lubricant. Annular grooves were machined in the end faces of the specimens to help maintain proper lubrication throughout the test. With this technique it was found that breakdown in lubrication occured only at high strains, typically greater than one. Also, at that strain, the error in flow strength due to friction was estimated to be less than 4% (see Appendix I).

4.2 Testing Procedure

It will be generally recognized that flow strength in metals and alloys at forging temperatures is strongly influenced by strain rate and temperature and by the microstructure of the alloy being formed. In this regard the size and shape of grains and the morphology of second phase particles can have a strong influence on deformation[19,40,42]. However, how strong or what the underlying mechanisms might be is not well documented for materials of the type considered here. From the results presented so far, it will be clear that grain size and grain size changes induced by forging should be taken into consideration for accurate analytical predictions of flow strength in these materials. Therefore, the effects of grain size need to be separated from those of strain rate and temperature.

To this end, the strain rate as well as the temperature were maintained constant during testing. Constancy of strain rate was achieved by keeping the velocity of the hydraulic ram proportional to the height of the compression specimen. This required an exponential decay of velocity with time (See Appendix I, Eq A-10) and was obtained using the voltage output from an RC circuit to control the position of the ram[41]. The range of strain rates examined in this work varied from 10^{-5} to 1 s^{-1} which covered that used in practice for isothermal forging of P/M superalloys (typically from 10^{-3} to 10^{-1} s^{-1}). It is generally agreed that for strain rates less than 10^{-1} s^{-1}, adiabatic heating of compression test pieces is minimal[43]. In the present study, adiabatic heating was neglected because of the slow strain rates used. However, the possibility that part of the effects observed might have been caused by an increase in test piece temperature was not excluded, particularly for high strain rate tests.

The temperature during testing was carefully monitored using thermocouples embedded into the compression die retaining collars. Testing was performed at three temperatures, 1050°C, 1100°C and 1150°C. More data were accumulated at the lowest of these temperatures because well below the solvus, the higher volume fraction of γ' was expected to slow down the microstructural changes induced by working, thereby making it easier to follow these changes. At the end of a test, the specimens were quenched to retain the microstructure present during testing for examination by optical and transmission electron microscopy.

Experiments were designed that allowed the effects of grain size to be separated from those of strain rate and temperature so that flow stress could be presented in terms of both strain rate and grain size at a given temperature. Furthermore, the evolution of the microstructure was characterized in terms of deformation conditions (strain rate and temperature) as well as in terms of current state of microstructure as needed for analytical predictions. How this was achieved is described in the following section.

5.0 RESULTS

Flow curves measured at 1050°C and different strain rates for fine grained and coarse grained compacts obtained by Hipping above the γ' solvus are compared in Figure 17. The flow curves have the same overall features, with the coarse grained material showing higher peak strengths and both compacts exhibiting softening during flow at all strain rates examined. By contrast, the microstructure of the two compacts evolved in quite different ways during compression. This is demonstrated in Figure 18 which compares as-worked microstructures for the fine grained compact (7 μm grain size) and a coarse grained compact obtained by presolutioning the fine grained material in the apparatus prior to testing to coarsen the grain size (50 μm grain size).

With the fine grained compact, there was a gradual refinement of the microduplex grain size which occurred homogeneously and uniformly throughout the test piece (see also Appendix I). By contrast, with the coarse grained material refinement occurred through the development of a necklace structure i.e. by the nucleation and growth of new grains, first along the original grain boundaries and subsequently along the interface between recrystallized and non recrystallized regions, in the manner described earlier, in conjunction with Figure 11. Also in this case, as was shown in Figure 11, the transformation did not progress to the same extent in every part of the compression piece. This makes it difficult to establish clear relationships between grain size and flow strength as needed for analytical purposes. While peak strength for coarse grained compacts may be regarded as characteristic of the initial coarse grained microstructure, the stress measured beyond this point is dictated by the development of a complex composite microstructure consisting of heterogeneously distributed regions of soft superplastic material (regions A in Figure 18) surrounding pockets of hard unrecrystallized material (regions B in Figure 18). For this reason the flow curve cannot be easily interpreted beyond peak strength. Therefore the testing of coarse grained compacts is of little value to develop constitutive relations for modelling flow. What it does provide, however, is a clear indication of the evolution of microstructure as it might be expected to occur in a complex forging. In this regard, important observations were made concerning the scale of the necklace structure and its growth which suggested how one might proceed to model the deformation of compacts in the coarse grained condition, beyond peak strength.

With continued straining, there appeared to be little change in the size of the grains within the transformed regions. In addition the size of new grains appeared to be of the same order of magnitude as that observed in initially fine grained material deformed under identical conditions. This is indicated for instance in the micrographs of Figure 18. Therefore, it may be possible to model the deformation of coarse-grained compacts on the basis of a constitutive relation for fine grained material, assuming that the proportion of the fine grained material continuously increases during flow, until in the end, the material becomes entirely fine grained, when sufficient deformation has been imparted. This requires a model for predicting the growth of the necklace structure and a constitutive relation for fine grained compacts. Therefore, further studies concentrated on establishing a flow strength-microstructure relationship in fine grained compacts.
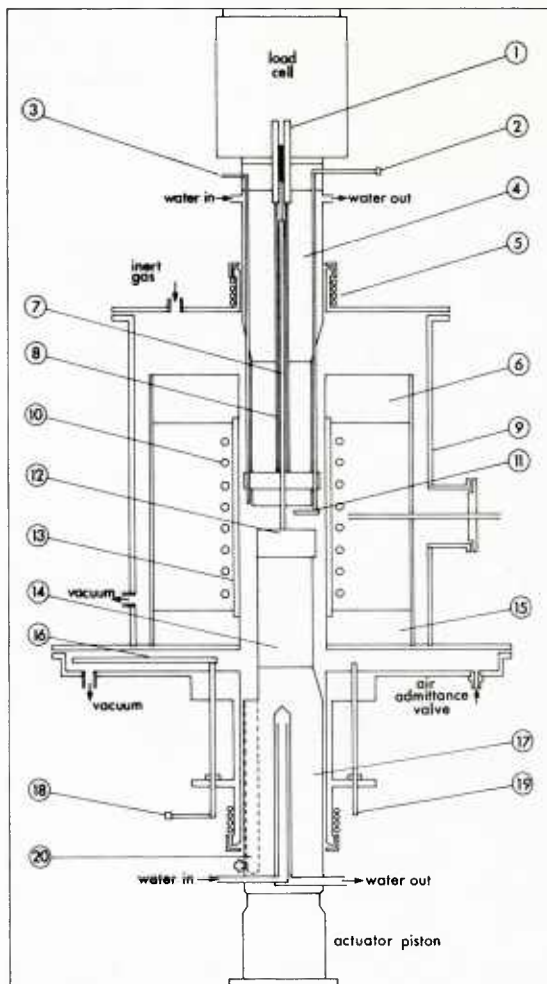
1. DISPLACEMENT TRANSDUCER
2. FLIPPER SHAFT HANDLE
3. INCONEL SHEATHED THERMOCOUPLE PROBE
4. TOP ANVIL SUPPORT
5. WATER COOLING COIL
6. TOP INSULATING BLOCK
7. TRANSDUCER EXTENSION PROBE
8. TRANSDUCER EXTENSION TUBE
9. COMPRESSION CHAMBER
10. INDUCTION COIL
11. FLIPPER
12. COMPRESSION DIE
13. SUSCEPTOR
14. BOTTOM ANVIL
15. BOTTOM INSULATING BLOCK
16. VACUUM DOOR
17. BOTTOM ANVIL SUPPORT
18. VACUUM DOOR HANDLE
19. VACUUM DOOR CLAMP
20. QUENCHING CHUTE

SCHEMATIC CROSS-SECTION OF THE INDUCTION HEATING COMPRESSION TRAIN

FIG 16   Schematic cross section of the environmental chamber and tooling. Note the displacement transducer which monitors the relative motion of the compression dies (No. 1 and 7), the heating coil (No. 10) and the rapid quenching capability (No. 11 and 20).
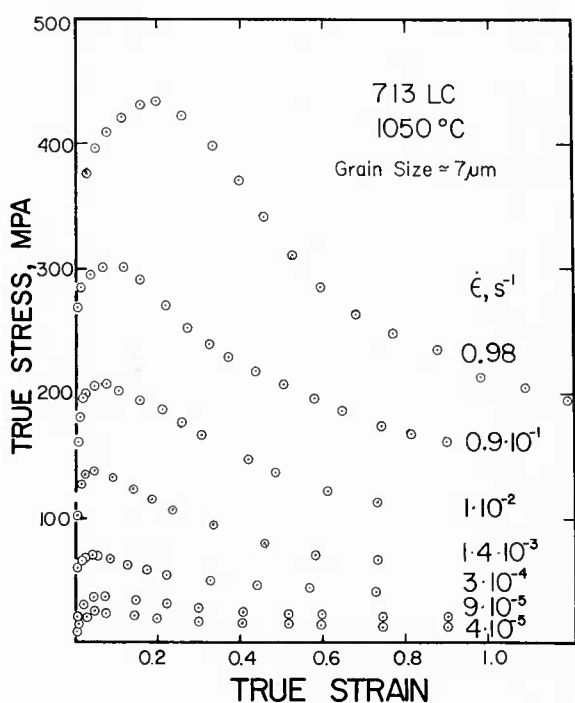
a
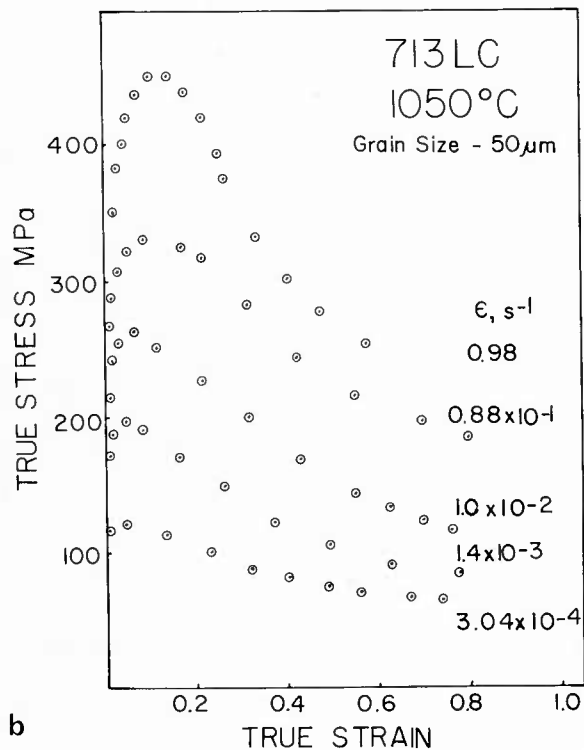
b

FIG 17   Flow curves for a) 7 μm and b) 50 μm grain size 713 LC compacts at 1050°C and different strain rates.
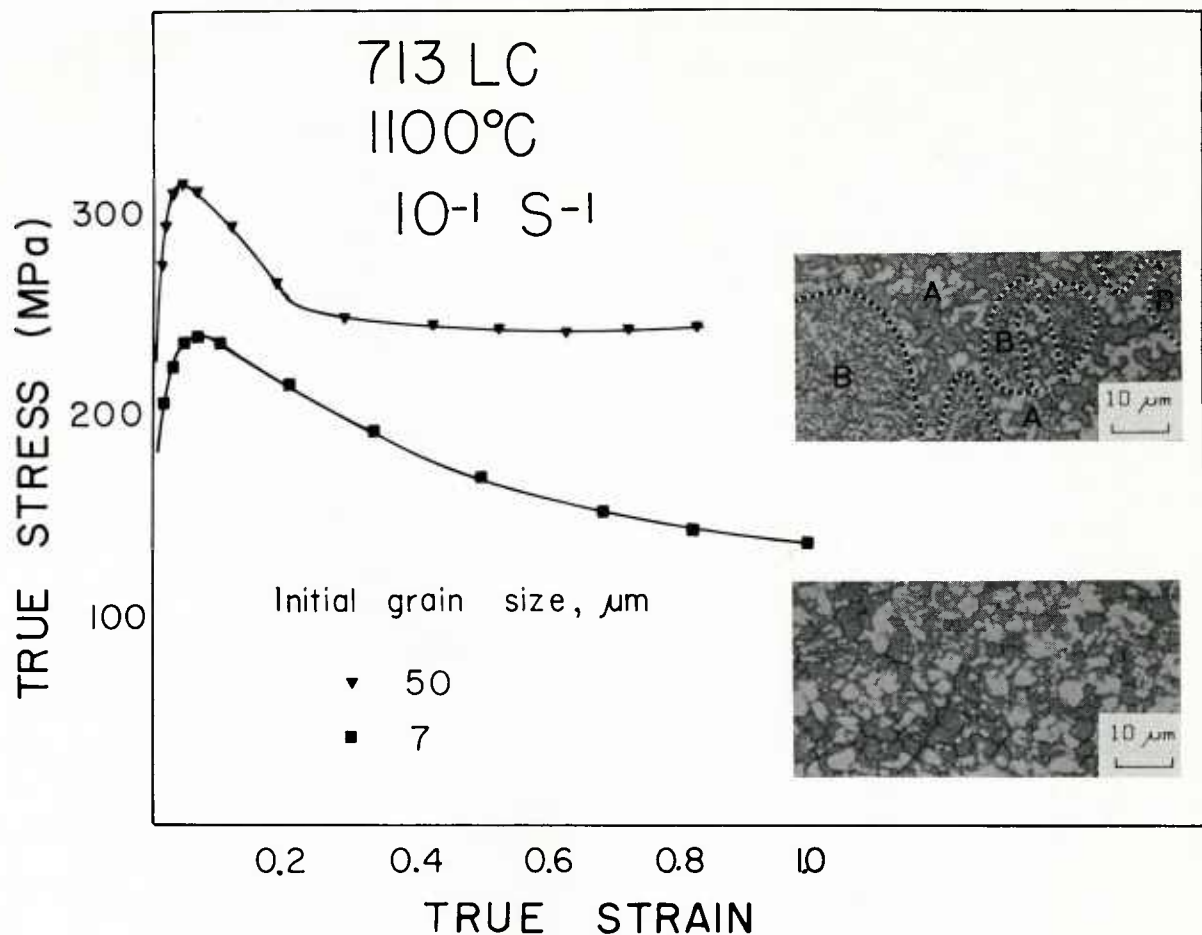
FIG 18 Flow curves and as-forged microstructures for 7 μm and 50 μm compacts deformed at 1100°C and a strain rate of 10^{-1} s^{-1}.
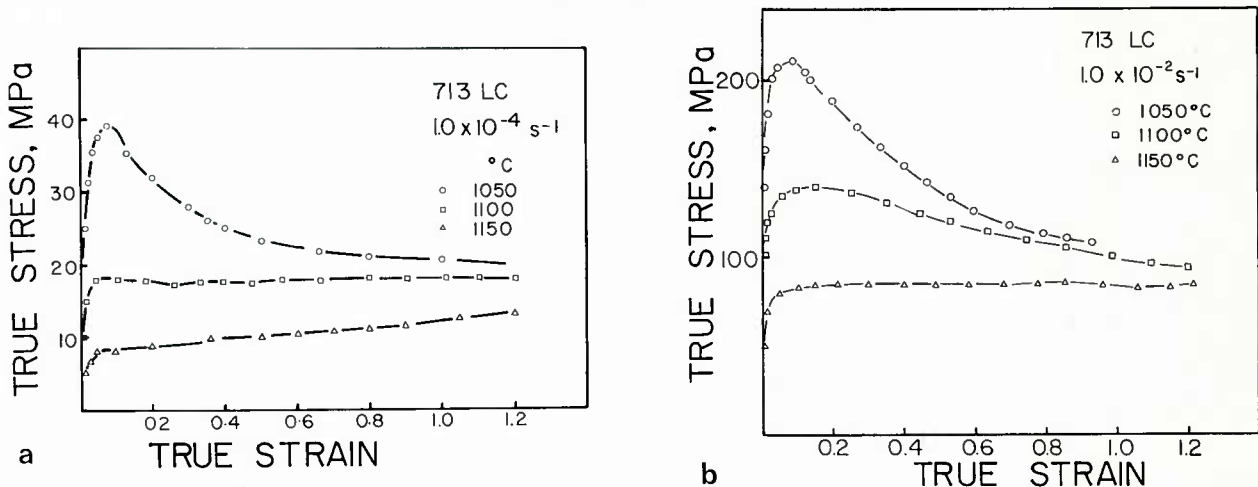

FIG 19 True stress true strain curves for fine grained powder processed 713 LC at different temperatures and strain rates. Note the occurence of hardening or softening during flow depending on testing conditions.

5.1 Flow Curves and As-Worked Microstructures in Fine Grained Compacts

Four important observations were made concerning the flow behaviour of the fine grained compact that need to be highlighted. Two are concerned with the shape of the flow curves and two with the effects of testing conditions on microstructure.

1.   The compact exhibited softening or hardening during flow and this depended on the strain rate and/or the temperature of the test, Figure 19. At 1100°C for instance, the compact flow softened at all rates examined, while at 1150°C both softening and hardening was observed. In general, more pronounced softening was observed at lower temperatures and/or faster strain rates. At the slow strain rate of 10^{-4} s^{-1} for instance, the compact flow softened at 1050°C and 1100°C but tended to harden during flow at 1150°C, Figure 19a. At a faster strain rate of 10^{-2} s^{-1}, the compact flow softened at all temperatures, Figure 19b.

2.   Once a sufficient amount of deformation had been introduced, the initial softening or hardening appeared to be followed by a regime of flow during which flow strength tended to remain constant while straining was continued. The strain for the onset of this "steady state" condition of deformation varied with testing conditions. Under conditions that led first to softening, it tended to decrease with an increase in temperature or a decrease in strain rate. Under conditions that led to hardening, it was greater than the maximum strains achieved in the tests and therefore no clear trend could be established. The onset of steady state flow in the hardening case may also have been obscured by the breakdown in lubrication at high strains which tended to induce upward curvatures in the flow curves.

3.   As regard the effects of deformation on microstructure, the average grain size of the material was found to increase or decrease during flow depending on the test strain rate and the test temperature, Figure 20. The grain size was refined under most testing conditions and this correlated with softening during flow. Meanwhile, an increase in grain size was noted which correlated with flow hardening, at the slowest strain rates and highest temperatures examined. The degree of refinement or coarsening, as applicable, are compared in Figure 21 for two different testing conditions. The microstructures shown are typical of thermomechanically processed fine-grained superalloy compacts, consisting of a microduplex arrangement of γ and γ' grains. Under all testing conditions, examined, the grain size remained equiaxed in spite of the large strains introduced.

4.   Finally, once sufficient deformation had been introduced, the grain size remained constant, as shown in Figure 20, and this could be correlated with the onset of steady state flow, Figure 19. It was also found that steady state grain size varied with testing conditions increasing with an increase in temperature or a decrease in strain rate. The extent by which grain size varied with testing condition is shown in Figure 22 for all the testing conditions examined in this work.

Grain size in this work was measured following Heynes' procedure[44], as a mean linear intercept. Since deformation was found to proceed by grain as well as interphase boundary sliding, as discussed later, both grain and interphase boundaries were included in determining the mean linear intercept of the microduplex structures. The average grain size of the fine grained compact prior to testing measured in the fashion was found to be in the range from 5 to 7 μm, tending to be slightly larger at 1150°C than at 1050°C because of the smaller volume fraction of γ' at the higher temperature.

Irrespective of the occurance of hardening or softening during flow, it was found that final flow stresses increased while final grain sizes decreased with an increase in strain rate at a given temperature, Figure 23. The trends observed for the range of strain rates examined can be represented by expressions of the form

$$\sigma_{ss} \propto \lambda_{ss}^{-n} \tag{1}$$

where σ_{ss} is the steady state flow stress, λ_{ss} is the average microduplex steady state grain size and n is an exponent which appeared to vary with test temperature. At 1050°C, the exponent n was of the order of 2. It must be pointed out that this value might have been somewhat lower had a steady state regime of flow been fully established at the fastest strain rates.

The correlation given by Equation 1 does not imply that steady state stresses are causually related to steady state grain sizes. The data contained in Figure 23 were collected at different strain rates and the correlation simply reflects the fact that both quantities are influenced by strain rate. (For a discussion to that effect, see Ref. 19, page 450). Reasons for presenting the data in this fashion will become evident later.

5.2 Interrupted Tests

The observation of a steady state regime of deformation with grain sizes that depended on the test strain rate suggested a testing procedure for separating the effects of grain size from those of strain rate and temperature. The procedure was an interrupted test technique which involved prestraining, unloading and immediately restraining in situ the compression test piece. By varying the prestrain conditions, different average microduplex grain sizes were produced, and their effects on flows strength were then directly evaluated from the flow curves generated during restraining. In these tests, the prestraining variables examined were strain and strain rate. These interrupted tests were performed at 1050°C only.

In tests where strain was the prestraining variable, as-quenched microstructures corresponding to increasing prestrains at constant strain rate were correlated with flow curves obtained upon restraining at a different strain rate. This allowed the effects of changes in grain size on flow strength to be evaluated. In tests where strain rate was the prestraining variable, a number of specimens were deformed to strains of the order of 1.0, or until steady state conditions appeared fully established, and as-quenched microstructures corresponding to these strains were correlated with flow curves obtained by restraining at different strain rates. This allowed the effects of grain size on flow strength at a given strain rate and the effects of grain size on strain rate sensitivity to be determined. Both interrupted test techniques are illustrated schematically in Figure 24. Flow curves for the fine grained 713LC compact obtained with each technique are also shown for discussion.

With increasing prestrain at a fixed strain rate, (10^{-1} s^{-1}) Figure 24c, a transition in flow behaviour was observed upon restraining at 1.4 10^{-3} s^{-1} from one where the material flow softened further during straining to one where flow strength rose instead continuously from the onset of plastic yielding. In all cases, however, stresses developed at high strains converged towards a steady state level which appeared to be independent of prior deformation history and to depend only on the imposed strain rate. For small and large prestrains, the convergence to steady state was incomplete. For a prestrain of 0.6, and a corresponding grain size of 2.2 μm, steady state flow was established within a true strain of about 0.2, Figure 24c. Changes in microstructures corresponding to this change in flow behaviour have been discussed elsewhere in detail[22-25]. Softening can be attributed to a gradual refinement of the average microduplex grain size by mechanisms which involve recrystallization of the γ phase and redistribution of the γ' phase including break up of the coarser γ' by intrusions of the γ phase and coalescence of the finer γ' particles. On the average, more grain and interphase boundary area becomes available for sliding, and as expected in a material which deforms primarily by grain boundary sliding, the flow stress decreases. By contrast, evidence has been provided that hardening may be attributed to an overall coarsening of the microduplex grain size[25].
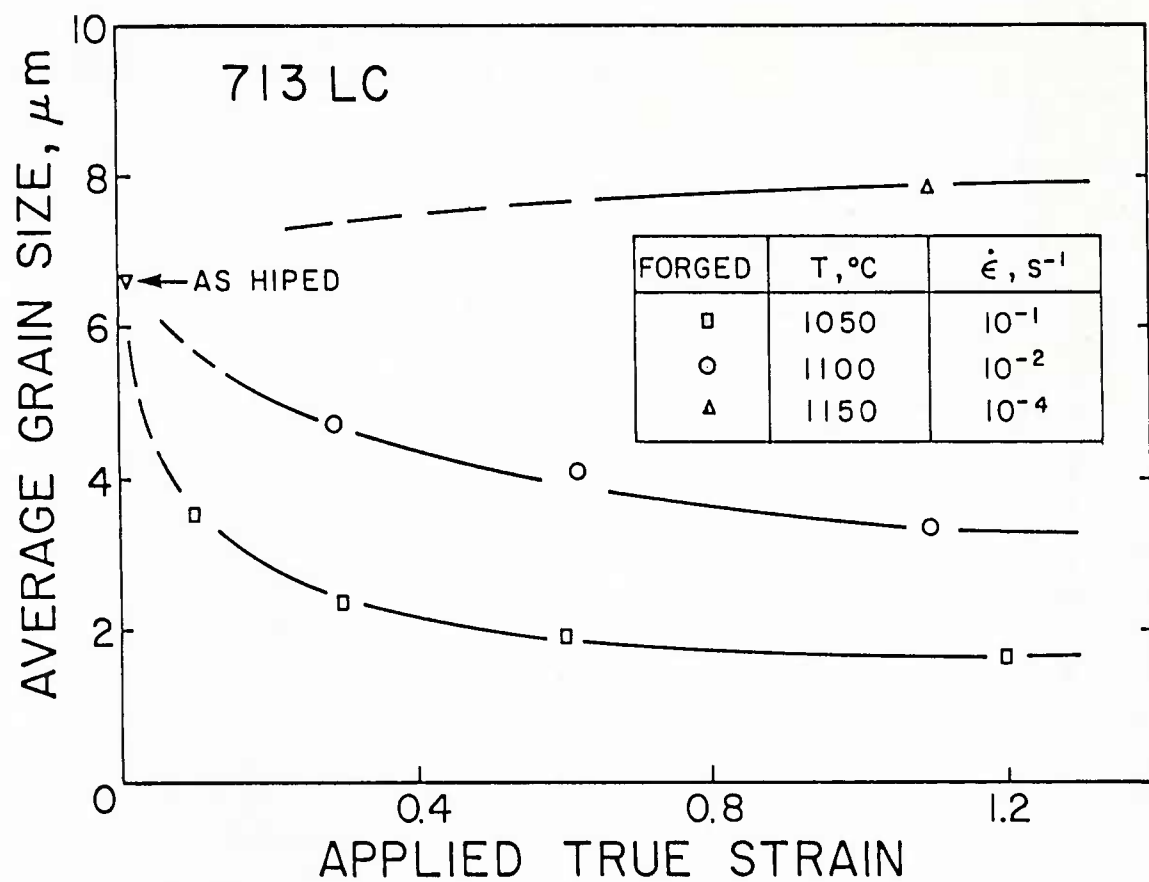
FIG 20   Effects of testing conditions and amount of straining on average grain size in 713 LC compacts.

a   b
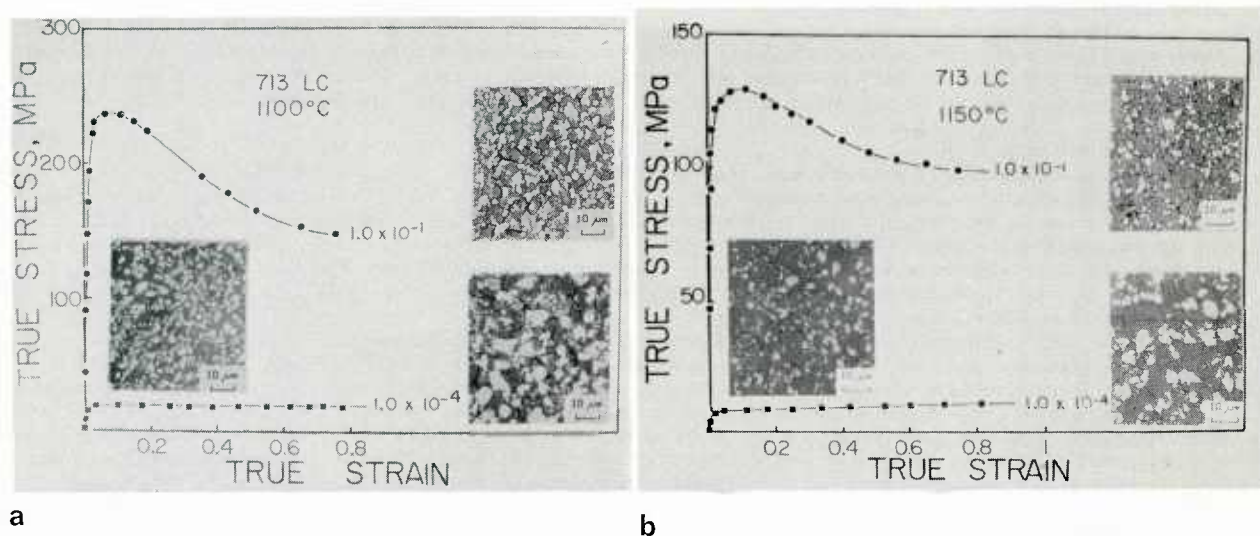
FIG 21   Effects of strain rate on flow strength <u>and</u> microduplex grain size at a) 1100°C and b) 1150°C in fine grained 713 LC compacts.
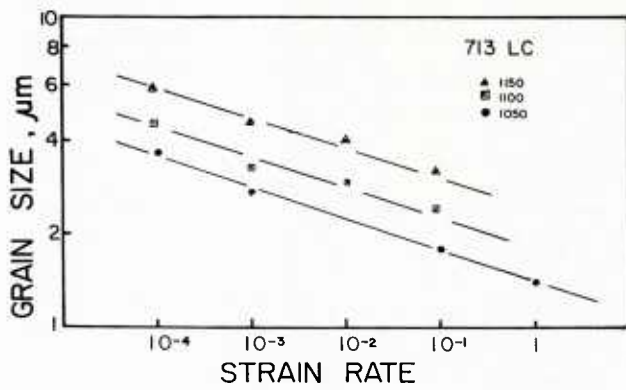
FIG 22   Effects of testing conditions on "steady state" grain size in powder processed 713 LC (see text for details).
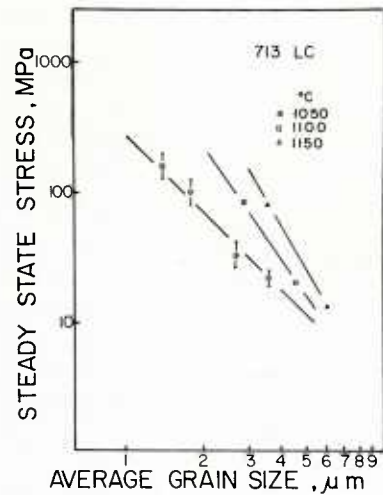
FIG 23   Apparent relationships between steady state flow stresses and steady state grain sizes at the three test temperatures used. The two variables are not causally related (see text for details).
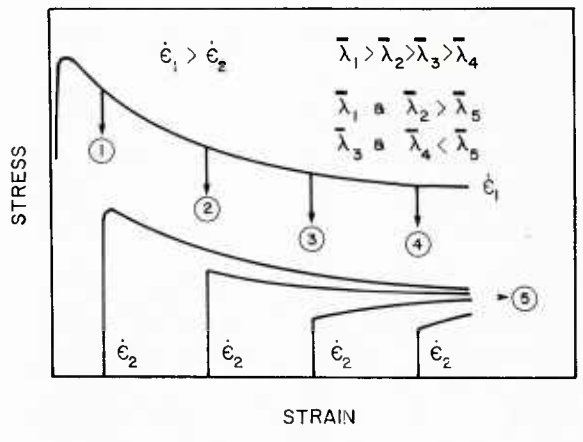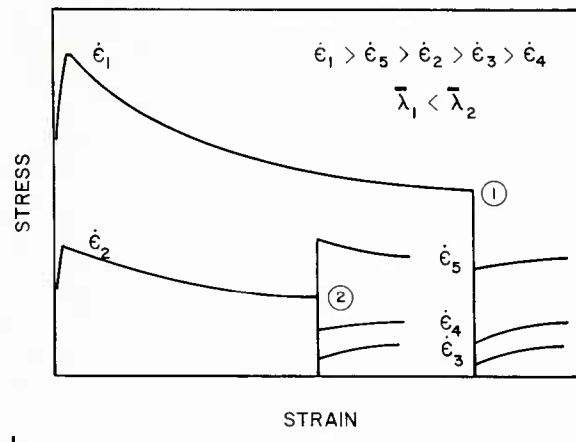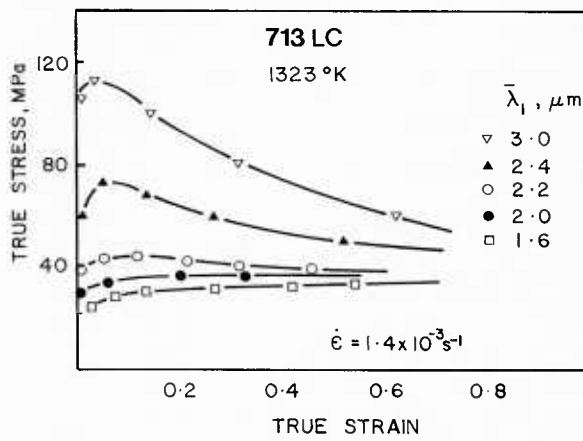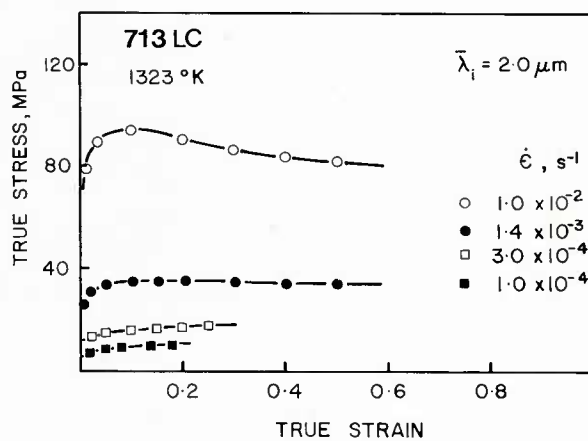

FIG 24   Schematic of interrupted tests used to separate the effects of grain size from those of strain rate and temperature. Specimens are prestrained to generate known microstructures, unloaded and restrained as shown. The prestrain variables are:

a)   amount of deformation
b)   strain rate

Data for the fine grained 713 LC compacts obtained with each method are also shown (c and d)

When the prestrain variable was stain rate, Figure 24d, peak flow stresses upon restraining were all reduced relative to those of the as-hipped material. This was because under all testing conditions, the grain size was refined relative to that of the as-hipped material. It was found, however, that differences in flow resistance were more pronounced after prestraining at faster strain rates. Again this was attributed to larger differences in grain size for this prestraining condition. It was also noted that either softening or hardening occurred upon restraining depending on the test strain rate and the grain size present upon resumption of the deformation. For instance, in material with an average microduplex grain size of 2.0 μm , Figure 21d (produced by prestraining at 10^{-1} s^1 to a strain of 0.6) softening occurred at 10^{-2} s^{-1} while hardening occurred at 10^{-4} and 3×10^{-4} s^{-1}.

The results of these interrupted tests have been analyzed and discussed at length elsewhere[25]. They all concurred on a number of points. Firstly, they confirmed that grain size has a strong influence on flow strength in P/M superalloys. Secondly, they indicated that steady state flow stresses and steady state grain sizes are independent of prior deformation history, depending only on the deformation strain rate at a given test temperature. And thirdly, they showed that transient flow behaviour prior to the onset of steady state flow varies with starting and finishing (steady state) grain sizes for a given set of testing conditions.

The effects of the starting grain size on yield strength for all testing conditions examined are shown in Figure 25. Here, offset yield stresses rather than peak strength, are used since several of the flow curves from which the data were derived exhibited hardening right from the onset of plastic yielding. It may be seen that the as-hipped material with the largest grain size had the highest flow strength. Its strain rate sensitivity

$$m = \frac{d \ln \sigma}{d \ln \dot{\varepsilon}} \qquad (2)$$

increased with decreasing strain rate from approximately 0.2 at the fastest strain rates to about 0.5 at the slowest strain rates. This is not unexpected from a material which exhibits superplastic characteristics. Strain rate sensitivities for different grain sizes obtained by the interrupted test technique were of the same magnitude although they remained of the order of 0.5 to increasingly higher strain rates as the starting grain size was decreased. The grain size dependence of flow strength at constant strain rate and temperature obtained by cross plotting the data from Figure 25 is shown in Figure 26. The dependency is of the form

$$(\sigma_{offset})\dot{\varepsilon},T \ \propto \ \lambda^P \qquad (3)$$

where λ is the average microduplex grain size at the <u>start</u> of the test and the magnitude of the grain size sensitivity index

$$p = (\frac{\delta \ln \sigma}{\delta \ln \lambda}) \ \dot{\varepsilon},T \qquad (4)$$

varies with strain rate and grain size. For finer grain sizes this index is of the order of 2 but it decreases with either an increase in strain rate or grain size.

It is interesting to note that the magnitude of the grain size sensitivity index, falls in the range normally reported for superplastic alloys, although it is somewhat higher than normal for the finer grain sizes examined.

5.0 DISCUSSION

The flow behaviour of the fine grained compact as presented in Figure 25, is generally consistent with deformation behaviour under superplastic conditions in fine grained superplastic alloys[45-47]. It will be generally recognized that a transition occurs in the strain rate sensitivity of fine grained superplastic alloys over a range of strain rate usually between 10^{-3} to 10^{-1} s^{-1} as observed in this work. At strain rates less than the transition strain rates, such alloys exhibit high strain rate sensitivities, typically of the order of 0.5 or more which compares to values of 0.25 or less for non superplastic alloys tested under identical conditions. In this low strain rate regime, known as Stage II deformation, plastic flow is predominantly governed by grain boundary sliding (gbs). Under such conditions flow strength is strongly influenced by grain size, as observed experimentally in the compacts under investigation.

At strain rates greater than the transition strain rates, the strain rate sensitivity decreases to values of 0.25 or less. In this high strain rate regime of superplastic deformation, known as Stage III, the deformation is predominantly governed by the motion of dislocations in the grain interiors (mdg, involving glide, crossglide and climb processes) and conventional hot working mechanisms operate[19,48]. Also the effects of grain size on flow strength are greatly reduced during Stage III as compared to Stage II. Most often, the transition from the condition where gbs dominates to one where deformation becomes predominantly governed by mdg occurs over a range of strain rates which may cover as much as three orders of magnitude in strain rates. The contribution from gbs gradually decreases as that from mdg increases when the strain rate is increased across this range. Both this transition and the two regimes of flow (Stage II and III superplasticity) are evident in Figure 25, with a strain rate sensitivity of 0.5. for all grain sizes examined at slow strain rates below 10^{-3} (Stage II) and a strain rate sensitivity of ~ 0.2 at high strain rates, typically greater than 10^{-1} s^{-1} (Stage III).

The transition from Stage II to Stage III deformation is of particular interest in this case, since it covers the range of strain rates most likely to be encountered during superplastic forging of discs. The transition is a region where both modes of deformation (gbs and mdg) occur simultaneously in parallel[49], each contributing different amounts of strain to the total deformation. A rate equation for discribing flow when strains are additive, as they are in this case, can be written as[49]

$$\dot{\varepsilon} = \dot{\varepsilon}_{gbs} + \dot{\varepsilon}_g \qquad (5)$$

where $\dot{\varepsilon}$ is the applied strain rate and $\dot{\varepsilon}_{gbs}$ and $\dot{\varepsilon}_g$ are appropriate stress functions for deformation by gbs and mdg, respectively, to relate flow stress in each case to macroscopic variables of deformation (strain rate and temperature) and to appropriate microscopic or state variables for describing the current state of microstructure[50]. With the appropriate stress functions, as discussed later, Equation 5 reduces to a 4th order polynomial of stress which can then be solved for stress for any given state of microstructure.

The relative contribution from gbs and mdg may be expected to vary with deformation conditions and the state of the microstructure. At slow enough strain rates, mdg contribution becomes negligible relative to the amount of deformation produced by gbs and Eq. 5 reduces to $\dot{\varepsilon} \sim \dot{\varepsilon}_{gbs}$. Conversely at high strain rates, intragranular regions are weaker than the grain boundaries and dislocation generation and propagation within the grain interiors become the primary source of plastic deformation. In this case Eq. 5 reduces to $\dot{\varepsilon} \sim \dot{\varepsilon}_g$. Evidence has been provided for materials of the type considered in this work that over the entire range of relevant strain rates, both modes of deformation may contribute to flow, with gbs persisting well into the apparent Stage III regime and conversely mdg being evident even at low strain rates in Stage II deformation, at least within some of the grains[51]. Dislocation activity in the grain

interiors of the present material must have been obviously sufficiently high, both at high and low strain rates at 1050°c, to provide the driving force for recrystallization, as observed .

In the material examined, the transition from Stage II to Stage III deformation was shifted to higher strain rates as the grain size was refined, Figure 25. This is again consistent with Eq. 5 since at a given stress level, more deformation by gbs may be expected in a material with a finer grain size[45-47]. Also, as deformation progressed, in a test at constant strain rate, the grain size was refined and the contribution from gbs was increased relative to that in the as-hipped fine grained material. As a result of this, the material flow softened until steady state conditions were achieved. Because of the fine grain sizes present under these conditions, typically from 1 to 5µm, (Figure 22), the dominant mode of deformation must be grain boundary sliding and therefore Eq. 5 reduces to $\varepsilon = \varepsilon_{gbs}$ for steady state conditions.

5.1 Phenomenology of Deformation in P/M Superalloys at Forging Temperatures and Strain Rates

From the evidence provided, the flow curve at constant strain rate and temperature, under typical isothermal forging conditions, can be decomposed into two regions that differ in the way the flow strength and microstructure evolve during plastic flow. As shown schematically in Figure 27, a transient flow regime (hardening or softening as demonstrated earlier) preceeds the onset of a steady state regime during which neither flow strength nor grain size continue to change with further straining. Evidence has been provided which indicates that flow stresses and grain sizes under steady state conditions are independent of the starting grain size. Both quantities, however, vary with the test strain rate at constant temperature. By contrast, transient flow depends both on strain rate <u>and</u> the microstructure in ways which can be rationalized however.

5.1.1 Transient Flow

It will be generally recognized that flow strength in superplastic alloys depends only on strain rate and grain size at constant temperature[45]. Under such conditions, the total derivative of the logarithm of the stress can be written as:

$$d \ln \sigma = (\frac{\delta \ln \sigma}{\delta \ln \dot{\varepsilon}})_{T,\lambda} \, d \ln \dot{\varepsilon} + (\frac{\delta \ln \sigma}{\delta \ln \lambda})_{T,\dot{\varepsilon}} \, d \ln \lambda \qquad (6)$$

or

$$d \ln \sigma = m \, d \ln \dot{\varepsilon} + p \, d \ln \lambda \qquad (7)$$

where σ is the stress, $\dot{\varepsilon}$ is the strain rate, λ is the average grain size and m and p are the strain rate sensitivity and grain size sensitivity exponents (from Eqs. 2 and 4) at constant structure and constant strain rate, respectively. During tests at constant strain rates, this reduces to

$$d \ln \sigma = p \, d \ln \lambda \qquad (8)$$

and since p is positive over the entire range of strain rates examined, (c.f Figure 26) the direction and rate of change in flow strength are predicted to be directly proportional to the direction and rate of change in grain size, i.e. $d\sigma/dt \propto d\lambda/dt$.

Meanwhile, the direction of change in grain size during transient flow is governed by the size of the initial grains, λ_i, relative to the size of the grains at steady state, λ_{ss}, which in turn is governed by the applied strain rate. With $\lambda_i > \lambda_{ss}$, $d\lambda/dt < 0$ and the flow stress decreases during flow, Figure 28. By contrast when $\lambda_i < \lambda_{ss}$, $d\lambda/dt > 0$ and the flow stress rises instead during deformation. Thus, depending on the sign of the initial to final grain size ratio, the fine grained compact will either soften or harden during transient flow. Where $\lambda_i \sim \lambda_{ss}$, the compact is at steady state from the onset of plastic yielding as shown in the middle schematic of Figure 28.

5.1.2 Steady State Flow

The possibility that a steady state regime of flow may prevail under superplastic conditions at high strains is perhaps not widely recognized in the superplastic literature. Its existence has been suggested, however[52], and strong evidence for its occurence in the present material has been provided. Neither the steady state regime nor the inverse correlation between steady state flow strength and steady state grain size, Figure 23 and Eq. 1, are entirely unexpected. A parallel can be drawn with the steady state regime known to prevail at high strains in metals and alloys under hot working conditions, where the inverse correlations between the size of dynamically recovered subgrains or dynamically recrystallized grains and steady state flow strength are well established[19,53]. However, while in the latter two cases, steady state is generally attributed to a balance between mechanisms of dislocation generation and restoration[19,48], steady state flow in the material under investigation has been attributed to a balance between grain coarsening and grain refinement[23,25]. During steady state, some grains may be expected to grow beyond the average equilibrium steady state grain size. With continued straining, the contribution from slip within those larger grains will become more prominent. This will raise in turn local driving forces for recrystallization and eventually lead to recrystallization of those deformed grains. The new recrystallized grains will then be fine enough to deform by gbs until they grow again to the point where they will recrystallize for reasons given earlier. Although somewhat hypothetical, steady state in this superplastic material may be regarded as a condition during which superplastic properties are simultaneously lost through growth and regenerated through refinement of the average microduplex grain size[25].

The phenomenology discussed so far is fully consistent with observations made at high strains concerning apparent strain rate sensitivities under steady state conditions. Peak flow strength for the fine grained compact and for the coarse grained compact obtained by consolidation above the γ' solvus are compared in Figure 27 with the corresponding steady state data. It may be seen that the apparent strain rate sensitivity

$$m_a = \frac{d \ln \sigma}{d \ln \dot{\varepsilon}} \qquad (9)$$

is much lower under steady state conditions than for the original as-hipped fine grained compact, both at low and high strain rates. This may be fully accounted for on the basis of the difference in grain size existing under steady state conditions in specimens deformed at different strain rates.

If the flow stress is only a function of strain rate and grain size at constant temperature, as assumed, then it may be shown from the rules of partial differentiation that the apparent strain rate sensitivity m_a is given by

$$m_a = m + p \frac{d \ln \lambda}{d \ln \dot{\varepsilon}} \qquad (10)$$

where m is the true strain rate sensitivity at constant structure, $(\delta \ln \sigma / \delta \ln \dot{\epsilon})_{\lambda,T}$, p is the grain size sensitivity exponent from Eq. 3, $(\delta \ln \sigma / \delta \ln \lambda)_{\dot{\epsilon},T}$ and the last term to the right of Eq. 10 accounts for the effects of strain rate on steady state grain size. Both the latter quantity and the grain size sensitivity exponent p were determined experimentally. From Figure 22, d ln λ/d ln $\dot{\epsilon} \sim -0.1$ and from Figure 26 or Eq. 3, p $\sim$ 2. Assuming that changes in grain size only start at strains corresponding to peak strength, that is to say, that peak strength values correspond to the flow stress of the material at constant grain size (the fine initial grain size in this case) then it can easily be shown that at steady state one should obtain for Stage II deformation at low strain rates, $m_a = 0.5 + 2 (-0.1) = 0.3$ which is as observed experimentally. The low apparent strain rate sensitivity at steady state and high strain rates ($m_a \sim 0$) may be due partly to increasing adiabatic heating effects with increasing strain rate which makes the interpretation more delicate in this case. The good correlation obtained otherwise between measured and predicted values lends support to the proposed deformation phenomenology.

5.1.3 Deformation Mechanism Map

On the basis of the deformation phenomenology discussed above, it is possible to develop a deformation mechanism map for isothermal conditions by plotting together the steady state data from Figure 23 with data on the grain size dependence of flow stress from Figure 26. This is shown in Figure 29. In this schematic, the steady state data line AB separates the stress-grain size field of the map into two regions within which different mechanisms operate. Below line AB, grain boundary sliding is the dominant mode of deformation, and the material is fully superplastic. Above line AB, the conditions of flow are only partially superplastic with the contribution from gbs relative to that from mdg decreasing, when both the strain rate and grain size are increased. This region corresponds to the transition region of Figure 25 discussed earlier. The deformation mechanism map predicts that the compact will harden during flow for a given grain size (broken line, Figure 29) if the strain rate is such that a coarser grain size is produced at steady state, Case 1, Figure 29. Conversely softening during transient flow is predicted for the same initial microstructure when the strain rate used is such that a finer grain size is produced at steady state. This would be expected to occur for all strain rates greater than $\dot{\epsilon}_2$, as in Case 2, Figure 29.

Presentation of flow stress data in the form of Figure 29 is useful because it provides the grain size and strain rate dependence of flow strength independently together with information on the direction of changes in grain size and flow strength during flow as a function of current values of grain size and strain rate. A variant for presenting the data which may perhaps appear more familiar is shown in Figure 30. Here, offset yield stresses are plotted against strain rates (solid lines) for different initial grain sizes, including the data for solution treated coarse grained compacts (50 μm grain size), in combination with steady state data (broken line). In this diagram, the intersection of the broken line with any of the full lines gives the value of the steady state grain size and steady state stress at the corresponding strain rate[13]. The diagram also allows one to predict the direction of change of stress and grain size during plastic flow at 1050°C as a function of applied strain rate. For instance, when the initial grain size is 1.5 μm and the strain rate is 1.4×10^{-3} s^{-1}, the compact flow hardens as the grain size grows until steady state conditions are reached. The flow stress and grain size then remain stable at $\sim$ 27 MPa and 2.5 μm respectively, case B Figure 30. By contrast, if the initial grain size is 6 μm, the compact flow softens as the grain size is refined, until steady state conditions are again established, case A Figure 30. As far as the solution treated coarse grained material is concerned, flow softening and grain refinement are predicted at all forging rates covered by the diagram, as observed experimentally.

While both diagrams (Figures 29 and 30) describe the magnitude of changes in flow strength and grain size neither of them indicate the rate at which these changes will occur. Experimental evidence suggests that this varies with grain size and testing conditions. For instance grain growth at 1050°C was found to be very slow and the rate at which the compact flow hardened remained slow accordingly. However the degree of hardening involved in this case was fully consistent with the proposed phenomenology[25].

5.2 Deformation Modelling

A methodology for modelling flow in fine grained compacts based on the deformation phenomenology of Figure 30 has already been proposed[15]. The approach which is detailed elsewhere relies on solving for the stress using Eq. 5 for any given state of microstructure. This is then coupled with magnitudes and rates of change in grain size to predict changes in flow strength and grain size as a function of the deformation history in an incremental fashion[15]. The required data on magnitude and rate of change of grain size are obtained from Figure 30 and from data of the type contained in Figure 20, respectively.

The methodology assumes that deformation follows a mechanical equation of state of the form $\sigma = f(\dot{\epsilon}, T, \lambda)$ where the stress is only a function of instantaneous values of strain rate, temperature and grain size. This is a reasonable assumption under superplastic conditions[45], and since the fine grained compacts are superplastic, it is applicable in this case. The methodology also implies that reliable materials data on magnitude and rate of change in grain size can be readily obtained as a function of instantaneous values of strain rate and grain size by the interrupted test techniques of the type introduced earlier. For fine grained compacts this is not an unreasonable requirement either, since under superplastic conditions, flow remains homogeneous and changes in grain size are small and occur uniformly throughout the test piece during compression. For coarse grained compacts however, flow is not superplastic, at least initially, and the microstructure evolves non uniformly by the heterogeneous nucleation and growth of a fine grained necklace structure in the manner described earlier. Therefore, the methodology developed for fine grained compacts is not directly applicable in this case.

To model the deformation behaviour in coarse grained compacts, it is necessary to develop a micro-structural model for necklace development and to identify a suitable stress function that can be used to relate stress to the variables of deformation $(\dot{\epsilon}, T)$ and to the microstructure at any stage of the transformation.

5.2.1 Microstructural Model

The microstructural evidence indicates that new grains first appear at original grain boundaries. More grains are then added in a layerwise fashion and the volume fraction transformed to the fine grained condition increases in the manner shown schematically in Figure 31. For modelling purposes, two assumptions are made concerning the nucleation and growth of this structure. Firstly, it is assumed that nucleation of the first layer is complete at the strain to peak strength. This strain is independent of strain rate and is of the order of 0.05 in the compacts. And secondly, it is assumed that the new grains, when fully developed, reach a size dictated by the applied strain rate which is given by the steady state data line of Figure 30. Thus, with continued straining, regions of soft superplastic material (small steady state grains of size d) develop whereby the continuity of the hard material (ie. the remainder of the original coarse grained microstructure) is broken, until in the end the soft material becomes continuous.

Because of these changes, the mechanisms of deformation will change with strain at constant applied strain rate. This is indicated in Figure 30 for 50 μm grain size material. Initially the deformation is primarily governed by
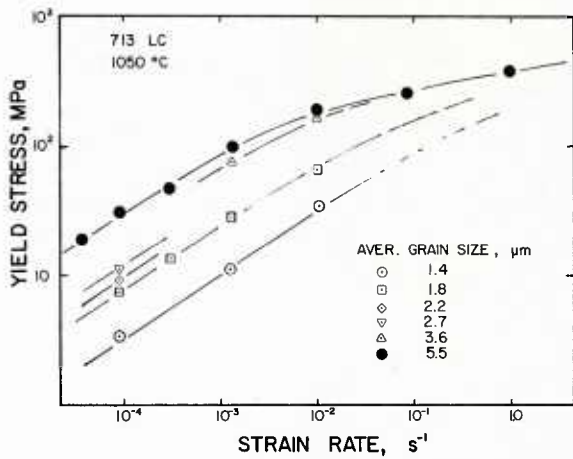
FIG 25 Effects of strain rate and average initial grain size on flow strength of fine grained 713 LC compacts at 1050°C.
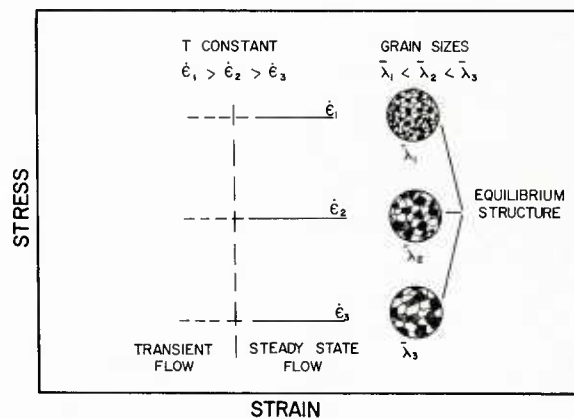

FIG 27 Schematic of the steady state portions of the flow curves and the corresponding average microduplex grains produced at three strain rates at constant temperature in P/M 713 LC compacts.
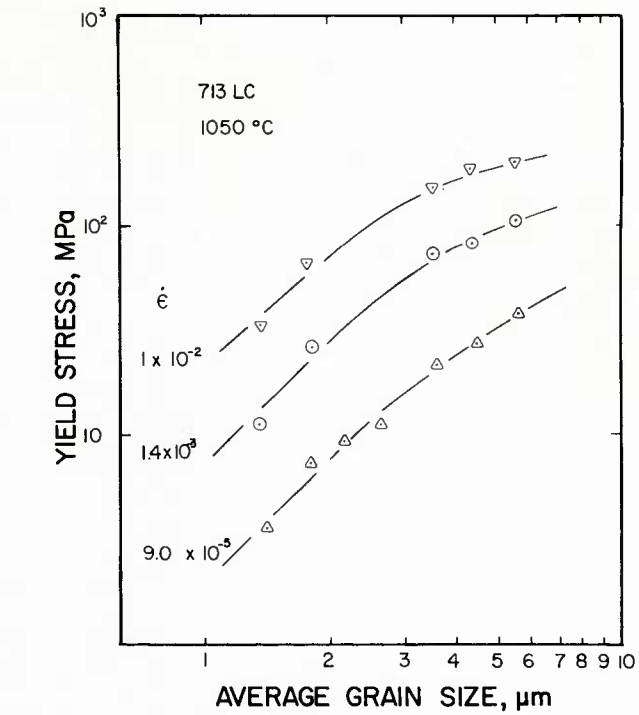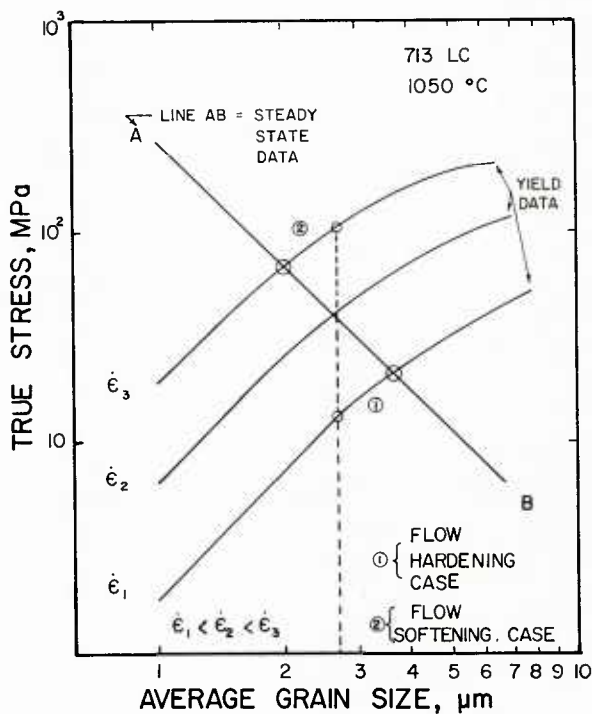
FIG 26 Effects of average microduplex grain size on the high temperature compressive yield strength of fine grained 713 LC compacts at 1050°C and three strain rates.
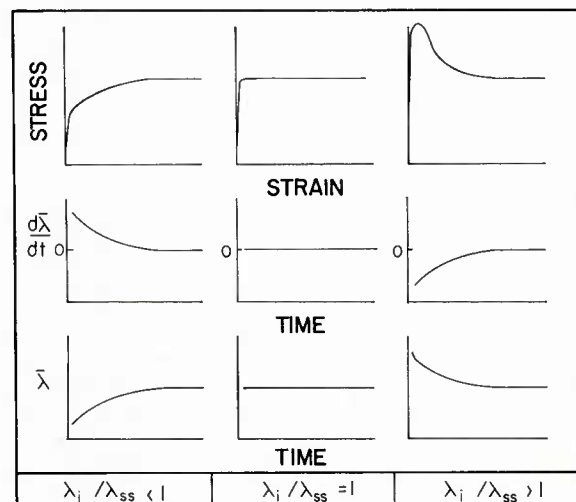

FIG 28 Effect of the ratio of initial grain size λ_i to the steady state grain size λ_{ss} on the shape of the flow curve in fine grained superplastic 713 LC compacts.

FIG 29 Constant temperature deformation mechanism map for fine grained superplastic 713LC compacts deformed below the γ' solvus.

mdg and Stage III conditions prevail. With continued straining, however, the deformation conditions fall below the Stage III/Stage II transition parting line and an increasing proportion of the material now deforms by gbs. When transformation is complete and the material is entirely fine grained, steady state conditions are maintained. At this point the flow stress and grain size are given by the steady state data line of Figure 30 at the appropriate strain rate.

To model the transition between peak and steady state stress, a stress function is required that can account for the heterogeneous distribution of hard and soft region within the material. The function must also be able to account for strain (time) dependent effects on the proportion of these hard and soft regions. As pointed out by other workers[54], the heterogeneity of microstructure can be accounted for by proper averaging of properties in the hard and soft regions. Several approaches to making these averages are possible. The two simplest assumptions are that the strain rate remains the same in each region, or alternatively that each region carries the same stress during deformation, Figure 32. The latter approach is more attractive since it is compatible with the occurence of micro and macroscopic flow localization, as observed experimentally in the coarse grained compacts. Mechanical equilibrium requires in this case that:

$$\dot{\epsilon} = F \, \dot{\epsilon}_{gbs} + (1 - F) \, \dot{\epsilon}_g \qquad (11)$$

where F is the volume fraction of material that deforms by gbs, $\dot{\epsilon}_{gbs}$ is the strain rate in the soft superplastic regions and $\dot{\epsilon}_g$ is the strain rate in the hard non superplastic regions. Initially F = 0 but during plastic flow, F progressively increases with increasing strain until steady state conditions are achieved at which time F = 1.

Koul and Immarigeon[20] have recently proposed that an Avrami type relation can be used to describe the fraction F transformed at any stage of deformation with

$$F = 1 - \exp(-ct^n) \qquad (12)$$

where c is a material parameter which depends on the nucleation and growth rate of new grains and n is a numerical constant which depends on the nucleation mechanism. These authors have argued that Cahn's formal treatment of rate theory for grain boundary transformation reactions[55] can be applied to describe the fraction transformed F right up to steady state conditions in a stepwise fashion. Several attempts have already been made to apply Cahn's treatment for describing dynamic recrystallization in steels under hot-working conditions[56,57]. A major difficulty in applying Cahn's treatment stems from the occurence of site saturation, a condition reached when the original grain boundaries become surrounded by a shell of transformed product and the transformation can only proceed therefrom by anisotropic growth of already formed grained. This predicts an elongated grain shape which is not observed in the present compacts. The necklace structure grows instead, by addition of equiaxed grains at the interface between the transformed and untransformed regions. This indicates that once the original grain boundaries are consumed, the conditions are set again for a new wave of recrystallization to occur at the periphery of the untransformed portion of the original grains. Therefore, it can be argued that Cahn's treatment can again be applied in a stepwise fashion using a reduced "effective" grain size equal to the size of the untransformed regions of the original grains. For the spherical model grain shown in Figure 33, the reduced effective grain size $\lambda(t)$ at any time during deformation is given by

$$\lambda(t) = \lambda - 2Nd \qquad (13)$$

where N is the number of steady state grain layers at time t, λ is the initial grain size and d is the steady state grain size. For analytical purposes, N is allowed to be a non integer.

Cahn's treatment[55] leads to two relations for describing the extent of transformation in the case of tranformation products nucleating at grain boundaries. In nucleation controlled reactions, the volume fraction transformed is given by:

$$F = 1 - \exp\left(-\frac{\pi}{3} \dot{N}_V \, G^3 \, t^4 \right) \qquad (14)$$

while for growth controlled reactions it is given by:

$$F = 1 - \exp\left(- 2 \, S \, Gt \right) \qquad (15)$$

where $\dot{N}_V$ is the grain boundary nucleation rate per unit volume of the assembly, G is the growth rate of new grains, and S is the grain boundary surface area per unit volume. Both relations were used as the basis for modelling necklace growth. The latter of the two was found more appropriate, as shown later.

The major difficulty with modelling necklace growth, resides in the assessment of the dynamic nucleation and growth rates of new grains during deformation. Both nucleation and growth rates may be expected to increase with strain rate, since their driving forces, i.e. dislocation densities, increase with strain rate at constant temperature[19]. These requirements were accommodated by relationships of the form

$$\dot{N}_V = \frac{36 \, K_1}{\lambda(t) \, d^2} \, \dot{\epsilon}_g^{5/2} \qquad (16)$$

and

$$G = K_2 \, \dot{\epsilon}_g^{1/2} \qquad (17)$$

for Eq. 14, as described in Appendix II, and by

$$G = K_3 \, \dot{\epsilon}_g \qquad (18)$$

for Eq. 15. Here K_1, K_2 and K_3 are material constants and $\dot{\epsilon}_g$ is the instantaneous local strain rate within the hard untransformed regions. The dependence of growth rate on strain rate is somewhat conjectural. There is no supporting experimental data for the choice of the strain rate exponent in Eqs. 16 or 17. In Eq. 16 the choice is based on other researchers findings[56,57] as described in Appendix II, while in Eq. 17 it is chosen to keep the exponent of Eq. 15 non dimensional.

Replacing the time t in Eqs. 14 and 15 by $(\epsilon_2 - \epsilon_1)/\dot{\epsilon}$, where ϵ_2 is the strain at time t, ϵ_1 is the strain at peak strength and $\dot{\epsilon}$ is the applied strain rate, gives:

$$F = 1 - \exp\left(-\frac{12 \, K_1 K_2^3}{\lambda(t) \, d^2} \, \dot{\epsilon}_g^4 \left[\frac{\epsilon_2 - \epsilon_1}{\dot{\epsilon}} \right]^4 \right) \qquad (19)$$
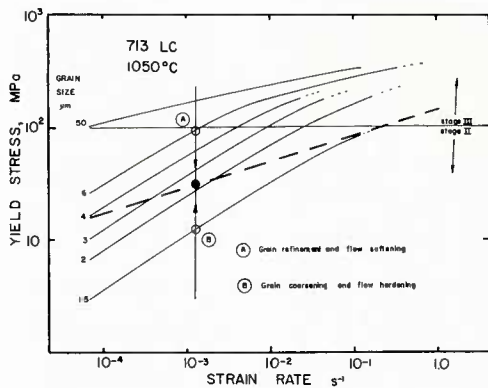
FIG 30 Effects of grain size on flow strength in 713 LC compacts. Solid lines are for offset yield stress data at constant grain size. Broken line represents steady state conditions as observed experimentally (see text for details).
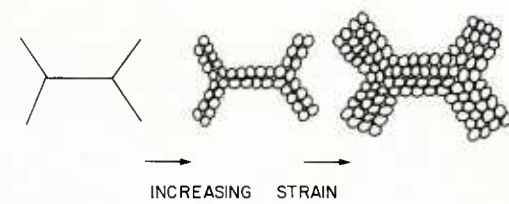
FIG 31 Schematic representation of the development of the necklace structure in coarse-grained compacts with increasing deformation.
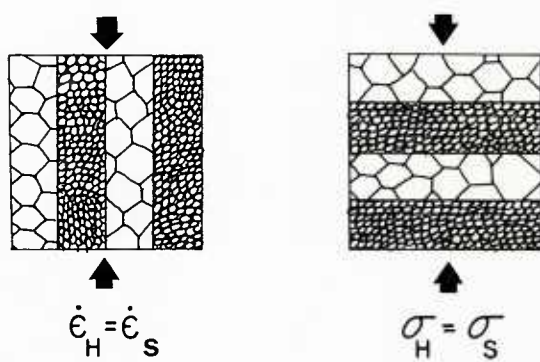

FIG 32 Schematic illustration for the orientation of hard and soft regions leading to a) iso-strain rate conditions ($\dot{\varepsilon}_H = \dot{\varepsilon}_s$) and b) iso-stress conditions ($\sigma_H = \sigma_s$) in each region.
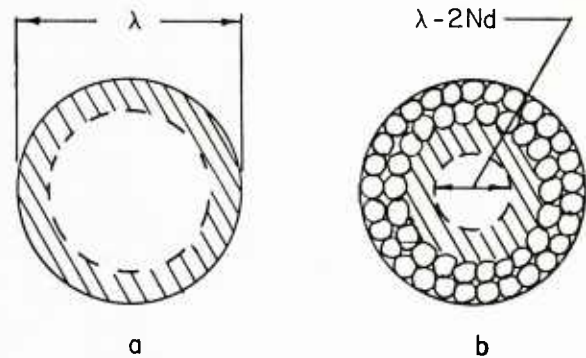
FIG 33 Single grain model with diameter λ showing layerwise addition of steady state grains of size d with increasing strain a) $\varepsilon = \varepsilon_1$ the strain at peak strength and b) $\varepsilon = \varepsilon_2$ for the strain at arbitrary time t_2.
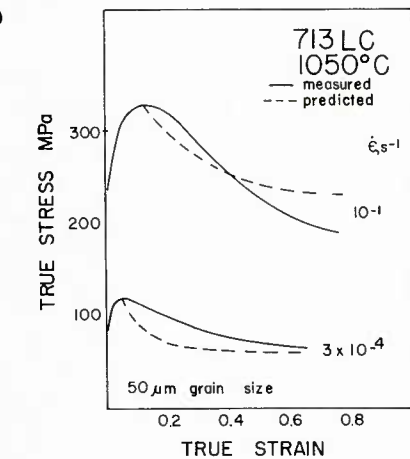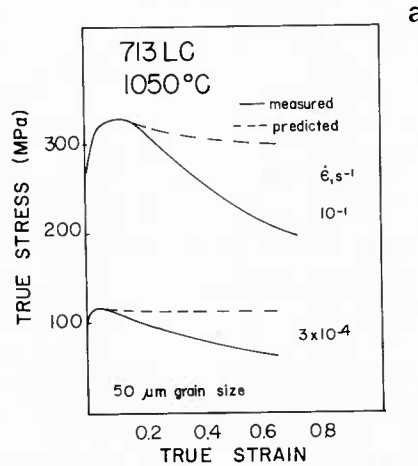

FIG 34 Comparision of simulated flow curves for 50 μm single grain model material with measured flow curves for 50 μm grain size compacts a) based on Eq. 1 9 b) based on Eq. 2 0. (see text for details).

for Eq. 14 and

$$F = 1 - \exp\left(-\frac{12 K_3}{\lambda(t)} \dot{\varepsilon}_g \frac{\varepsilon_2 - \varepsilon_1}{\dot{\varepsilon}}\right) \tag{20}$$

for Eq. 15.

5.3.2 Constitutive Relation

Substitution for $\dot{\varepsilon}_{gbs}$ and $\dot{\varepsilon}_g$ in Eq. 11 can be made using any of the well accepted models for grain boundary sliding and intragranular deformation. To this end a generalized equation of the form.

$$\varepsilon = \frac{AD\mu b}{kT} \left(\frac{b}{\lambda}\right)^P \left(\frac{\sigma - \sigma_0}{\mu}\right)^n \tag{21}$$

can be used with particular constants for each mechanism. Here A is a material constant, D is the active diffusion coefficient, μ is the shear modulus (temperature dependent) b is the Burger's vector, k is Boltzman constant, T is the temperature, λ is the grain size, σ is the stress and σ_0 is a back stress which arises as a consequence of interactions between moving dislocations and a range of microstructural features that oppose their motion[58,59]. Little information exists on the origin and magnitude of back stresses in powder processed alloys of the type considered here. For simplicity it is assumed that the primary source of back stress in the compacts under investigation is the fine intergranular γ' present in the grain interiors. An estimate of around 40 MPa was made for the coarse grained compacts based on measurements reported for a similar high γ' volume fraction cast alloy[58]. However, in the fine grained compact where most of the γ' is present as separate grains in the microduplex structure, the intragranular back stress contribution is comparatively small and can therefore be neglected[20].

Several theories have been developed for gbs under superplastic conditions when the grain size is very small. A critical review of these models has recently been published[60]. Several of the proposed theories predict very similar and eventually correct strain rates at a given applied stress in the region of optimum superplasticity i.e in Region II. With most theories, p = 2, n = 2 and Eq. 20 reduces to:

$$\dot{\varepsilon}_{gbs} = \frac{A_1 D_{gb} \mu b}{kT} \left(\frac{b}{\lambda}\right)^2 \left(\frac{\sigma}{\mu}\right)^2 \tag{22}$$

where D_{gb} is a coefficient for grain boundary diffusion.

Several other theories[61-64] have also been developed for intragranular flow in precipitation hardened alloys based on climb controlled mechanisms which lead to relations of the form of Eq. 21 with p = 0 and n = 4, often described as power law relationships:

$$\dot{\varepsilon}_g = \frac{A_2 D_v \mu b}{kT} \left(\frac{\sigma - \sigma_0}{\mu}\right)^4 \tag{23}$$

Here D_v is a coefficient for volume diffusion. It is shown elsewhere that reasonable fits to the data can be achieved with these two relations for compacts both in the fine grained and the coarse grained condition[20]. Combining Eqs. 22 and 23 in Eq. 11 with either of Eqs. 19 and 20, for instance with Eq. 20, gives the constitutive relation for flow in coarse grained compacts:

$$\left\{ \begin{array}{l} \dot{\varepsilon} = F \dfrac{A_1 D_{gb} \mu b}{\lambda\, kT} \left(\dfrac{b}{\lambda}\right)^2 \left(\dfrac{\sigma}{\mu}\right)^2 + (1 - F) \dfrac{A_2 D_v \mu b}{kT} \left(\dfrac{\sigma - \sigma_0}{\mu}\right)^4 \tag{24} \\[2mm] F = 1 - \exp \dfrac{-12 k_3}{\lambda(t)} \dot{\varepsilon}_g \dfrac{\varepsilon_2 - \varepsilon_1}{\dot{\varepsilon}} \tag{25} \end{array} \right.$$

The first of the two relations reduces to a 4th order polynomial in stress which can be solved for any given value of F i.e. at any stage of transformation. The calculated stress can then be used to determine from Eq. 23 the effective strain rate in the untransformed regions, $\dot{\varepsilon}_g$, which governs the rate at which the transformation progresses (c.f Eq. 25). As a first approximation σ_0 is assumed to remain constant in this calculation. The measured ε_g is then used in Eq. 25 to determine changes in F with time and the procedure repeated to determine changes in flow strength and microstructure through an iterative procedure. The condition $\lambda(t) = d$ (c.f Eq. 13) provides the criterion for the onset of steady state which signals that transformation is complete.

As the transformation progresses and the effective strain rate within the untransformed regions, $\dot{\varepsilon}_g$ decreases, an increase in the size of new steady state grains can be expected. This can be either neglected, on the grounds that the changes will be small over the range of likely rates or it can be taken into consideration as part of the iterative procedures[20]. In this case the constitutive relations, Eqs. 24 and 25, are modified to read[20]:

$$\dot{\varepsilon} = \Sigma \frac{F_i}{d_i^2} \frac{A_1 D_{gb} \mu b^3}{kT} \left(\frac{\sigma}{\mu}\right)^2 + (1 - \Sigma F_i) \frac{A_2 D_v \mu b}{kT} \left(\frac{\sigma - \sigma_0}{\mu}\right)^4 \tag{26}$$

$$F = \Sigma F_i = \Sigma \left[1 - \exp\left(-\frac{12 k_3}{\lambda - 2 \Sigma N_i d_i} \dot{\varepsilon}_{gi} \left(\frac{\varepsilon_{i+1} - \varepsilon_i}{\dot{\varepsilon}}\right)\right)\right] \tag{27}$$

where i = 1, 2, 3, ..., n are the iteration steps. Necklace development is followed in terms of N_i the number of steady state grains added. This is determined by substituting in an equation of the form $N_i = \lambda(t)_i F/2d_i$. Finally, changes in average grain size can be monitored if required by an equation of the form $\lambda_i = \lambda/2(\Sigma N_i) + 1$ where N_i is the number of steady state grain layers of diameter d_i formed during the iteration.

To assess the validity of the proposed model, and assumptions made, flow curves were simulated for a single grain of the model material with a diameter of 50 μm using the iterative procedure (Eq. 26 and 27) for strain increments of 0.1. Simulations were also performed assuming that growth of the necklace structure is controlled by the nucleation rather than the growth of new grains i.e. by using Eq. 14 rather than Eq. 15 as the basis for modelling the fraction F transformed.

Predicted flow curves are compared in Figure 34 with the experimentally determined flow curves that were obtained by compression testing at high and low strain rates in the range of interest to isothermal forging. Since the development of the necklace structure is not uniformly distributed within the test piece, with a number of regions remaining totally untransformed, Figure 11, the "true" flow curve of the material, representative of a uniformly distributed transformation, can be expected to be lower than the measured flow curves. For this reason it is concluded that necklace development is growth rather than nucleation controlled, since only when the development of the necklace structure is assumed to be growth controlled, do the predicted flow curves fall below the measured curves. Thus, the use of Eq. 15 appears more physically realistic for modelling necklace growth, providing the anomaly of a crossover at higher strain rates is ignored. This crossover is linked to flow localization and gross plastic instability in the test piece at the fastest strain rate. It is interesting to note that a solution of the form $F = 1 - \exp(-C/\lambda\, t^{1.3})$ where C is a constant and λ is the grain size has been shown to describe reasonably well the progress of dynamic recrystallization in steels[57]. This relation is similar to that of Eq. 20 of this work and is derived from Eq. 15 by allowing for a continuous change in the specific active grain boundary area for nucleation of new grains[57].

In principle, the methodology proposed herein for modelling plastic flow in coarse grained compacts can be used in conjunction with the finite element method to follow transformation among elements of a finite element mesh under conditions where the strain rate and the microstructure do not remain constant but vary instead from element to element as a result of strain and strain rate gradients[20]. It is beyond the scope of this work to demonstrate this. However, it must be emphasized that in the end, the ability to predict accurately the microstructure produced in billets deformed under well controlled conditions of temperature, strain rate and lubrication will provide the critical assessment for the validity of the proposed model and assumptions made.

6.0 CONCLUSIONS

Carefully controlled compression tests have been used to assess the effects of microstructure on flow strength in P/M superalloy compacts. This has shown that grain size has a strong influence on the flow behaviour of these materials. Based on observations of the interdependence between evolving microstructure and flow strength, a phenomenological model for plastic flow has been introduced and a methodology for modelling deformation at isothermal forging temperatures and strain rates in this class of alloys has been developed. In this regard a constitutive relation that allows the prediction of flow strength and changes in microstructure during flow has been developed. It has also been suggested that the constitutive relation could be used in conjunction with the finite element method to predict microstructures in forgings for optimization of properties in forged turbine discs.

REFERENCES

1. T. Altan, G.D. Laboti and V. Nagpal, Application of Process Modelling in Massive Forming Processes, in Process Modelling, Fundamentals and Applications to Metals, Eds. T. Altan, H. Burte, H. Gegel and A. Male, Pub. ASM, Metals Park, Ohio, Materials/Metalworking Technology Series, 1983, pp. 77-99.

2. G.H. Gessinger, Die Anwending der Sluperplastizitat in der Umformtechnik, Tadex-Rundschau, 1977, p. 124.

3. J.W.H. Price and J.M. Alexander, A Study of the Isothermal Forming or Creep Forming of a Titanium Alloy, Proc. 4th North American Metalworking Research Conference, 1976, p. 46.

4. J.G. Malas, H.L. Gegel, S.I. Oh and G.D. Lahoti, Metallurgical Validation of a Finite-Element Programme for the Modelling of Isothermal Forging Processes, in Proc. Symp. on Experimental Verification of Process Models, Eds. C.C. Chen, Pub. ASM, Metals Park, Ohio, (1983), pp. 358-372.

5. S. Kobayashi, Thermoviscoplastic Analysis of Metal Forming Problems by the Finite Element Method, in Numerical Methods in Industrial Forming Processes, Eds. J.F.T. Pittman, R.D. Wood, J.M. Alexander and O.C. Zienkiewicz, Pub. Pineridge Press, Swansea, U.K. (1982), pp. 17-25.

6. C.R. Boer, P. Gudmundson and N. Rebelo, Comparison of Elasto-Plastic FEM, Rigid-Plastic FEM and Experiments for Cylinder Upsetting, in Ref. 5, pp. 217-226.

7. S.I. Oh, J.J. Park, S. Kobayashi and T. Altan, Application of FEM Modelling to Simulate Metal Flow in Forging a Titanium Alloy Disc, Jour. of Engineering for Industry, Vol. 105, 1983, pp. 251-258.

8. J-P. Immarigeon, The Superalloys, Materials for Gas Turbine Hot Section Components, Canadian Aeronautics and Space Journal, Vol. 27, No. 4, December 1981, pp. 336-350.

9. H.M. Burte and H.L. Gegel, The Role of Process Modelling in the Future of Materials Science and Technology, in Ref. 1, pp. 1-26.

10. J-P. Immarigeon and W. Wallace, Trends in Superalloy Powder Processing, MPR, Vol. 38, No. 10, October 1983, pp. 537.

11. G.H. Gessinger, Recent Development in Powder Metallurgy of Superalloys, Keynote Paper, International Conf. on Powder Metallurgy Superalloys, Zurich, 1980.

12. D.M. Carlson, P/M AF115 Dual Property Disc Process Development, Proc. 4th Int. Conf. on Superalloys, Pub., ASM, Metals Park, 1980, pp. 501-512.

13. J-P. Immarigeon, D. Morphy and A.K. Koul, Selective Thermomechanical Treatments for Dual-Property Superalloy Disc Forgings, Proc. Seminar on P/M Superalloys, Coord. S. Reichman and J.K. Tien, International Powder Metallurgy Conf., Toronto, 1984, pp. 97-119.

14. J-P. Immarigeon, Discussion Summary, Fundamental Aspects of Net Shape Processing, AGARD Conf. Proc., NO. 256 on Advanced Fabrication Processes, Florence, 1978, D3-4.

15. R.L. Hewitt, J-P. Immarigeon, and P.H. Floyd, Determination and Presentation of Flow Stress Data for Use in Isothermal Forming Analyses, Proc. 8th North American Manufacturing Research Conference, Society of Manufacturing Engineers, Dearborn, MI, 1980, pp. 129-134.

16. S.L. Semiatin and J.J. Jonas, Formability and Workability of Metals: Plastic Instability and Flow Localization, ASM Monograph, in press.

17. A.S. Argon, Preface in Constitutive Relations in Plasticity, Ed. Argon, Pub. The MIT Press, Cambridge, Mass., 1975.

18. E.W. Hart and J.F. Thomas, Material Constitutive Relations in the Modelling of Mechanical Processing, in Ref. 1, pp. 355-363.

19. H.J. McQueen and J.J. Jonas, Recovery and Recrystallization During High Temperature Deformation in Treatise on Materials Science and Technology, Vol. 6, Plastic Deformation of Materials, Ed. R.J. Arsenault, Pub. Academic Press, N.Y., 1975, pp. 393-493.

20. A.K. Koul and J.P. Immarigeon, Modelling of Plastic Flow in Coarse Grained Nickel-Base Superalloy Compacts Under Isothermal Forging Conditions, to be published.

21. W. Wallace, J-P. Immarigeon, J.M. Trenouth and B.D. Powell, Control of Grain Structure During Superalloy Powder Processing, AGARD Conference Proceedings No. 200, on Advanced Fabrication Techniques in Powder Metallurgy and Their Economic Implications, April 1976, Paper No. 9, pp. 1-13, Also published as NRC, NAE, LTR-ST-812, November 1975.

22. J-P. Immarigeon, W. Wallace and G. Van Drunen, The Hot Working Behaviour of Mar-M200 Superalloy Compacts, Proc. 3rd International Symposium, on Superalloys - Metallurgy and Manufacture, Claitor's Publishing Division, Baton Rouge, 1976, pp. 463-472. Also published as NRC, DME/NAE Quarterly Bulletin, 1, 1977, pp. 1-12.

23. A.Y. Kandeil, J-P. Immarigeon, W. Wallace and M.C. de Malherbe, Flow and Fracture Behaviour of Mar-M200 Powder Compacts During Isothermal Forging, Metal Science, Vol. 14, No. 10, 1980, pp. 493-499.

24. A.Y. Kandeil, J-P Immarigeon, W. Wallace and M.C. de Malherbe, Thermomechanical Processing of a Nickel-Base Superalloy Compact, High Temperature Technology, Vol. 1, No. 4, pp. 201-207, 1983.

25. J-P. Immarigeon and P.H. Floyd, Microstructural Instabilities During Superplastic Forging of a Nickel-Base Superalloy Compact, Met. Trans., Vol. 12A, 1981, pp. 1177-1186.

26. G.H. Gessinger and R.F. Singer, Superalloys-Principles and Applications, Riso International Symp. on Metallurgy and Material Science IV/Deformation of Multiphase and Particle Containing Materials, September 1983, pp. 15-26.

27. W. Wallace, H.B. Dunthorne, and R.A. Sprague, Microstructures and Mechanical Properties in a Turbine Disc Fabricated from Astroloy Powder, Can. Met. Quart., Vol. 13, (3), 1974, pp. 517-527.

28. R.T. Holt and W. Wallace, Impurities and Trace Elements in Nickel-Base Superalloys, International Metals Reviews, No. 203, March 1976, Also published as NRC, NAE, LTR-ST-760, March 1975.

29. R. Thamburaj, W. Wallace, Y.N. Chari and T.I. Prakash, Microstructures and Mechanical Properties of Alloy APK 1, Powder Metallurgy, Vol. 27, No. 2, 1984.

30. R. Thamburaj, A.K. Koul, W. Wallace and M.C. de Malherbe, Prior Particle Boundary Precipitation in P/M Superalloys, Proc. PM 84, Int. Conf. and Exhibition, Toronto, June 1984.

31. J.B. Moore and R.L. Athey, US Patent No. 3,519,504, 1970.

32. R.L. Hewitt, J-P. Immarigeon, W. Wallace, A.Y. Kandeil and M.C. de Malherbe, Isothermal Forging at the National Aeronautical Establishment, DME/NAE Quarterly Bulletin No. 1978(4), National Research Council, Ottawa, Canada, 1978.

33. A.Kasak, U. St. Clair and V. R. Thompson, US Patent No. 3,698,962, 1972.

34. S.H. Reichman, and J.W. Smyth, Superplasticity in P/M IN-100 Alloy, Int. Jour. Powder Metllurgy, Vol. 6, No. 1, 1970, pp. 65-75.

35. L.N. Moskovitz, R.M. Pelloux and N.J. Grant, Properties of IN-100 Processed by Powder Metallurgy, Proc. 2nd Int. Conf. on Superalloys - Processing, Metals and Ceramic Info. Centre, MCIP Rep. 72-10, 1972, pp. Z-1 to Z-25.

36. J.M. Larson, F.A. Thompson and R.C. Gibson, T/P Processing, An Advanced P/M Superalloy Technique in Ref. 22, pp. 483-493.

37. W. Wallace, R.T. Holt and E.P. Whelan, Properties of 713LC Compacts Hot Isostatically Pressed at Super-Solidus Temperatures, J. Testing and Evaluation, 3(2), 1975, pp. 113-120.

38. W. Wallace and T. Terada, Unpublished results, NAE, Ottawa, 1974.

39. R.T. Holt, The Extrusion of 713LC Powder Below the γ' Solvus, NRC, NAE, LTR-ST-1146, Ottawa, Canada, February 1980.

40. H.J. McQueen and J.J. Jonas, Hot Workability Testing Techniques, in Metal Forming: Interrelation Between Theory and Practice, Ed. A.L. Hoffmanner, Plenum Publishing Corp., 1971, pp. 393-428.

41. J-P. Immarigeon, A.Y. Kandeil, W. Wallace and M.C. de Malherbe, A Hot Compression Testing Apparatus for the Study of Isothermal Forging, J. Testing and Evaluation, Vol. 8, No. 6, November 1980, pp. 273-281.

42. J.J. Jonas and M.J. Luton, Flow Softening at Elevated Temperatures, in Advances in Deformation Processing, Ed. J.J. Burke and V. Weiss, Plenum Press, New York, 1978, pp. 215-243.

43. P. Dadras and J.F. Thomas, Characterization and Modelling for Forging Deformation of Ti 6242, Metallurgical Transactions, Vol. 12A, November 1981, pp. 1867-1876.

44. ASTM Standard Methods for Determining Average Grain Size, Designation E112-82.

45. T.H. Alden, Review Topics in Superplasticity in Ref. 19, pp. 225-266.

46. J.W. Edington, K.N. Melton and C.P. Cutler, Superplasticity, Progress in Material Sciences, Vol. 21, 1976, pp. 61-158.

47. T.G. Langdon, Experimental Observations in Superplasticity in Proc. Symp. on Superplastic Forming of Structural Alloys, Ed. N.E. Paton and C.H. Hamilton, TMS AIME, 1982, pp. 27-40.

48. H.J. McQueen and B. Baudelet, Comparison and Contrast of Mechanisms, Microstructures, Ductilities in Superplasticity and Dynamic Recovery and Recrystallization, Proc. 5th ICSMA, Aachen, August 1979, ed. Haasen et al., Pergamon Press, 1979, pp. 329-336.

49. R.C. Gifkins, Transitions in Creep Behaviour, TMS/568, Chapman and Hall Limited, 1970.

50. H.J. Frost and M.F. Ashby, Deformation Mechanism Maps, Pergamon Press, 1982, p. 3.

51. R.G. Menzies, G.J. Davies and J.W. Edington, Microstructural Changes during Superplastic Deformation of Powder Consolidated Nickel-Base Superalloy IN-100 Metal Science, Vol. 16, pp. 483-494 (see also pp. 356-362), 1982.

52. C. Hammond, Superplasticity in Titanium Alloys, in Ref. 47, pp. 131-145.

53. C.M. Sellars, Recrystallization of Metals during Hot Deformation, in Creep of Engineering Materials and of the Earth, Phil. Trans. Roy. Soc. London, Vol. 288, 1978, pp. 147-158.

54. W.D. Nix, J.C. Gibeling and K.P. Fuchs, The Role of Long Range Internal Back Stresses in Creep of Metals in Mechanical Testing for Deformation Model Developments, Ed. Rohde and Swearengen, ASTM STP 765, 1982, pp. 301-321.

55. J.W. Cahn, The Kinetics of Grain Boundary Nucleated Reactions, Acta Metall., Vol. 4, 1956, pp. 449-459.

56. W. Roberts and B. Ahlblom, A Nucleation Criterion for Dynamic Recrystallization During Hot Working, Acta. Met., Vol. 26, 1978, pp. 801-813.

57. W. Roberts, H. Boden and B. Ahlblom, Dynamic Recrystallization Kinetics, Metal Science, March-April 1979, pp. 195-205.

58. R.A. Stevens and P.E.J. Flewitt, The Dependence of Creep Rate on Microstructure in a γ' Strengthened Super-alloy, Acta Metall., Vol. 29, pp. 867-882, 1981.

59. R.R. Jensen and J.K. Tien, Creep and High Temperature Deformation of Simple Metals and Superalloys in Metallurgical Treatises, Ed. J.K. Tien and J.F. Elliott, TMS, AIME, 1981, pp. 529-550.

60. R.C. Gifkins and T.G. Langdon, Comments on Theories of Structural Superplasticity, Mater. Sci. Eng., Vol. 36, 1978, pp. 27-33.

61. R. Lagneborg and B. Bergman, The Stress/Creep Rate Behaviour of Precipitation-Hardened Alloys, Met. Sci., January 1976, pp. 20-28.

62. S. Puroshothaman and J.K. Tien, Role of Back Stress in the Creep Behaviour of Particle Strengthened Alloys, Acta. Metall., Vol. 26, 1978, pp. 519-528.

63. J-P. Dennison, P.D. Holmes and B. Wilshire, The Creep and Fracture Behaviour of the Cast Nickel-Based Superalloy IN100, Mat. Sci. Eng., Vol. 33, 1978, pp. 35-47.

64. H. Burt, J-P. Dennison and B. Wilshire, Friction Stress Measurements during Creep of Nimonic 105, Met. Sci., May 1979, pp. 295-300.

ACKNOWLEDGEMENTS

APPENDIX I

The major difficulty with the compression test in terms of preserving homogeneity of flow is the occurence of friction at the die/specimen interfaces. Friction was minimized in this study by using molten glass lubricants (sodium/calcium borosilicate frits with varying amounts of magnesia and alumina, molten at the test temperature) and by using dies with highly polished hard faces. To further improve lubrication, annular grooves were machined in the end faces of the specimen. The grooves entrapped the lubricant which was then squeezed during compression between the specimen and the dies under the large hydrostatic pressure generated within the entrapped liquid. This helped maintain proper lubrication throughout a test and it was found that breakdown in lubrication only occurred at high strains, typically greater than one.

The geometry of the compression test piece used for this study is shown in Figure AI-1. The specimens were right circular cylinders with a height to diameter ratio of ~1.5. Dimensions of the lubricating grooves are also indicated. The efficiency of the grooves/lubricant combination can be appreciated by comparing the end faces of compressed specimens with the end face of an undeformed test piece, Figure AI-2. The grooves remained concentric and uniformly separated with increasig strain and there was no evidence of cylindrical surface foldover even after a true strain of 0.7. This, coupled with the relative absence of barreling, and the absence of macroscopic shear flow localization within the bulk of the specimen, as evidenced by the diametral section shown in Figure AI-3, indicates

that flow remained nearly homogeneous within most of the volume of the specimen during compression. Some degree of inhomogeneity was evident near the end faces as indicated by the splayed edges. This was probably the result of the high pressure built up within the glass lubricant trapped in the outer groove. Under those well lubricated conditions, it can be argued[1] that deviations from ideal deformation are likely to occur only near the end faces and that the stress therefore remains uniform uniaxial compression within most of the volume of the specimen.

The efficiency of lubrication in the tests was further evaluated by comparing the flow curves obtained under identical testing conditions for specimens with different height to diameter ratios (constant diameter). As the height of the specimen is decreased relative to its diameter, frictional end effects may be expected to become more prominent. If lubrication is poor and end effects are severe, one may then expect substantial increases in the observed flow strength[2]. Under the present conditions, however, there was little variation in flow strength with a change in d/h from 0.4 to 2.0 as shown in Figure AI-4. Furthermore, the marginal increases in flow strength for identical strain levels were not more pronounced at high strains, as shown in Figure AI-5. Thus, end effects were indeed minimal in the present test and remained so even at high strains.

It is assumed that the flow strength in a specimen of infinite height (obtained by extrapolation to d/h = 0 in Figure AI-5) represents the flow strength under frictionless conditions (2), it is possible to obtain an estimate of the coefficient of friction, using the data from Figure AI-5 and the expression for the average axial stress in a cylinder loaded in compression under Coulomb friction (3). When this is done, one obtains a coefficient of friction $\mu \sim 0.04$. Therefore, assuming that μ remained constant up to a strain of one, the frictional contribution to the measured flow stress at that strain was less than 4%.

The true stress in the context of this work is defined as the measured load L divided by the <u>instantaneous</u> cross sectional area of the test piece A:

$$\sigma = \frac{L}{A} \tag{A-1}$$

The instantaneous area of the test piece is calculated assuming constancy of volume from the instantaneous height of the test piece h using the relation

$$A = \frac{A_0 \, h_0}{h} \tag{A-2}$$

where A_0 and h_0 are the initial cross sectional area and initial height of the cylindrical test piece, respectively.

The true incremental strain is defined as

$$d\epsilon = \frac{dh}{h} \tag{A-3}$$

so that the true strain is given by

$$\epsilon = \ln \frac{h}{h_0} \tag{A-4}$$

or

$$|\epsilon| = \ln \frac{h_0}{h} \tag{A-5}$$

to account for the negative sign of compressive strains.

From these definitions, constancy of strain rate throughout a test requires that

$$\frac{d\epsilon}{dt} = \frac{dh}{h} \frac{1}{dt} = \dot{\epsilon} = \text{constant} \tag{A-6}$$

or

$$v = \dot{\epsilon} h \tag{A-7}$$

where v is the hydraulic ram velocity at a strain rate $\dot{\epsilon}$. Thus, constancy of strain rate requires that the ram velocity be maintained proportional to the height of the specimen. As the latter decreases during testing, so must the ram velocity.

Solving for

$$\frac{dh}{h} = \dot{\epsilon} \, dt \tag{A-8}$$

gives

$$h = h_0 \exp\left(-|\epsilon| t\right) \tag{A-9}$$

or

$$v = v_0 \exp\left(-|\epsilon| t\right) \tag{A-10}$$

Therefore the ram velocity must decrease exponentially with time. With the present apparatus this is obtained using the voltage output from an RC circuit to control the position of the ram. With this technique, strain rate is determined by the time constant (1/RC) of the RC circuit. This can easily be adjusted as required by changing the resistive value of the RC circuit, while the capacitive element is kept constant[4].

References for Appendix I

1. T.C. Hsu, "A Study of the Compression Test for Ductile Materials", Materials Research and Standards, Vol. 9, No. 12, 1969. pp. 20-53.

2. M. Cook and E.C. Larke, "Resistance of Copper and Copper Alloys to Homogeneous Deformation in Compression", Journal of the Institute of Metals, Vol. 71, 1945, pp. 371-390.

3. W.A. Backofen, Deformation Processing, Addison-Wesley Publishing Company, 1972, p. 165.

4. J-P.A. Immarigeon, P. Adams, and R. Kulchyski, "Analog Function Generator for Constant True Strain Rate During Uniaxial Compression with an MTS Testing Machine", LTR-57-786, National Aeronautical Establishment, NRC, Ottawa, Canada, 1975.

4-27
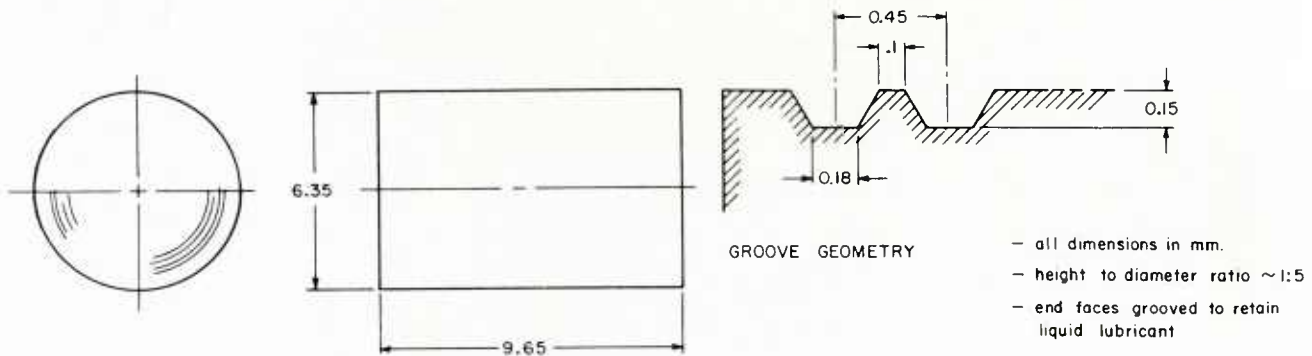
FIG A1-1   Specimen geometry including details of the geometry of grooves machined in the end faces for retaining the liquid glass lubricant used to reduce friction between the tooling and test piece.
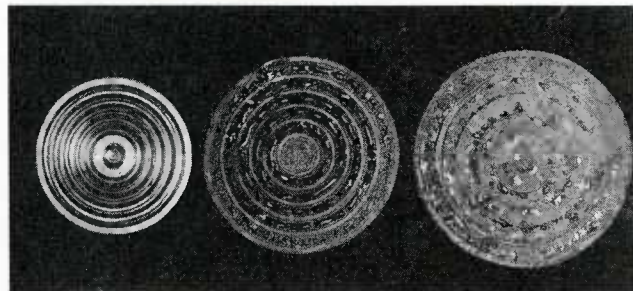

FIG A1-2   End faces of specimens before and after compression. The uniform concentric expansion of the lubricating grooves are indicative of the efficiency of lubrication in these tests.
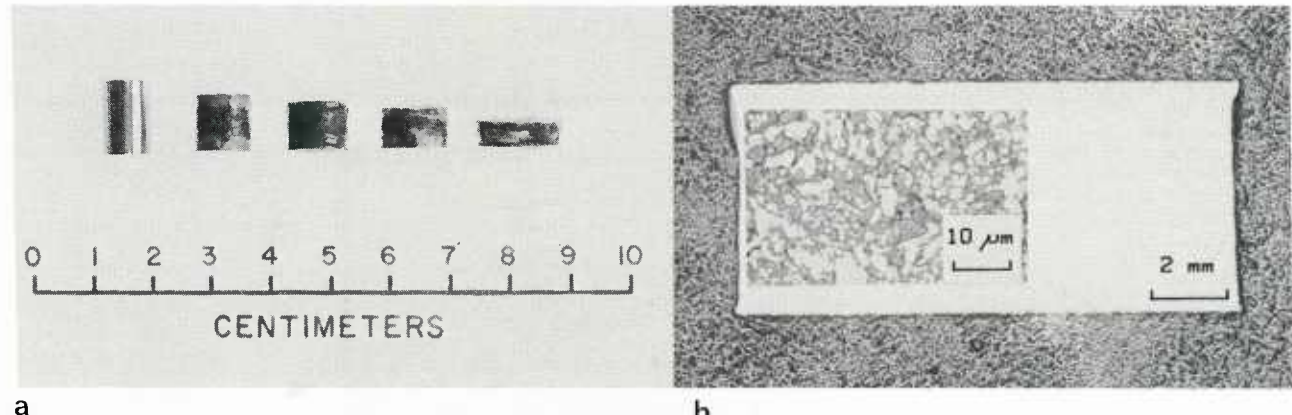

FIG A1-3   Compression tests pieces after varying reductions in height showing a) relative absence of barelling and b) lack of shear flow localization within the test piece.
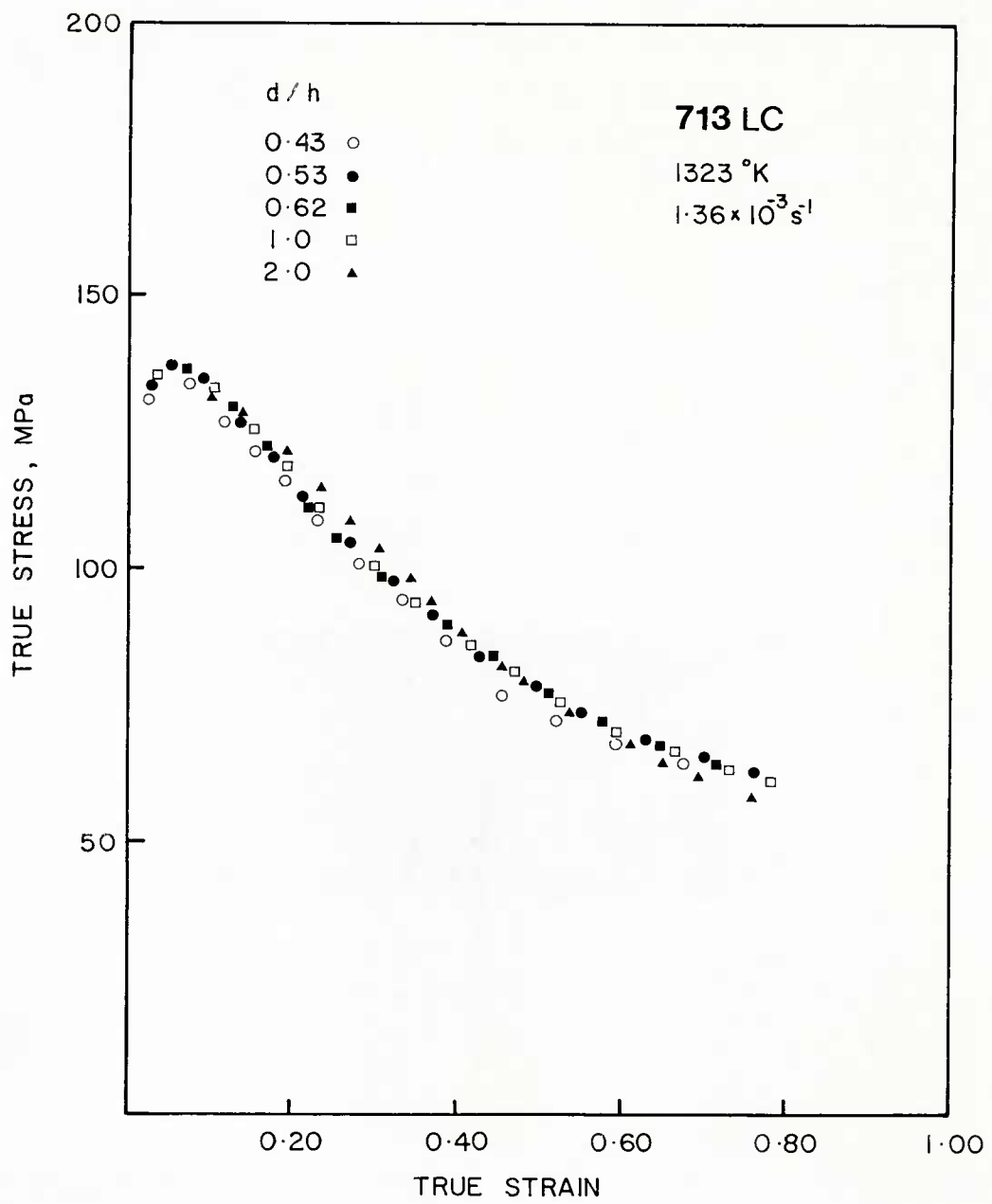
FIG A1-4   Stress-strain curves of specimens with different height to diameter ratios tested under indentical conditions.
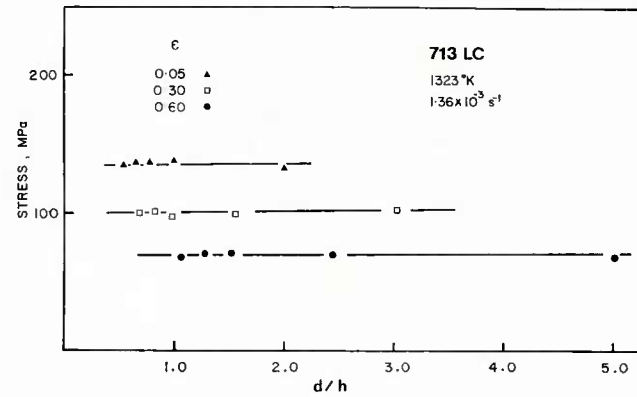

FIG A1-5   Effects of d/h ratio on flow strength during compression.

APPENDIX II

Modelling for Nucleation and Growth Rates of New Steady State Grains in the Development of the Necklace Structure

by A.K. Koul, N.A.E.

Consider the spherical grain of diameter 'λ' being deformed under isothermal conditions at a strain rate of $\dot{\epsilon}$ s^{-1}. After a certain time 't_1', i.e. a strain ϵ_1, steady state grains of diameter 'd' are about to form near the grain boundaries as shown below.

a   b
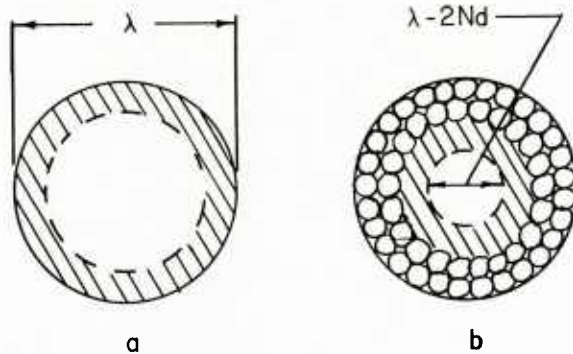
Nucleation of the first layer starts near the grain boundary because under hot working conditions shear stresses near the grain boundaries significantly exceed the homogeneous shear stresses[1], resulting in a rapid build up of dislocation near the boundary and therefore a high local driving force for recrystallization.

As deformation progresses, new grains grow to their steady state size d at which point a new layer is added and the process repeated with the addition of successive layers until transformation is complete.

At time t_2, the total amount of strain imparted is 'ϵ_2' and the total number of steady grains within the parent grain is n_s. The volume of the parent grain $V = \pi \lambda^3/6$ and the volume of remaining grain after a strain 'ϵ_2' is given by $V_n = \pi \lambda_n^3/6$. Therefore the volume of the parent grain transformed 'V_t' is given by,

$$V_t = V - V_n = \frac{\pi}{6}(\lambda^3 - \lambda_n^3) \qquad \text{(AII-1)}$$

The volume transformed 'V_t' is also given by the product of the number of steady state grains and the volume of the individual steady state grain,

$$V_t = n_s \cdot \frac{\pi}{6} d^3 \qquad \text{(AII-2)}$$

or

$$n_s = \frac{\lambda^3 - \lambda_n^3}{d^3} \qquad \text{(AII-3)}$$

If N represents the number of steady state grain layers formed after a strain ϵ_2, then $\lambda_n = \lambda - 2Nd$ as shown. Substituting for λ_n in Equation (AII-3), we get,

$$n_s = \frac{\lambda^3 - (\lambda - 2Nd)^3}{d^3}$$

or

$$n_s = \frac{6Nd\lambda^2 - 12N^2d^2\lambda + 8N^3d^3}{d^3} \qquad \text{(AII-4)}$$

The second and third term in equation (4) are considerably smaller than the first term and can therefore be neglected. Therefore:

$$n_s = 6N\lambda^2/d^2 \qquad \text{(AII-5)}$$

The number of steady state grains per unit volume $N_v = n_s/V$ and, $N_v = 36N/\pi d^2$, since $V = \pi\lambda^3/6$. The nucleation rate per unit volume, $\dot{N}_v$, is given by,

$$\dot{N}_v = \frac{36}{\pi \lambda d^2} \frac{dN}{dt} \qquad \text{(AII-6)}$$

It is necessary to assume an expression for 'N' to calculate N_v through equation (AII-6). Prior to assuming an expression for N, let us focus our attention on the growth rate 'G' and from here draw any positive conclusions regarding the nature of expression for 'N'.

Roberts and Ahlblom[2] write an expression for 'G' under fixed deformation conditions of strain, strain rate and temperature, where,

$$G \simeq 1.05 - 1.25 \, m \, z \rho_{oc} \qquad \text{(AII-7)}$$

where 'm' is the grain boundary mobility, 'z' is the dislocation line energy and ρ_{oc} is the critical dislocation density necessary for dynamic recrystallization to proceed. Equation (AII-7) can be approximated to a form, $G \propto \rho_{oc}$, or $G \propto (\dot{\epsilon}_g)^{1/2}$ since $\rho_{oc} \propto \dot{\epsilon}_g^{1/2}$ in the present case. Thus:

$$G = K_2 \dot{\epsilon}_g^{1/2} \qquad \text{(AII-8)}$$

where K_2 is a proportionality constant. The fraction 'F' transformed (section 5.3.1, Equation 14) is represented by,

$$F = 1 - \exp\left(\frac{-\pi}{3} \dot{N}_v G^3 t^4\right)$$

or after combining with Eqs. AII-6 and AII-8:

$$F = 1 - \exp\left(\frac{-\pi}{3} \dot{N}_v K_2^3 \dot{\varepsilon}_g^{3/2} t^4\right) \tag{AII-9}$$

In accordance with equation (AII-9), $N_v \propto \dot{\varepsilon}_g^{5/2} t$, such that $\dot{N}_v G^3 \propto \dot{\varepsilon}_g^4$ which maintains equation (AII-9) in a dimensionless state, as required in an avrami relation. Following this argument it becomes evident that,

$$N_v = K_1 \dot{\varepsilon}_g^{5/2} t \tag{AII-10}$$

where K_1 is a proportionality constant and 'N' can be a non-integer number. Combining equations AII-6, AII-8 and AII-10, the fraction 'F' transformed under fixed deformation conditions can be expressed as,

$$F = 1 - \exp\left(\frac{-12}{\lambda(t)d^2} K_1 K_2^3 \dot{\varepsilon}_g^4 \frac{\varepsilon_2 - \varepsilon_1}{\dot{\varepsilon}}^4\right) \tag{AII-11}$$

Similarly, when using Eq. 15 of section 5.3.1 to calculate the fraction 'F' transformed, with $S = 6/\lambda(t)$ one gets:

$$F = 1 - \exp\left(\frac{12}{\lambda(t)} G t\right) \tag{AII-12}$$

To maintain the dimensionless nature of the above equation, $G = K_3 \dot{\varepsilon}_g$, where K_3 is constant in μm, and finally:

$$F = 1 - \exp\left(\frac{-12 K_3}{\lambda(t)} \dot{\varepsilon}_g \frac{\varepsilon_2 - \varepsilon_1}{\dot{\varepsilon}}\right) \tag{AII-13}$$

References for Appendix II

1. C.M. Sellars, Recrystallization of Metals during Hot Deformation in <u>Creep of Engineering Materials and of the Earth</u>, Phil. Trans. Roy. Soc. London, Vol. A 288, pp. 147-158, 1978.

2. W. Roberts and B. Ahlblom, A Nucleation Criterion for Dynamic Recrystallization during Hot Working, Acta. Metall., Vol. 26, pp. 801-813, 1978.

CONTROL OF MICROSTRUCTURE DURING HOT WORKING OF Ti-6242

H. L. GEGEL, Y. V. R. K. PRASAD, S. M. DORAIVELU, J. C. MALAS,
J. T. MORGAN, K. A. LARK, and D. R. BARKER
AFWAL/Materials Laboratory
Wright-Patterson Air Force Base, Ohio 45433 USA

ABSTRACT

A new method of modeling the dynamic material behavior which explicitly describes the dynamic metallurgical processes occurring during hot deformation is presented. The approach in this method is to consider the workpiece as the only part of the total processing system which dissipates power and to evaluate the dissipated power co-content J from the constitutive equation. The optimum processing conditions of temperature and strain rate are those corresponding to the maximum or peak in J. It is shown that J is related to the strain-rate sensitivity (m) of the material and reaches a maximum value (J_{max}) when m = 1. The efficiency of the power dissipation (J/J_{max}) through metallurgical processes is shown to be an index of the dynamic behavior of the material and is useful in obtaining a unique combination of temperature and strain rate for processing and also in delineating the regions of internal fracture. In this method of modeling, no a priori knowledge or evaluation of the atomistic mechanisms is required, and the method is effective even when more than one dissipation process occurs, which is particularly advantageous in the hot processing of commercial alloys having complex microstructures. This method has been applied to the modeling of the behavior of Ti-6242 during hot forging. The behavior of ($\alpha + \beta$) and β preform microstructures has been examined, and the results show that the optimum condition for hot forging of these preforms is obtained at 927°C (1200 K) and a strain rate of 10^{-3} s^{-1}. Variations in the efficiency of dissipation with temperature and strain rate are correlated with the dynamic microstructural changes occurring in the material.

INTRODUCTION

The general goals of a hot-working process such as forging are

    (1) to achieve the desired geometry (size, shape, tolerance) of a part with adequate defect control;

    (2) to develop a controlled microstructure to yield the desired properties and in-service performance; and

    (3) to optimize the economic aspects of production, including the conservation of materials and energy.

Many engineers continue to consider "processing" primarily in terms of goal (1) given above and consider obtaining desired microstructures and properties to be the function of subsequent and often unrelated post-deformation processing thermal treatments. Increasingly, with the development and use of materials whose properties are a function of their entire processing history, it becomes necessary to consider goals (1) and (2) simultaneously--combining shape making with microstructure control. The process engineer of the future must use processing to control and affect trade-offs or compromises between microstructures, absence of defects, and geometry while also seeking the economic optimum demanded by goal (3).

Control of the microstructure during hot working requires answers to two fundamental questions:

    (1) What conditions does the forming process demand that the workpiece material withstand?

    (2) How does the workpiece material respond to the demands imposed by the process?

The answer to question (1) can be provided by realistically modeling the particular hot-deformation process (for example, isothermal forging) using advanced numerical simulation methods. In recent years, hot-forming processes have been successfully modeled using a rigid-viscoplastic finite-element method (1,2) which predicts deformation behavior at selected points in each element (node) by application of a variational principle. These analytical models give an admissible solution which is based upon the initial boundary conditions which are input to the finite-element model. However, use of these simulation techniques for designing and controlling real manufacturing processes requires that optimal or desired solutions be obtained, i.e., the simulations must be realistic and adequate for the intended application. Realistic simulations can be obtained if and only if the personality of the material behavior under processing conditions can be input into the finite-element model of the deformation process. Thus, the first question, which deals with defining what the process demands of the workpiece, can be answered by process-simulation studies in the computer without prototype testing on the shop floor, but the simulative technique cannot--in its present form--describe how the workpiece will dissipate the applied energy.

The second question, which deals with how the workpiece material responds to the demands of the process, can be answered only if the mechanical behavior of the workpiece material has been adequately characterized under conditions of processing. Constitutive equations relating the flow stress to the strain, strain-rate, and temperature are generally used to input material behavior to the finite-element model. They are experimentally evaluated using mechanical testing techniques (3) and are represented either in the form of empirical rate equations (4) which aid in identification of the specific atomistic rate-controlling mechanisms or in the form of simple algebraic equations (5) which are easy to use in process modeling. Neither of these forms used to represent the mechanical behavior under conditions of processing is sufficient for describing the response of the material to the demands of the process.

Another material-behavior model is required for describing how the workpiece will dissipate the instantaneous power applied to it by the process. For example, the forging press will provide instantaneous power to the workpiece in the amount described by the equation

$$\bar{\sigma}\,\dot{\bar{\varepsilon}} = \sigma_1\dot{\varepsilon}_1 + \sigma_2\dot{\varepsilon}_2 + \sigma_3\dot{\varepsilon}_3 \qquad [1]$$

where $\bar{\sigma}$ is the effective stress, $\dot{\bar{\varepsilon}}$ the effective strain-rate, and the terms on the right-hand side are the products of principal stress and principal strain rate.

The workpiece will dissipate the instantaneous power supplied by the mechanical system by a metallurgical process which is commensurate with the power level supplied. For example, fracture processes dissipate energy efficiently when the energy is supplied at a very high rate. Metallurgical processes such as superplastic flow dissipate energy with equal efficiency, but the energy must be supplied by the mechanical system at a lower and more controlled rate in order to make this deformation process possible. Thus, to control microstructures and avoid defect generation, a new type of material-behavior model must be developed which describes how the workpiece dissipates power to satisfy the demands of the process. The new model must provide information which is consistent with the unifying aspects of the finite-element model in such a way that it can become a nonholonomic constraint in the finite-element model for obtaining optimal solutions.

A new approach to describing material behavior under conditions of processing is called dynamic material modeling. It is an outgrowth of constitutive-equation development and is based on theoretical principles stemming from the analysis of physical systems and irreversible thermodynamics of metallurgical systems. It will be shown in this paper that the dynamic material model accurately describes the influence of prior processing history on the material behavior during processing and that the concepts can be applied to control microstructures in a forged product. The new model is based on understanding the physical workings of the variational principle when a solution at a finite-element node is obtained.

The variational-principle functional ϕ for a rigid viscoplastic material is written as (5)

$$\phi = \int E(\dot{\bar{\varepsilon}}^*) \, dv - \int \underset{\sim}{F} \cdot \underset{\sim}{V^*} \cdot ds + \frac{1}{2} \int K(\dot{\varepsilon}_{kk})^2 dv \qquad [2]$$

where

$\int E(\dot{\bar{\varepsilon}}^*) \, dv$ = work function = $\int \bar{\sigma} \cdot d\dot{\bar{\varepsilon}}$

$\int \underset{\sim}{F} \cdot \underset{\sim}{V^*} \cdot ds$ = boundary function which takes into account the frictional force (F) and admissible velocity V*

K = large positive constant which penalizes the dilational strain

$\dot{\varepsilon}_{kk}$ = strain-rate component

$\bar{\sigma}$ = effective stress = flow stress

$\dot{\bar{\varepsilon}}$ = effective strain rate

The work function takes into account the metallurgical phenomena which occur during hot working, and the variational and extremum principles used in the finite-element method implicitly sort them out. The numerical method offers several admissible solutions to a given plasticity problem. It is often desirable to arrive at a unique or optimum solution, and this is possible only if the dynamic material behavior is incorporated explicitly into the finite-element method. The interconnective material constraints, however, are too complicated to be written directly in algebraic form. The development of a processing map (6,7) delineating the "safe" temperature-strain rate regimes for processing represents a major step toward acceptable solutions. Often, the "safe" regime defined by these maps is still a wide area (7) which provides several combinations of temperature and strain rate at which processing can be carried out. In this paper a method of modeling the dynamic material behavior in terms of a parameter which defines unique T-$\dot{\varepsilon}$ combination(s) for hot forming is presented and applied to the hot upsetting of Ti-6Al-2Sn-4Zr-2Mo-0.1Si (Ti-6242) alloy--a material of interest in the dual-property disk application (8). The hot-deformation characteristics of this alloy in relation to the microstructure (3,9-11) have been studied earlier.

MODELING OF DYNAMIC MATERIAL BEHAVIOR

The basis for the modeling of dynamic material behavior is the unifying theme for the modeling of physical systems, as developed by Wellstead (12); here systems are viewed as energy manipulators. In the metal-processing system, certain elements are stores and sources of energy, while the workpiece is the basic device for dissipating energy. The constitutive equation for the workpiece material is an analytical relation describing the variation of flow stress with process variables, namely, temperature and strain rate. This equation is an intrinsic characteristic of the workpiece material and describes the manner in which the energy is converted at any instant into a form--usually thermal or microstructural--which is not recoverable by the system. Thus, hot working is modeled in terms of management of several irreversible thermodynamic processes which are controlled by the rate of energy input and subsequent dissipation of that energy by dynamic metallurgical processes.

A typical constitutive relation for a simple dissipator is schematically represented in Fig. 1(a) in the form of the variation of flow stress (effort) with strain rate (flow) at constant temperature and strain. At any given strain rate, the instantaneous power P absorbed by the workpiece during plastic flow is given by

$$\sigma \cdot \dot{\epsilon} = \int_0^{\dot{\epsilon}} \sigma \cdot d\dot{\epsilon} + \int_0^{\sigma} \dot{\epsilon} \cdot d\sigma \qquad [3(a)]$$

or

$$P = G + J \qquad [3(b)]$$
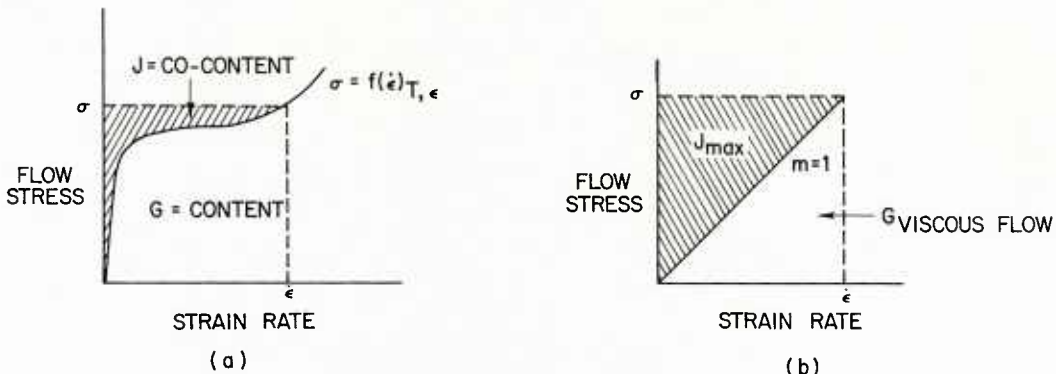
Fig. 1. (a) Schematic representation of G content and J co-content for workpiece having a constitutive equation represented by curve $\sigma = f(\dot{\epsilon})$. Total power of dissipation is given by the rectangle. (b) Schematic representation showing J_{max} occurs when strain-rate sensitivity (m) of material is equal to one.

In Fig. 1(a) the areas below and above the curve are $G = \int_0^{\dot{\epsilon}} \sigma \cdot d\dot{\epsilon}$ (dissipator content) and $J = \int_0^{\sigma} \dot{\epsilon} \cdot d\sigma$ (dissipator co-content), respectively. The G term represents the power dissipated by plastic work, most of which is converted into viscoplastic heat; the remaining small part is stored as lattice defects. The dissipator power co-content J is related to the metallurgical mechanisms which occur dynamically to dissipate power. The G content is the work function in Eq. [2], while the J co-content is a complementary set in the variational procedure. The dynamic material behavior can be modeled explicitly in terms of variations in the power co-content J with the process parameters.

Evaluation of Power Co-content J

The constitutive equation which describes the empirical relation between the flow stress σ and the strain rate $\dot{\epsilon}$ at any temperature can be expressed as

$$\dot{\epsilon} = A \sigma^n \qquad [4]$$

where A is a constant and n the stress exponent. The term n is related to the strain-rate sensitivity m of the material as

$$m = \left(\frac{\Delta \log \sigma}{\Delta \log \dot{\epsilon}}\right)_T = \frac{1}{n} \qquad [5]$$

In the hot-working range for pure metals (2), m (or n) is temperature- and strain-rate independent; but in complicated alloy systems, it has been shown (3) to vary with temperature and strain rate.

At any given deformation temperature, J is evaluated by integrating Eq. [4] as follows:

$$J = \int_0^{\sigma} \dot{\epsilon} \cdot d\sigma = A \frac{\sigma^{n+1}}{n+1} \qquad [6]$$

By combining Eqs. [4], [5], and [6], the J co-content can be related to the strain-rate sensitivity as

$$J = \frac{\sigma \cdot \dot{\epsilon} \cdot m}{m+1} \qquad [7]$$

In the above integration the strain-rate dependence of m represents the flow trajectory taken by the system to reach the flow stress σ; according to the variational principle, this is always the path which provides the maximum dissipation co-content J ("natural" configuration) (12). From Eq. [7] the value of J at a given temperature and strain rate may be estimated from the flow stress and the strain-rate-sensitivity factor m. The value of J reaches its maximum (J_{max}) when m = 1, and the workpiece acts as a linear dissipator; thus,

$$J_{max} = \frac{\sigma \cdot \dot{\epsilon}}{2} \qquad [8]$$

In this case, one-half of the power is dissipated as material flow and the other half is dissipated as viscous heat [schematically shown in Fig. 1 (b)]. The behavior of superplastic materials approaches this extreme. The other extreme occurs for materials which are strain-rate insensitive and those which do not flow. In these cases J is zero.

The analogy for the above behavior is found in electrical systems where J_{max} corresponds to good electrical conductors and J = 0 corresponds to insulators. Common engineering materials processed at high temperatures exhibit flow behavior which falls somewhere between these two extremes. These materials are analogous to resistors in electrical systems, and their flow behavior under dynamic conditions may be characterized in terms of the J co-content. For a given power input to the system, the material flow will be maximum when the workpiece dissipates the highest possible power through dynamic metallurgical processes, i.e., the J co-content reaches its highest value.

The effect of J on the plastic flow of materials can be visualized if the power-dissipation capacity of the workpiece is expressed in terms of efficiency of dissipation, η, which is defined as the ratio of J to J_{max}. From Eqs. [7] and [8], it follows that

$$\eta = \frac{J}{J_{max}} = \frac{2m}{m + 1} \qquad [9]$$

In simple terms the efficiency represents the dissipating ability of the workpiece as normalized with respect to the total power input to the system.

Several dynamic metallurgical processes contribute to power dissipation during hot working of materials, and these processes have characteristic ranges of efficiencies of dissipation. Often in materials having complicated microstructures or in two-phase alloys, these processes occur simultaneously and/or interactively. Thus, the evaluated value of J will be the overall result of these interactions. Metallurgical processes such as dynamic recovery, dynamic recrystallization, internal fracture (void formation or wedge cracking), dissolution or growth of particles or phases under dynamic conditions, dynamic spheroidization of acicular structures, and deformation-induced phase transformation or precipitation under dynamic conditions contribute to the changes in the dissipated power co-content J. When two major dissipation processes having different characteristics occur simultaneously, the value of J will reach its maximum when the energy of dissipation of one process equals that of the other. This is somewhat analogous to what happens in electrical systems (13) having a variable resistor where the load power reaches a maximum when the line and load resistances are equal. For processing of materials the most favorable conditions are those which provide the highest J dissipated in the most efficient fashion (highest η) and lie within the "safe" regions.

The power co-content J serves as the most useful index for characterizing dynamic material behavior in processing for the following reasons:

1. It defines unique combinations of T and $\dot{\epsilon}$ for processing (peak values of J and η) and also separates the regimes which produce internal fracture.

2. Being a power term, it is an invariant and, hence, applicable to any state of stress.

3. It can be used conveniently as a non-holonomic constraint in the finite-element method.

4. It is a continuum parameter and can be integrated with the finite-element analysis.

5. In its estimation no specific atomistic rate-controlling mechanisms need be evaluated or assumed, although its variation with temperature and strain rate reflects the dominating dissipating mechanism. This aspect is advantageous, particularly when more than one mechanism is operating during hot forming.

6. From it, an algorithm can be developed which can be incorporated into process control.

MODELING OF HOT DEFORMATION OF Ti-6242

Ti-6242 is a near-α, $\alpha + \beta$ titanium alloy whose hot-working characteristics are very sensitive to the initial preform microstructure and processing variables. A processing technique is presently being developed for producing a dual-property turbine disk using these characteristics to synthesize microstructures which result in good tensile and low-cycle-fatigue properties in the bore region and good creep and stress-rupture properties in the rim region. For evaluating the constitutive behavior of this material, two different preform microstructures have been investigated (3): equiaxed $\alpha + \beta$ and acicular $\alpha + \beta$ or transformed β. The first is an equilibrium microstructure of globular α in a matrix of transformed β (referred to as $\alpha + \beta$), while the second corresponds to a non-equilibrium transformed-β microstructure showing acicular α in the β matrix (referred to as β microstructure hereafter). Dadras and Thomas (3) have evaluated the relationship between the flow stress (σ), temperature (T), strain rate ($\dot{\epsilon}$), and strain (ϵ) for these two starting preform microstructures using a hot-compression test. At small strain (0.04) the dependence of log σ upon (1/T) was linear for the ($\alpha + \beta$) preform, while dual-mode or bilinear behavior was reported for the β microstructure which exhibits a transition at about 930°C (1203 K). The strain-rate sensitivities as obtained by the stress-relaxation technique were dependent upon strain rate and temperature for both preform microstructures (3). These results suggest that the thermally activated behavior of this material is complicated and cannot be characterized by the apparent activation energy using conventional activation analysis of the hot-deformation process. In the following discussion, the constitutive behavior of Ti-6242 has been analyzed on the basis of the dynamic modeling method outlined earlier, and microstructural correlations have been attempted.

Hot Deformation of the ($\alpha + \beta$) Preform

Variation of the flow stress with strain rate and temperature for the ($\alpha + \beta$) microstructure is shown in Figs. 2(a) and 2(b), corresponding to strains of 0.04 and 0.6, respectively. Data reported by Dadras and Thomas (3) (in the strain-rate range 10^{-3} to 10^{-1} s^{-1}) and Lewis (14) (1 s^{-1}) are represented in this plot. At each test temperature and strain rate, the strain-rate sensitivity m (Eq. [5]) is evaluated by fitting a polynomial equation to log σ-vs.-log $\dot{\epsilon}$ curves and obtaining the derivatives. The m values thus obtained are shown in Figs. 3(a) and 3(b) as a function of temperature and strain rate for strains of 0.04 and 0.6, respectively. The instantaneous power dissipated by the material, the J co-content, at different temperatures and strain rates of deformation is estimated using Eq. [7] and is shown in Fig. 4. The J value decreased gradually with increasing temperature and is higher at higher strain rates. A diffused peak is discernible at high strain rates. The efficiency of dissipation defined by Eq. [9] is also evaluated and plotted as a function of temperature at different strain rates in Figs. 5 and 6. Some important features of these plots are:
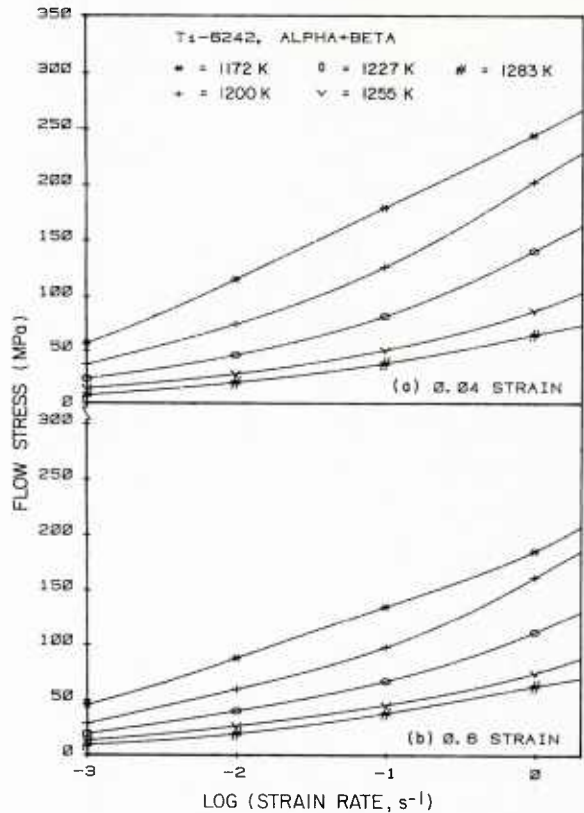
Fig. 2. Variation of flow stress with strain rate at different temperatures for Ti-6242 α + β preform (a) 0.04 strain and (b) 0.6 strain.
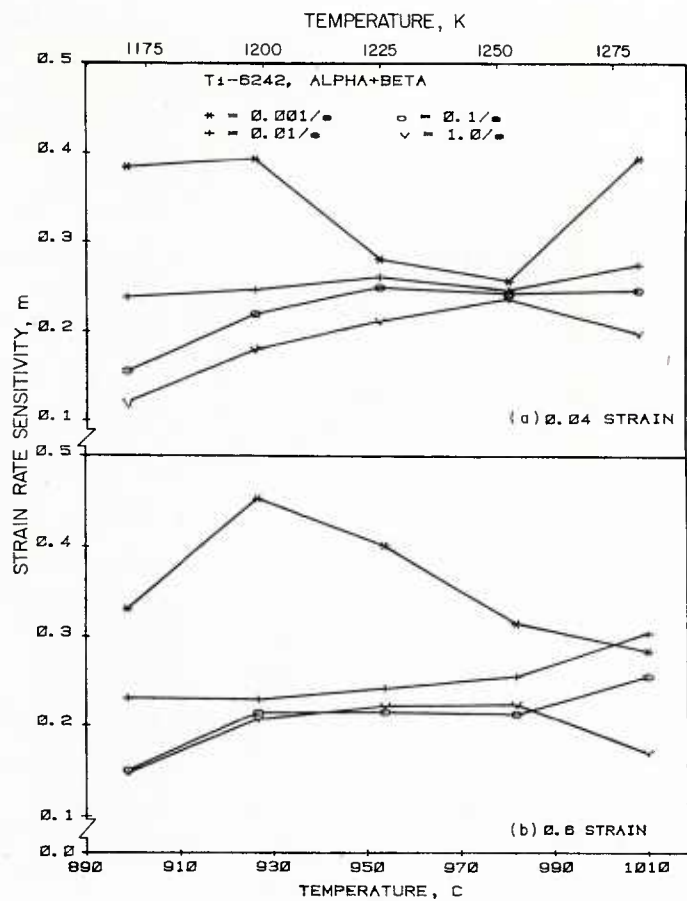

Fig. 3. Variation of strain-rate sensitivity (m) with temperature at different strain rates in Ti-6242 α + β preform (a) 0.04 strain and (b) 0.6 strain.
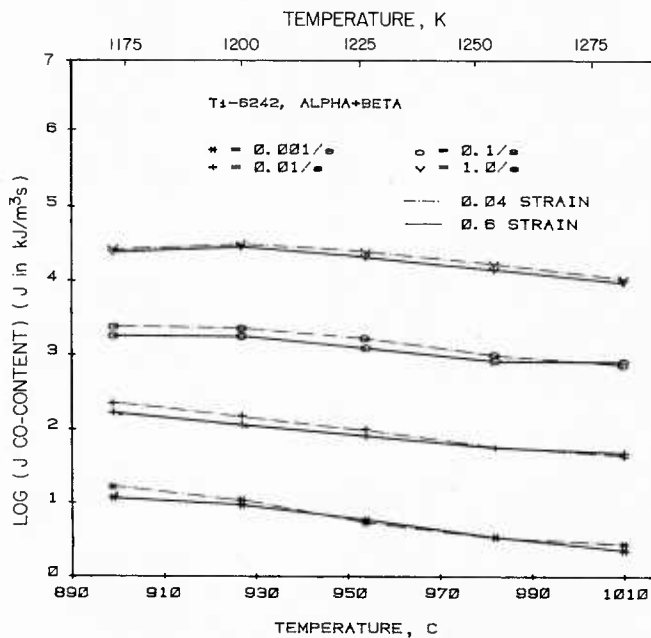

Fig. 4. Variation of J co-content with temperature at different strain rates in Ti-6242 α + β preform. Effect of strain is not significant.
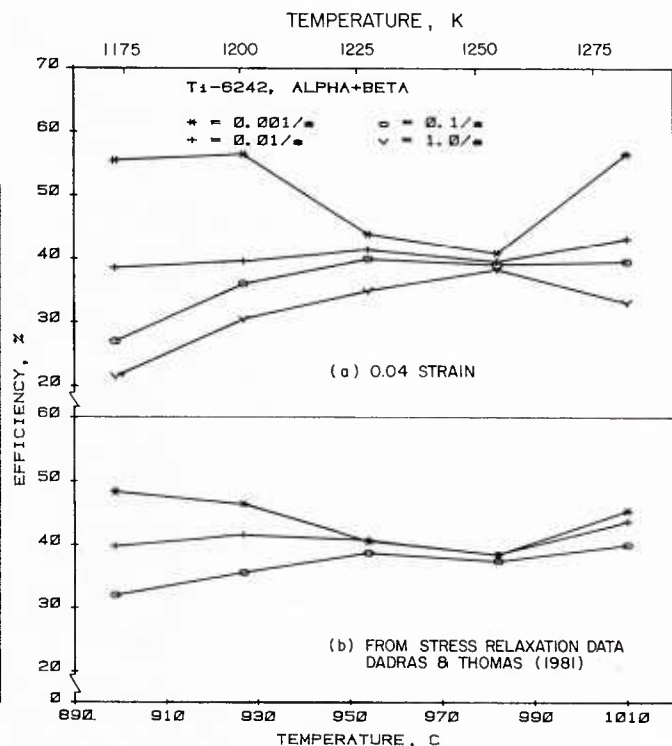

Fig. 5. (a) Variation of efficiency of dissipation with forging temperature for Ti-6242 α + β preform at a strain of 0.04 for different strain rates. (b) Efficiency of dissipation calculated from m obtained by stress-relaxation technique [Dadras and Thomas (3)].

1. The efficiency of power dissipation is higher at lower strain rates.
2. At each strain rate, the efficiency of power dissipation passes through a peak in the temperature range 899-982°C (1172-1255 K).
3. At 982°C (1255 K) the efficiency of dissipation obtained at all strain rates converges.
4. At 1010°C (1283 K) the efficiency of dissipation is again strain-rate dependent, being higher at lower strain rates.
5. The features described above are essentially unchanged when the strain is increased from 0.04 to 0.6, as is evident from a comparison of Figs. 5 and 6.

The efficiency of dissipation calculated from the m values obtained by Dadras and Thomas (3) from the stress-relaxation technique is shown in Fig. 5(b) as a function of temperature at different strain rates. These variations are in good agreement with those given by Fig. 5(a), although small differences in the magnitudes of the individual values exist.

In the temperature range 899-982°C (1172-1255 K) (α + β field), the processing is best carried out at 927°C (1200 K) and 10^{-3} s^{-1}, where the efficiency reaches its peak value (Figs. 5 and 6). As the strain rate is increased, the efficiency of dissipation decreases and a wider range of temperature exists for processing, the minimum temperature being 927°C (1200 K). The J variation with temperature (Fig. 4) shows diffused peaks at 927°C (1200 K) for strain rates of 0.1 and 1 s^{-1}; hence, a temperature of 927°C (1200 K) is preferable for processing even at these strain rates.

The variation of efficiency of dissipation with temperature and strain rate is shown in the form of a three-dimensional map in Fig. 7. The surface represented by these variations, although a complex one, highlights the regimes of processing which correspond to a high efficiency of dissipation. Another
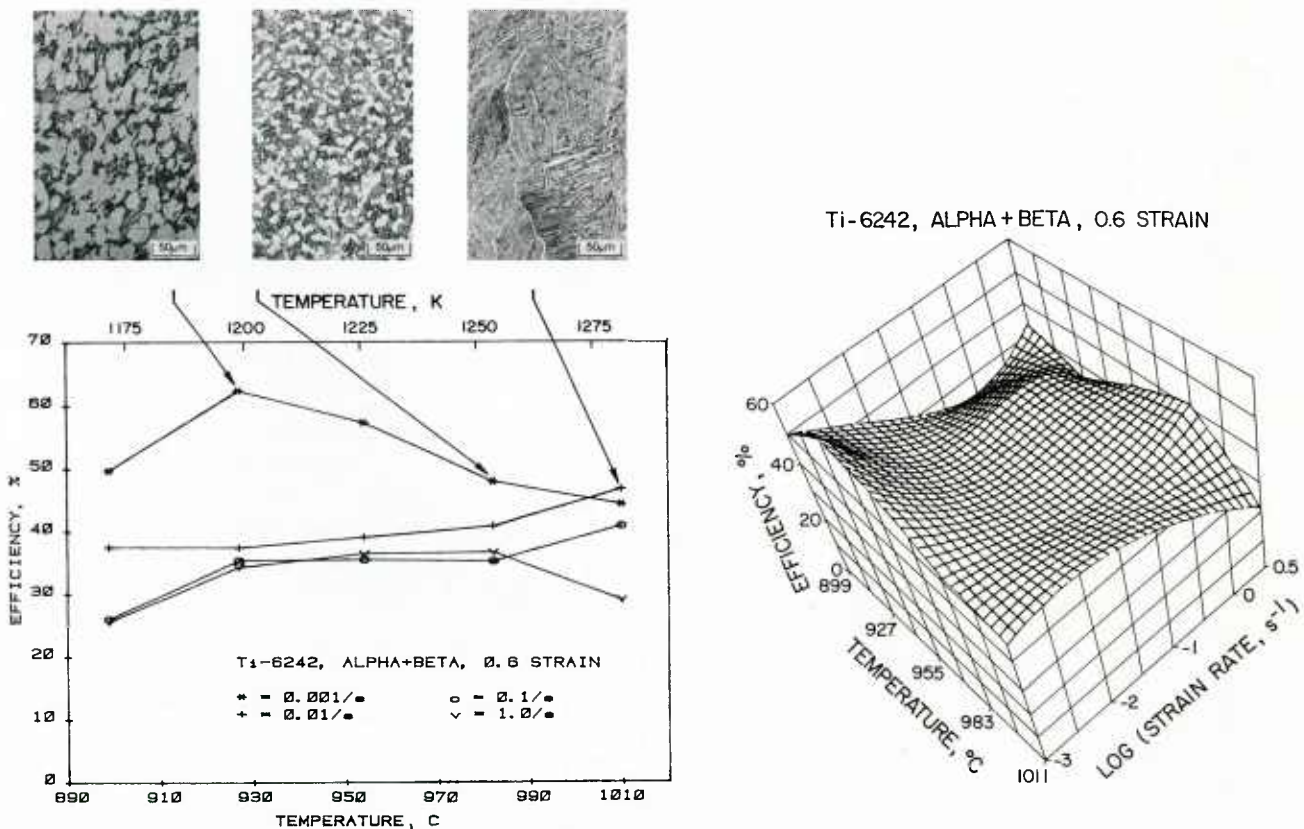

Fig. 6. Variation of efficiency of dissipation through metallurgical processes with forging temperature for Ti-6242 α + β preform at strain of 0.6 for different strain rates. Typical microstructures corresponding to particular processing temperatures and strain rates also shown.


Fig. 7. Three-dimensional plot showing variation of efficiency of dissipation with temperature and strain rate for Ti-6242 α + β preform at 0.6 strain.

method of representing these results is shown in Fig. 8 which is a contour map of constant efficiencies. The contour map is a two-dimensional representation of Fig. 7 and is another convenient way to locate the processing regimes. For example, the optimum processing conditions of 927°C (1200 K) and 10^{-3} s^{-1} are striking in Fig. 8.

The metallurgical processes which are responsible for the observed variations may be identified by examining the microstructures. Typical microstructures recorded on Ti-6242 α + β material under different temperature and strain-rate conditions are shown in Fig. 6, with a view toward correlation with the efficiency variations.

It is known that the β-transus for this material is at about 990°C (1263 K); and near this temperature, power dissipation occurs essentially by the phase transformation α + β → β. This phase transformation produces contraction (11) and its strain-rate dependence is not very significant, as evident from quantitative metallographic observations (9) which show that the volume percent of primary-α at 982°C (1255 K) is nearly the same in specimens deformed at different strain rates. This accounts for the

TEMPERATURE, K

Fig. 8. Map showing constant efficiency contours in strain rate-temperature frame for Ti-6242 α + β preform at 0.6 strain.
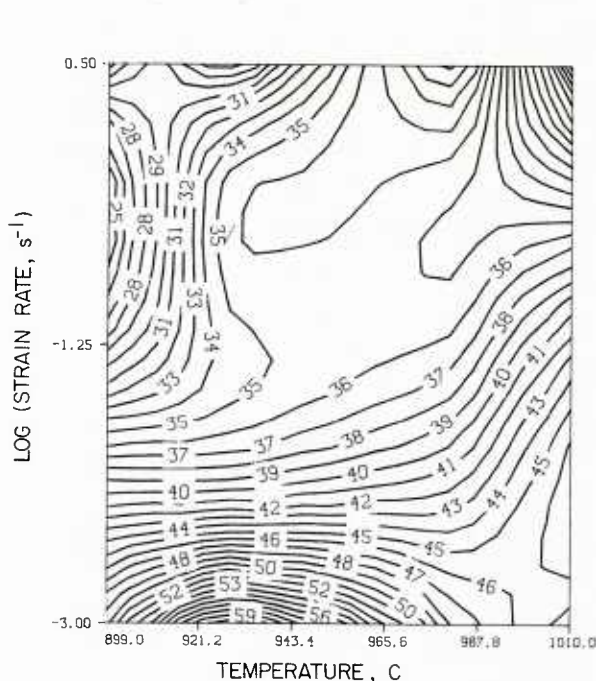
Fig. 9. Variation of J co-content with temperature for different strain rates in Ti-6242 β-preform. Effect of strain is also shown.

converging trend of dissipation curves for different strain rates at 982°C (1255 K). Careful microstructural examination of the material deformed at 927°C (1200 K) and 10^{-3} s^{-1} revealed recrystallization of the globular-α phase in the α + β microstructure (Fig. 6). Furthermore, it has been shown by Semiatin, et al. (9), that the primary-α content in the microstructure decreases with increasing temperature, i.e., α + β → β transformation occurs to a greater extent. Thus, at least two important power-dissipation processes occur during hot deformation of α + β preforms--dynamic recrystallization and α + β → β phase transformation. The peak in the efficiency-temperature curve represents the temperature at which the power of dissipation (rate of energy dissipation) due to dynamic recrystallization is equal to that due to phase transformation. On the left of the peak, dynamic recrystallization dominates; while on the right, phase transformation is dominant. The peak is diffused over a wider temperature range when these two processes balance their rates of energy dissipation over this range.

At 1010°C (1283 K) the material is deforming as a β phase, and the grain size is large (250-350 μm) (3,9). There is no evidence of dynamic recrystallization. On the other hand, grain-boundary sliding is a possibility at lower strain rates and causes wedge cracking which could, in turn, also dissipate energy with high efficiency. Dissipation by this mechanism is reduced at higher strain rates since grain-boundary sliding is less; the data in Fig. 5(a) support this. At higher strain rates, dissipation can occur by dynamic recovery processes. Metallographic examination of specimens deformed at 1010°C (1283 K) and at low strain rates revealed the transformed-α phase in the wedge-crack or intergranular-crack morphology. This phase occurs because the specimens undergo a non-equilibrium phase transformation when air cooled; for the thermodynamic reasons outlined earlier (11), the transformed-α preferentially forms at sites of high tensile-hydrostatic stress.

Hot Deformation of the β Preform

Analysis similar to that described above for α + β preform materials has been carried out on β-preform material also. The variation of the J co-content with test temperature for different strain rates is shown in Fig. 9 for strains of 0.04 and 0.6. These plots are very similar to those obtained on the α + β preform (Fig. 4). The efficiency of dissipation (Eq. [9]) is plotted as a function of temperature for different strain rates in Fig. 10. These variations are considerably different from those obtained on the α + β preform (Figs. 5 and 6). Referring to Fig. 10(a) (strain of 0.04), when the material is deformed at 10^{-3} s^{-1}, a drop in the efficiency of dissipation is evident at temperatures higher than 954°C (1227 K). At higher strain rates (10^{-1} and 1 s^{-1}), a diffused efficiency peak occurs between 927°C (1200 K) and 954°C (1227 K). At 10^{-2} s^{-1}, however, the efficiency of dissipation increases with an increase in temperature beyond 927°C (1200 K). Figure 10(b) shows the efficiency of dissipation calculated from the strain-rate sensitivity measured using the stress-relaxation technique (3). Except for the value at 927°C (1200 K) and 10^{-3} s^{-1}, the data show trends similar to those in Fig. 10(a). The three-dimensional efficiency-temperature-strain rate map and the corresponding contour map for the β-Ti-6242 at a strain of 0.04 are shown in Figs. 11 and 12, respectively. The drop in the efficiency of dissipation at 982°C (1255 K) and 10^{-3} s $^{-1}$ is clearly revealed in these maps.

For a strain of 0.6, the efficiency variations are shown in Fig. 13; and the corresponding three-dimensional maps and efficiency contours are shown in Figs. 14 and 15, respectively. These figures show that two well-defined peaks occur in the temperature-strain rate regime--one at 927°C (1200 K) and 10^{-3} s^{-1} and the other at 927°C (1200 K) and 1 s^{-1}. The behavior at strain rates of 10^{-2} and 10^{-1} s^{-1} remains the same as for low strains. The data clearly show that optimum forging conditions for the β-preform are 927°C (1200 K) and 10^{-3} s^{-1}; and if the forging is carried out at high strain rates (1 s^{-1}), the best temperature would still be 927°C (1200 K).
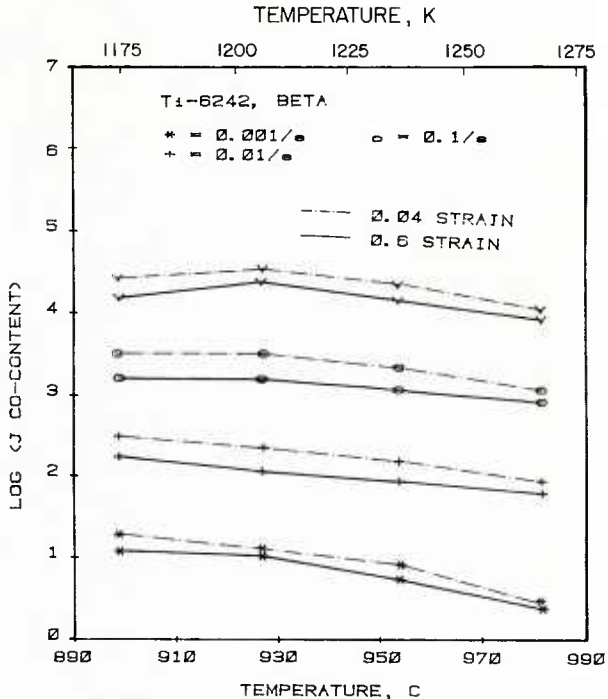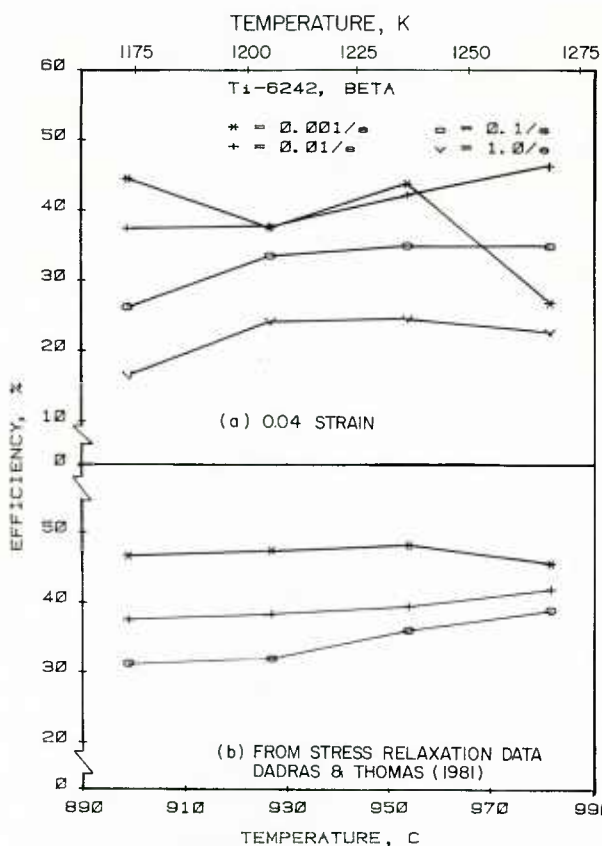
Fig. 10. (a) Variation of efficiency of dissipation with temperature of forging for β-preform of Ti-6242 at a strain of 0.04 for different strain rates. (b) Efficiency of dissipation calculated from m obtained by stress-relaxation technique [Dadras and Thomas (3)].

Ti-6242, BETA, 0.04 STRAIN

Fig. 11. Three-dimensional plot showing variation of efficiency of dissipation with temperature and strain rate for Ti-6242 β-preform at 0.04 strain.

Fig. 12. Map showing constant efficiency contours in strain rate-temperature frame for Ti-6242 β-preform at 0.04 strain.
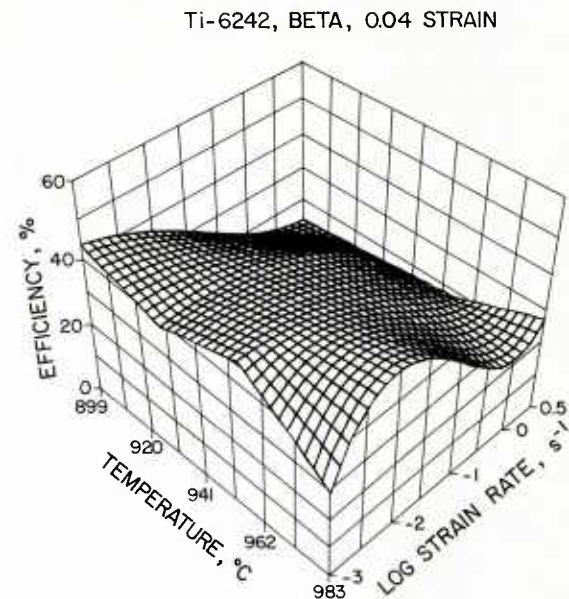
Fig. 13. Variation of efficiency of dissipation through metallurgical processes with forging temperature for Ti-6242 β-preform at a strain of 0.6 for different strain rates. Typical microstructures corresponding to particular processing temperatures and strain rates also shown.
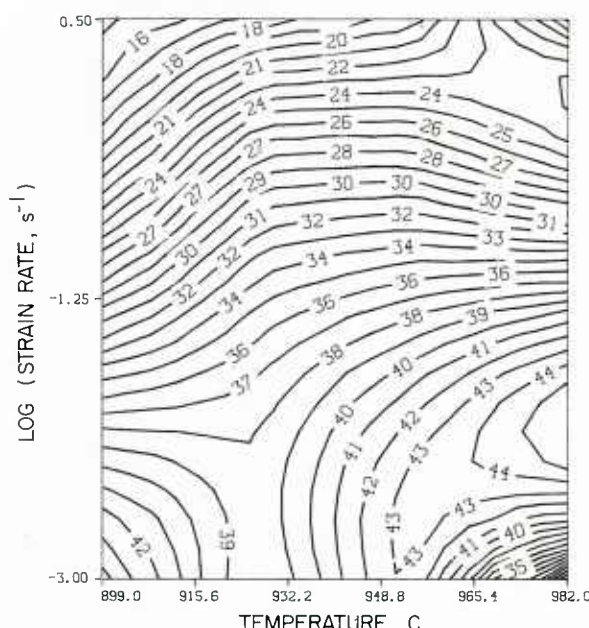
Ti-6242, BETA, 0.6 STRAIN
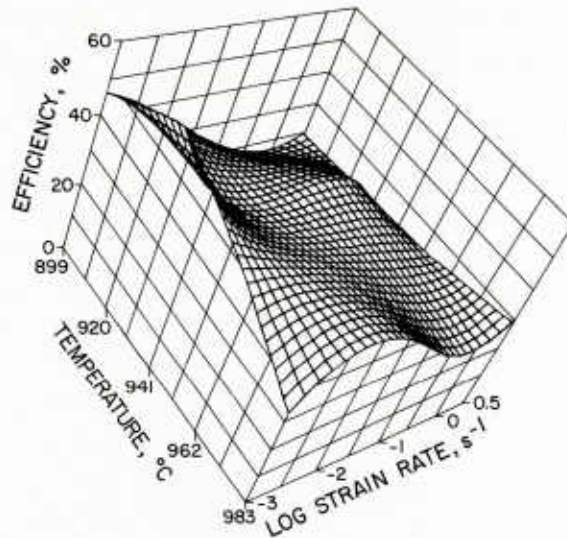
Fig. 14. Three-dimensional plot showing variation of efficiency of dissipation
with temperature and strain rate for Ti-6242 β-preform at 0.6 strain.
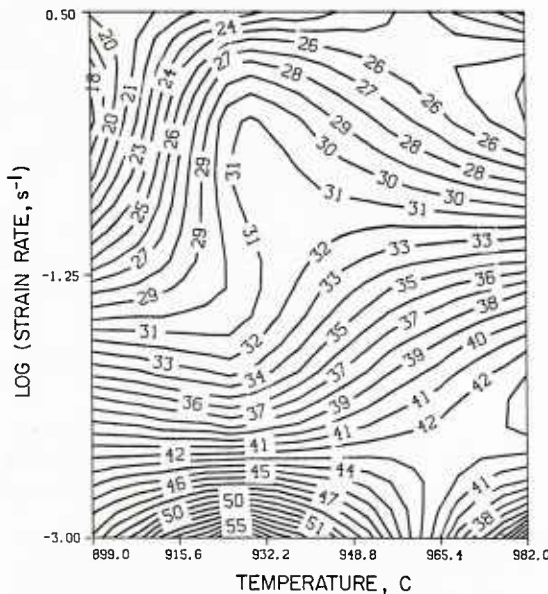
Fig. 15. Map showing constant efficiency contours in strain rate-
temperature frame for Ti-6242 β-preform at 0.6 strain.

    Correlation between efficiency variations and metallurgical changes is provided in Fig. 13. The
microstructures in Fig. 13 reflect the metastable nature of the β-preform which shows a tendency toward
reaching a more stable microstructural form--the α + β structure. From the metallographic evidence
available, the large drop in efficiency at 10^{-3} s^{-1} and temperatures beyond 927°C (1200 K) (Fig. 13) is
associated with the precipitation of transformed-α from the metastable-β structure (3,9). At lower
strains this precipitation occurs at higher temperatures (> 954°C or 1227 K) [Fig. 9(a)]. At lower strain
rates ($\leq 10^{-2}$ s^{-1}), some grain-boundary sliding also occurs, resulting in wedge cracks and grain-boundary
cavities (11,15,16) which aid in energy dissipation. Thus, the two opposing dissipation processes are (1)
the precipitation of transformed-α (which reduces the rate of energy dissipation) and (2) wedge cracking
and grain-boundary cavitation (which increase the rate of energy dissipation). At high strain rates
(~ 1 s^{-1}), grain-boundary sliding is minimal; while at 10^{-3} s^{-1}, the precipitation of transformed-α is
more dominant than grain-boundary sliding. It is interesting to note that the transformed-α occurs at
wedge cracks and grain-boundary cavities (11) and this is a dynamic process in view of the metastable
nature of the β-preform microstructure. At 10^{-2} s^{-1}, wedge cracking dominates (16) at temperatures above
927°C (1200 K) and, hence, the efficiency of dissipation increases with an increase in temperature. At
899°C (1172 K) the dissipation processes involved are local kinking of β-platelets and spheroidization,
the former dominating at higher strain rates (~ 1 s^{-1}) and the latter at lower strain rates ($\sim 10^{-3}$ s^{-1}).

APPLICATION OF DYNAMIC MODELING TECHNIQUES

    Dynamic material-modeling techniques were applied to a hypothetical problem for producing a control-
led microstructure gradient in a subscale disk forged under isothermal conditions at approximately 927°C
at a nominal strain-rate of 5×10^{-2} s^{-1}. The forging preform was designed in such a way that the
transformed-β microstructure would transform to the equiaxed α + β microstructure in the center region of
the disk and the transformed-β microstructure in the rim-region would remain essentially unchanged in the

final product after heat treatment. The research objective was to obtain a microstructure in the center region which would exhibit good low-cycle-fatigue properties, and at the same time, a microstructure in the rim-region which would possess good fracture toughness and creep resistance. The mechanical properties shown in Table I satisfy the requirements of the experiment to test the concept of dynamic material modeling, and the controlled microstructures are shown in Fig. 16.

TABLE I

MECHANICAL PROPERTIES OF Ti-6242 DISKS FORGED AT 900°C (1173 K)
AND SOLUTION HEAT TREATED AT 955°C (1228 K)*

	Center Region	Outer Region
Room-Temperature Tensile Properties		
Yield Strength, MPa	652	636
Ultimate Tensile Strength, MPa	705	668
Elongation, Pct.	7	4
Reduction in Area, Pct.	15	11
565°C Tensile Properties		
Yield Strength, MPa	363	353
Ultimate Tensile Strength, MPa	438	436
Elongation, Pct.	20	22
Reduction in Area, Pct.	49	43
Time to 0.1 Pct. Creep Strain,[†] Hr.	188	330
Fracture Toughness, MPa $\sqrt{m}$	52	70

*Followed by aging at 595°C (868 K) for 8 hr. and air cooling.
[†]Test Conditions: 510°C (783 K)/240 MPa.
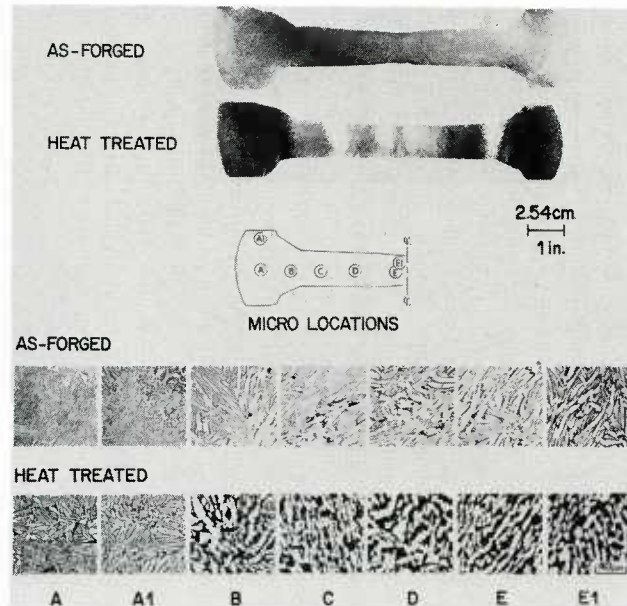

Fig. 16. Structural features of disk produced by selected forging and heat treating combinations.

SUMMARY

A method of modeling dynamic material behavior which explicitly describes the dynamic metallurgical processes occurring during hot deformation has been presented. Following a systems approach, the instantaneous power co-content (J) dissipated by the workpiece is evaluated by considering it to be the only part of the total system which dissipates energy and whose constitutive equation relates stress and strain rate. It is shown that J is related to the strain-rate sensitivity (m) of the material and reaches a maximum value (J_{max}) when m = 1. The efficiency of dissipation (J/J_{max}) is a characteristic of the metallurgical process responsible for the dissipation and can lead to a unique combination of temperature and strain rate for processing and also delineate regions of internal fracture. This method of modeling is effective even when several metallurgical processes occur simultaneously during hot deformation, since no prior knowledge or evaluation of the atomistic mechanisms is required.

The above method has been validated by modeling Ti-6242 material during hot forging. The analysis revealed that the optimum forging condition for forging both α + β and β-preform microstructures is obtained at 927°C (1200 K) and 10^{-3} s^{-1}. A good correlation between the efficiency variations and microstructural changes occurring during hot deformation could be established in this material. For the α + β preform, dynamic recrystallization and phase transformation are important in the temperature range 899-982°C (1172-1255 K), while at 1010°C (1283 K) dissipation at low strain rates occurs by wedge cracking. Regarding the β-preform, local kinking of β-platelets, spheroidization of the acicular structure, precipitation of transformed-α and wedge cracking have been shown to influence the efficiency of dissipation.

REFERENCES

1. H. J. McQueen and J. J. Jonas: Metal Forming - Interrelation between Theory and Practice, A. L. Hoffmanner, ed., Plenum Press, New York, 1971, p. 393.

2. J. J. Jonas, C. M. Sellars, and W. J. McG. Tegart: Met. Rev. 1969, vol. 14, p. 1.

3. P. Dadras and J. F. Thomas, Jr.: Met. Trans. A, 1981, vol. 12, p. 1867.

4. C. H. Lee and S. Kobayashi: Trans. ASME, J. Engr. Ind., 1973, vol. 95, p. 865.

5. S. I. Oh: Int. J. Mech. Sci., 1982, vol. 24, p. 479.

6. R. Raj: Met. Trans. A, 1981, vol. 12, p. 1089.

7. K. P. Rao, S. M. Doraivelu, H. Md. Roshan, and Y. V. R. K. Prasad: Met. Trans. A, 1983, vol. 14, p. 1671.

8. G. D. Lahoti, S. L. Semiatin, S. I. Oh, T. Altan, and H. L. Gegel: Advanced Processing Methods for Titanium, D. F. Hasson and C. H. Hamilton, eds., TMS-AIME, Warrendale, PA, 1981, p. 23.

9. S. L. Semiatin, J. F. Thomas, Jr., and P. Dadras: Met. Trans. (to be published).

10. S. L. Semiatin and G. D. Lahoti: Met. Trans. A, 1981, vol. 12, p. 1705.

11. H. L. Gegel: Proceedings of Symposium on Experimental Verification of Process Models, 1981 Metals Congress, September 21-23, 1981, Cincinnati, C. C. Chen, ed., ASM, Metals Park, OH, 1983, p. 32.

12. P. E. Wellstead: Introduction to Physical System Modeling, Academic Press, New York, 1979, pp. 9, 144.

13. C. S. Siskind: Electrical Circuits, McGraw Hill Book Co., New York, 1965, p. 565.

14. G. K. Lewis: AFWAL-TR-80-4162, AFWAL Materials Laboratory, Wright-Patterson Air Force Base, OH 45433, 1980.

15. H. L. Gegel, S. Nadiv, and R. Raj: Scripta Met., 1980, vol. 14, p. 241.

16. J. C. Malas, H. L. Gegel, S. I. Oh, and G. D. Lahoti: Proceedings of Symposium on Experimental Verification of Process Models, 1981 Metals Congress, September 21-23, 1981, Cincinnati, C. C. Chen, ed., ASM, Metals Park, OH, 1983, p. 358.

Numerical Methods in Metalforming

Nuno Rebelo

University of Oporto School of Engineering
Rua dos Bragas
4099 Porto, Portugal

INTRODUCTION

Metal forming processes are almost as old as mankind. Like many other branches of technology, scientific analysis and development have accompanied their evolution. The complexities of the theories involved, together with the amount of parameters, have, however, precluded what was achievable in many other cases, i.e., elegant, easy-to-use closed-form solutions or reasonably accurate equations describing the phenomena and which can be immediately used in applications.

At the very heart of metal forming analysis is the theory of plasticity. Initially proposed late last century by von Mises and Hencky, it reached a stabilized form in the early sixties (1), and for infinitesimal analysis only. A brief description of this theory follows in point 2. The large deformation theory is still being developed today.

The infinitesimal theory of plasticity, simplified by discarding the elastic part of deformation (also known as the flow theory) has produced several approximate methods of analysis that have proved very useful in metal forming. We will present the basic assumptions that lead to the uniform deformation method, the slab method, the upper-bound method and the slip-line field method.

The availability of computers with relatively inexpensive, large amounts of number-crunching capabilities fostered the development of the finite element method. Originally used in structural analysis, it rapidly expanded into other fields, and has been applied to metal forming analysis since the early seventies. This is the area in which most of the recent work in this field has been done. Two schools have developed in the finite element analysis. The first one is based on the rigid plastic approach (the flow theory) for which the infinitesimal theory of plasticity has been sufficient. It leads to relatively simple formulations which have allowed its users to attack the difficult problems specific to metal forming applications. The second one is based on the more complete elasto-plastic approach which almost always requires a large deformation theory of plasticity. The formulations are more complicated and have followed, if not actually led to, developments in the theory itself. Today it can simulate forming processes as intricate as the flow approach. This lecture will end with an introduction to the fundamental concepts of the finite element method.

It should be mentioned here that another numerical method recently made its appearance in the metal forming field: the boundary element method. Although quite promising for structural analysis, it is still too soon to judge its merits as regards its applications to metal forming plasticity.

INFINITESIMAL THEORY OF PLASTICITY

For a complete, consistent, and very elegant presentation of the infinitesimal theory of plasticity, the reader is referred to reference (1). This paper which wraps up years of development, shows that all the theory can be derived from three basic assumptions:

1) At any time, t, the infinitesimal deformation $\varepsilon_{ij}(\underset{\sim}{x},t)$ can be decomposed as a sum of

$$\varepsilon_{ij}(\underset{\sim}{x},t) = \varepsilon_{ij}{}^{E} + \varepsilon_{ij}{}^{P}$$

an elastic part and of a plastic part.

2) A yield function (surface) in stress space exists.

3) Material is stable, i.e., any increase in deformation will not produce a decrease in the flow stress.

We will describe the same theory herein, but in a less formal manner, stressing the physical considerations behind it.

To begin with, there are several physically observed phenomena that are usually ignored, such as

      a. Influence of strain-rate on the elastic limit
      b. Creep
      c. Bauschinger effect
      d. Histeresis loops
      e. Anisotropy. Anisotropy is only usually introduced for sheet metal forming analysis, and in most cases only for that direction perpendicular to the plane of the sheet (r value); for the extension of the theory to anisotropy, see Hill (2).

f. Size effects

g. In all rigid-plastic analysis, the elastic part of deformation.

Yield Criteria

We are searching for those stress states which will make the material yield. If we consider that these stress states define a yield surface in stress space, it means that any stress state inside the surface corresponds to an elastic state, and any stress state on the surface corresponds to a plastic state.

It is known that in metals, plastic deformation is produced by dislocations which implies that plastic deformation is incompressible, and any hidrostatic state of stress does not produce yielding. Therefore, the yield surface must be cylindrical, with an axis defined by $\sigma_x = \sigma_y = \sigma_z$.

One also concludes that only shear stresses produce yielding. Hence the most simple yielding criteria one can devise is to say that the material will yield when the maximum shear stress reaches a certain value.

$$\frac{\sigma_1 - \sigma_3}{2} = \pm \text{ constant}$$

where

$\sigma_1 = $ maximum principal stress

$\sigma_3 = $ minimum principal stress

This is the Tresca yield criterium, proposed in 1864. One determines the value of the constant when testing a specimen. In a tensile test,

$$\sigma_1 = \sigma_Y \quad \text{(yield stress)}$$

$$\sigma_2 = \sigma_3 = 0 \tag{1}$$

therefore

$$\sigma_1 - \sigma_3 = \pm \sigma_Y$$

In a torsion test,

$$\sigma_1 = -\sigma_3 = \sigma_Y \quad \text{(yield shear stress)}$$

$$\sigma_2 = 0$$

therefore

$$\sigma_1 - \sigma_3 = \pm 2\tau_Y \tag{2}$$

One may now want to include all stress components in the yield criterium. However, the yield or flow stress is proper to the material. This means it should not depend on the chosen axis, and is thus a function of the stress tensor invariants only.

$$I_1 = \sigma_x + \sigma_y + \sigma_z$$

$$I_2 = -(\sigma_x\sigma_y + \sigma_y\sigma_z + \sigma_z\sigma_x) + \tau_{xy}^2 + \tau_{yz}^2 + \tau_{zx}^2$$

$$I_3 = \begin{vmatrix} \sigma_x & \tau_{xy} & \tau_{xz} \\ \tau_{xy} & \sigma_y & \tau_{yz} \\ \tau_{xz} & \tau_{yz} & \sigma_z \end{vmatrix}$$

As hidrostatic stress does not cause yield, one may consider the deviatoric stresses

$$\sigma'_i = \sigma_i - p \qquad p = \text{average stress}$$

and a function of its invariants J_1, J_2, J_3, where $J_1 = 0$. We should then define the yield surface as

$$f(J_2, J_3) = \text{constant}$$

The most simple form one can think of is

$$J_2 = \text{constant}$$

which is the von Mises criterium proposed in 1913. This can be written in the general form,

$$\left[(\sigma_x - \sigma_y)^2 + (\sigma_y - \sigma_z)^2 + (\sigma_z - \sigma_x)^2 + 6(\tau_{xy}^2 + \tau_{yz}^2 + \tau_{zx}^2)\right] = \text{constant}$$

Again, in a tensile test

$$\tau_x = \tau_y \quad \tau_y = \tau_z = \sigma_{xy} = \sigma_{yz} = \sigma_{zx} = 0$$

$$2\tau_y^2 = \text{constant}$$

or

$$\frac{1}{\sqrt{2}} \left[(\tau_x - \tau_y)^2 + (\tau_y - \tau_z)^2 + (\tau_z - \tau_x)^2 + 6(\sigma_{xy}^2 + \sigma_{yz}^2 + \sigma_{zx}^2)\right]^{1/2} = \sigma_Y \quad (3)$$

In a torsion test

$$\frac{1}{\sqrt{2}} \left[(\tau_x - \tau_y)^2 + (\tau_y - \tau_z)^2 + (\tau_z - \tau_x)^2 + 6(\sigma_{xy}^2 + \sigma_{yz}^2 + \sigma_{xz}^2)\right]^{1/2} = \sqrt{3}\sigma_Y \quad (4)$$

What the expressions (1) and (4) mean is, that if we determine the yield surface say, with a tensile test, then the two criteria will not predict yielding at the same point in torsion, or vice-versa.

The left-hand side of equation (3) is commonly represented by $\bar{\tau}$ and known as effective stress or equivalent stress. It is the combination of the stress components that indicates how close the stress state is to the yield surface, or that which is equivalent to the uniaxial test.

If we accept that material is stable, then the yield surface must be convex. Otherwise it would be possible to have changes in plastic state (plastic deformation) with a decrease in the equivalent stress.

If one represents the yield surfaces in a principal stress space, seen from the $\tau_1 = \tau_2 = \tau_3$ axis, one obtains the following representation. (Figure 1)

The Tresca yield surface is the inner hexagon, and the von Mises yield surface is the circle.

Isotropy and absence of the Bauschinger effect impose symmetry with respect to the six lines represented. Convexity requires that all admissible yield surfaces be between the Tresca hexagon and the outer hexagon. The von Mises yield criterium follows experiments pretty well, and there is no point in further complicating the theory, with such close limits.

Work Hardening

Consider that after yielding, there was a small amount of plastic deformation $d\varepsilon^P$. Upon unloading and loading again, the yield surface may have been altered (hardening) and $\sigma_Y = g(d\varepsilon^P)$. As the plastic deformation keeps volume constant, one would expect g to be a function of the shear components of deformation.

It has been shown experimentally that anything can happen to the yield surface upon plastic deformation. Material parameters play a role, the path of deformation is very important, and anisotropy usually develops in the material after it has been plastically deformed. There are several theories in the literature as to how to take the various phenomena into account. These, however, are usually hard to handle in applications, and the great majority of the analysis is made with the so-called isotropic hardening. This means that the effect of plastic deformation on the yield surface is its isotropic expansion.

As the effective stress becomes the scalar "measure" of the stress tensor, a similar effective strain increment can be defined as an isotropic combination of shear-like terms in the strain increments.

$$d\bar{\varepsilon} = \frac{\sqrt{2}}{3} \left[(d\varepsilon_x^P - d\varepsilon_y^P)^2 + (d\varepsilon_y^P - d\varepsilon_z^P)^2 + (d\varepsilon_z^P - d\varepsilon_x^P)^2 + \right.$$

$$\left. \frac{3}{2} (d\gamma_{xy}^{P\,2} + d\gamma_{yz}^{P\,2} + d\gamma_{zx}^{P\,2})\right]^{1/2}$$

the factor $\frac{\sqrt{2}}{3}$ was conveniently chosen so that $d\bar{\varepsilon} = d\varepsilon$ in a uniaxial test.

In isotropic hardening we then have,

$$\tau_Y = g(d\bar{\varepsilon})$$

As the plastic deformation proceeds, one cannot calculate $\bar{\varepsilon}$ out of the comonents of ε^P. In fact, one can always recover any original shape after some plastic deformation, by imposing some more appropriate plastic deformation. Therefore, the components of ε^P have no meaning other than an overall change in geometry. The real amount of plastic deformation is measured by integrating $d\bar{\varepsilon}$ which is always positive.

$$\bar{\varepsilon} = \int d\bar{\varepsilon}$$

After a finite amount of deformation

$$\sigma_Y = g(\bar{\varepsilon})$$

and the yield surface is defined by

$$\bar{\sigma} = g(\bar{\varepsilon})$$

with its expansion following the uniaxial stress strain curve as shown in Figure 2.

2.3 Plastic Deformation

The permanent character of plastic deformation, and the fact that unlike in elasticity, one can obtain a certain configuration via an infinite variation of the amounts of plastic deformation, lead us to conclude that a state of stress only provides information for the increment of strain which it produces. In order to obtain the components of such strain increments, we start with the two following physically acceptable assumptions:

a) The principal stress directions coincide with the principal strain increment directions;

b) The principal shear components of strain increment are proportional to the principal shear stress components;

from which one can conclude:

$$\frac{d\varepsilon_x^P}{\sigma'_x} = \frac{d\varepsilon_y^P}{\sigma'_y} = \frac{d\varepsilon_z^P}{\sigma'_z} = \frac{d\gamma_{xy}^P/2}{\tau_{xy}} = \frac{d\gamma_{xz}^P/2}{\tau_{xz}} = \frac{d\gamma_{yz}^P/2}{\tau_{yz}} = d\lambda$$

By inserting these 6 equations in the definition of $d\bar{\varepsilon}$, one obtains:

$$d\bar{\varepsilon} = \frac{2}{3} \, d\lambda \, \bar{\sigma}$$

and the 6 equations become:

$$d\varepsilon_x^P = \frac{d\bar{\varepsilon}}{\bar{\sigma}} \left[\sigma_x - \frac{1}{2}(\sigma_y + \sigma_z)\right] \tag{5}$$

$$d\varepsilon_y^P = \frac{d\bar{\varepsilon}}{\bar{\sigma}} \left[\sigma_y - \frac{1}{2}(\sigma_x + \sigma_z)\right] \tag{6}$$

$$d\varepsilon_z^P = \frac{d\bar{\varepsilon}}{\bar{\sigma}} \left[\sigma_z - \frac{1}{2}(\sigma_x + \sigma_y)\right] \tag{7}$$

$$d\gamma_{xy}^P = \frac{d\bar{\varepsilon}}{\bar{\sigma}} \, 3\tau_{xy} \tag{8}$$

$$d\gamma_{yz}^P = \frac{d\bar{\varepsilon}}{\bar{\sigma}} \, 3\tau_{yz} \tag{9}$$

$$d\gamma_{xz}^P = \frac{d\bar{\varepsilon}}{\bar{\sigma}} \, 3\tau_{xz} \tag{10}$$

With the aid of equation (3) one can write the yield surface equation in the following fashion:

$$h(\bar{\sigma}) = 0 \qquad \bar{\sigma} - \sigma_Y = 0$$

or

$$\frac{1}{\sqrt{2}}\left[(\sigma_x - \sigma_y)^2 + (\sigma_y - \sigma_z)^2 + (\sigma_z - \sigma_x)^2 + 6(\tau_{xy}^2 + \tau_{yz}^2 + \tau_{xz}^2)\right]^{1/2} - \sigma_Y = 0$$

Let's now calculate

$$\frac{\partial h}{\partial \sigma_x} = \frac{1}{\sqrt{2}} \, \frac{1}{2}\left[(\sigma_x - \sigma_y)^2 + (\sigma_y - \sigma_z)^2 + (\sigma_z - \sigma_x)^2 + 6(\tau_{xy}^2 + \tau_{yz}^2 + \tau_{xz}^2)\right]^{-1/2} \times$$

$$\times \left[2(\sigma_x - \sigma_y) - 2(\sigma_z - \sigma_x)\right] =$$

$$= \frac{1}{\bar{\sigma}}\left[\sigma_x - \frac{1}{2}(\sigma_y + \sigma_z)\right] \tag{11}$$

When one compares (11) with (5) one obtains

$$d\varepsilon_x^P = d\bar{\varepsilon} \, \frac{\partial h}{\partial \sigma_x} \tag{12}$$

and similarly:

$$d\varepsilon_y^P = d\bar{\varepsilon} \; \frac{\partial h}{\partial \bar{\tau}_y} \tag{13}$$

$$d\varepsilon_z^P = d\bar{\varepsilon} \; \frac{\partial h}{\partial \bar{\tau}_z} \tag{14}$$

$$d\gamma_{xy}^P = d\bar{\varepsilon} \; \frac{\partial h}{\partial \bar{\tau}_{xy}} \tag{15}$$

$$d\gamma_{yz}^P = d\bar{\varepsilon} \; \frac{\partial h}{\partial \bar{\tau}_{yz}} \tag{16}$$

$$d\gamma_{xz}^P = d\bar{\varepsilon} \; \frac{\partial h}{\partial \bar{\tau}_{xz}} \tag{17}$$

Equations (13-17) show that the plastic strain increments are normal to the yield surface. In fact, one can mathematically derive this result from the stability assumptions from where assumptions a) and b) in this section become natural consequences.

When one wants to extend the theory to viscoplasticity, or consider other types of material behaviour, equations such as (12) which explicit the existence of a "plastic potential" become a common point of departure.

PROBLEM SOLUTION

Any metal forming problem is a boundary value problem, in which we have a volume V of material, bound by a surface S, as in Figure 3. Compatibility equations and equilibrium equations apply within the volume. In order to simplify the equations, we will use a tensor notation in the equations. The first means, that for any load producing an infinitesimal strain increment field $d\varepsilon_{ij}$, we must be able to derive such a field from a displacement increment field du_i through

$$d\varepsilon_{ij} = \frac{1}{2} (du_{i,j} + du_{j,i}) \tag{18}$$

where ,j means derivative with respect to x_j.

The plastic part of strain increments satisfy incompressibility:

$$d\varepsilon_{ii}^P = 0 \tag{19}$$

The second means that any load producing a stress field τ_{ij} in which body loads q_i are present, the following applies:

$$\tau_{ij,j} + q_i = 0 \tag{20}$$

where a summation convention is implied. Furthermore, one can subdivide the surface in two parts; one in which forces/unit area T_i are applied S_T, in which force boundary conditions have to be satisfied.

$$\tau_{ij} n_j = T_i \tag{21}$$

where n_j are the components of a unit vector, normal to the surface.

The other part, S_D, where displacement increments are applied dU_i, thus

$$du_i = dU_i \tag{22}$$

The stresses and strain increments produced by a certain load are related by constitutive equations. The body may be divided in two parts; one, E, in which yielding does not take place, and where elasticity equations apply:

$$d\varepsilon_{ij} - \alpha \Delta T \delta_{ij} = K_{ijkl} \tau_{ij} \tag{23}$$

with K_{ijkl} being elasticity constants, and α the thermal expansion coefficient.

The other part, E-P, where yielding has occurred; here the yield criteria applies:

$$\bar{\tau} = \tau_y \tag{24}$$

and elasticity and plasticity stress strain relations follow:

$$d\varepsilon_{ij} - d\varepsilon_{ij}^P - \alpha \Delta T \delta_{ij} = K_{ijkl} \tau_{ij} \tag{25}$$

$$d\varepsilon_{ij}^P = \frac{d}{\bar{\tau}} \; \frac{\partial h}{\partial \bar{\tau}_{ij}} \tag{26}$$

It becomes obvious that it is very difficult to obtain closed form solutions that satisfy all of these requirements. In fact, there are only about four or five of these complete solutions in the literature, all for very simple problems.

Even if one considers rigid-plastic materials, equations 18, 19, 20, 21, 22, 24 and 26 have to be satisfied, with the risk of having part of volume E becoming rigid, with an undetermined stress field. The following table gives all the requirements for a rigid-plastic analysis.

```
                        ┌─────────────────────────────┐
                        │  MECHANICS OF DEFORMATION   │
                        └─────────────────────────────┘
             ┌──────────────────┐           ┌──────────────────┐
             │     STRESS       │           │   DEFORMATION    │
             │  REQUIREMENTS    │           │  REQUIREMENTS    │
             └──────────────────┘           └──────────────────┘

  ┌────────────────────────────┐  ┌──────────────┐  ┌────────────────────────────────────┐
  │ 1.  EQUILIBRIUM EQUATIONS   │  │              │  │ 1.  COMPATIBILITY EQUATIONS         │
  │                             │  │  FLOW RULE   │  │                                     │
  │ 2.  YIELD CRITERIUM         │  │ (STRESS-STRAIN│ │ 2.  INCOMPRESSIBILITY               │
  │                             │  │  RELATIONS)  │  │                                     │
  │ 3.  MATERIAL FLOW           │  │              │  │ 3.  DISPLACEMENT BOUNDARY CONDITIONS│
  │     PROPERTIES              │  └──────────────┘  └────────────────────────────────────┘
  │                             │
  │ 4.  STRESS BOUNDARY         │
  │     CONDITIONS              │
  └────────────────────────────┘
```
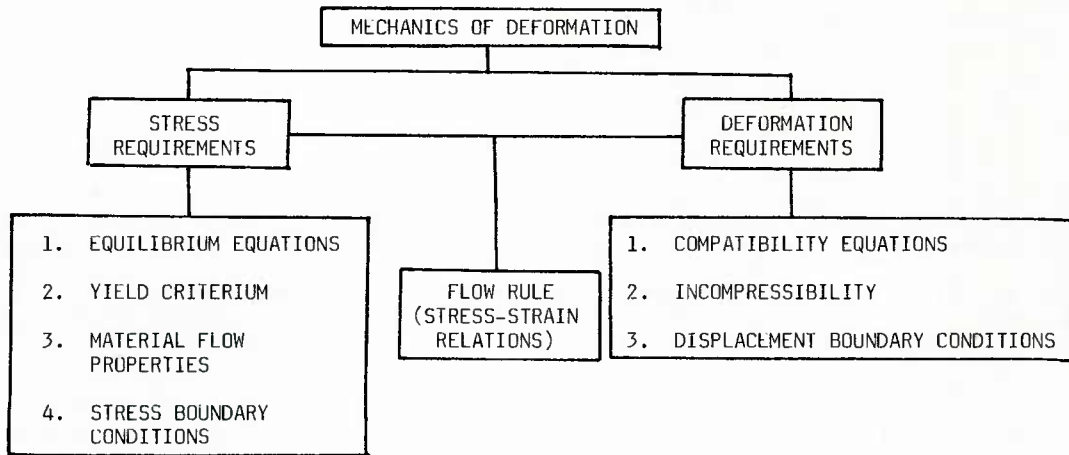
Given the difficulties in satisfying all the equations, several approximate numerical solutions have been developed through the years, even before the theory was completely defined.

We will next present the fundamentals of the most common procedures that lead to approximate solutions through more or less easy computations, all based on rigid-plastic material behaviour.

UNIFORM DEFORMATION

This is the most simplistic approach possible. It is assumed that the material deforms uniformly as in an uniaxial test (possibly in plane strain), the amount of deformation being determined by the geometric restrictions of the system - displacement boundary conditions. The flow rule is easily applied, and some kind of load can be directly calculated. However, if the load in question is not that one, we can go a step further and consider the work necessary to produce the deformation.

$$W = V \, \sigma_y \int_{l_0}^{l} \frac{dl}{l}$$

W - work
V - volume
σ_y - average flow stress
$\dfrac{dl}{l}$ - deformation increment

If one knows the displacement of the forces producing the deformation of volume V, usually out of geometric considerations, they can be determined by equating the above work to the work of such forces.

The forces are always lower than the real ones, as the material usually deforms with distortions, and there is friction at the boundaries.

Looking at Table I, compatibility, incompressibility, the flow rule and yield criterium are satisfied. The flow properties of the material are usually averaged for the amount of deformation. Displacement and stress boundary conditions are violated. Because of that, the displacement field can be quite different from the real one.

The textbook example application of this procedure is the determination of the maximum area reduction in a single drawing pass.

SLAB METHOD

The slab method is an approximate method based on pure equilibrium and yield requirements. For that, one assumes that plane surfaces of the material remain plane, which is quite false if friction is high. One divides the deforming part in slices (or slabs) limited by such plane surfaces. Figure 4 shows a typical division.

Friction is usually described by the coefficient μ - tangential stress = μ times normal stress p, or by a friction factor m - tangential stress = m times the shear yield stress of adjacent material. Note that the sign of the friction stresses depends on which direction the material is flowing.

The plane surface assumption implies that the directions x,y in plane strain or r,z for an axisymmetrical problem are principal stress and strain directions. The Mises yield criterium is written thus:

$$\sigma_y - \sigma_x = -\frac{2}{\sqrt{3}}\sigma_Y \quad \text{plane strain}$$

$$\sigma_z - \sigma_r = -\sigma_Y \quad \text{axysymmetric}$$

One also assumes that the flow stress σ_Y is constant in each slab, although it may change from slab to slab. With these assumptions we can write equilibrium equations for each slab along direction x (consider plane strain for example):

$$(\sigma_x + d\sigma_x)(h + dh) - \sigma_x h + \frac{pdx}{\cos\alpha}\sin\alpha + p\frac{dx}{\cos\beta}\sin\beta -$$

$$-\tau\frac{dx}{\cos\alpha}\cos\alpha - \tau\frac{dx}{\cos\beta}\cos\beta = 0$$

neglecting second order terms

$$hd\sigma_x + \sigma_x dh + pdx(tg\alpha + tg\beta) - 2\tau dx = 0$$

$$dx = \frac{dh}{tg\alpha + tg\beta}$$

$$h\,d\sigma_x + \sigma_x dh + pdh - 2\frac{\tau\,dh}{(tg\alpha + tg\beta)} = 0$$

assuming that

$$\sigma_y \approx -p$$

the yield criterium becomes

$$\sigma_x - \sigma_y = \frac{2}{\sqrt{3}}\sigma_Y \approx \sigma_x + p = \frac{2}{\sqrt{3}}\sigma_Y \quad d\sigma_x = d\sigma_y$$

therefore

$$d\sigma_y + \left(\frac{2}{\sqrt{3}}\sigma_Y - \frac{2\tau}{(tg\alpha + tg\beta)}\right)\frac{dh}{h} = 0$$

In general, one uses τ according to the type of friction considered. There may be slight variations in the geometrical simplifications according to the external definition of the problem.

The procedure for solving a problem is to divide the deforming area in parts so that an equation such as above can be determined. One can then integrate the equations of each part, starting with a part that has a known boundary condition, such as a free surface normal to the x direction:

$$\sigma_x = 0$$

$$\sigma_y = \frac{-2}{\sqrt{3}}\sigma_Y$$

If a rigid zone forms, it is possible to separate it from deforming zones by shear lines, whose position can be optimized during the solution. The load is obtained by integrating σ_y along the surface. Incremental deformations for a given configuration are obtained by using the flow rule and incompressibility. The geometry can then be updated for a new configuration, and the problem restarts. In this way, for instance, it is possible to simulate a forging process.

When we look at Table I, we see that the slab method only uses the stress requirements and approximations are made at the equilibrium equations level in order to obtain a solution. The deformation part is derived from that solution, and there are no guarantees of being correct.

The whole solution procedure can be automated in computer programs (3), which, due to the simplicity of the calculations, are most suitable for coupling with interactive graphical displaying and serve as a computer aid to designers or operators of metal-working processes.

UPPER BOUND METHOD

A kinematically admissible displacement increment field is one that satisfies the deformation requirements of Table I. A statically admissible stress field is one that satisfies the stress requirements of Table I.

Consider now for a material point the stress tensor τ_{ij} and the strain increment tensor $d\varepsilon_{ij}$ solution of a problem, and the stress tensor $\tau_{ij}*$ obtained through equations (26) from a kinemetically admissible strain increment tensor $d\varepsilon_{ij}*$. Figure 5.

Convexity of yield surface lets us write $(\tau_{ij}* - \tau_{ij})\, d\varepsilon_{ij}* \geqslant 0$ and integrating over the volume

$$\int_V (\tau_{ij}* - \tau_{ij})\, d\varepsilon_{ij}* \geqslant 0 \tag{27}$$

Consider next, equilibrium equations without body forces (normal situation in metal forming):

$$\tau_{ij,j} = 0 \tag{28}$$

and a kinematically admissible displacement increment field du_i*. By multiplying this displacement vector at any point by equations (28) we obtain the scalar

$$\tau_{ij,j} du_i* = 0$$

which integrated over the volume yields

$$\int_V \tau_{ij,j}\, du_i*\, dV = 0$$

$$\int_V \left[(\tau_{ij}\, du_i*)_{,j} - (\tau_{ij}\, du_{i,}{}^*{}_{j}) \right] dV = 0$$

Applying the divergence theorem and symmetry of the stress tensor

$$\int_S \tau_{ij}\, du_i*\, n_j\, dS - \int_V \tau_{ij}\, du_i*{}_{,j}\, dV = 0$$

$$\int_S T_i\, du_i*\, ds - \int_V \tau_{ij}\, d\varepsilon_{ij}*\, dV = 0$$

The meaning of this expression is that the work done by the stress field on a kinematically admissible displacement increment field equals the work done by the external loads on the same displacement field.

A feature of kinematically admissible displacement increment fields is that they allow for tangential discontinuities along surfaces. In such cases, the volume integral is interpreted as the summation of the volumes limited by external surfaces and discontinuity surfaces, and to the surface integral we add such discontinuity surfaces.

$$\int_S T_i\, du_i*\, dS - \int_{S_S} \zeta |du*|\, dS_S - \int_V \tau_{ij}\, d\varepsilon_{ij}*\, dV = 0 \tag{29}$$

where ζ is the tangential shear stress along the discontinuity, and $|du*|$ the relative displacement increment.

When we use inequality (27), (29) becomes

$$\int_S T_i\, du_i*\, ds \leqslant \int_V \tau_{ij}*\, d\varepsilon_{ij}*\, dV + \int_{S_S} \zeta_Y\, |du*|\, dS_S$$

where ζ_Y is the shear yield stress of the material.

We now separate S in S_T and S_D, where $du_i = du_i*$

$$\int_{SD} T_i\, du_i\, dS \leqslant \int_V \tau_{ij}*\, d\varepsilon_{ij}*\, dV + \int_{S_S} \zeta_Y\, |du*|\, dS_S - \int_{S_T} T_i\, du_i*\, dS_T \tag{30}$$

The physical meaning of expression (30) is as follows: For all possible kinematically admissible displacement fields, the work done by the associated stress field in the volume and surface discontinuities, minus the work done by the known forces along the stress boundary, equate to an amount of work that is greater or equal to the work done by the unknown forces along the displacement boundary.

This upper bound theorem is widely applied in metal forming to determine a load estimate to perform a certain operation. This load estimate is always greater than the real one. One considers families of kinematically admissible displacement fields, defined by a finite amount of parameters left as variables. For each, the right-hand side of inequality (30) is calculated, and a minimum is found with respect to the above-mentioned

variables. This minimum gives the closest load estimate within such families. These estimates (and the particular displacement fields associated to them) are more or less close to reality according to the "quality" of the fields initially considered, and depending a lot on the engineering "feeling" and experience of the user. Therefore this method which is very handy and relatively easy to apply, can only be implemented with separate computer programs for specific problems (configurations), which already contain families of fields created by the programmer.

We refer the reader to (4) and (5) for a number of applications of this method.

When we look at Table I, we see that this method is based on the deformation requirements only, incidentally satisfies the stress boundary conditions, and uses the flow rule to compute stresses. There are no guarantees that these stresses are the correct ones.

SLIP-LINE FIELD METHOD

This is a method that follows all the requirements of Table I, i.e., it gives an exact solution, provided we extend our initial simplifying assumptions as follows: the material, besides being rigid-plastic and isotropic, does not work-harden, and the deformation is a plane strain one. The attraction of a complete solution is counter-balanced by the difficulty in its application. By the time we were able to apply computer programs of this method to reasonably general and complicated geometries, the finite element method had made its appearance. This can deal with a wider range of problems in more precise detail for equally large amounts of computations. Thus, the Slip-line field method is falling into disuse today. Reference (2) provides the theoretical background; (6) and (7) have several applications. Here we will only present the main features of its equations.

Consider a plane strain deformation on the x-y plane. We see that at any given point, the stress field is determined by two variables only: the mean pressure (minus the average stress) and the inclination $\emptyset$ of the principal shear stress direction with respect to the xy direction. The yield criterium is automatically included through the shear yield stress along these principal directions. The two equilibrium equations, in terms of p and $\emptyset$ can be solved by the characteristics method. The characteristics are orthogonal and define, for each point, the principal shear stress directions. They thus define an orthogonal network of slip-lines. They are usually designated by α lines and β lines, according to the convention shown in Figure 6. The integration of the equation produces:

$$p + 2\tau_Y \emptyset = \text{constant} \qquad \text{along } \alpha \text{ line}$$

$$p - 2\tau_Y \emptyset = \text{constant} \qquad \text{along } \beta \text{ line}$$

It is the restriction of plane strain that allows one to solve the stresses, regardless of the strains.

The slip-line field has to be constructed to satisfy both displacement and stress boundary conditions; this is not a straight-forward matter, except in simple cases, and requires some experience. It might be necessary to carry out some experiments in order to obtain clues on how such fields should be.

Let du_x and du_y be the displacement increments in the x and y directions. When p and $\emptyset$ are known, we can use the incompressibility equation

$$du_{x,x} + du_{y,y} = 0$$

and manipulate compatibility equations through the Mohr circle to obtain:

$$\frac{d\gamma_{xy}}{(d\varepsilon_y - d\varepsilon_x)/2} = \text{cotg } \emptyset$$

These two equations result in a system of partial differential equations in du_x and du_y that can be again solved by the characteristics method. Obviously, the characteristic lines are, again, the slip lines, and the integration produces:

$$d(du_\alpha) - du_\beta d\emptyset \qquad \text{along } \alpha \text{ line}$$

$$d(du_\beta) + du_\alpha d\emptyset \qquad \text{along } \beta \text{ line}$$

Again, it is easy to calculate the displacement increments only in very simple fields.

FINITE ELEMENT METHOD

The finite element method is a mathematical technique for the solution of boundary value problems, eigenvalue problems and initial value problems. It is very flexible at the problem geometry definition level, but it requires large amounts of calculations. Hence, its development with the availability of inexpensive computers: the finite element programs accept a large variety of problems, and the computer carries out the calculations.

Together with Computer Aided Design techniques, finite elements are the area of Process Modelling in which most research and development is being done today. We will therefore spend some time explaining the basics of it, so that our next lecture can deal with the specific formulation and its applications.

The basic idea behind finite elements is to divide the domain into pieces or elements, approximately write the equations governing the problem for each element, as a function of selected values, put all elements together, apply boundary conditions to some of those selected values, and solve such values. Once this has been done, one goes back to the element equations to obtain the approximate solution variables of the problem. In terms of Table I, the finite element method is like a refined upper-bound method.

There is a large amount of theoretical background and procedural work involved which cannot be explained in a short time. We will try to highlight the greatest amount of features possible in a hand-workable example. There is abundant literature on the subject, and references (8-9) should provide the interested reader with enough background.

Let us assume that we are to analyze with finite elements, the one-dimensional problem of stretching a bar made of a linear elastic material, by imposing a load L at one end, and fixing the other end. Figure 7. For simplicity's sake, let us divide the bar in two elements. Figure 8. Each element contains two nodes. Figure 8 shows the overall configuration and the configuration of the two local elements.

The essence of the finite element theory is that everything will be described in terms of what happens at the nodes. We have to select a basic variable, in this case, a displacement u. When its field is known, we can calculate strains and, through constitutive equations, stresses. Surface integration of stresses produces loads. We are, therefore, able to determine u, and, if this has been correctly done, everything else is derivable. Now, instead of dealing with the infinite amount of u fields possible (kinematically admissible), we can deal with the infinite amount of vectors u_i, where the subscript i denotes node i (thus, $\underline{u}$ is a three-dimensional vector).

We have to define a field within each element that is uniquely defined by $\underline{u}^{(j)}$ - vector of nodal variables belonging to element u. In this case, a linear one, such as

$$u^{(1)} = u_2^{(1)} \frac{x - x_1^{(1)}}{x_2^{(1)} - x_1^{(1)}} + u_1^{(1)} \frac{x_2^{(1)} - x}{x_2^{(1)} - x_1^{(1)}} \qquad (31)$$

This is the essence of the finite element approximation. (31) is usually written as

$$u^{(i)} = \lfloor N_1 N_2 \rfloor^{(1)} \begin{Bmatrix} u_1 \\ u_2 \end{Bmatrix}^{(1)} \qquad (32)$$

where N_1 and N_2 are usually called shape functions or interpolation functions. These functions are at the element level as shown in Figure 9, and at the global level, in the present case, as shown in Figure 10. Now, the strain is calculated at the element level by

$$\varepsilon = u_{x,x} = \begin{bmatrix} N_{1,x} & N_{2,x} \end{bmatrix}^{(j)} \begin{Bmatrix} u_1 \\ u_2 \end{Bmatrix}^{(j)} \qquad (33)$$

$$= \frac{u_2^{(j)} - u_1^{(j)}}{x_2^{(j)} - x_1^{(j)}} \qquad \text{in which } N_{2,x} = -N_{1,x}$$

In a one-dimensional case, Hooke's law produces

$$\tau = E \varepsilon \qquad (34)$$

and the force on the node (2) of element (j) is

$$F_2^{(j)} = A^{(j)} \tau \qquad \text{A - crossectional area}$$

equilibrium of element requires that

$$F_1^{(j)} + F_2^{(j)} = 0$$

therefore

$$F_1^{(j)} = -A^{(j)} \tau$$

or

$$\begin{Bmatrix} F_1 \\ F_2 \end{Bmatrix}^{(j)} = A^{(j)} E \begin{bmatrix} -N_{1,x} & -N_{2,x} \\ +N_{1,x} & +N_{2,x} \end{bmatrix} \begin{Bmatrix} u_1 \\ u_2 \end{Bmatrix}^{(j)}$$

making $k^{(j)} = A^{(j)} E N_{2,x}$

$$\begin{Bmatrix} F_1 \\ F_2 \end{Bmatrix}^{(j)} = \begin{bmatrix} k & -k \\ -k & k \end{bmatrix}^{(j)} \begin{Bmatrix} u_1 \\ u_2 \end{Bmatrix}^{(j)}$$

or

$$\underset{\sim}{F}^{(j)} = \underline{k}^{(j)} \underset{\sim}{u}^{(j)}$$

We have the equations of the two elements

$$\begin{cases} F_1^{(1)} = k^{(1)} u_1^{(1)} - k^{(1)} u_2^{(1)} \\ F_2^{(1)} = -k^{(1)} u_1^{(1)} + k^{(1)} u_2^{(1)} \\ F_1^{(2)} = k^{(2)} u_1^{(2)} - k^{(2)} u_2^{(2)} \\ F_2^{(2)} = -k^{(2)} u_1^{(2)} + k^{(2)} u_2^{(2)} \end{cases}$$

in order to put everything together, or to assemble it, one imposes

$$u_2^{(1)} = u_1^{(2)}$$

$$F_2^{(1)} + F_1^{(2)} - F_2 = 0 \qquad\qquad F_1^{(1)} - F_1 = 0 \qquad\qquad F_2^{(2)} - F_3 = 0$$

where F_i is an externally applied force at node i, in this case $F_2 = 0$, $F_3 = L$, and F_1 is unknown

$$\begin{Bmatrix} F_1 = \\ 0 = \\ F_3 = \end{Bmatrix} \begin{Bmatrix} k^{(1)} & -k^{(1)} & 0 \\ -k^{(1)} & k^{(1)} + k^{(2)} & -k^{(2)} \\ 0 & -k^{(2)} & k^{(2)} \end{Bmatrix} \begin{Bmatrix} u_1 \\ u_2 \\ u_3 \end{Bmatrix} \qquad \text{or } \underline{K}\ \underset{\sim}{u} = \underset{\sim}{F}$$

As u_i is known and equal to zero, we can eliminate its equation as follows:

$$\begin{bmatrix} 1 & 0 & 0 \\ 0 & k^{(1)} + k^{(2)} & -k^{(2)} \\ 0 & -k^{(2)} & k^{(2)} \end{bmatrix} \begin{Bmatrix} u_1 \\ u_2 \\ u_3 \end{Bmatrix} = \begin{Bmatrix} 0 \\ 0 + k^{(1)} \times 0 \\ F_3 - 0 \times 0 \end{Bmatrix}$$

note that the unknown force corresponded to a known displacement. The two known forces correspond to unknown displacements. Any degree of freedom will need to have specified displacement or force. Note that the system of equations obtained is symmetric. There are a number of numerical procedures to solve such a system of equations based on the Gaussian elimination. The most used today are the skyline solution and the frontal solution, both computationally very effective. After one has established $\underset{\sim}{u}$,

$$\underline{K}\ \underset{\sim}{u} = \underset{\sim}{F} \tag{35}$$

gives the unknown forces (of course, it should also reproduce the imposed forces). (33) and (34) produce the strains and stresses at the elements.

This hap-hazard way of proceeding may be called a natural approach, and this is how it all began in the early sixties. In less simple problems, it may not be so straight-forward to proceed, and for that there are other mathematical ways of looking into finite elements.

Consider a functional

$$J = \int (\tfrac{1}{2} E A \Sigma^2)\, dx - L\, u|_{x3} \tag{36}$$

which happens to represent the total potential energy of the bar: the first term is the elastic strain energy, and the second is the externally applied force potential energy. Let us look into the stationarity of such functional with respect to the displacement field u, by making its first variation equal to zero

$$\delta J = 0$$

$$\delta J = \int EA\varepsilon \, \delta\varepsilon \, dx - L \, \delta u \big|_{x_3} = 0$$

$$= \int A\tau \delta u,_x dx - L \, \delta u \big|_{x_3} = 0$$

$$= A\tau \, \delta u \big|_{x_3} - A\tau \delta u \big|_{x_1} - L \, \delta u \big|_{x_3} - \int A\tau,_x \delta u \, dx = 0$$

We obtain the field u that produces a stationary value of J if, for any arbitrary variation u, the first variation of J, δJ is zero. From the arbitrariness of δu, we then get:

$$A\tau,_x = 0 \qquad \text{along the bar} \tag{37}$$

$$A\tau = L \qquad \text{at } x = x_3 \tag{38}$$

$$A\tau = 0 \qquad \text{at } x = x_1 \tag{39}$$

Equation (37) is the equilibrium equation, and equation (38) is the boundary condition $F_3 = L$. Therefore, the stationary situation of the potential energy almost solves our problem. The missing point was at the boundary $x = x_1$. However, if we restrict all possible displacement fields to the kinematically admissible ones, then $u = 0$ at $x = x_1$ and $\delta u = 0$ at $x = x_1$. Equation (39) disappears then and $A\tau$ will be whatever it will have to be. This is the variational approach to the BVP: if one can construct an appropriate functional of a field variable that satisfies some lower order boundary conditions, said essential boundary conditions, the value of the variable that makes the functional stationary will satisfy the differential equation on the domain and automatically, the higher order boundary conditions, said suppressible boundary conditions. The finite element approximation consists of substituting all possible field variables u by a combination of variables defined by the nodal values,

$$u = \underline{N} \, \underline{u}$$

The functional $J(u)$ becomes a function of nodal values $J_1(\underline{u})$. The stationary situation of J_1 hopefully is an approximation to the stationary situation of J. That is obtained by algebra.

$$dJ_1 = \frac{\partial J_1}{\partial u_i} \qquad du_i = 0$$

or a set of equations

$$\frac{\partial J_1}{\partial \underline{u}} = \underline{0} \tag{40}$$

in our specific case

$$J_1 = \int \frac{1}{2} E A \, \underline{u}^T \, \underline{N},_x{}^T \underline{N},_x \, \underline{u} \, dx - L \, \underline{N} \, \underline{u} \big|_{x_3} \tag{41}$$

and we leave it to the reader to find that $dJ_1 = 0$ yields as before

$$\underline{K} \, \underline{u} = \underline{F} \tag{35}$$

To make sure that it is possible to calculate the equations at the element level, and then add them, we have to ensure that in J_1 the total integral is the sum of element integrals. We note that equilibrium equation corresponds to a second derivative of u, and the problem is said to be of the order of 2p with p = 1. The functional has derivatives of the first order, or p. The shape functions must have continuous derivatives at least to order p within an element and continuous derivatives at least to order p-1 through the boundaries. The first requirement is referred to as completeness, and the second, compatibility. In our particular case, it means to make sure the forces applied at each node are well-defined.

Another way of looking at finite element approximations is through a weighted residuals method, in particular a Galerkin one. Assume again that one considers displacement fields that satisfy essential boundary conditions. Then, an approximate field produces an error within the volume

$$\varepsilon_I = \tau,_x \tag{42}$$

which we try to minimize in some way. With the Galerkin method, we look at a small variation δu produced by a variation of the nodal values

$$\delta u = N_i \, \delta u_i$$

Such a small variation will produce a variation in the error $\delta\varepsilon_I$, and we accept the best approximation when that becomes zero on the whole volume, i.e.,

$$\int \varepsilon_I \, N_i \, \delta u_i \, dV = 0 \tag{43}$$

which produces a set of equations equal to the number of nodal variables, as each can vary independently.

By substituting we have

$$\int A \, \sigma,_x \, N_i \, \delta u_i \, dx = 0$$

in order to reduce the order of the derivatives one can integrate by parts

$$\int A \sigma \, N_{i,x} \, \delta u_i \, dx - A\sigma \, N_i \delta u_i \Big|_{x_3} = 0$$

(note that $\delta u_i = 0$ at $x = x_1$).

or, using (33) and (34)

$$\int A \, E \, \delta \underset{\sim}{u}^T \, \underline{N},_x^T \, \underline{N},_x \, \underset{\sim}{u} \, dx - L \, \delta \underset{\sim}{u}^T \underline{N}^T \Big|_{x_3} = 0$$

Now the arbitrariness in $\delta \underset{\sim}{u}$ allows us to write the set of equations

$$\int A \, E \, N,_x^T \, N,_x \underset{\sim}{u} dx - L \, \underline{N}^T \Big|_{x_3} = \underset{\sim}{0}$$

which is equal to

$$\underline{K} \, \underset{\sim}{u} = \underset{\sim}{F} \tag{35}$$

as before. The main advantage of looking at the problem in this perspective is that one does not need to worry about finding a functional. In fact, for many problems, it does not exist.

We have already referred that, provided completeness and compatibility are satisfied, we can work at the element level, calculate all necessary integrals, and then add them up, or assemble them. In the example described, the integrals are very easy to calculate. However, in most applications, they are very difficult, if not impossible to obtain in closed form. Hence the common procedure of numerical integration. Simply stated, one substitutes the integral by a weighted sum of function values

$$\int f(x) \, dx = \sum_{i=1}^N W_i f(p_i) \tag{44}$$

where N is the number of integration points, W_i are the weights, and p_i are the locations of the integration points. Numerical analysis textbooks provide these locations and weights, as well as the accuracy obtainable with the procedure. An added advantage of numeric integration is that if all the equations are expressed in dimentionless local (natural) coordinates, it is very easy to program and automate the integrations.

REFERENCES

(1) Naghdi, P.M. "Stress-Strain Relations in Plasticity and Thermoplasticity", in Plasticity, Proceedings 2nd Symposium on Naval Structural Mechanics, Pergamon, 1960.

(2) Hill, R. "The Mathematical Theory of Plasticity", Oxford Clarendon Press, 1950.

(3) Altan, T., Oh, S., and Gegel, H. "Metal Forming Fundamentals and Applications", American Society for Metals, 1983.

(4) Johnson, W. and Mellor, P.B. "Engineering Plasticity" Van Nostrand Reinhold, 1973.

(5) Avitzur, B. "Handbook of Metal Forming Processes", John Wiley & Sons, 1983.

(6) Rowe, G.W. "Principles of Industrial Metalworking Processes", Arnold, 1977.

(7) Johnson, W. and Kudo, H. "The Mechanics of Metal Extrusion", Manchester University Press, 1962.

(8) Zienkiewicz, O.C. "The Finite Element Method", McGraw Hill (UK), 1977.

(9) Bathe, K.J. "Finite Element Procedures in Engineering Analysis", Prentice-Hall, 1982.
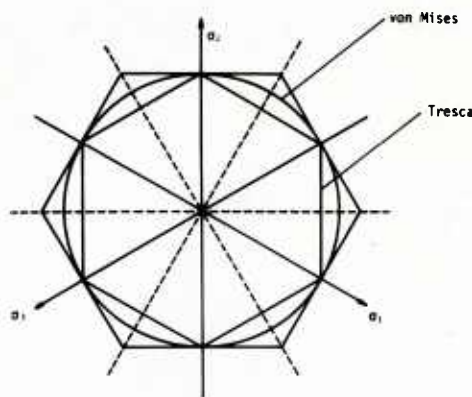
Fig 1 _ Yield surfaces in principal stress space

Fig 2 _ Expansion of yield surface with work-hardening
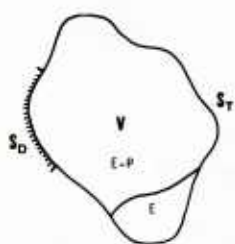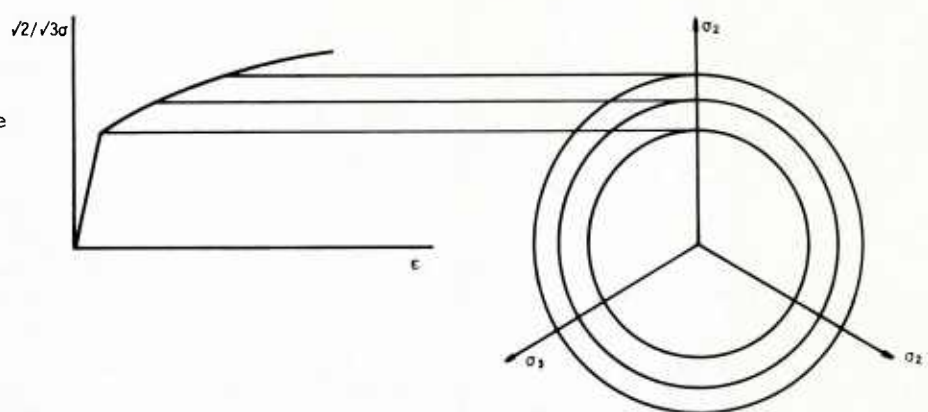

Fig 3 _ Solid mechanics boundary value problem
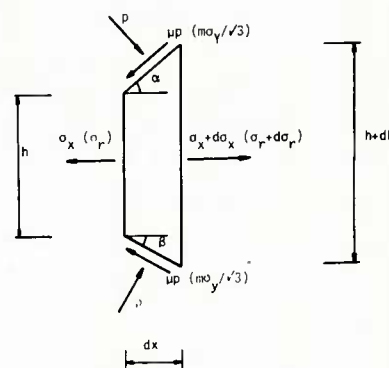
Fig 4 _ Slab
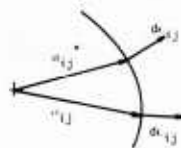
Fig 5 _ Correct and kinematically admissible strain rate
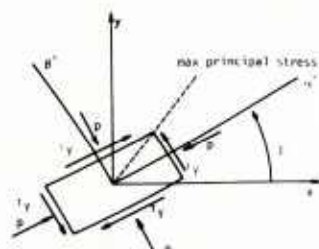

Fig 6 _ Slip line conventions

Fig 7 _ Bar stretching

Fig 8 _ Bar division into elements
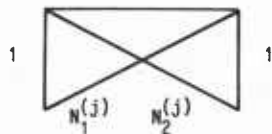

Fig 9 _ Element shape functions
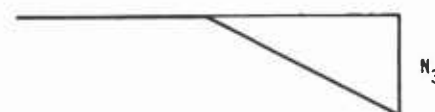
Fig 10 _ Global shape functions

Finite Element Simulation of Forging Processes

Nuno Rebelo

University of Oporto School of Engineering
Rua dos Bragas
4099 Porto, Portugal

INTRODUCTION

We will present in this lecture a finite element formulation for rigid-thermovisco-plastic metal forming analysis. This is based on the work of Kobayashi and his students over a decade (1-4). The actual theories will only be referenced to make space for the finite element equations themselves and for the algorithms that allow one to follow a deformation process by time steps.

The great advantage of finite-elements is that once the program is written, one can change the geometry of the problem completely by merely changing the input data. Therefore we advance our knowledge by classes of difficulties instead of by specific applications. The rigid-plastic formulation has proven accurate and robust enough for one to be able to dedicate oneself to the specific problem of metal forming. These problems will be reviewed here in the context of forging.

Next, sample solutions will be presented, highlighting the detailed variable distribution obtained.

In spite of the flexibility of finite element analysis, the complexity of problems treated nowadays is incompatible with hand entry of the data. Graphical pre and post processors are important tools today, allowing analysis to pass from the researcher to the analyst. With these tools input data can be interactively created and checked on a graphics screen, and the results displayed in easily understandable drawings.

Finally, one must consider that finite-element analysis is only a part of the design process and therefore, its integration into the automation of such a process is necessary by interfacing with CAD/CAM systems.

BACKGROUND EQUATIONS

Deformation

As far as deformation is concerned, the theory is not much more complicated than the one presented in the previous lecture. For the sake of simplicity, we will use tensor notation now, and instead of dealing with displacement increments, we will deal with velocities. A look at all the equations involving displacement increments will show that they are homogeneous in time; one can divide those increments by dt and obtain velocities all over.

The constitutive equations - stress-strain rate relations presented in the previous lecture - can be written in the form

$$\dot{\varepsilon}_{ij} = \frac{3}{2} \frac{\dot{\bar{\varepsilon}}}{\bar{\sigma}} \sigma'_{ij} \tag{1}$$

where we recall that σ'_{ij} is the deviatoric stress tensor.

These equations are extendable exactly in the same form to include viscoplasticity. The theory is based on the work of Perzyna (5), and this particular application was developed in (3). It basically amounts to starting at the convex and regular yield surface concept and a strain rate vector normal to such a surface. An originally static yield surface, corresponding to zero strain rate, expands more or less as a function of the strain rate. The difference in the end result now is that $\bar{\sigma} = \sigma_Y$ is a function of the effective strain rate $\dot{\bar{\varepsilon}}$. Note right away that σ_Y may be a function of temperature without it influencing the deformation theory.

The deformation process of the rigid-thermoviscoplastic materials is associated with the following boundary value problem. At a generic stage in the process of quasi-static distortion, the shape of the body, the internal distribution of temperature, the state of inhomogeneity, and the current values of material parameters are supposed to be given or to have been determined already. The velocity vector is prescribed on a part of the surface S_V, together with traction on the remainder of the surface S_T. Equilibrium equations and compatibility and incompressibility equations are satisfied by the stress and velocity field solutions.

To solve the boundary value problem, a weak form of the equilibrium equations is used. Neglecting body forces, and for quasistatic problems equilibrium equations are

$$\sigma_{ij,j} = 0 \tag{2}$$

Multiplying by an arbitrary perturbation of the velocity field, and integrating over the volume

$$\int_V \tau_{ij,j} \, \delta u_i \, dV = 0 \tag{3}$$

By using divergence theorem, symmetry of the stress tensor, and imposing $\delta u_i = 0$ in S_v

$$\int_V \tau_{ij} \, \delta \dot{\varepsilon}_{ii} \, dV - \int_{S_T} F_i \, \delta u_i \, dS_T = 0 \tag{4}$$

F is the surface traction.

Among the velocity fields that satisfy incompressibility and velocity boundary conditions, the solution of the problem is the one for which any arbitrary $\delta \underline{u}$ will satisfy (4).

The incompressibility condition can be stated as

$$\dot{\varepsilon}_{ij} = 0 \tag{5}$$

and it is imposed by means of a Lagrangian multiplier λ, that happens to be equal to the average stress

$$\int_V \tau'_{ij} \, \delta \dot{\varepsilon}_{ij} \, dV - \int_{S_T} F_i \delta u_i \, dS_T + \int_V \lambda \delta \dot{\varepsilon}_{ii} \, dV + \int_V \dot{\varepsilon}_{ii} \, \delta \lambda \, dV = 0 \tag{6}$$

Now the solution is the velocity field and average stress fields that satisfy prescribed boundary velocities, and that for any arbitrary perturbation $\delta \underline{u}, \delta \lambda$, satisfy equation (6).

Energy Balance

Considering that a hot metalworking process does not take long, and that temperature changes are due mainly to plastic work and losses to the environment, a simple Fourier law for heat flux is used, with isotropic conductivity

$$q_i = K_1 \, T_{,i}$$

where q_i is the heat flux through a unit surface normal to the direction i, and T is the temperature.

The first law of thermodynamics, stating balance of energy, can be written locally as

$$\alpha \tau'_{ij} \, \dot{\varepsilon}_{ij} + K_1 \nabla^2 T - pc \, T = 0 \tag{7}$$

where pc is the volume specific heat of the material, $\sigma'_{ij} \dot{\varepsilon}_{ij}$ represents the rate of heat generated per unit volume due to plastic deformation. The parameter α, which we usually fix at $\alpha = 0.9$ takes care of the fact that a small percentage of the plastic work is used in structural changes, and avoids having to take into consideration other internal energy terms.

The thermal problem is an initial value problem in which initial temperatures are specified, energy balance has to be satisfied through equation (7), and on the surface of normal n a heat flux is prescribed. This latter can be either a direct one

$$K_1 \, \frac{\partial T}{\partial n} = q_n^d$$

or a radiation heat flux

$$K_1 \, \frac{\partial T}{\partial n} = q_n^r = \sigma \varepsilon (Te^4 - Ts^4) \tag{8}$$

where

σ – Stephan Boltzman constant

ε – emissivity of the surface

Te – environment temperature

Ts – surface temperature

or a convection heat flux

$$K_1 \, \frac{\partial T}{\partial r} = q_n^c = h(Te - Ts) \tag{9}$$

where h – surface heat transfer coefficient.

To solve the initial value problem, a weak form again of the heat balance equation is used. Multiplying (7) by an arbitrary perturbation of the temperature field, and integrating over the volume we get

$$\int_V K_1 T_{,ii} \delta T \, dV - \int_V pc \, \dot{T} \, \delta T \, dV + \int_V \alpha \sigma'_{ij} \dot{\varepsilon}_{ij} \, \delta T \, dV = 0$$

By using divergence theorem we get

$$\int_V K_1 T_{,i} \, \delta T_{,i} \, dV + \int_V pc\dot{T} \delta T \, dV - \int_V \alpha \sigma'_{ij} \dot{\varepsilon}_{ij} \delta T \, dV -$$

$$-\int_S q_n \delta T \, dS = 0 \tag{10}$$

The solution to the problem is the sequence of temperature fields along time that for any arbitrary perturbation δT satisfy (10).

FINITE ELEMENT EQUATIONS

Consider the body being studied divided in m elements connected by n nodes. The velocity field in (6) and the temperature field in (10) are approximated by

$$u = \underline{N}^T \underline{v} \tag{11}$$

$$T = \underline{N}^T \underline{T} \tag{12}$$

where

$\underline{v}$ - vector of nodal point velocities

$\underline{T}$ - vector of nodal point temperatures

$\underline{N}$ - interpolation function vector

$\underline{N}$ - interpolation function matrix

The integrals of the previous equations are the sum of integrals over each element, provided completeness and compatibility are satisfied. The highest derivative being of order one, C^0 continuity is sufficient. We will make the derivations for bilinear isoparametric four node elements, which are the most commonly used in applications. Thus, the same interpolation functions apply for the coordinates, say r and z in axisymmetric problems

$$r = \underline{N}^T(s,t)\underline{r} \tag{13}$$

$$z = \underline{N}^T(s,t)\underline{z}$$

Figure 1 shows a general element, s and t being the natural coordinates.

A single value of the Lagrangian multiplier λ is assigned to each element. This lower order interpolation is used in order not to overconstrain the system. It produces the same effect as the well-known technique of reduced integration when a penalty function constraint is imposed.

Velocity Equations

The strain rate tensor can be written in a vector form (with all of its components)

$$\dot{\underline{\varepsilon}} = \underline{B} \, \underline{v} \tag{14}$$

matrix $\underline{B}$ containing appropriate spatial derivatives of interpolation functions. And the effective strain rate is expressed in the form

$$\dot{\bar{\varepsilon}} = (\dot{\underline{\varepsilon}}^T \, \underline{D} \, \dot{\underline{\varepsilon}})^{1/2} = (\underline{v}^T \underline{B}^T \, \underline{D} \, \underline{B} \, \underline{v})^{1/2} = (\underline{v}^T \, \underline{P} \, \underline{v})^{1/2} \tag{15}$$

Substitution in (6) yields

$$\sum_{j=1}^m \left\{ \int_{V_j} \frac{\sigma_Y}{\dot{\bar{\varepsilon}}} \delta \underline{v}^T \, \underline{P} \, \underline{v} dV_j - \int_{S_{F_j}} \delta \underline{v}^T \, \underline{N} \, \underline{f} \, dS_{F_j} \right.$$

$$\left. + \int_{V_j} \lambda \delta \underline{v}^T \underline{B}^T \, \underline{c} dV_j + \int_{V_j} \underline{v}^T \underline{B}^T \, \underline{c} \, \delta \lambda \, dV_j \right\} = 0 \tag{16}$$

where

$$\underline{c}^T \dot{\underline{\varepsilon}} = \dot{\varepsilon}_{ii} \tag{17}$$

Due to the arbitrariness in $\underset{\sim}{v}$ and λ the following system of nonlinear equations in $\underset{\sim}{v}$ and linear in λ is obtained

$$\sum_{j=1}^{m} \left\{ \int_{V_j} \sigma_Y \frac{P}{\dot{\bar{\varepsilon}}} \underset{\sim}{v}\, dV_j - \int_{S_{F_j}} \underset{\sim}{N}\, \underset{\sim}{T}\, dS_{F_j} + \lambda_j \int_{V_j} \underline{B}^T \underset{\sim}{c}\, dV_j \right\} = 0 \tag{18}$$

$$\int_{V_j} \underset{\sim}{v}^T \underline{B}^T \underset{\sim}{c}\, dV_j = 0$$

These equations have the form

$$\underline{f}(\underset{\sim}{v} \cdot \lambda) = \underline{0} \tag{19}$$

and are solved by the Newton-Raphson procedure. Making series expansion and keeping only the first two terms,

$$\underline{f}(\underset{\sim}{v}, \lambda) \approx \underline{f}(\underset{\sim}{v}_n, \lambda) + \frac{\partial \underline{f}}{\partial \underset{\sim}{v}}(\underset{\sim}{v}_n, \lambda)\Delta \underset{\sim}{v}_n = 0 \tag{20}$$

The result is the following system of equations linear in λ and $\Delta \underset{\sim}{v}$

$$\left[\begin{array}{c|c} \sum\limits_{j=1}^{m} \left\{ \int_{V_j} \sigma_Y \frac{P}{\dot{\bar{\varepsilon}}}\, dV_j + \int_{V_j} \underline{R}\, dV_j \right\} & \int_{V_j} \underline{B}^T \underset{\sim}{c}\, dV_j \\ \hline \int_{V_j} \underline{B}^T \underset{\sim}{c}\, dV_u & 0 \end{array} \right] \left\{ \begin{array}{c} \Delta \underset{\sim}{v} \\ \hline \lambda \end{array} \right\} \tag{21}$$

$$= \left\{ \begin{array}{c} \sum\limits_{j=1}^{m} \left[\int_{S_{F_j}} \underset{\sim}{N}\, \underset{\sim}{T}\, dS_{F_j} - \int_{V_j} \sigma_Y \frac{P}{\dot{\bar{\varepsilon}}} \underset{\sim}{v}\, dV_j \right] \\ \hline \int_{V_j} \underset{\sim}{v}^T \underline{B}^T \underset{\sim}{c}\, dV_j \end{array} \right\}$$

where

$$\underline{R} = \left(-\sigma_Y \dot{\bar{\varepsilon}}^{-3} + \frac{\partial \sigma_Y}{\partial \dot{\bar{\varepsilon}}} \dot{\bar{\varepsilon}}^{-2} \right) \underset{\sim}{v}^T \underline{P}^T \underline{P}\, \underset{\sim}{v} \tag{22}$$

Numerical quadrature using 2×2 points is used in the calculation of the integrals. After each iteration, the values of v are updated as

$$\underset{\sim}{v}_{n+1} = \underset{\sim}{v}_n + \beta \Delta \underset{\sim}{v}_n \tag{23}$$

where β is a deceleration coefficient, $0 < \beta < 1$. The values of β are chosen according to the convergence character of the system of equations.

A drawback in the Newton-Raphson method is that it requires an initial guess for the velocity field. This initial guess, when not easy to find, can be calculated as follows. Assume any reasonable value for $\dot{\bar{\varepsilon}}$. Then equation (18) becomes linear in $\underset{\sim}{v}$ and λ, for which they are solved. Then $\dot{\bar{\varepsilon}}$ is updated, and the procedure is repeated a couple of times.

Temperature Equations

Making

$$M_{ij} = N_{i,j} \tag{24}$$

and substituting with (12) and (10)

$$\sum_{j=1}^{m} \left[\int_{V_j} k_1 \delta \underline{T}^T \underline{M}\, \underline{M}^T \underline{T}\, dV_j + \int_{V_j} \rho c \delta \underline{T}^T \underset{\sim}{N}\, \underset{\sim}{N}^T \dot{\underline{T}}\, dV_j \right.$$

$$\left. - \int_{V_j} q \delta \underline{T}^T \underset{\sim}{N}\, dV_j - \int_{S_{q_j}} q_n \delta \underline{T}^T \underset{\sim}{N}\, dS_{q_j} \right] = 0 \tag{25}$$

due to arbitrariness in $\underset{\sim}{T}$ the following system of equations is obtained

$$\sum_{j=1}^{m} \left[\int_{V_j} k_1 \, \underline{M} \, \underline{M}^T dV_j \underset{\sim}{T} + \int_{V_j} pc \, \underset{\sim}{N} \, \underset{\sim}{N}^T dV_j \dot{\underset{\sim}{T}} \right.$$

$$\left. - \int_{V_j} q \underset{\sim}{N} dV_j - \int_{S_{q_j}} q_n \underset{\sim}{N} \, dS_{q_j} \right] = 0 \tag{26}$$

or

$$\underline{C} \, \dot{\underset{\sim}{T}} + \underline{K} \, \underset{\sim}{T} - \underset{\sim}{Q} - \underset{\sim}{Q}_n = \underset{\sim}{0} \tag{27}$$

where

$$\underset{\sim}{Q} = \int_V \alpha \sigma'_{ij} \, \dot{\varepsilon}_{ij} \, dV \tag{28}$$

$$\underset{\sim}{Q}_n = \int_{S_r} \nabla \varepsilon \, (Te^4 - Ts^4) \, \underset{\sim}{N} \, dS_r + \int_{S_C} h(Te - Ts) \, \underset{\sim}{N} \, dS_C +$$

$$+ \int_{S_1} h_1 \, (Td - Tw) \, \underset{\sim}{N} \, dS_1 + \int_{S_f} q_f \, \underset{\sim}{N} \, dS_f \tag{29}$$

In (29) the first component is the contribution of the heat radiated into the body, and the second, the contribution of the heat transferred by convection. The third term is identical to the second and corresponds to the heat transferred between a workpiece and a die, described in a convection-like manner. The fourth term is the heat generated by friction at an interface, where q_f is half of the friction force multiplied by a relative velocity.

Time Dimension

In order to describe a deformation process in time, integration of equations (1) and (27) has to be done. As far as the strain equation is concerned, the assumption of no inertial effects requires that for small intervals of time, velocities and strain rates change by very small amounts. Therefore, the strains at time $t + \Delta t$ are obtained from strains and strain rates at time t

$$\varepsilon_{t + \Delta t} = \varepsilon_t + \dot{\varepsilon} \Delta t \tag{30}$$

Updating the configuration using velocities is done in the same way.

To integrate equation (27) a one-step method is used. Otherwise, the storage requirements would escalate too much. Convergence of a scheme requires consistency and stability. Consistency is satisfied by an approximation of the type

$$\underset{\sim}{T}_{t + \Delta t} = \underset{\sim}{T}_t + \Delta t \times \left[(1-\beta) \dot{\underset{\sim}{T}}_t + \beta \dot{\underset{\sim}{T}}_{t + \Delta t} \right] \tag{31}$$

where β is a parameter varying between 0 and 1.

Equations (21) and (27) are highly coupled, making a simultaneous solution of their finite element counterparts necessary.

An implementation of the algorithm previously described, considering $T_{t + \Delta t}$ as a primary dependent variable, has been elaborated in order to include the coupling of the solution of stress equilibrium equations with heat balance.

The sequence of calculations to be performed in one time step Δt is as follows:

a) assume that the initial temperature field $\underset{\sim}{T}_o$ is known;

b) calculate initial velocity field;

c) calculate initial temperature rates $\dot{\underset{\sim}{T}}_o$;

d) calculate

$$\hat{\dot{T}} = -\frac{1}{\beta \Delta t} \cdot \underset{\sim}{T}_o - \frac{(1-\beta)}{\beta} \cdot \dot{\underset{\sim}{T}}_o$$

e) update displacements and strains;

f) use the old velocity field for first approximate temperature calculations

$$\underset{\sim}{R} = \underset{\sim}{Q}_{\Delta t}^{(1)} - \underline{C} \, \hat{\dot{\underset{\sim}{T}}}$$

solve

$$(\underline{K} + \frac{1}{\beta \Delta t}\ \underline{C}) \cdot \underset{\sim \Delta t}{T}^{(1)} = \underset{\sim}{R}\ \text{for}\ \underset{\sim \Delta t}{T}^{(1)}$$

g) calculate new velocity field;

h) calculate second values for temperatures

$$\underset{\sim}{R} = \underset{\sim \Delta t}{Q}^{(2)} - \underline{C}\ \dot{\underset{\sim}{T}}$$

solve

$$(\underline{K} + \frac{1}{\beta \Delta t}\ \underline{C}) \cdot \underset{\sim \Delta t}{T}^{(2)} = \underset{\sim}{R}\ \text{for}\ \underset{\sim \Delta t}{T}^{(2)}$$

i) iterate until convergence;

j) calculate new temperature rate

$$\dot{\underset{\sim \Delta t}{T}} = \dot{\underset{\sim}{\hat{T}}} + \frac{1}{\beta \Delta t}\ \underset{\sim \Delta t}{T}$$

We treat the workpiece and the dies separately. In this way we greatly reduce the number of equations to be solved simultaneously, which in turn reduces computing costs. Because of the heat transfer at the interface, die and workpiece equations contain temperatures of each other, and the solution is found iteratively. This brings no increase in cost because iterations with respect to velocities have to be done anyway. Realistic heat transfer coefficients at the interface do not produce instabilities in the iteration process.

FORGING SPECIFICS

Once the formulation and the finite element equations are written, one might think that problems can be immediately solved. In classical structural analysis type of problems, it might be so because real problems are not far from the typical boundary value problem we have been talking about in abstract terms. Let us look again at the schematics of it, as you can see in Figure 2.

Where we have a volume in which equilibrium equations, compatibility equations and constitutive equations, together with heat balance equations have to be satisfied; and there is a surface, on part of which velocities are imposed, and in the rest of which forces are imposed, together with convection, radiation, etc., and heat transfer boundary conditions.

Let us pick up now one of the simplest forging problems one can think of, ring compression, and take a closer look at the situation, as shown in Figure 3.

There is the ring in which we search for variables such as displacements, velocities, strains, strain-rates, stresses, temperatures, being deformed by dies that have a certain speed, and which deform also (hopefully elastically), and with heat conduction through them. The boundaries are made of ring free boundaries, contact boundaries, and die free boundaries. Along the contact boundaries, there are prescribed velocities in the vertical direction but prescribed forces (friction) in the horizontal direction. Heat transfer includes radiation and convection along the free boundaries, and convection-like terms through the interface in the contact areas.

Current programs consider the dies as rigid, i.e., the elastic deformations of such dies are too small to interfere with the deformation of the workpiece and with its dimensional accuracy. However, simultaneous solution of heat transfer equations in workpiece and dies is necessary in warm forging, hot die forging and isothermal forging, because heating of dies not only interferes with the heat transfer but may affect its structural integrity.

In a problem like ring compression, when one considers reasonably high friction, a neutral zone develops which brings up two important features.

First, a rigid zone within the deforming body develops. In rigid-plastic analysis, stresses are undetermined for zero strain rate. Whenever some regions in a non-uniform deformation process become rigid, or almost nondeforming, the system of equations (21) becomes very ill-conditioned. In fact, $\dot{\bar{\varepsilon}}$ being in the denominator, produces some very large values in the matrices. To obviate that, material behaviour is modified, and a strain-rate offset $\dot{\varepsilon}_0$ below which stress drops linearly to zero is imposed (2), as shown in Figure 4. This offset value is chosen because of numerical reasons only, and should not be related to real material behaviour. Values of 2 orders of magnitude smaller than an average strain rate in the deformation have given successful results.

In the elements in which $\dot{\bar{\varepsilon}} < \varepsilon_0$, equations (21) and (22) are conveniently modified.

Boundary tractions imposed in metal forming problems are mainly frictional forces. The modeling of these forces is traditionally made in two ways: by means of a friction coefficient and by means of a friction factor. A directly applied friction coefficient leads to non-symmetric matrices and is not commonly used in bulk deformation metal forming. A friction factor, defined by the equation

$$\tau = mk_y \tag{32}$$

where

τ - shear friction stress

k_y - shear yield stress of the material

m - friction factor

was used in the examples presented here. Although friction modeling is still empirical, and somewhat far from reality as has been pointed out in a recent survey paper (6), we believe that until further research clarifying the correct mechanisms is done, consistent ways of modeling should be used so that different analyses may be compared and, more importantly, experimental data can be quantified.

A major problem is faced when a point of reverse relative velocity between workpiece and die exists, and its position is not known a priori, like the neutral line. The orientation of the friction force changes at that point, so an abrupt jump in its value shows up, rendering equations (21) very ill-conditioned. Chen and Kobayashi (2) have made the problem amenable by substituting such step functions for an arc tangent function, as close to the step as desired. The final equation for the friction force is given by

$$f = -mk_y \left\{ \left(\frac{2}{\pi} \right) \tan^{-1} \left(\frac{V_R}{a} \right) \right\} \underset{\sim}{t} \tag{33}$$

where

m - friction factor ($0 \leqslant m \leqslant 1$);

k_y - shear yield stress;

V_R - magnitude of relative velocity between die and workpiece;

a - constant several orders of magnitude less than the die velocity.

The introduction of this frictional force requires linearization in the corresponding surface integrals of equation (18), modification of the contents of equation (21) but not its form.

The next specific problem we encounter is the fact that along time, the geometry changes. Up to reasonable amounts of deformation the bulk changes do not present a problem; however, the boundary conditions do change. Part of the surface that was free comes in contact with the dies, therefore becoming restricted in the normal direction, and with frictional forces applied in the tangential direction. The type of heat transfer changes too, of course. The possibility of defining one or more dies, moving or not, with arbitrary shape, together with all the geometric verifications and adaptations requires some programming, but does not really follow any theory in particular. A scheme with which we have worked, geometry-wise (7), defines dies by a sequence of points which have to be entered in a certain sequence as defined in Figure 5. Each two consecutive points define a segment to which an inclination corresponds. If there is a node touching a given segment, its inclination defines the direction of the friction forces, and its normal, the direction of the velocity restriction. The sequence of activities, deformation-wise, are:

1) Start with the preform in contact with one or more dies;
2) Approach the other dies until first point is touched;
3) Initialize the problem;
4) Calculate velocity field;
5) Determine minimum time for another point to touch a die;
6) Choose time increment;
7) Update positions, strains;
8) Update boundary conditions
9) Force sliding nodes onto surface;
10) Repeat from 4) on.

After very large amounts of deformation, the initial mesh may distort and some elements may even degenerate, after which not only do the calculations become unreliable, but it may be impossible to obtain any results. This situation requires starting again with a new mesh, to which the relevant variables will have to be transposed. As far as the deformation part is concerned, the strains need to be carried from step to step because of work hardening. So one has to interpolate them from the element values of the old mesh into the element values of a new mesh. With respect to heat transfer analysis, it is the temperatures that one has to interpolate from nodal values of the old mesh into nodal values of a new mesh. These procedures cannot be done by hand and intermediate programs have to be written for them. We will describe the software developped in conjunction with graphical pre and post processors that deals with this problem in a semi-automatic way (8). Figure 6 shows the connections between such software.

We start with a commercially available finite-element pre and post processor. An original mesh is created, as well as the geometry of the dies (by means of a series of linear beams). Information on nodal restrictions is input also at this level. This program writes all the information received into a file, in a format called "universal".

Then, an intermediate completely interactive program that we have called Sinter reads the universal file, and asks for all other necessary information for running the finite element program. This information includes the boundary nodes, precisions on die interface nodes, operating conditions, and so on. It writes a binary file with most of information and a very small formatted file which contains control information.

The finite element code accesses both the control and the binary file and executes the number of steps required. It appends the results of pre-selected steps to the binary file, and prints whatever information was indicated in the control parameters.

With the intermediate program one can access again the binary results of the stored steps and write them in another universal file, or then create a new control file that will make the finite element code restart the analysis at any intermediate point.

The pre and post processor can access the new universal file and display the results in terms of distorted meshes, isoline plots of all result variables, nodal forces or plots of variables along selected lines.

If, upon examining the results, the analyst decides that a remesh is necessary, he can again use the intermediate program to create a new type of universal file. This one contains only the dies and the boundary points. With the pre processor he can start with the data of such file and create a new mesh, which in turn will be again written on a start-like universal file. Finally, the intermediate program will access both the old and the new mesh automatically interpolating the necessry variables, and interactively asking for the operating parameters. As a result, a new control file is written, and a new binary file is started. The finite element code interprets these as in a starting process.

I would like to emphasize again that during a complete analysis no files are created by hand. Geometry and meshes are interactively created on a graphics screen, and the intermediate code Sinter operates uniquely by questions and answers, with some suggested values for less obvious parameters.

I would like to make a few comments on the interpolations done during remeshing, realizing that there are, in the literature, several ways of doing this, and that my own procedures have evolved since I started using them a couple of years ago.

In the analysis referred to in this text, an average value of strain is calculated at each element which can be seen as the value at the center. The interpolation procedure for strains goes as follows: networks of element centers, old and new, are set aside as shown in Figure 7; then, for each new center, the three closest old centers are searched for; finally, the strain values are linearly interpolated (or extrapolated).

The temperatures are nodal values. In order to interpolate it is necessary to find into which old element a new node falls. Then this element is divided in triangles and the temperature is linearly interpolated in such triangles.

SAMPLE SOLUTIONS

To illustrate the capabilities of the formulations presented, we will start with the above-mentioned ring compression. One quarter of a ring with an o.d. : i.d. : height ratio of 6 : 3 : 2 is shown in Figure 8, with a mesh laid on it (4). The material is Aluminium 1100, at an original temperature of 427°C, being deformed by dies at room temperature.

The die velocity simulated a mechanical press at 90 strokes per minute, and a reduction in height of 50% was done in 1% steps. A friction factor of m=1 was applied. These conditions attempt to simulate an experiment by Nagpal, Lahoti and Altan (9). The heat transfer material properties were taken from the literature.

Figure 9 compares the decrease in inner diameter vs reduction in height obtained in the present calculations with the experimental point of Nagpal et al., and with previous solutions not including temperature effects. When the effect of temperature is included, the effect of chilling by the dies causes relatively small sliding along the interface and results in more decrease in inner diameter than the case without temperature effect.

Figure 10 shows the ring profiles after 48.5% reduction. The agreement is excellent between computed and experimental profiles.

Grid distortions, indicating the flow of material after 20 and 50% reduction, are presented in Figures 11 and 12. The neutral zone is distinctively traceable, and the large amounts of folding are evident. Their equivalent effective strain distributions, clearly showing the nonuniform deformation, are given in Figures 13 and 14. The most deformed areas are the original corners in contact with the die, and the least deforming regions are noticeable near the neutral axis.

In Figures 15 and 16 temperature contours in both ring and die are presented. The temperature field is dominated by the heat flow from the workpiece to the die, and only near the equator, temperatures rise slightly. Temperature differences across the workpiece die interface decrease from 407 K initially, to around 220 K at the end of deformation.

Our next example shows the versatility of boundary condition treatment. It is the forging in plane-strain of a turbine blade cross-section. Figure 17 shows the die profile with the preform. This is one of several verifying simulations that reproduce experiments done with plasticine. Therefore isothermal conditions and plasticine material properties were used. Figures 18 and 19 show the influence of friction conditions. In the first, m=0.3 was used, and the material slid down the cavity. With m=0.6 in the second, this did not happen and mostly only crushing took place. Remeshing was done at this point, and Figure 20 shows the profile that was sent to the pre processor for the creation of "new mesh" presented in Figure 21.

Figures 22 and 23 show the strain distributions before and after remeshing which agree reasonably well. The side areas have deformed very little, and most of the deformation occurred in a shear-like zone between the original zones of contact.

Finally, Figure 24 shows some steps further in the deformation, with the material entering the flash on the right-hand side.

A third example (10) simulates the forging of a rib. This is a quite common and hard forging feature because very high pressures are necessary to obtain a complete filling. Again, isothermal forging conditions were used. Figure 25 shows the starting configuration, and Figure 26, the distorted mesh after completely filling the die cavity when frictionless condition is simulated. In this case, no remeshing was necessary. However, when one applies friction, with m=0.4, two remeshes were needed to reach the same deformation, as shown in Figure 27. The material has a hard time going around the corner; friction makes the material in the lower contact areas stick to the die, therefore overstretching the elements.

A LOOK AHEAD

As we have stated before, a finite element analysis is only a part of the design process. Actually, given the amount of computer time involved, and the intricacies of obtaining a solution, it is not yet quite feasible to do extensive optimization with this type of analysis. Problems like preform and blocker design, positioning of preform, parting lines, flash design, etc., etc., have to be solved prior to the finite element analysis, either by empirical methods, or more simple calculation procedures which lend themselves to interactive trials and corrections. The finite element analysis should be done then as a more accurate verification, providing data for die calculations.

After this, dies and preforms still have to be manufactured. It becomes obvious that if one wants to automate the production process, the finite element part should be integrated in the general automation tools.

CAD/CAM systems are today the basis for computerized design, for data transmission between customer and forger, and between designer and actual manufacturer. Therefore, the software we have talked about in this lecture will, in the future, be connected to such CAD/CAM systems. The pre and post processor should be able to accept data coming from a CAD database, and be able to send back corrections. Material properties and operating conditions should be accessed by programs like our Sinter from manufacturing and know-how databases. Furthermore, whatever knowledge is created by the simulation should be incorporated in such databases.

REFERENCES

(1) Lee, C.H. and Kobayashi, S. "New Solutions to Rigid Plastic Deformation Problems using a Matrix Method" Trans. of ASME, J. of Eng. for Industry, vol. 95, p. 865 (1973).

(2) Chen, C.C. and Kobayashi, S. "Rigid Plastic Finite Element Analysis of Ring Compression" Applications of Numerical Methods to Forming Processes, ASME, AMD, vol. 28, p. 163, (1978).

(3) Oh, S. I., Rebelo, N., and Kobayashi, S. "Finite Element Formulation for the Analysis of Plastic Deformation of Rate-Sensitive Material for Metal Forming", Metal Forming Plasticity, IUTAM Symposium, Tutzing, Germany, p. 273 (1978)

(4) Rebelo, N. and Kobayashi, S. "A Coupled Analysis of Viscoplastic Deformation and Heat Transfer - I Theoretical Considerations/II Applications" Int. J. Mechanical Sciences, vol. 22, pp 699-707 (1980).

(5) Perzyna, P. "Thermodynamic Theory of Viscoplasticity", Adv. Applied Mech., vol. 11, p. 313 (1971).

(6) Wilson, W.R.D. "Friction and Lubrication in Bulk Metal Forming Processes", J. of Appl. Metalworking, vol. 1, p. 7 (1979).

(7)   Rebelo, N., Rydstad, H., and Schröder, G.   "Simulation of Material Flow in Closed-Die Forging by Model Techniques and Rigid-Plastic FEM", Numerical Methods in Industrial Forming Processes, Proc. Int. Conference, Swansea, p. 237 (1982).

(8)   Rebelo, N., Ham, B., and Boer, C.R. "A FiniteElement Package for Metal Forming Simulation", submitted for publication.

(9)   Nagpal, V., Lahoti, G.D., and Altan, T. "A Numerical Method for Simultaneous Prediction of Metal Flow and Temperatures in Upset Forging of Rings", ASME Paper No. 77, WA/PROD-37 (1977).

(10)   Rebelo, N. and Boer, C.R. "A Process Modeling Study of the Influence of Friction During Rib Forging", 12th North American Manufacturing Research Conference, p. 146 (1984).
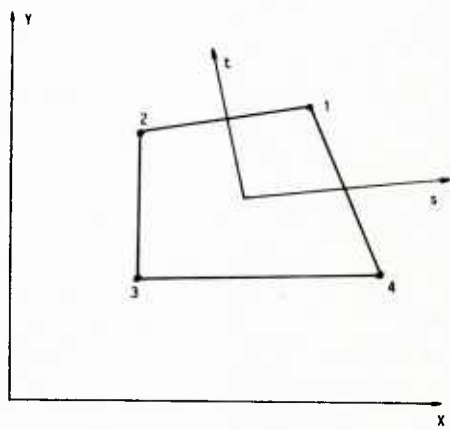
Fig 1 _ Quadrilateral element and natural coordinate system
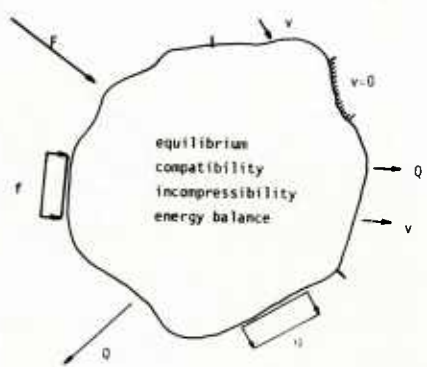
Fig 2 _ General form of a solid mechanics problem
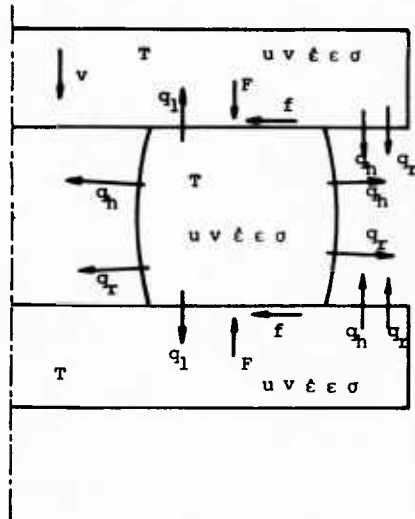
Fig 3 _ Typical forging problem
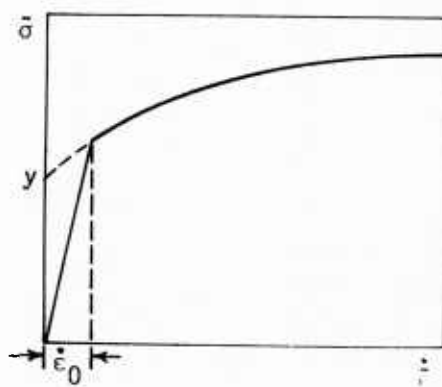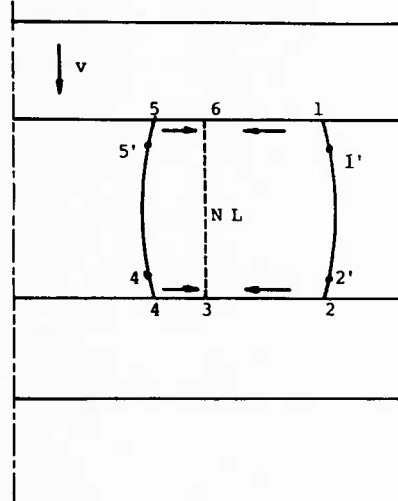
Fig 4 _ Schematic stress strain curve for rigid viscoplastic materials and modification with offset strain rate
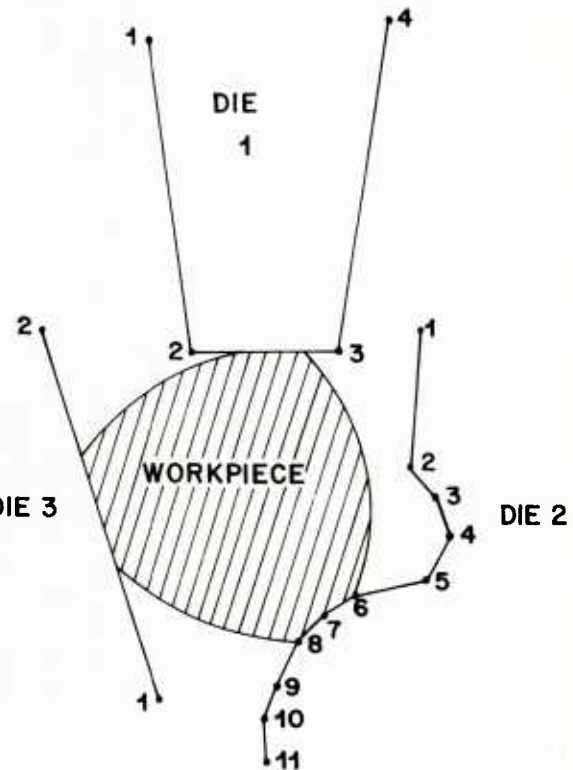
Fig 5 _ Definition of arbitrarily shaped dies
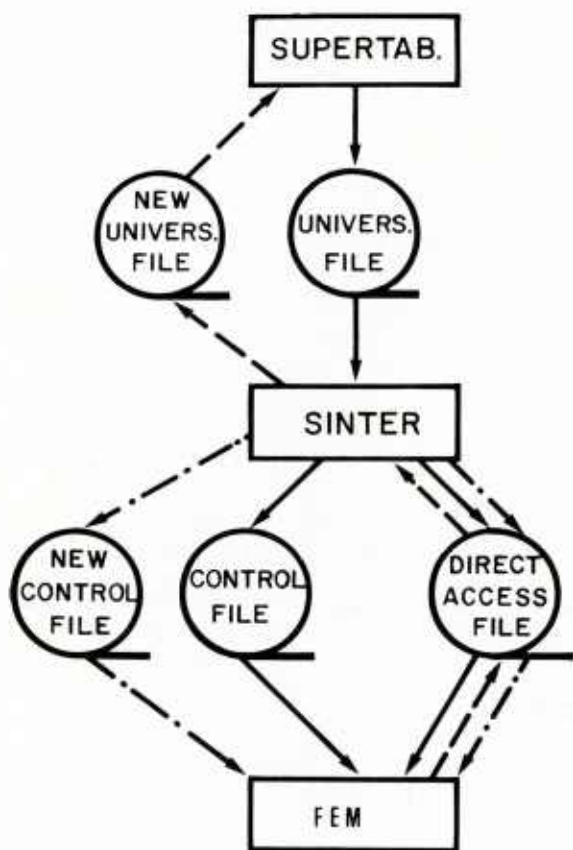
Fig 6 _ Software for forming simulation
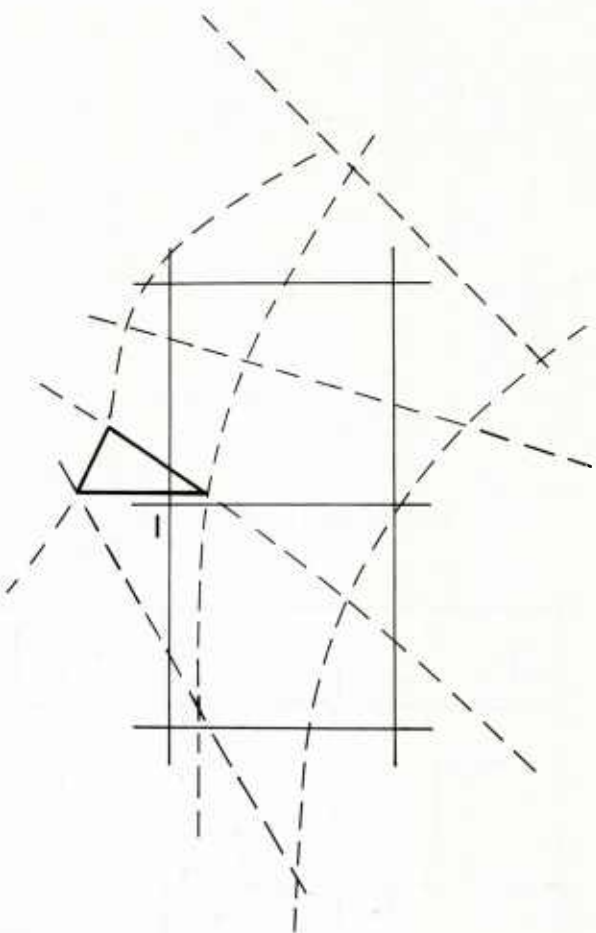
Fig 7 _ Strain interpolation scheme
during remeshing
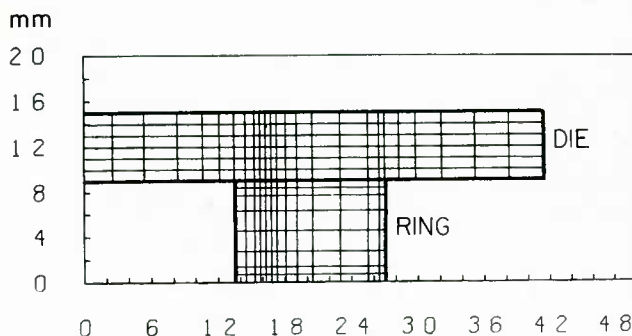
Fig 8 _ Initial mesh for ring
compression
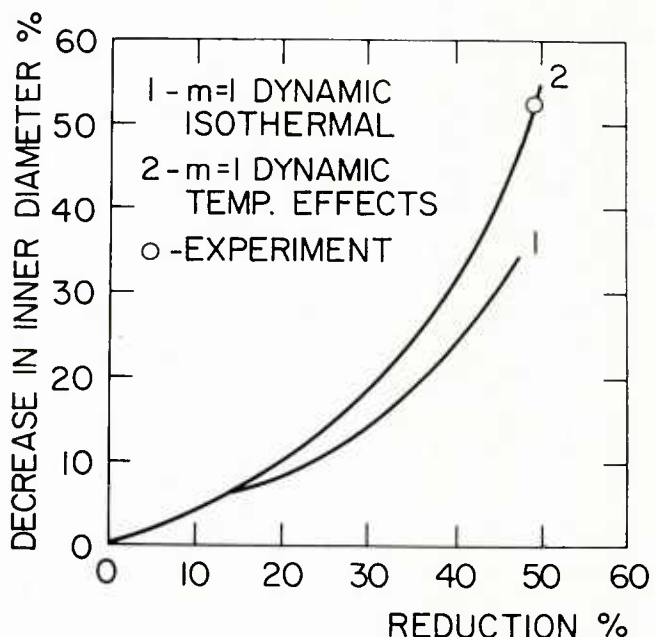
Fig 9 _ Change of ring inner diameter
as function of reduction in
height

| 1 | m=1 DYNAMIC ISOTHERMAL
| 2 | EXPERIMENTAL
| 3 | m=1 DYNAMIC TEMP. EFFECTS
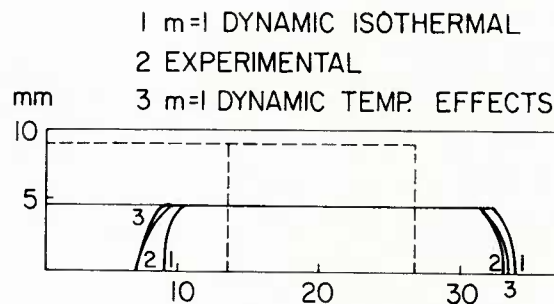
Fig 10 _ Deformed ring profiles
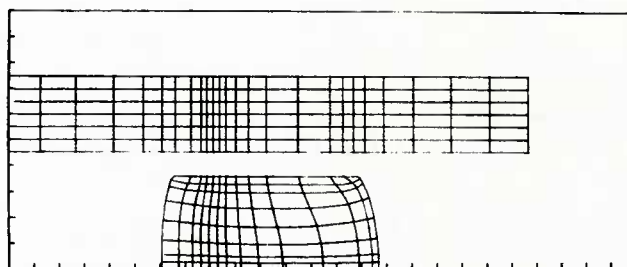
Fig 11 _ Grid distortion of ring
at 20% reduction in height
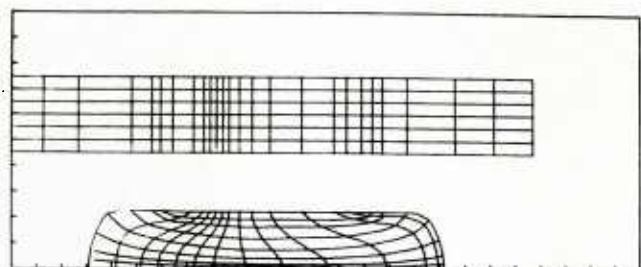
Fig 12 _ Grid distortion of ring
at 50% reduction in height
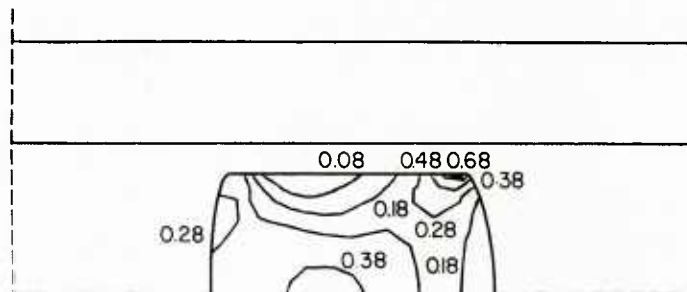
Fig 13 _ Strain distribution of ring
at 20% reduction in height
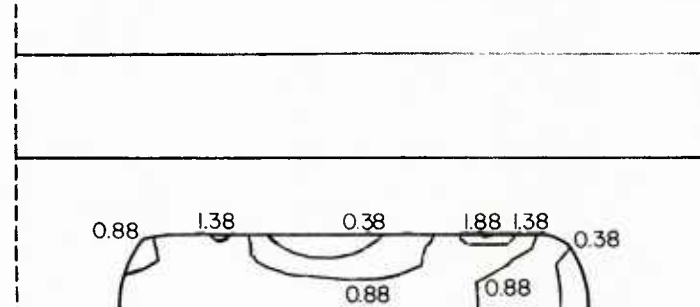
Fig 14 _ Strain distribution of ring
at 50% reduction in height
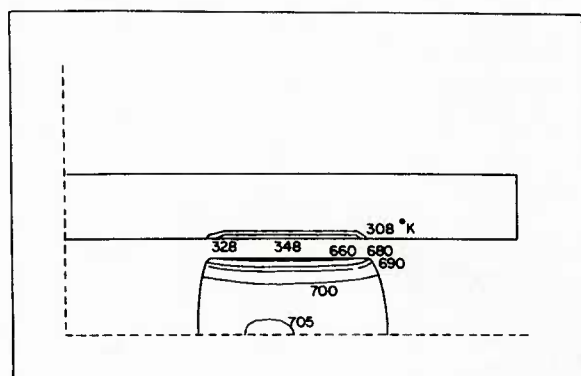
Fig 15 _ Temperature contours of ring
at 20% reduction in height
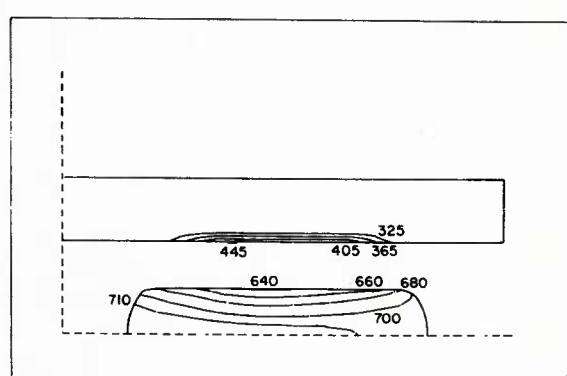
Fig 16 _ Temperature contours of ring
at 50% reduction in height
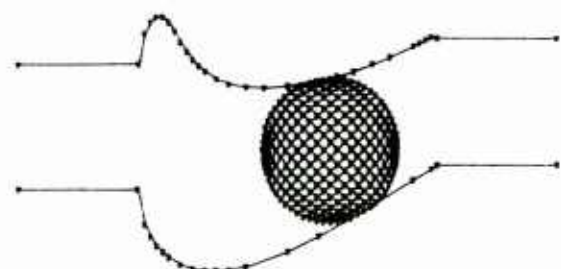
Fig 17 _ Preform for forging simulation
of turbine blade crossection
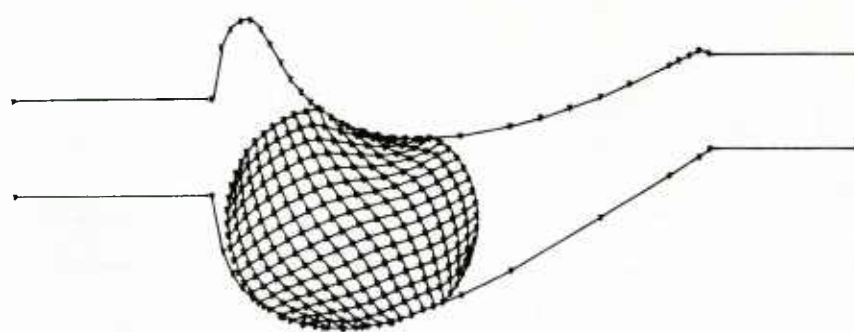
Fig 18 _ Blade crossection deformation with m=0.3

Fig 19 _ Blade crossection deformation with m=0.6
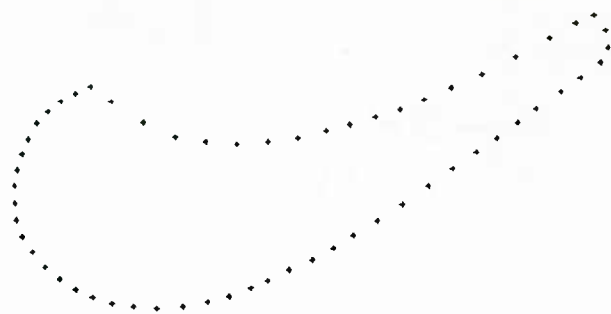
Fig 20 _ Profile sent for remeshing

Fig 21 _ New mesh

2: 3.4E-1
3: 6.6E-1
4: 9.7E-1
5: 1.3E00
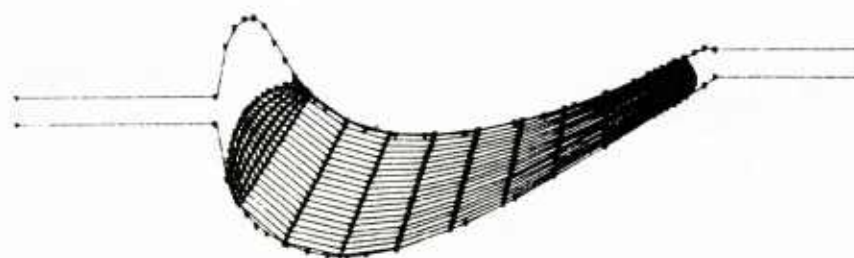
Fig 22 _ Strain distribution before remeshing

2: 3.4E-1
3: 6.5E-1
4: 9.7E-1
5: 1.3E00

Fig 23 _ Strain distribution after remeshing
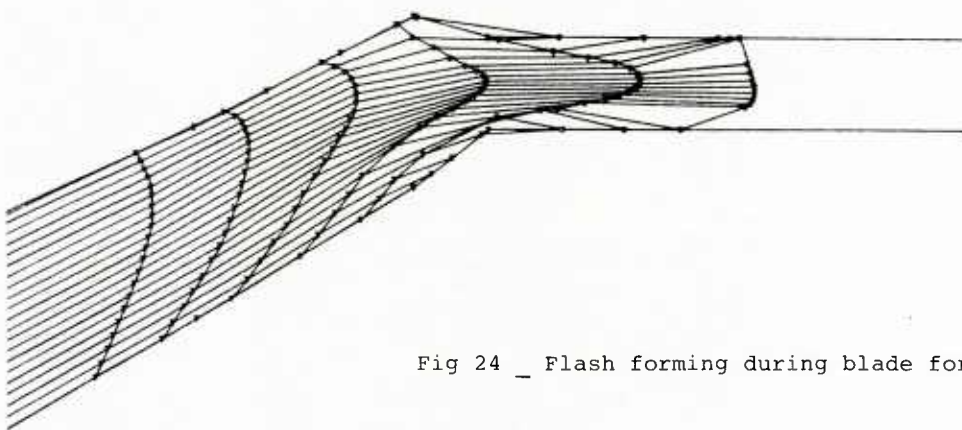
Fig 24 _ Flash forming during blade forging

11.4°

Die #1

R=3

Die #2
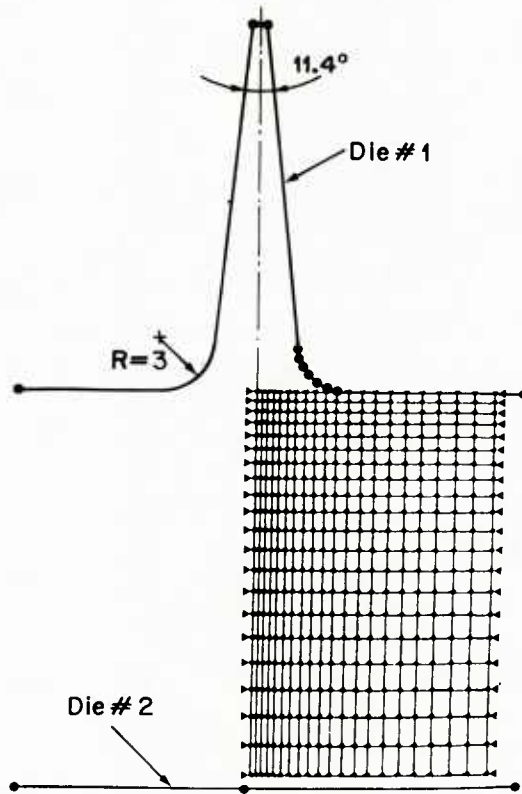
Fig 25 _ Initial model of rib forging
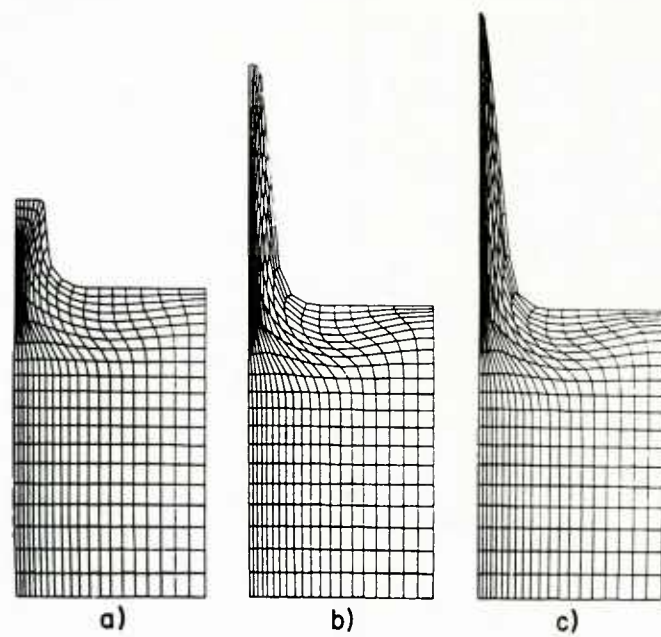
Fig 26 _ Deformed rib meshes (m=0.)
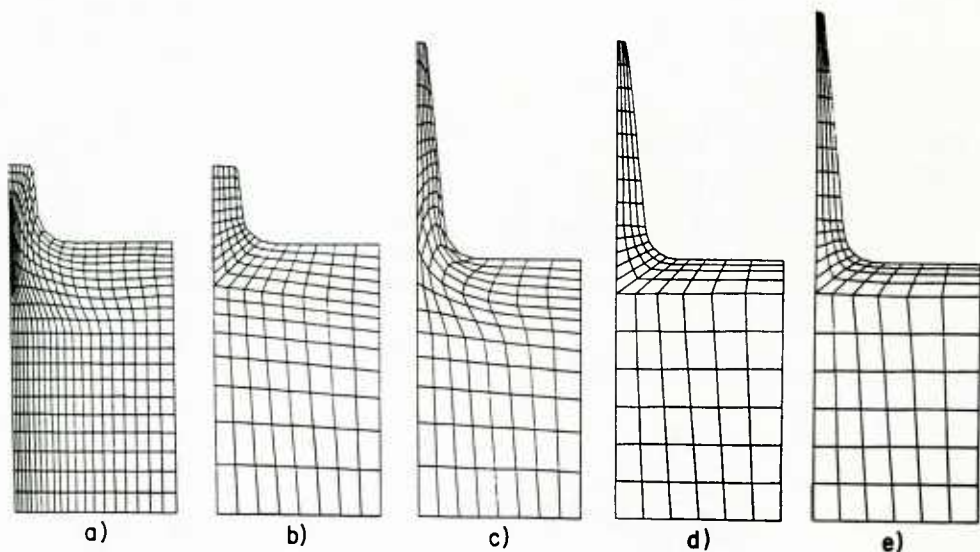
Fig 27 _ Deformed rib meshes (m=0.4)

COMPUTER-AIDED DESIGN OF EXTRUSION DIES BY METAL-FLOW SIMULATIONS

H. L. GEGEL, J. C. MALAS, J. S. GUNASEKERA, J. T. MORGAN, and S. M. DORAIVELU
AFWAL/Materials Laboratory
Wright-Patterson AFB, OH 45433 USA

ABSTRACT

A general-purpose, thermoviscoplastic finite-element program called ALPID has been combined with advanced CAD/CAM techniques for die design. A die-design package was used for generating the coordinates of the billet/workpiece and die geometries. This geometric data base was integrated along with the constitutive material-behavior model and interface-effects model into the analysis package, and many simulations were carried out for extrusion processes. Metal-flow simulations were obtained for different die geometries such as conventional shear dies of 180 deg., conical dies, and streamlined dies having different die lengths and extrusion ratios in order to study the effect of die geometry upon metal flow during extrusion and also to achieve uniform strain distribution for controlling the final microstructure and shape of the component without forming defects. Experimental results are also presented along with analytical predictions for the purpose of demonstrating the capability, accuracy, and efficiency of the finite-element analysis and application of these techniques to the solution of industrial problems in these areas. Interfacing of quality control, group technology, and economic analysis to process and geometric modeling is also discussed for the benefit of the extrusion industry presently in the process of implementing this technology.

INTRODUCTION

The availability of computers makes possible the analysis of metal flow during complex metalworking processes such as closed-die forging and extrusion of net-shape products. The finite-element method (FEM) coupled with geometric-modeling aids and suitable pre- and post-processors has proven to be the most practical means of accurately solving metalworking problems. The FEM is becoming a practical aid for die design and manufacturing as well as for the production of components having controlled micro-structures and properties in near-net-shape geometries.

The present paper describes progress in the CAD/CAM of extrusion dies by metal-flow simulation. The conventional criterion used for optimization of die geometry (die length) in extrusion or wire drawing is minimum extrusion or drawing force. The FEM allows other criteria to be used in the optimization of design and geometry. FEM simulations make it possible for the following criteria to be met:

(a) Homogeneous deformation, (i.e., attainment of an acceptable velocity field in the deformation zone without abrupt velocity discontinuity).
(b) Arising from (a), a uniform strain and strain-rate distribution in the deformation zone.
(c) The correct combination of hydrostatic-stress (J_1) and shear-stress (J_2') components during deformation within the die.
(d) Avoidance of sudden change of hydrostatic stress from compressive to tensile at the die exit.

Detailed implications of these conditions for specific materials are discussed in the following section.

The computer has become a key element in the integration of various elements such as part design, process analysis, and die design into an overall CAE system, as shown in Fig. 1. Of the several methods available for analytical modeling of the extrusion process, the following were employed in the present study: 1) the slab method which, although it provides only approximate answers, can be adopted for complex three-dimensional geometry including re-entry shapes, 2) the upper-bound method which provides relatively good estimates of upper-bound force but does not provide accurate details of the local stress and strain distributions [Gunasekera and Hoshino (1) extended this method to all nonre-entry sections],

- PART DESIGN
- PROCESS ANALYSIS
- DIE DESIGN

- NC DIE MANUFACTURING AND INSPECTION

PROCESS MODELING

DIE GEOMETRY

CNC MACHINE

- NET SHAPE EXTRUSION

DIES

PROCESS CONTROL

EXTRUSION PRESS
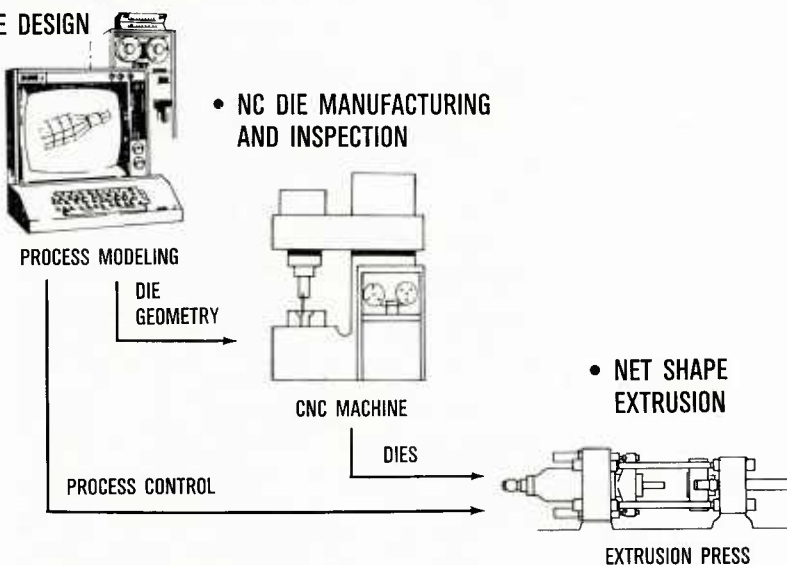
Fig. 1. Computer-Aided-Engineering Perspective.

and 3) the finite-element method (FEM) which is at present limited to two-dimensional axisymmetric, plane-strain, and plane-stress problems. The FEM is the most popular of these methods because it can provide accurate solutions to problems involving very complex die geometries, material behavior, and boundary conditions. Moreover, this method can provide accurate distributions (contours) of process variables such as stress, strain, strain rate, and temperature. The results can be interactively used to redesign the dies and/or control other process variables in an automated factory environment. Integration of FEM analysis with CAD/CAM, group technology, and economic analysis has the potential to reduce the lead time involved in design and manufacturing, to improve the quality of the product, to enhance communication between designers and manufacturers, to reduce manufacturing costs, and, in general, to improve overall productivity in the design/manufacturing cycle.

THE EXTRUSION PROCESS AND ITS APPLICATIONS

Extrusion is a primary metal-forming operation which is characterized by its ability to produce long structural shapes and induce very large strains in the product in a single operation. It is useful in manufacturing various shapes including rounds (produced generally by using shear dies) and also in conditioning billet materials for improving their workability for further manufacturing operations such as forging. Extrusion is also a popular process for consolidating particulate materials.

METAL-FLOW SIMULATION USING FEM

The approach used in this study follows the original work of Kobayshi and co-workers (2). The computer program ALPID which makes use of the above approach was developed by Oh (3) who made important contributions to the original FEM formulation by adding convenient features such as capabilities for handling arbitrary die geometries and remeshing. Details of the FEM formulation and some of its applications to the solution of practical problems can be found elsewhere (4-5). The current effort was directed toward the application of this method--in conjunction with CAD/CAM of dies--to specific metal-forming problems such as those involving streamlined extrusion dies.

Effect of Geometry on Round-to-Round Extrusions

The FEM program was employed in the modeling of flow for round-to-round extrusions using a variety of die geometries, the objective being to determine the optimum geometry which would satisfy the criteria discussed earlier for a given material under selected process conditions. The die shapes were shear, conical, parabolic, and streamlined surface (generated on the basis of radius or area).

The shear die is the most common one used in industry, particularly for conventional aluminum extrusions. The design and manufacture of this die are relatively easy. However, correction for thermal expansion/contraction and die deflection due to loading must be taken into account for proper dimensional control of the product. The length of the die land is also important. Figure 2(a) shows the velocity field for a 9:1 reduction using a shear die; the arrows represent the magnitude and direction of the velocity vector of various points in the deformation zone. The results are compared with those obtained for other die geometries.

The conical die, which is relatively easy to design and manufacture, is also fairly well known and is being used for conventional and hydrostatic extrusions. In this case material flow is more uniform than for the shear die. However, the conical die may induce some turbulence near the die exit due to the abrupt change of material flow at that point, as shown in Fig. 2(b).

The parabolic die has smooth entry; but the exit is sharp, creating turbulence and discontinuity in the velocity, as shown in Fig. 2(c).

Streamlined dies have smooth entry and exit, thus avoiding sharp velocity discontinuities at the exit or entry side, as shown in Fig. 2(d). Hydrostatic stress and effective strain distributions for
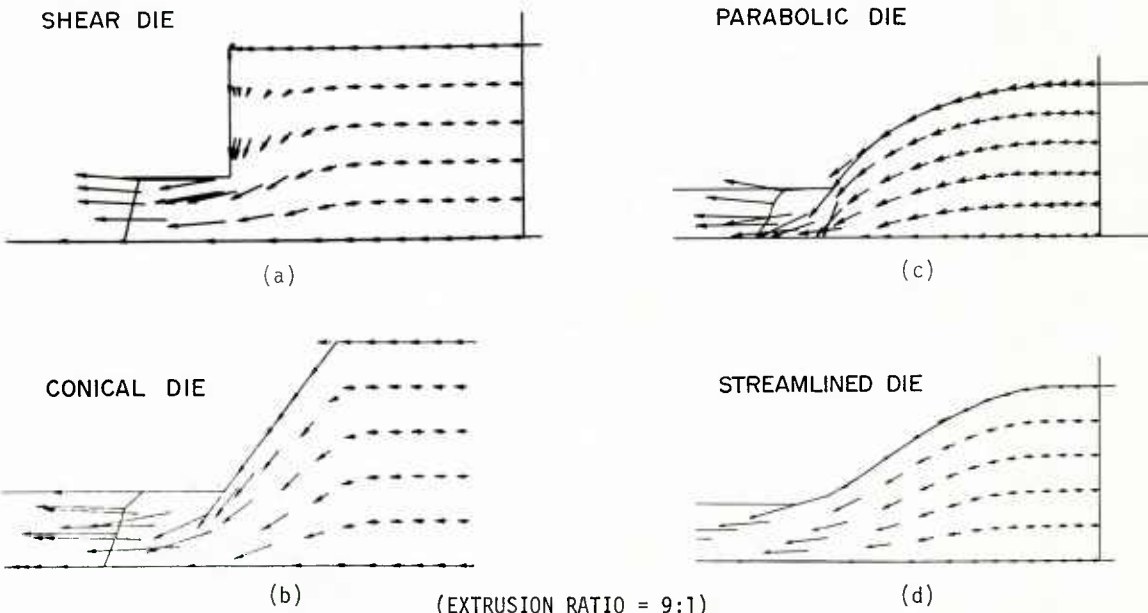

Fig. 2. Results of Metal-Flow Simulations for Different Die Geometries.

these dies are shown in Fig. 3. Two types of streamlined dies are available, both based on cubic spline fits. The first is based on the radius (along the axis of extrusion) at the die entry and exit; the second is based on the cross-sectional area at the die entry and exit. The splines differ in shape for these two cases. The general parametric representation is explained in Appendix I. Experience has shown that both types of streamlined dies have applications, the type depending on the material used and other process parameters. However, the results of the analysis indicate that the die surface generated based on radius tends to produce a better combination of hydrostatic and shear stresses and homogeneous material flow which is required for the production of quality products.
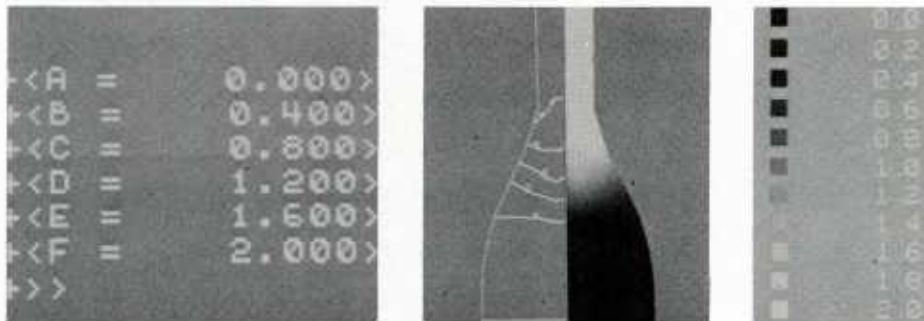
Fig. 3(a). Effective Strain Distribution in Deformation Zone When Streamlined Die is Used.
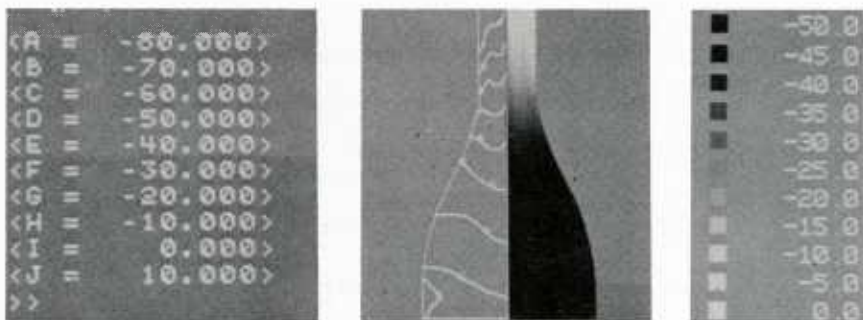
Fig. 3(b). Hydrostatic Stress Distribution in Deformation Zone When Streamlined Die is Used.

Based on a comparison of different die geometries and shapes (both analytical using FEM and physical using experimental results), it was concluded that the optimum die geometry for round-to-round extrusions of the material tested is a streamlined die (a cubic spline) based on radius. Hence, for determination of the effect of other variables such as die length, friction, and material, this die was chosen.

Effect of Die Length

In the past, optimization of die length (or semi-cone angle) for both wire drawing and extrusion has been undertaken using the minimum forming-force criterion. A typical force-vs.-die-length curve is shown in Fig. 4. The argument put forth is that a shorter die length reduces die/material frictional work but increases redundant work due to abrupt reversal of the velocity direction. A longer die length, on the other hand, produces a higher frictional work component but reduces redundant work. An optimum die length can be selected, as shown in Fig. 4. When extruding exotic material or metal-matrix composites with
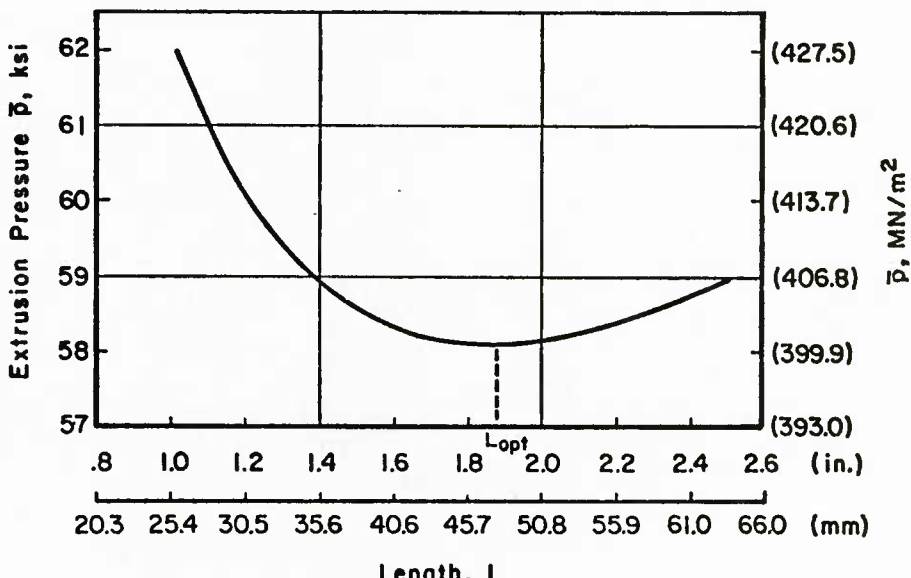

Fig. 4. Extrusion Pressure vs Die Length (Used for Selection of Optimum Die Lengths) (from Ref. 6).

fibers, this criterion may be inappropriate. In this case optimization must be carried out on the basis of material flow rather than minimum extrusion force, the objective being to maintain near-homogeneous deformation. Figure 5 shows the results of modeling using two different die lengths. The 50-mm die creates turbulence near the die exit and, hence, is unacceptable for producing a homogeneously deformed product. The 75-mm die is acceptable. Hence, for these given conditions (i.e., 9:1 extrusion ratio of round-to-round, friction factor m = 0.3), the aspect ratio for the die should be at least one in order to achieve a near homogeneously deformed product. For a higher extrusion ratio, a longer aspect ratio is required.

(a)   (b)   (c)
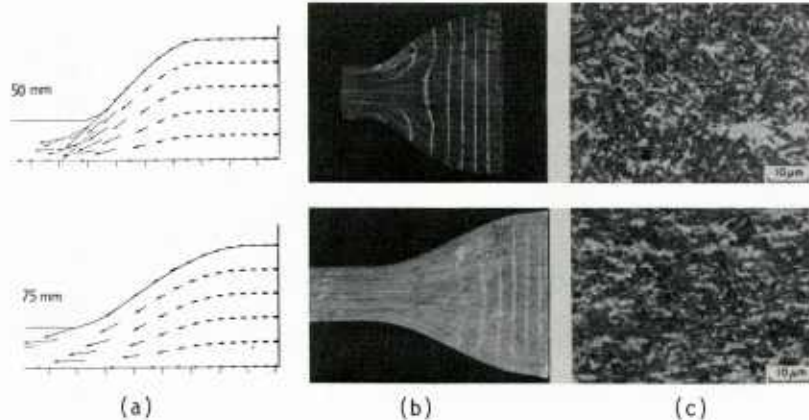
Fig. 5.   (a) Results of Analytical Modeling, (b) Results of Physical Modeling, and (c) Micro-structure of Extruded Product through Streamlined Dies of 50-mm and 75-mm Length.

Effect of Friction

In order to study the effect of friction on material flow, the die length (for an extrusion ratio of 9:1) was fixed at 75 mm (i.e., L/D = 1). Figure 6 shows the various stages of the ram position for two


(a)

m = 0.1

(1 UNIT = 25.4 mm)

(b)

m = 0.3
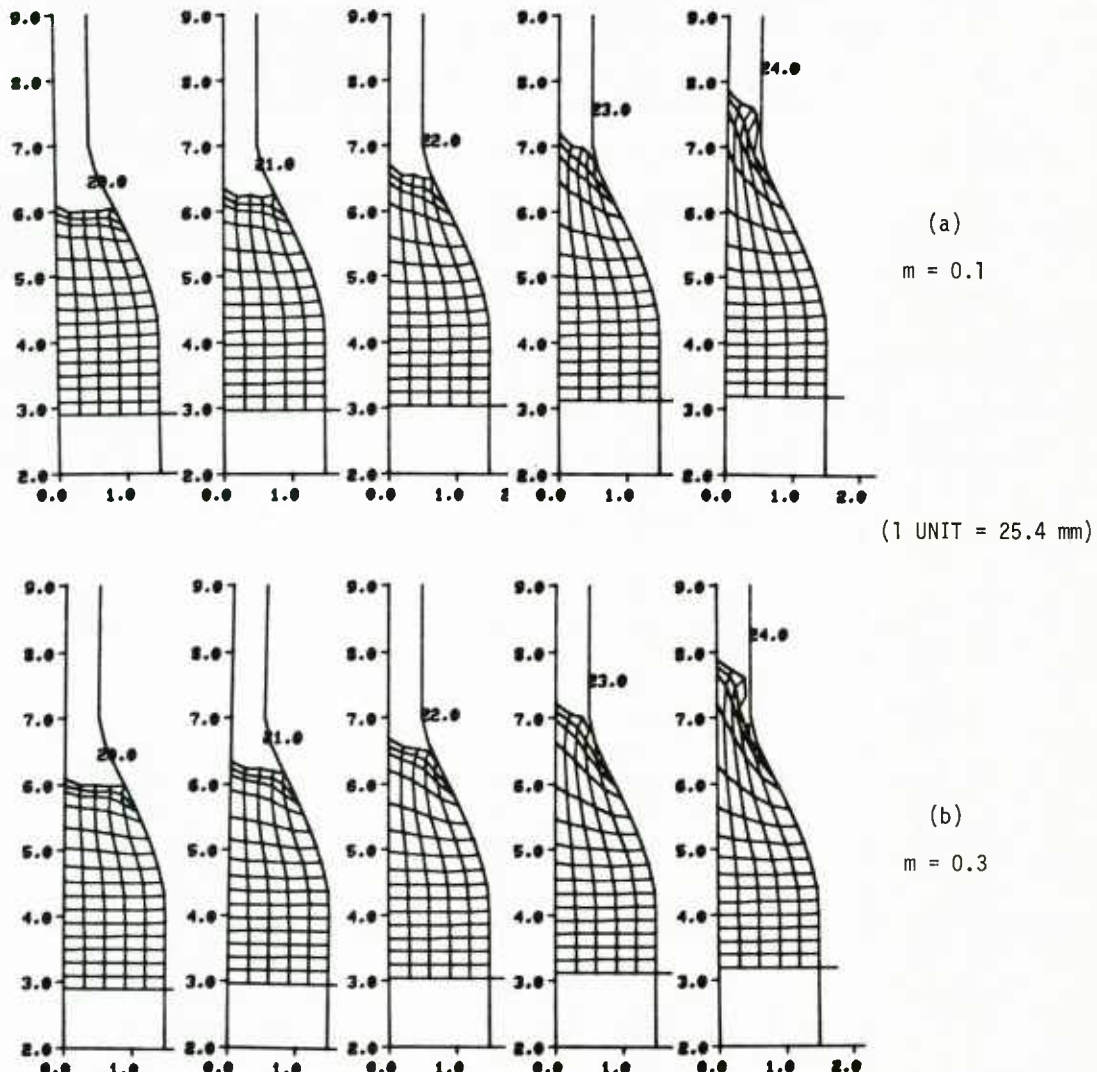
Fig. 6.   Metal-Flow Simulations through Streamlined Dies for Different Frictional Conditions.

frictional conditions, m = 0.1 and m = 0.3, all other variables being held constant. The analytical modeling results show very little difference in grid distortions and velocity fields. It is concluded that the effect of friction on material flow pattern is negligible for a small variation in frictional conditions.

GEOMETRIC MODELING AND DIE DESIGN

Formerly, the design of a complex die was a tedious procedure requiring up to one manweek of effort. However, innovative concepts for the design of complex extrusion dies have now been developed. The post-processor for displaying three-dimensional geometries used in conjunction with these concepts in the present study was a graphics program called MOVIE.BYU, developed at Brigham Young University (USA). With this package the die geometry can be rotated and zoomed. The post-processor for manufacturing the electrode for EDM of the die was the UCC-APT program which is compatible with an APPLICON system.

Recently Gunasekera developed a fully interactive die-design package which incorporates innovative concepts and principles of die design and is capable of generating the following die shapes: straight (conical), convex, concave, parabolic, streamlined die based on radius, and streamlined die based on area.

The present and future versions of the die-design package and a package for designing shear dies will be capable of generating the surface of the dies used to produce the round-to-round and round-to-any structural shapes and multi-hole and shear dies. This die-design package is considered to be the only software capable of designing dies for re-entrant product shapes.

APPLICATION

For a number of applications in the aerospace industry, streamlined die design would be advantageous for increasing product yield and enhancing mechanical properties. This type of die is now being considered for certain structural shapes and workpiece combinations. These components generally have severe part geometries, and the workpiece material would be characterized as having poor workability. This combination of conditions can be found in almost every structural alloy family, which includes aluminum, steel, titanium, and nickel-base alloys. Failure in these alloy systems is usually attributed to center-burst phenomena or porosity due to the decohesion of second-phase particles from the matrix material.

The standard shear dies used by industry to extrude the common aluminum alloys are, in general, not satisfactory for the more advanced alloys being developed for the aerospace industry. The internal shearing and rigid-body rotations in the workpiece material caused by the die geometry produce defects and fracture in some cases. The streamlined extrusion dies control the flow field and minimize the residual stresses caused by non-uniform material flow.

By definition, a streamlined extrusion die is one whose material velocity profile remains constant during reduction of the billet from its entry to exit of the die. Friction between the workpiece and the die surface in actual practice prevents "ideal" metal flow from occurring; therefore, the problem is to find a practical compromise in die design and in the process parameters (temperature, strain rate) in order to achieve the goal of approximating streamlined flow. Through process modeling, this goal can be achieved with a minimum number of trial-and-error iterations. The rigid-viscoplastic FEM discussed earlier was used to simulate the process on the computer and to select the proper die geometry and processing conditions. The die geometry was modeled using the die-design package and this model, in turn, was used to formulate the FEM model.

COMPUTER-AIDED DESIGN AND MANUFACTURE OF FLAT-FACE DIES

Flat-face (or shear) dies are primarily used for extruding aluminum alloys. Basically they consist of a flat disc of tool steel containing one or more shaped orifices (7). The metal is forced to extrude through these orifices to give the desired sections. The detailed design of the die involves determining the following parameters:

1. The optimum number of shaped orifices in the die.
2. The location of the orifices relative to the billet axis for uniform metal flow through each orifice.
3. The orientation of the orifices.
4. Modification of the orifice geometry to correct for thermal shrinkage and die deflection under load.
5. Determination of the bearing length for balancing the metal flow.

Figure 7 is a flowchart for a typical interactive CAD program (7). Examination of this chart shows that the process used to design flat-face dies is largely based upon experience-based technology. The method of analysis used is the so-called slab method. It ignores redundant work and does not output a velocity field or temperature field but does estimate the stress field. Its primary use is to predict the load and energy required to determine the capacity of an extrusion press, and it provides the stresses on tools. This method seems to be adequate for designing flat-face dies. In the CAD approach to designing these dies, the cross section of the extrusion is input into the program in the form of X,Y coordinates. Fillets and corner radii are also included. These parameters are used by the program to calculate various geometric parameters such as cross-sectional area, perimeter, shape-complexity factor, location of centroid, and size and location of a circumscribing circle.

The number of extrusion orifices in the die is based upon the capabilities of a specific press and the alloy to be extruded. Each available extrusion press is classified according to such characteristics as load capacity, container length and diameter, maximum billet length, and runout length. These data would be stored in a data table. Load and yield calculations are made to determine whether a certain press has adequate capacity and whether the yield is sufficient. The number of openings is based upon practical specifications input by the user, maximum extrusion length, and/or maximum material yield. These factors subsequently determine the optimum billet size.

```
                    ╭─────────────╮
                    │    START    │
                    ╰──────┬──────╯
                           ▼
              ┌──────────────────────────┐
              │     READ SECTION DATA    │
              └────────────┬─────────────┘
                           ▼
              ┌──────────────────────────┐
              │ CALCULATE SECTION PARAMETERS │
              │     AND DISPLAY SECTION  │
              └────────────┬─────────────┘
                           ▼
              ┌──────────────────────────┐
              │   SELECT PRESS AND ALLOY │
              │ DETERMINE MINIMUM NUMBER OF OPENINGS │
              └────────────┬─────────────┘
                           ▼
              ┌──────────────────────────┐
              │  SELECT NUMBER OF OPENINGS │
              │ DETERMINE PRODUCTION RATE AND YIELD │
              └────────────┬─────────────┘
                           ▼
              ┌──────────────────────────┐
              │   LOCATE OPENING(S) ON DIE │
              └────────────┬─────────────┘
                           ▼
                        ╱NUMBER╲
                =1  ◄──╱OF OPENINGS╲──►  >1
                       ╲    ?    ╱
                        ╲      ╱
         ┌──────────────────┐      ┌──────────────────────┐
         │ DIE CAVE COMPENSATION │◄──►│ BRIDGE STRESS ANALYSIS │
         └──────────────────┘      └──────────────────────┘
                           ▼
              ┌──────────────────────────────────┐
              │ TONGUE STRESS ANALYSIS AND COMPENSATION │
              └────────────────┬─────────────────┘
                               ▼
              ┌──────────────────────────┐
TO START      │      BEARING DESIGN      │
              └────────────┬─────────────┘
                           ▼
         NO             ╱ DONE? ╲
      ◄───────────────╱          ╲
                       ╲        ╱
                         │ YES
                         ▼
                    ╭─────────────╮
                    │     END     │
                    ╰─────────────╯
```

Fig. 7. General Operation of the Design Package for Flat-Face Extrusion Die.

The extrusion orifices are positioned in such a way as to balance the material flow. Certain minimum clearances are established between the die openings in order that the die and backup tooling will have sufficient strength to withstand the extrusion pressures. Clearances are also maintained between the die opening and the cylinder wall to avoid flow of the outside surface of the billet into the product. The positions of the openings are also selected in such a way as to cause the center of gravity of the opening to coincide with that of the billet segment feeding the opening.

Since the analytical method employed permits predictions of the tooling stresses, die deflection corrections are made and a tool-strength analysis is performed to predict the bending and shear stresses in the die, backer, and bolster due to the extrusion pressure. This capability allows the user to predict the need for support tooling. These CAD capabilities facilitate obtaining the desired tolerances in the extruded product. The final step in the die design is to determine the proper die bearing lengths. The die bearing is a function of section thickness at a given position from the die center, and this information is stored in the computer data file for use in making such determinations.

The flat-face dies are subsequently manufactured using the geometries generated during the design stage through numerical control techniques. The most common methods involve some form of electro discharge machining (EDM). Two basic types of EDM machines--wire and electrode--exist. Both are, in general, computer numerically controlled (CNC) devices. When the conventional electrode EDM machine is used, the electrode is produced by CNC end milling, using coordinates automatically generated by the CAD/CAM software. If the wire EDM machine is selected for producing the die openings, the back side of the die, i.e., the bearing areas, must still be machined by conventional CNC end milling or by conventional EDM which requires an electrode. If templates for dimensional quality control are required, the CAD/CAM software can be used to generate these also.

DISCUSSION

CAD/CAM techniques coupled with advanced analytical methods such as the FEM are proving to be very useful for the analysis of deformation processes and for the design and manufacturing of dies. Of all the numerical methods available for simulating the various metalworking processes, the FEM is the most useful. Its major limitation is associated with the analysis of large three-dimensional deformation. However, as faster methods of analysis become available, the three-dimensional FEM will enjoy greater popularity. Presently, the FEM for process simulation is practically restricted to plane-strain or plane-stress axisymmetric analysis. The method has been used very effectively to evaluate various process parameters such as die length, die shape, and effect of friction. The limitation of the analysis is that in its present stage of development, the program can solve only two-dimensional axisymmetric, plane-strain, and plane-stress problems. The extension to three-dimensional non-axisymmetric problems is in progress. However, for non-axisymmetric extrusion, a "shape-complexity" factor can be incorporated to define the degree of complexity of the product geometry. This factor can also be combined with results of two-dimensional or axisymmetric FEM analysis to provide approximate predictions for non-axisymmetric extrusion.

The results of analytical modeling (i.e., velocity profiles and distribution of stress, strain, and strain rate) can be used to control the process variables (die length, die shape, temperature, ram speed, and lubrication) to achieve a desired result. This feed-back loop can be effectively used in the computer to model the process more accurately, resulting in precise process-control parameters which will, in turn, provide proper quality control of the end product.

The computer can also be used to store information on analytical modeling of similar components or products, as in group technology, which will aid die designers and process engineers in selecting optimum process variables based on previous experience and modeling of similar part families. Economic analysis must also be performed to investigate available alternatives. For example, the use of streamlined dies may produce quality products but may be costly in terms of tool and die design and manufacturing.

CONCLUSIONS

In this paper a new approach for the design of extrusion dies based on metal-flow simulations has been proposed. It is extremely important to establish the criteria used for optimizing a given process or die-design procedure. Different criteria usually yield different optimum process parameters. In the present investigation, the conventional minimum-force criterion for the design of dies does not automatically guarantee optimum metal-flow conditions. The material behavior has been given priority over other factors such as ram force because of the importance of obtaining products having the required mechanical properties.

The present study has shown the correlation between material flow and process variables; in some cases (for example, die length and geometry), a strong correlation was found but in others (for example, interfacial friction), the correlation was weak. This paper has demonstrated the importance and potential of modeling by means of the computer. The computer has also been used to design dies based on the results of modeling. The potential economic advantages of modeling and CAD of dies (although not quantified at this stage) are clear, including reduced lead times, reduced cost, and improved quality assurance.

REFERENCES

1. Gunasekera, J. S. and Hoshino, S., "Extrusion of Non-Circular Sections Through Shaped Dies," Annals International Institute of Production Engineering Research (CIRP) Vol. 29, 1980, pp. 141.

2. Kobayashi, S., "Thermoviscoplastic Analysis of Titanium Alloy Forging," AFWAL-TR-81-4130, 1981, Air Force Wright Aeronautical Laboratories, Wright-Patterson AFB, OH.

3. Oh, S. I., "Finite Element Analysis of Metal Forming Processes with Arbitrarily Shaped Dies," International Journal of Mechanical Science, Vol. 24, 1982, p.479.

4. Chen, C. C. and Kobayashi, S., "Rigid-Plastic Finite-Element Analysis of Plastic Deformation in Metal-Forming Processes," AFML-TR-79-4105, 1979, Air Force Materials Laboratory, Wright-Patterson AFB, OH.

5. Oh, S. I., Lahoti, G. D., and Altan, T., "ALPID - A General Purpose FEM Program for Metal Forming," Proceedings of the 9th NAMRE, The Pennsylvania State University, State College, PA, 1981, p. 83.

6. Negpal, V. and Allen, T., "Computer-Aided Design and Manufacturing for Extrusion of Aluminum, Titanium, and Steel Structural Parts," Final Report under Contract DAAG46-75-C0054, 1976, Battelle Columbus Laboratories, Columbus, OH.

7. Altan, T., Oh, S., and Gegel, H., Metal Forming: Fundamentals and Applications, American Society for Metals, Metals Park, OH, 1980, pp. 220-223.

APPENDIX I

GENERALIZED STREAMLINED DIE (PARAMETRIC REPRESENTATION)
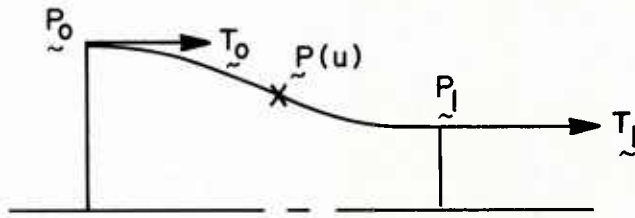
The generalized streamlined die can be defined by the point vectors P_0 and P_1 which represent the end points on the die entry and exit, respectively, and the tangent vectors T_0 and T_1 which represent the direction and magnitude of the tangent vectors at P_0 and P_1, respectively. The four vectors P_0, P_1, T_0, and T_1 completely describe the spline. The shape or the geometry of the spline can be changed by modifying one or more of the four vectors. The interpolation formula for a cubic spline is given below. For any parametric value u varying from 0 to 1 (representing the ends of the spline), it is possible to obtain a point on the curve. Intermediate points on the die P(u) can be expressed as

$$\underline{P}(u) = \underline{P}_0 + u \cdot \underline{T}_0 + u^2 \cdot [3(\underline{P}_1 - \underline{P}_0) - 2\underline{T}_0 - \underline{T}_1] + u^3[-2(\underline{P}_1 - \underline{P}_0) + \underline{T}_0 + \underline{T}_1]$$

or

$$\underline{P}(u) = \underline{P}_0(1 - 3u^2 + 2u^3) + \underline{T}_0(u - 2u^2 + u^3) + \underline{P}_1(3u^2 - 2u^3) + \underline{T}_1(-u^2 + u^3)$$

and

$$\frac{d\underline{P}}{du} = \underline{T}(u) = \underline{P}_0(-6u + 6u^2) + \underline{T}_0(1 - 4u + 3u^2) + \underline{P}_1(6u - 6u^2) + \underline{T}_1(-2u + 3u^2)$$

This spline satisfies the following boundary conditions:

at die entry, u = 0,

$$\underline{P}(o) = \underline{P}_0$$

$$[\frac{d\underline{P}}{du}]_{u=0} = \underline{T}(o) = \underline{T}_0$$

at die exit, u = 1,

$$\underline{P}(1) = \underline{P}_1$$

$$[\frac{d\underline{P}}{du}]_{u=1} = \underline{T}(1) = \underline{T}_1$$

$$\underline{P}(u) = [ix(u), jy(u), kz(u)]$$

MODELLING TEMPERATURE CHANGES DURING HOT WORKING OPERATIONS

C. M. Sellars
Department of Metallurgy, The University,
Mappin Street, Sheffield S1 3JD, England

SUMMARY

Finite difference methods have been applied to determine radial heat transfer in round billets under conditions of hot extrusion, and in flat slabs during hot rolling. The principles of the computing procedures are outlined, together with the approximations adopted to eliminate iterative procedures and to obtain an accurate estimate of the surface temperature as well as of the temperature of the internal elements. In both situations, heat transfer coefficients at the surface have been determined experimentally and these coefficients can then be applied to other geometrical conditions to give excellent agreement with observation.

INTRODUCTION

Hot working operations generally take place at temperatures above about 0.6 of the absolute melting temperature of the metal. Under these conditions the flow stress is sensitive to the strain rate and temperature of deformation and the microstructural evolution is particularly sensitive to temperature. An accurate knowledge of temperatures in the different working processes and in laboratory tests is therefore a prerequisite for quantitative correlation between them, but, both in the working operations and during testing at high strain rates, temperature changes continuously. No simple experimental technique can give a complete picture of the temperature changes throughout the workpieces. Limited experimental data must therefore be combined with modelling to solve the problem.

There are three basic contributions to the heat balance in any working process:
  (i) heat loss to the environment by radiation and convection,
 (ii) heat loss to the tools (rolls) by conduction,
(iii) heat gain due to the work of deformation.
The heat losses can only occur through the surfaces of the workpiece, whereas the heat gain is generated internally, so that severe temperature gradients are set up. These are strongly influenced by the changes in geometry that take place during the working process. While, in principle, it is possible to set up complete differential equations for the heat flow, these cannot generally be solved analytically and it is therefore necessary to solve them numerically by a finite difference method.

In considering the computational procedures that should be adopted, it must be recognised that there are films of oxide and possibly of lubricant on the metal surfaces during working processes and the magnitude of the terms contributing to the heat balance cannot therefore be predicted from first principles, but rely on experimental measurements. The accuracy of prediction of any model is therefore limited by the accuracy with which the experimental parameters have been determined. This means that absolute mathematical accuracy of the solutions is not essential, particularly if this would require very extended computing times. It is, however, necessary to check the influence of approximations on the results obtained to ensure that these are reasonable. Combining such computer modelling with limited experimental observations to provide the heat transfer data at the interface and to check the accuracy of predictions thus provides a powerful method of resolving the complex problems of the temperature changes during working operations.

This paper illustrates the results of applying this philosophy to the processes of hot extrusion and of hot rolling of flat products.

HOT EXTRUSION

During the process of extrusion, particularly as applied to steels and other high melting temperature alloys, temperature changes take place from the moment a billet is removed from the reheating unit until the operation is complete. The various contributions to the overall heat balance for a particular cross-section in a billet may be summarized as:
  (i) loss to the environment as the billet is transferred to the extrusion container,
 (ii) gain due to the work done on upsetting the billet to fill the container bore,
(iii) loss through the lubricant film to the container after the billet has been upset and the cross-section of interest is moving towards the deformation zone near the die,
 (iv) gain due to the work of sliding friction between the billet and container,
  (v) gain due to deformational work as the material flows through the die,
 (vi) loss due to melting of the lubricant pad to provide a film of lubricant through the die,
(vii) loss by heat transfer to the die,
(viii) loss from the extruded product to the environment.

Contributions (i) to (vii) all interact with the deformation process itself and are therefore of importance both in determining the extrusion pressure and in controlling the microstructure of the product, whereas contribution (viii) occurs after deformation is complete and influences only the microstructure of the product observed after cooling to

room temperature.

Experimental investigations of temperature changes in 76mm dia billets of steel extruded to round bar were made by Hughes and by Nair (1,2) for hot extrusion conditions and later these were extended to warm extrusions (3). Measurements were made using embedded thermocouples and an optical pyrometer to determine the temperature changes at certain positions in the material before and after it passes through the die. These measurements enabled a complete heat balance to be obtained with satisfactory accuracy, and showed that contributions (ii), (iv), (vi) and (vii) were relatively small. They also established that, when the temperature changes were known, laboratory data on flow stress of the steels as a function of strain rate and temperature could be used to calculate extrusion pressures as a function of ram travel, ram speed and reheating temperature, which are in close agreement with observed pressures. For the 76mm dia billets the experimentally derived temperatures thus provided a basis for understanding and calculating the effects of process variables. They also provided experimental values of surface heat transfer coefficients required in a temperature model.

The philosophy adopted in modelling the temperature changes during extrusion was to concentrate on the major contributions, i.e. (i), (iii) and (v), and to use relatively crude approximations for the others, which had been shown to have only minor effects, so that even relatively large errors in estimating their values would be negligible in practical terms. It was also recognised that, except close to the front and back end of the billet, only radial heat flow is important, so a one-dimensional model would be satisfactory for most purposes.

Outline of the Mathematical Model

The model considers radial heat flow and uses a finite difference technique with subdivision of the billet and container into elements of equal area. This form of subdivision was selected to minimize the number of elements for accurate representation of temperature gradients, which increase in steepness from centre to surface. It has a further advantage that when gradients are parabolic in terms of radius, the algebra is simplified.

Details of the model, which calculates temperature during transfer of the billet to the container and after upsetting in the container, are given elsewhere (4). The temperature in any element of the billet is calculated at the end of a small time interval δt from knowledge of the temperatures in adjoining elements at the beginning of the interval, and of the thermal properties of each element.

If an element adjoins the surface, the mean heat-transfer rate per unit area at the end of the time interval determines the local temperature gradient. During the period of transfer of the billet from the reheating furnace to the container, the surface heat transfer is that characteristic of air cooling which has been determined experimentally from measurements of the temperature of stainless steel billet cooled in still air (5). The length of the billet was $\sim$10 times its diameter and thus the billet was effectively an infinite cylinder. The surface temperature was measured by means of a thermocouple and a pyrometer; good agreement between the two sets of measurements was found for an emissivity of 0.84. From these observations an empirical air-cooling heat flowrate of the form

$$h_a = -6746 + 21.2T_s + 4.763 \times 10^{-8}(T_s + 273)^4 \quad Wm^{-2} \tag{1}$$

was obtained, where T_s is the surface temperature in $^{\circ}$C. After the billet is placed in the container into which it is initially a loose fit, the ram is brought into contact and pressure is applied. As the pressure is applied, the billet is first upset to fill the container, although a film of lubricant is still trapped between the surface of the billet and the surface of the container. The thickness of this lubricant film depends on the ease with which the lubricant flows at the surface temperature of the billet. This lubricant film acts as a thermal barrier between the billet and the container and the flow of heat through this barrier governs the temperature change in billet and container. The surface heat flow after upset is assumed to be proportional to the temperature difference between the surface of the billet and the surface of the container at all times. The constant of proportionality is the heat-transfer coefficient through the lubricant film (C, $kWm^{-2}K^{-1}$), which was found by comparison of computed and experimentally measured cooling curves. In most of the computations the thermal properties characteristic of the mean temperature of the billet at the beginning of the time interval were used. This simplification saved a great deal of computation, and the maximum error was no more than 2K in any part of the billet for periods of up to 10s after upset.

The billet and container were each divided into 16 elements of equal area for the majority of computations. It was also assumed that the surface temperature of the billet or container is related to the temperatures of the surface elements by a parabolic curve which depends on the instantaneous rate of heat transfer at the surface. This approximation enabled the mean heat transfer rate during a time increment to be derived without iteration and considerably simplified the computing. The other important variable in the computations is the time increment δt. A stability criterion gives the time increment that must not be exceeded, and this increases with increasing billet radius. Thus, if a minimum amount of computing is to be done, a longer time interval may be taken for larger billets.

Temperature Changes

(a) During Transfer

In the model, cooling during transfer and before upset has been considered as air cooling. What happens in practice (6) is that for glass or Fuminite lubrication the billet is rolled down a lubricant-covered tray (∿7s), and is then inserted into the container, in which it is a loose fit. For Molyslip lubrication the billet is transferred directly to the container, to which the lubricant has been previously applied. Although heat transfer in these situations is expected to be complex, it had been observed previously (1) that the net heat loss was very similar to that in still air, and this was confirmed in the majority of cases by the present computations using equation (1).

(b) After Upset

Examples of experimentally determined curves for cooling, after upsetting of billets reheated to temperatures in the range 710°-1280°C, are shown in Fig. 1. The reheating temperature, the depth of the inserted thermocouple, the time of air cooling before upset, and the heat-transfer coefficient are indicated beside each curve. At the higher temperatures in Fig. 1 the billets were lubricated with Fuminite, but at a reheating temperature of 710°C either low-temperature melting point glass (G) or Molyslip (M) was used. The other difference between the high-temperature curves and those for a reheating temperature of 710°C is that in the former case the billets were austenitic, but at 710°C they were ferritic.

By trial and error, the appropriate value of C was found to give the best fit to each experimental curve. Some indication of the effect of change in C upon the computed points is given in Fig. 1, for comparison with the experimental curve obtained with a thermocouple at a depth of 12.5 mm, and a reheating temperature of 1070°C. The calculated points for C = 6 are in very close agreement with experiment, whereas those for C = 8 are up to 10K below the experimental curve. The derived values of C are plotted in Fig. 2 against the computed surface temperatures of the billet before upset.

Figure 3 shows a family of cooling curves computed for different depths in a billet upset from a reheating temperature of 1170°C after 15s cooling in air. The value of C = 9, taken from Fig. 2 for these conditions, was used in the computation. The same results are shown in the form of temperature distributions at different times after upset in Fig. 4. The surface temperatures of both billet and container change very rapidly in the first second, and rather slowly thereafter, because the rate of heat transfer from the billet is a function of the difference between the two surface temperatures. The solid, broken, and chain lines in the container, which become discernibly different for times of 5 and 10s, result from different assumptions about the heat flow from the outer container element considered in the computations. It is clear that, whichever assumption is made, the surface temperature of the container is not influenced for times of less than 10s and, thus, there can be no influence on temperature within the billet up to this time.

Simplified Approach

Although the complete temperature distributions are of interest, the temperatures of most importance are the mean temperature, as this determines the extrusion pressure (2) and properties of the product, and the surface temperature, as this determines the behaviour of the lubricant. In this context, mean temperature $\bar{T}$ is defined (1) as the uniform temperature which gives the same heat content as for the billet with a radial temperature gradient, i.e.

$$T = \frac{2}{R^2} \int_0^R rTdr \qquad (2)$$

where T is the temperature at radius r, and R is the outer radius of the billet.

An example of the dependence of these two temperatures on billet radius is shown in Fig. 5. It can be seen that the change in mean temperature varies inversely with billet size, whereas surface temperature depends on billet size to a relatively small extent.

From extensive computations for different billet sizes, reheating temperatures, container temperatures, transfer times and heat transfer coefficients (C) between billet and container, a series of master graphs were developed (4), which enable the mean temperature and surface temperature at entry to the die to be simply estimated to accuracies of ± 5K and ± 10K, respectively. These are within the uncertainties of ascribing the correct value of C for a particular extrusion.

(c) During Extrusion

As the billet slides down the container, the work done against sliding friction between the billet and container causes only a small temperature rise when the coefficient of friction is low, as in steel extrusion, and this may be neglected. In contrast, deformation at the die zone gives a large rise in temperature

$$\Delta T = \frac{P_o}{s\rho} \simeq 0.2\ P_o \qquad (3)$$

when the extrusion pressure (P_o) at the die zone is in N/mm^2. Equation (3) assumes adiabatic conditions in the die, which is a good approximation for steel extrusion. By adding ΔT to the mean temperature at entry to the die zone, the mean temperature of the extrusion emerging from the die is obtained. These values are in good agreement with observation, as shown in Fig. 6, and from them a mean extrusion temperature (T_{ext}) can be defined for any cross section of the billet and can then be used to calculate extrusion pressures (2). Defining $\bar{T}_{ext}$ as the mean of the die entry and die exit temperatures seems adequate for this purpose. One useful application of the computed temperatures (or those estimated from the master graphs) is that they enable extrusion limit diagrams to be determined from laboratory data on the hot deformation properties of the material or from a relatively new extrusion data (7). An example of such a diagram is shown for high speed steel in fig. 7, which also illustrates the agreement of the predicted diagram with practical observation.

The current widespread use of micro-computers has now made the graphical approach largely unnecessary (except possibly as a teaching aid). Work is now in hand to develop a simplified model using heat flow through the lubricant to a "phantom" container. This eliminates the need to consider elements in the container and speeds up the computing time sufficiently for two-dimensional heat flow to be handled in reasonable times (on a BBC micro-computer) so that longitudinal as well as radial temperature gradients can be determined.

HOT ROLLING

During rolling of flat products, the contributions to the heat balance may be summarised as:

(i) loss to the environment as the slab is transferred from the reheating furnace and between roll stands
(ii) loss to the rolls during each rolling pass
(iii) gain due to the deformational work during each rolling pass
(iv) loss from the rolled product to the environment, which may involve special water cooling arrangements.

These are the equivalent contributions to the major ones during extrusion and have been modelled in a similar way. For experimental rolling, contribution (i) is simply air cooling, but in industrial rolling this is modified by the presence of the roller tables and by the high pressure descaling that takes place before some passes. Contribution (ii), roll cooling, is very much faster than air cooling due to the large thermal mass of the rolls and the problem is made more complex by the reduction in thickness in each stand. Experimentally it is possible to embed thermocouples in slabs and measure the temperature as the material is rolled, but these only stand up to a limited number of passes, typically three or four. The type of results obtained are illustrated in fig. 8. Thermocouples can only be placed at a limited number of positions so a complete picture of the temperature distribution cannot be obtained. However, these measurements again provide a basis of experimental heat transfer data, which can be applied in a model for both experimental and industrial rolling conditions.

Outline of the Mathematical Model

In the case of rolling of wide slab or plate a one dimensional finite difference model can be used to calculate the temperature at any point as a function of time, but with narrow slab or flats a two dimensional model is required. Fig. 9 shows the type of heat flow net used for the finite difference computations (5). There is again the problem of relating the surface temperature to the temperature of the surface element when steep gradients are developed. As for extrusion, it is assumed that the temperature at the surface and the temperature at the centre of the surface element both lie on a parabola centred on the centre of the slab. This enables the surface temperature to be obtained without iteration once the temperature characteristic of the surface element is known. If there are steep temperature gradients in the material, the difference in thermal properties between each element should be taken into consideration, but it was again found satisfactory to assume that all of the elements have the thermal properties associated with the mean temperature of the slab.

In developing the model for rolling, in addition to the two-dimensional consideration of heat flow, two other features make it more complex than the model for extrusion. Firstly, in extrusion the major heat loss to the container occurs when the shape of the elements is constant and not when material is passed through the die. In contrast, during rolling the model must take account of the change in geometry of the elements in the slab, with those in the roll remaining constant in size, fig. 10. Secondly, contact times in rolling are short (fractions of a second) and therefore a large number of small elements is desirable for accuracy, with the consequence that the maximum increment of time that can be used between computations is very short, if stability of the solutions to the heat flow equations is to be maintained. Times between passes are relatively long (up to 10s of seconds), leading to inordinately lengthy running times for the program if the small time increments required during the passes are retained for computations of multi-pass rolling. As a compromise, the element thickness was split into three equal parts just before a pass and then enlarged again immediately afterwards. This required care to ensure that there was no change in temperature gradient and no heat loss or gain during these manipulations.

Temperature Changes

(a) During Air Cooling

For air cooling, the heat transfer rate given by equation (1) was applied in the model. The form of temperature gradient predicted in the thickness and width directions in small slabs is shown in fig. 11, which also illustrates the agreement obtained with experimental measurements.

(b) During Rolling

It was found that temperature changes measured during nominally identical rolling passes varied considerably from slab to slab, presumably because of variations in the surface oxide condition. On the basis that oxide thickness is reduced during rolling in proportion to slab thickness, the model allows the heat transfer coefficient to increase proportionately. It was then found that a unique value of the coefficient (C, kW m^{-2} K^{-1}) could be applied to the different passes in a multi-pass experimental rolling schedule. When the correct value is selected, the model gives very satisfactory agreement with measured temperature changes, fig. 12. As for the case of extrusion, the appropriate value of C is found by trial-and-error comparison between experimental and predicted temperatures at the centre of the slab. They fall in the range 50-500 kW m^{-2} K^{-1} depending on the steel and reheating conditions. The model then enables the complete temperature history of all positions within the slab to be accurately determined. This is important both in relation to the microstructural changes and to the rolling forces, which will be discussed elsewhere.

Fig. 12 illustrates that steep temperature gradients are developed through the thickness during a pass and that these take up to several seconds before they are reduced by conduction within the slabs during the time interval between passes. Measurement of surface temperatures must therefore take heed of this. In industrial rolling, the time required to eliminate steep temperature gradients is frequently not available between passes and in any case, even measurement of surface temperatures may be difficult. Use of the computer model with "typical" values of C thus frequently provides a more reliable way of determining temperatures than trying to measure them directly. Certainly, it provides a reliable way of filling in the temperature history during rolling if the pass reductions and time intervals are known and one or two "spot" temperatures have been measured and can be used to cross-check the predictions. The model has been used for this purpose in a number of projects related to industrial rolling.

Currently the concepts applied to flat product rolling are being modified to model temperature changes in rod rolling. At the same time, the same form of simplification as used in extrusion, i.e. that of considering a "phantom" roll is being adopted to enable computations to be carried out in reasonable times on a microcomputer.

REFERENCES

1. K.E. Hughes and C.M. Sellars, J. Iron Steel Inst. 1972, 210, 661-669.
2. K.E. Hughes, K.D. Nair and C.M. Sellars, Metals Tech., 1974, 1, 161-169.
3. K.E. Hughes, R.L. Plaut and C.M. Sellars, Metals Tech., 1982, 9, 360-367.
4. J.A. Whiteman and C.M. Sellars, Metals Tech., 1981, 8, 10-21.
5. R.A. Harding, Ph.D. Thesis, University of Sheffield, 1976.
6. K.E. Hughes, Metall. and Mater. Technol. 1973, 5, 572-578.
7. K.E. Hughes and C.M. Sellars, Metallurgist, 1974, 6, 201-206.
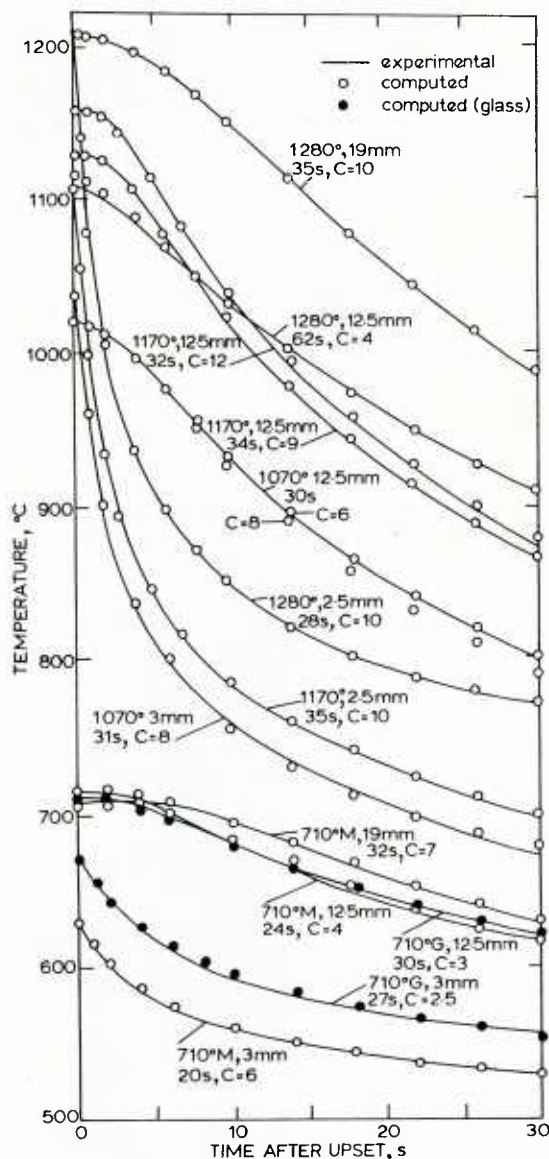
Fig. 1. Experimental and computed cooling curves for 38mm radius mild steel billets after upsetting in extrusion container preheated to 280°C: reheating temperature (°C), radial depth for curve, transfer time before upset, and heat-transfer coefficient (C, kW m^{-2}K^{-1}) are shown beside each curve; for high reheating temperatures lubricant was Fuminite, and for low reheating temperatures either Molyslip (M) or low softening point glass (G) was used (4).
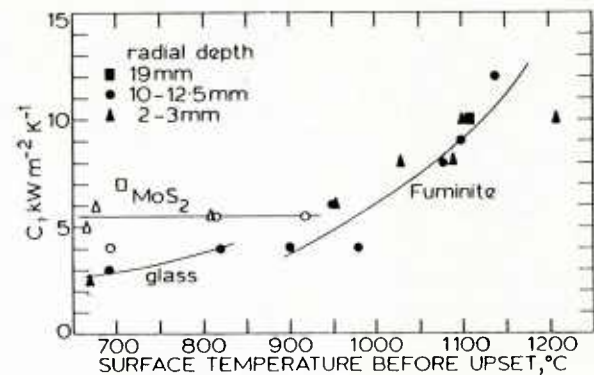
Fig. 2. Heat-transfer coefficient after upset, derived from experimental cooling curves at radial depths shown, as function of billet surface temperature before upset (4).

Fig. 4. Computed temperature distributions for 38mm radius mild steel billet reheated to 1170°C and air cooled for 15s before upsetting in container preheated to 280°C (4).

Fig. 3. Cooling curves after upsetting for different radial depths in 38mm radius mild steel billets reheated to 1170°C and air cooled for 15s (4).
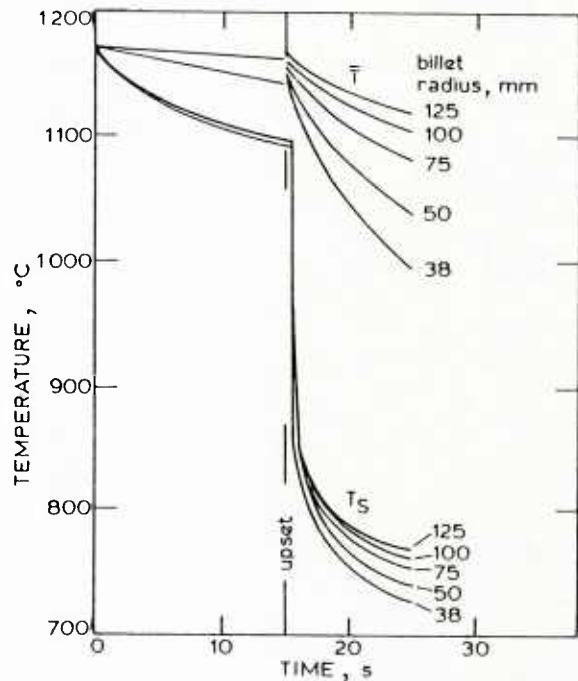
Fig. 5. Computed curves (C = $9kWm^{-2}K^{-1}$) for variation of mean temperature $\bar{T}$ and surface temperature T_s with time for billets of different radius reheated to 1170°C and upset in container preheated to 300°C (4).
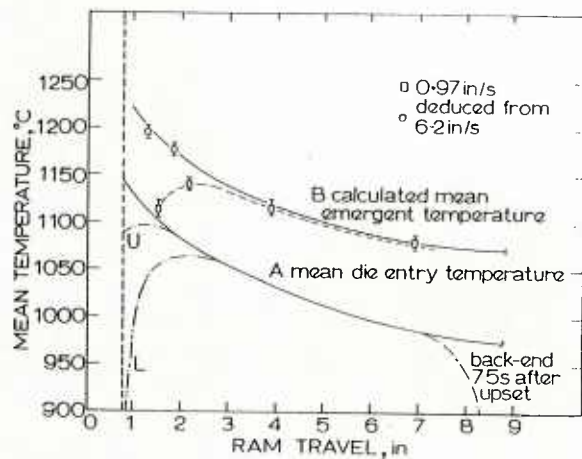
Fig. 6. Change in mean temperature with ram travel during extrusion at 25 mm/s of 76mm dia mild steel billets reheated to 1170°C. Solid curve A shows mean die entry temperature assuming radial heat loss only; chain lines show estimated effects of heat loss through the front and back ends. Solid curve B shows the mean emergent temperature calculated from curve A assuming adiabatic conditions. Data points are experimental measurements (1).
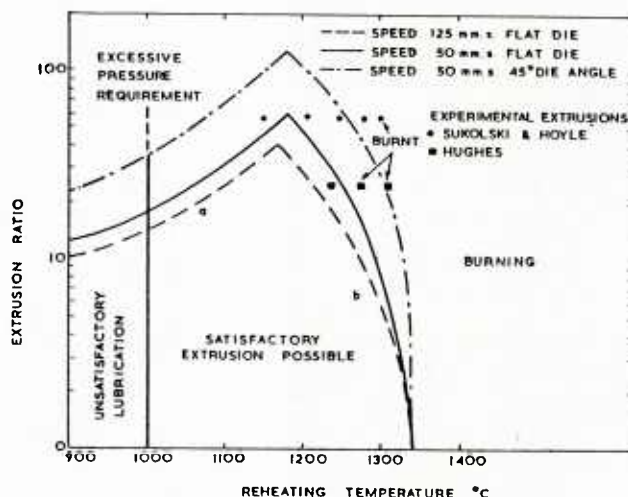
Fig. 7. Extrusion limit diagrams for 18/4/1 high speed steel (Billets 76 dia x 200 mm after upset).
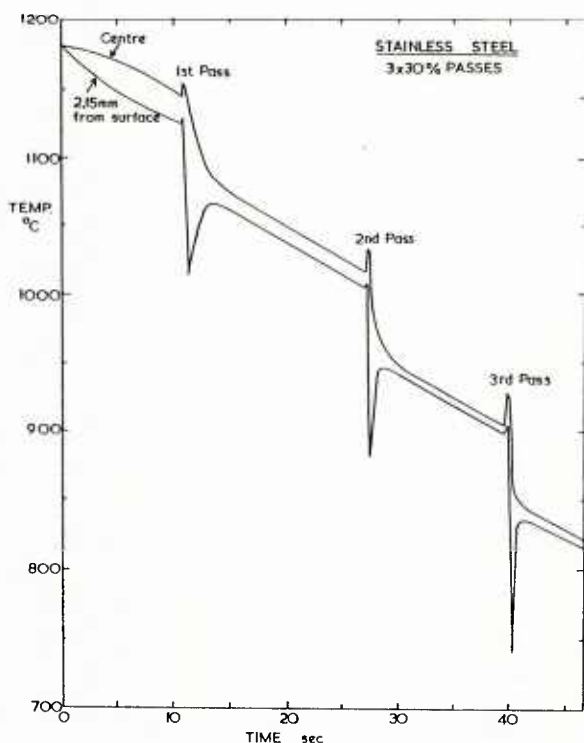
Fig. 8. Measured temperature-time curves during hot rolling of 19 mm thick stainless steel slab by 3 x 30% passes (5).
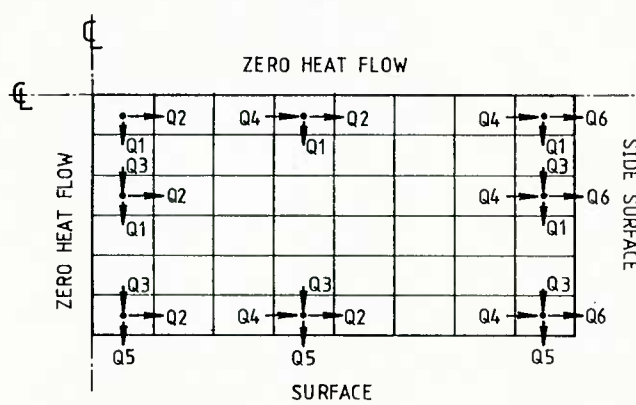
Fig. 9. Grid of elements used to compute two dimensional heat flow (Q) in the cross section of a slab (5).
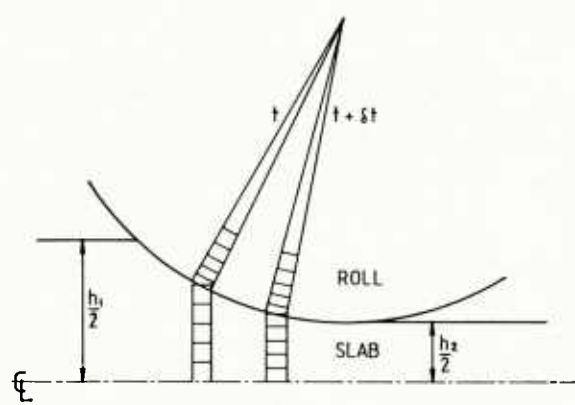
Fig. 10. Change in dimensions of elements in the slab during a rolling pass (5).
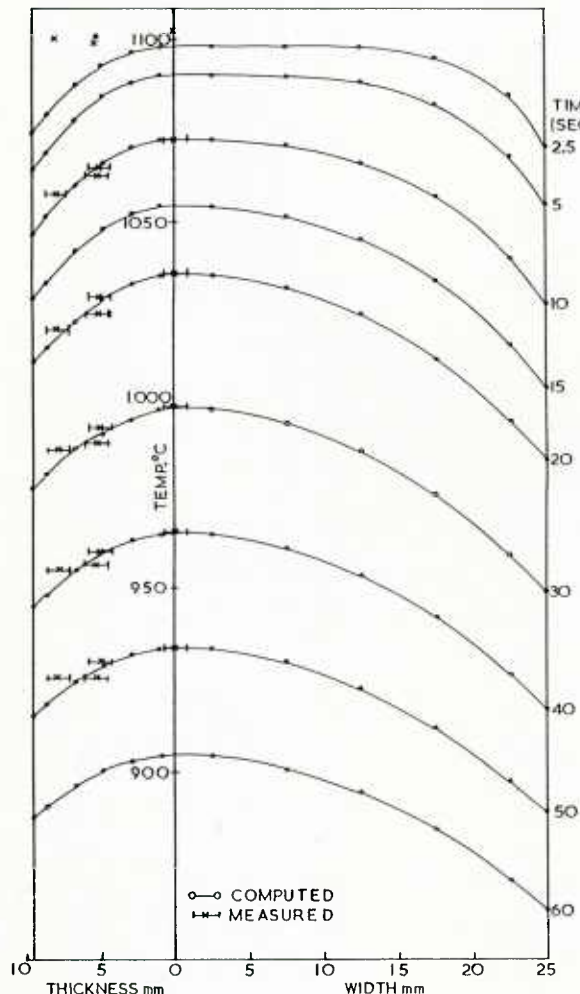
Fig. 11. Computed temperature gradients through the thickness and width of a 19mm x 50mm stainless steel slab as a function of time during air cooling. Crosses show experimental measurements (5).
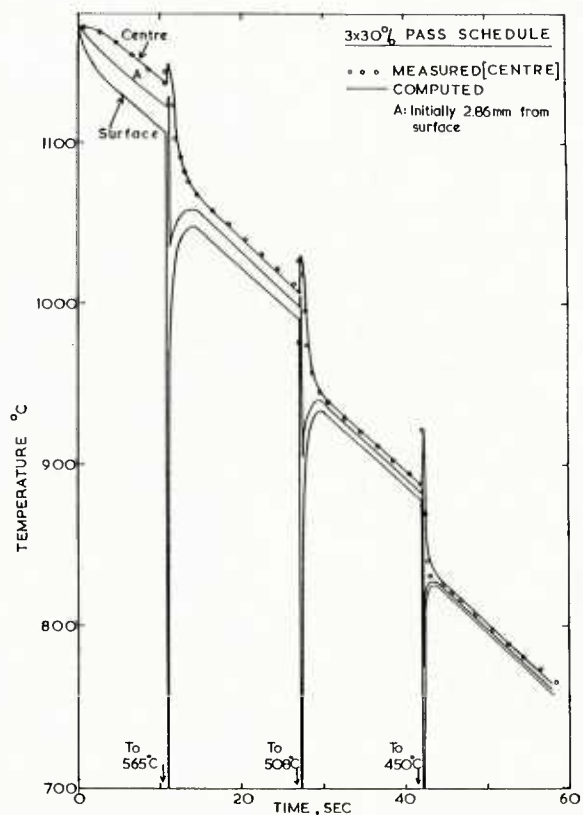
Fig. 12. Comparison of computed temperature changes with measurements made during experimental rolling of a 19mm thick slab of stainless steel in 3 passes of 30% reduction. Roll radius 70mm, speed 200mm s^{-1}, C = 200 kW m^{-2} K^{-1} (5).

MODELLING MICROSTRUCTURAL CHANGES DURING HOT ROLLING OF STEELS

C. M. Sellars
Department of Metallurgy, The University,
Mappin Street, Sheffield S1 3JD, England

SUMMARY

Commercial hot rolling operations take place in a series of passes, each of which may impose a different strain and strain rate on the steel and may take place at different time intervals and temperature from other passes. Each of these individual deformation variables influences the structural changes that take place during deformation and after deformation, as material travels from one pass to the next. Quantitative equations have been developed to describe their effects on the rate of recrystallisation between passes, on the recrystallised grain size produced and on the rate of subsequent grain growth. The way in which these equations can be used to model the evolution of microstructure is discussed for both plate rolling and hot strip rolling. The results of the modelling are shown to give good quantitative agreement with experimental observations on carbon-manganese steel and on austenitic stainless steel.

INTRODUCTION

The properties of hot worked materials depend on the microstructures developed during the working operation. It is increasingly recognised that considerable benefits can be obtained by controlling the thermomechanical processing conditions to produce the optimum microstructure. In the case of steels, the most important structural variable is ferrite grain size, which is determined by the austenite grain size developed at the end of hot working and by the cooling rate after working. Optimum working conditions can be established from trials carried out in the works, but this can be a time consuming and costly exercise. The alternative is to model the microstructural changes from a basis of laboratory data on the processes that contribute to them and to use the model to predict the optimum working conditions.

During deformation at the strain rates and temperatures of interest in hot working operations, all metals undergo work-hardening and dynamic recovery and some may also undergo dynamic recrystallization. The microstructures produced by these processes are unstable and, on holding at temperature after the end of deformation, further structural changes occur by static recovery, recrystallization, and grain growth. In hot rolling operations, the dynamic and static structural changes that take place during and between passes interact to determine the overall evolution of microstructure. The physical metallurgy of these processes is discussed in detail elsewhere [1,2] and will only be considered briefly here as a basis for understanding the quantitative relationships required for computer modelling.

PHYSICAL METALLURGY

During hot deformation of steels in the austenitic condition, the flow stress initially rises with strain as a result of work-hardening and recovery; dislocation density rises and a subgrain structure tends to develop. Because dynamic recovery is relatively slow, the subgrain boundaries are ill formed, and sufficient strain energy is stored to nucleate dynamic recrystallization when a critical strain ε_c is reached. This provides an additional softening mechanism and, as illustrated in Fig. 1(a), results in a peak in flow stress, followed by a fall until a steady-state level is reached after a strain interval ε_x in which a large fraction of recrystallization has taken place. The dynamic softening processes are thermally activated, giving a dependence of stress σ on strain rate $\dot{\varepsilon}$ and temperature T, which, in the case of steels in the austenitic condition, can be described in terms of the Zener-Hollomon parameter Z as

$$Z = \dot{\varepsilon} \exp Q/RT = A \exp \beta\sigma \qquad (1)$$

over the range of conditions of interest in hot rolling. Values for the activation energy Q and for the constants A and β depend on the steel composition. For example, Q for C-Mn steels is typically 312 kJ/mol, for type 304 stainless steel is 410 kJ/mol and for type 316 is 460 kJ/mol. Fig. 2 illustrates the equivalence of stress strain curves for different combinations of $\dot{\varepsilon}$ and T leading to similar values of Z.

Dynamic Recrystallisation

Dynamic recrystallisation involves the nucleation of new grains, which takes place at the original grain boundaries. The original grain size (d_o) as well as the deformation conditions therefore influences the critical strain ε_c. In practice this strain is difficult to measure, but at least for C-Mn steels, it is $\sim 0.8\varepsilon_p$, the strain to the peak stress, which is easily measured, as illustrated in fig. 2. Analysis of data on C-Mn steels [4] leads to a relationship:

$$\varepsilon_p = A \, d_o^{0.5} \, Z^{0.15} \qquad (2)$$

where A depends on steel composition and is 4.9×10^{-4} for C-Mn steel when d_o is in μm. For typical rolling conditions ε_p varies from about 0.2 to 0.5. For HSLA steels containing Nb, ε_p may be up to 2x to 3x these values at low rolling temperatures.

Static Recrystallisation

After deformation, softening by static recovery and recrystallisation takes place with time at rates which depend on the prior deformation conditions and the holding temperature. In particular, as illustrated in fig. 1(b), below some critical strain for static recrystallisation, limited softening takes place by static recovery, which involves only fine-scale changes in the deformed structure. This critical strain is probably $\lesssim 0.05$, at least for C-Mn steels. Above this strain but below ε_c for dynamic recrystallisation, classical recrystallisation involving nucleation and growth of new grains takes place. An example of the form of recrystallisation curves obtained for a low-alloy steel is shown in Fig. 3. The curves generally follow an Avrami equation of the form

$$X_V = 1 - \exp - C(t/t_F)^k \tag{3}$$

where X_V is the fraction recrystallised in time t, t_F is the time for some specified fraction of recrystallisation (say 0.5), k is a constant, and $C = - \ln (1 - F)$. For the curves shown $k = 2$, which is consistent with the value observed for other steels deformed to strains $<\varepsilon_c$. With this relationship $t_{0.05} = 0.27t_{0.5}$ and $t_{0.95} = 2.08t_{0.5}$, i.e. recrystallisation proceeds over about one order of magnitude in time.

When ε_c is reached, nuclei are present in the structure at the end of deformation. This modifies the static recrystallisation process and it is then sometimes called "metadynamic" rather than "static" recrystallisation, as shown in fig. 1(b). With increasing strain beyond ε_c this mode of recrystallisation becomes more important. It again follows the form of equation (3), but with a lower value of k. This change in mechanism is reflected by an abrupt change in the dependence of recrystallisation rate on strain, as illustrated in fig. 4.

Analysis of the recrystallisation kinetics of a range of C-Mn steels (4) leads to the relationships for the time to 50% recrystallisation

$$t_{0.5} = 2.5 \times 10^{-19} d_o^2 \varepsilon^{-4} \exp \frac{300\ 000}{RT}$$
$$(\varepsilon \lesssim 0.8\varepsilon_p) \tag{4}$$

$$t_{0.5} = 1.06 \times 10^{-5} Z^{-0.6} \exp \frac{300\ 000}{RT}$$
$$(\varepsilon \gtrsim 0.8\varepsilon_p) \tag{5}$$

The lack of influence of Z in equation (4) is somewhat surprising and it does appear in the equivalent relationships for other steels.

The grain size produced by static recrystallisation (d_{rex}) is also sensitive to the deformation variables and for C-Mn steels is described by the equations

$$d_{rex} = 0.5\ d_o^{0.67}\ \varepsilon^{-1} \tag{6}$$
$$(\varepsilon \lesssim \varepsilon^*)$$

$$d_{rex} = 1.8 \times 10^3\ Z^{-0.15} \tag{7}$$
$$(\varepsilon \gtrsim \varepsilon^*)$$

$$\text{where } \varepsilon^* = 0.57\ d_o^{0.17}\ \varepsilon_p \tag{8}$$

which gives values of ε^* somewhat greater than $0.8\ \varepsilon_p$ (i.e. than ε_c) for grain sizes expected in hot rolling.

Grain Growth

Once recrystallisation is complete, further grain growth takes place as a function of time and temperature. This follows a relationship of the form

$$d^n = d_{rex}^n + A (\exp - Qgg/RT)\ t \tag{9}$$

where theory gives the value of $n = 2$. Experimentally, higher values are frequently observed to fit the data, particularly at short times, as shown for example in fig. 5. Such high exponents are not realistic and probably reflect a change of A with time, e.g. the data in fig. 5 can be fitted by two lines with $n = 2$, a high value of A for short times and a much lower value for longer times.

Transformation to Ferrite

The above relationships and equivalent ones for other steels describe the micro-structural development in austenite. For the transformable steels, the ferrite grain size determines room temperature properties and depends on the austenite grain size, the retained strain in unrecrystallised austenite and the cooling rate (4). The effects of each of these variables are not yet fully quantified although the general trends are well recognised, as shown in fig. 6.

ROLLING CONDITIONS

The relationships given in the previous section are expressed in terms of equivalent tensile strain and strain rate. These are related to the variables of an individual pass in flat product rolling as

$$\varepsilon = \frac{2}{\sqrt{3}} \ln \left(100/(100-R) \right) \tag{10}$$

where R is the percentage reduction in thickness and the factor $2/\sqrt{3}$ enters the equation because deformation occurs under nearly plane strain conditions. True strains calculated in this way are normally in the range 0.15 to 0.7, but these equations neglect redundant shear strains that occur during rolling, so slightly underestimate the true values. Under hot rolling conditions high frictional forces occur between the stock and the rolls and the strain rate rises rapidly to a maximum at entry and then falls to zero at exit of the rolls. Equivalent mean true strain rates for a pass can be determined from a number of alternative equations available in the literature, for example

$$\dot{\varepsilon} = V \left[\frac{2}{D(ho-hf)} \right]^{\frac{1}{2}} \varepsilon \tag{11}$$

where V is periferal roll speed D, is roll diameter and ho and hf are initial and final thickness.

A rolling schedule involves a series of roughing passes followed by a series of finishing passes which can be represented as illustrated in fig. 7. This also shows the rapid change in mean temperature that takes place with time during the rolling operations. Because of the temperature sensitivity in equations (4), (5) and (9), these variations in temperature must be allowed for in modelling microstructure changes. This is done by defining a temperature compensated time

$$W = t \exp - Q/RT \tag{10}$$

or, for varying temperature,

$$W = \Sigma \, \delta t_i \exp - Q/RT_i \tag{11}$$

where δt_i is the time interval for a small incremental change in temperature, T_i. Use of this value and the equivalent value of W_F instead of t and t_F in equation (3) gives satisfactory agreement with observations made with changing temperature conditions after a deformation.

OUTLINE OF THE MATHEMATICAL MODEL

The model requires input of the rolling variables and an initial grain size after reheating. It then determines the structure produced after the first pass and uses this to input appropriate values of d_0 and accumulated strain into the calculations for the second pass etc. The principle is illustrated in fig. 8 and Table 1 for a hypothetical isothermal rolling schedule with constant pass reduction of 40.5% ($\varepsilon = 0.6$) and a constant time interval between passes of 10s. The conditions are chosen so that recrystallisation is incomplete between passes. Even considering only two grain sizes (coarse and fine), the structure rapidly becomes complex. In this model, the separate recrystalled and unrecrystalled fractions are assumed to behave independently in subsequent passes e.g. for the second pass there is a fraction X with $d_0 = d_{rex}$ from the first pass and zero retained strain, and a fraction (1-X) with $d_0 = d_0$ for the original grains and the retained strain from the first pass. The new strain of the second pass is simply added to the retained strain of the unrecrystalled fraction and the recrystallisation kinetics and grain size change are computed for each fraction. There is some experimental evidence to support these simple assumptions.

Clearly, for changing temperature conditions it is advantageous to carry out the sequence of calculations by computer and to report the structures as some suitable average value, which can be compared with metallographic observations. For simplicity, fractions of recrystallisation of <0.05 are assumed to be zero and fractions > 0.95 are assumed to be complete in regions of a given initial structure. Grain growth is considered to start only when recrystallisation in complete. The effect of this assumption and of taking different average values of the structure on the expected mean grain size is illustrated in fig. 9. The solid line is simply a weighted average of the recrystallised and unrecrystallised grain sizes (d_{rex} and d_0), whereas the chain line recognises the fact that as the recrystallised grains grow they consume the original grains. The latter is therefore more realistic.

TYPICAL RESULTS FROM MODELLING

The results illustrated are mainly for C-Mn steel, for which the basic equations were given earlier, but equivalent equations are available for Nb HSLA steel, Ti steel and types 304 and 316 stainless steels.

The major effects of rolling can be seen by considering idealised plate rolling schedules illustrated in fig. 10, which involve 15% reduction in each pass, with 20 sec between passes. The predicted grain size changes are shown in fig. 11. For all conditions these show progressive grain refinement as a result of recrystallisation between passes, with grain growth playing a significant role at intermediate thicknesses when the recrystallised grain sizes are relatively small, but the temperature is still high. This effect is particularly significant for the higher reheating temperature, fig. 11(a). Reheating to the higher temperature also leads to full recrystallisation between passes except at the end of finishing 20 mm plate from 200 mm slab. After reheating to the lower temperature recrystallisation is incomplete in 20 mm plate between a number of finishing passes and the mean grain sizes arise from considerably mixed grain structures. Ferrite grain sizes derived from these austenite structures are predicted to become finer with decreasing plate thickness and decreasing reheating temperature, in reasonable agreement with observation from plate rolling trials.

A direct comparison between predicted and observed austenite grain sizes is shown in fig. 12 for a vacuum-melted C-Mn steel. The effect of coarse initial grain sizes, which may be produced by extended reheating times caused by mill breakdown, or by changing from wrought to continuously cast slab, is shown in fig. 13. Clearly, after a relatively few passes differences in microstructure are predicted to be eliminated so that identical finished product structures are obtained, in agreement with practical experience. In fig. 14 the effect is shown of changing pass schedule from the idealised one of constant 15% reduction (fig. 10) to one where the percentage reduction decreases towards the end of the schedule in a manner more typical of practice. It can be seen that the change of schedule has most effect on the final structure when recrystallisation is complete between all passes, i.e. for the higher reheating temperature and 60 mm plate.

OVERALL PROCESS MODELLING

The limitation of the above simple microstructural model is that it requires an input of the strain, strain rate, temperature and time of each pass. The mean strain and strain rate in a rolling pass are simple to calculate from equations (10) and (11). However, as discussed elsewhere, the estimation of the mean temperature in a pass and of the temperature changes between passes requires complex computations. Leduc (6) combined the temperature model with the microstructural model so that only the reheating temperature, time intervals, speeds, pass reductions and spread of the rolling schedule need be input, together with an estimate of the austenite grain size after reheating. The program then computes the temperature and microstructural distributions through the thickness of flat products at all stages of rolling. An example of the predictions for the centre and surface during commercial rolling of C-Mn steel strip is given in fig. 15. From the upper half of the figure it can be seen that the predicted surface temperature on the delay table between roughing and finishing is in close agreement with the measured value, but the predicted value after finishing is about 30°C too high. This discrepancy arises from the fact that the chilling effect of the high pressure descalers before the finishing mill was overlooked. The lower half of the figure shows the corresponding changes in austenite grain size, from which the final ferrite grain size predicted after cooling is also in good agreement with observation.

The combined program gives increased ease of application of the modelling to industrial rolling, but, additionally, in combining the original programs Leduc translated them into FORTRAN, to be run on a main-frame computer. This increased computing capacity enabled him to further extend the program to compute the flow stress of each element in the material as it progresses through each pass. The flow stress computations were based on parametric equations developed to describe experimental stress-strain curves in terms of the strain-rate and temperature of deformation. During rolling, these equations are assumed to be equations of state, so that the flow stress is obtained as a function of the instantaneous strain, strain rate and temperature in each element.

The structural changes produced by static recovery and recrystallisation between passes cause a restoration of the flow stress by removing the effects of work hardening introduced in the previous pass. Although the relationship between fractional restoration of flow stress and fraction recrystallised is non-linear, it is unique and calculable. In modelling the flow stress in multi-pass rolling, the effects of initial microstructure in each pass are therefore taken into account. This is a most important feature of the overall process modelling approach. The model uses the flow stresses to calculate the expected rolling loads, torques and power requirements for each pass. These reflect the mean microstructural effects in the material at entry to each pass.

In C-Mn steels the rapid recrystallisation kinetics mean that complete, or nearly complete, static recrystallisation occurs between most passes during normal rolling schedules. However, in stainless steels, for example, recrystallisation is much slower and the effects of retained hardening between passes can be of importance, as illustrated for type 316 stainless steel in fig. 16. This figure shows data points for the mean plane strain flow stress in 3-pass experimental rolling schedules. The results are plotted against the average temperature of the material during a particular rolling pass and show

clearly that second and third passes give significantly higher flow stresses than first passes because of the lack of recrystallisation in the interpass times. The broken lines give the stresses computed from Leduc's model, modified to incorporate parametric equations for the stainless steel determined from plane strain compression tests. Although there are some minor discrepancies between the predicted curves and the mean lines through the experimental data, the overall agreement is satisfactory. This reflection of the microstructural changes in rolling loads opens up the exciting possibility that comparison of predicted loads with records from commercial rolling should enable the load records to be used to check whether the state of recrystallisation between passes agrees with the model predictions. This would pinpoint the critical passes where control of variables should have the major effect on product structure and properties.

REFERENCES

1. J.J. Jonas, C.M. Sellars and W.J.McG. Tegart, Met. Rev., 1969, 14, 1-24.
2. H.J. McQueen and J.J. Jonas, "Treatise on Materials Science and Technology, vol. 6, Plastic Deformation of Materials", Academic Press, New York, 1975, pp393-493.
3. C.M. Sellars and J.A. Whiteman, Met. Sci., 1979, 13, 187-194.
4. C.M. Sellars, "Hot Working and Forming Processes", Ed. C.M. Sellars and G.J. Davies, Metals Soc. (London) 1980, pp3-15.
5. C.M. Sellars and J.A. Whiteman, The Metallurgist, 1974, 441-447.
6. L.A. Leduc, Ph.D. Thesis, University of Sheffield, 1980.
7. R.A.N.M. Barbosa, Ph.D. Thesis, University of Sheffield, 1983.
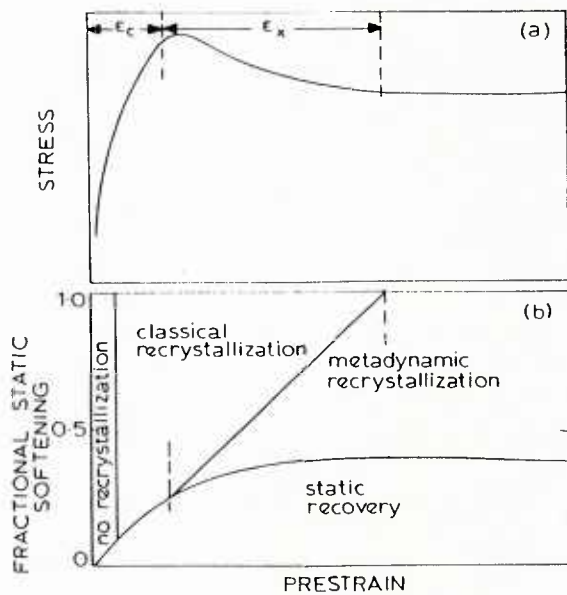
Fig. 1. Schematic representation of (a) relationship between stress/strain behaviour during deformation, and (b) mechanisms of static softening that take place after deformation (3).
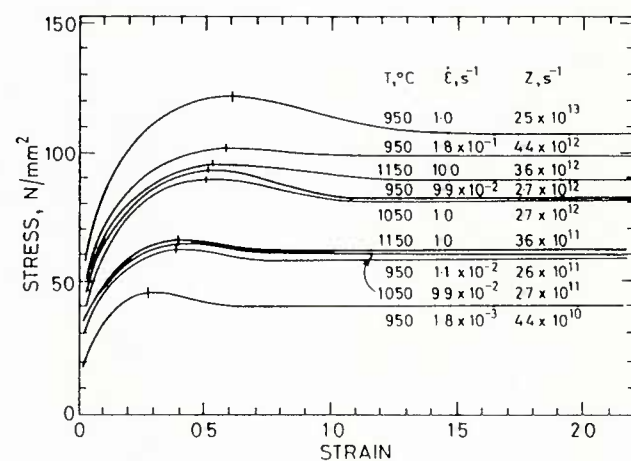
Fig. 2. Equivalent stress-equivalent tensile strain curves obtained from torsion tests on low-alloy steel (AISI 5140) of initial grain size 110μm (4).
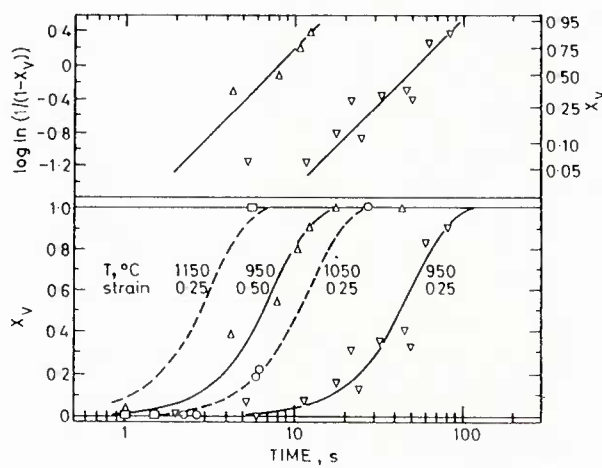
Fig. 3. Recrystallisation curves for low-alloy steel (AISI 5140) of initial grain size 110μm deformed and annealed at the temperatures indicated and at an equivalent strain rate of 1 s^{-1} (4).
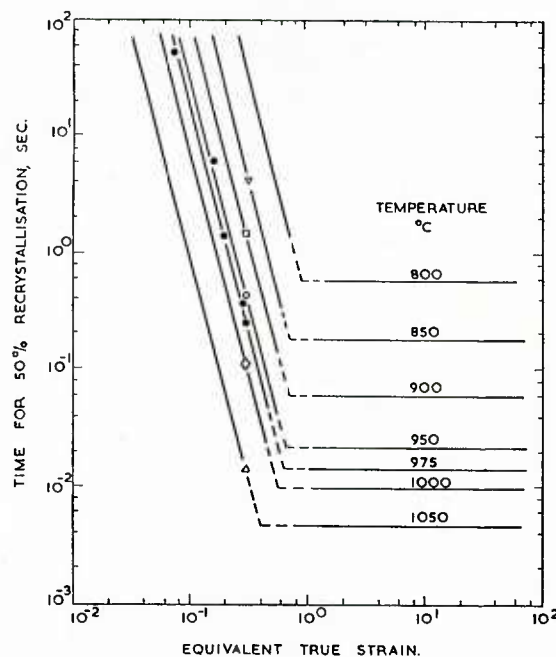
Fig. 4. Time to 50% static recrystallisation as a function of strain for C-Mn steel (5).
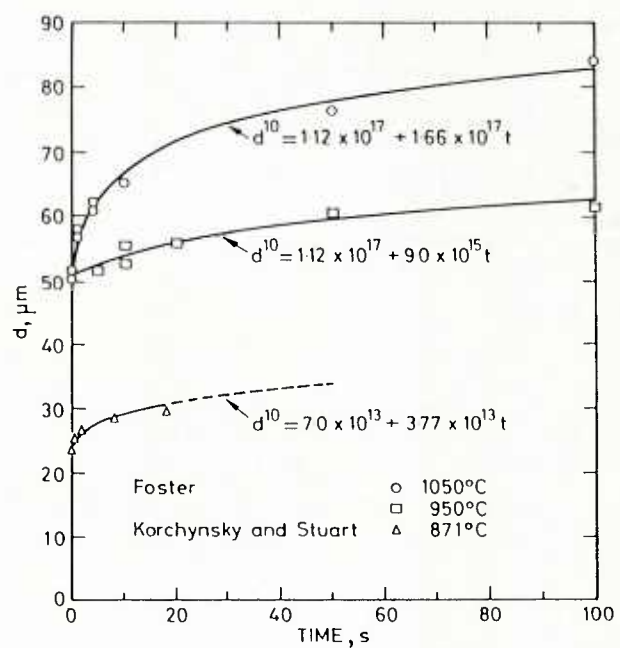
Fig. 5. Grain growth as function of time after complete static recrystallisation in C-Mn steels (4).
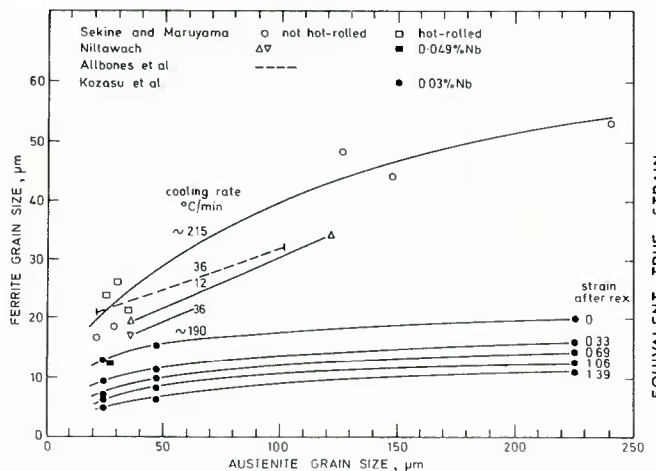
Fig. 6. Dependence of ferrite grain size after transformation during cooling on austenite grain size and retained strain in austenite grains (4).
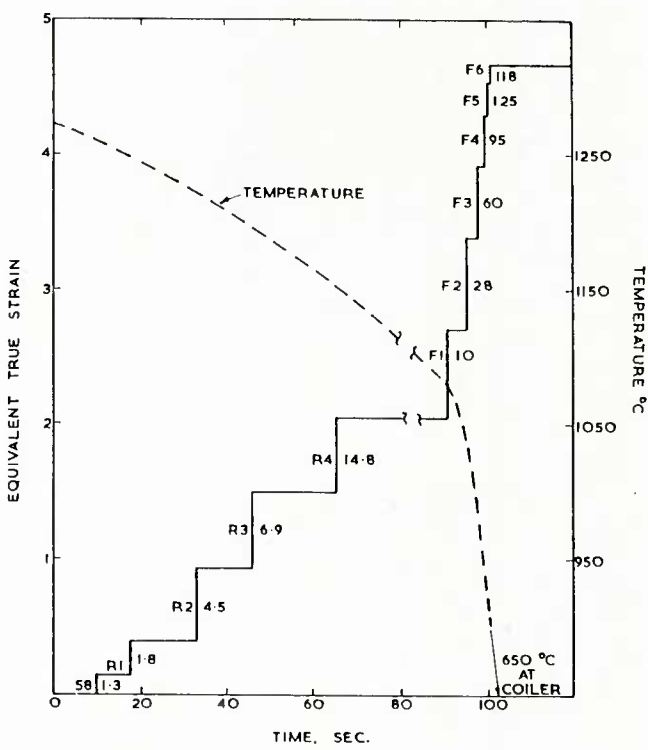
Fig. 7. Typical schedule for rolling 216 mm slab to 2 mm strip (tinplate). Mean equivalent true strain rates for each pass are indicated for an exit speed of 9.5 m/s. (Data provided by BSC Strip Mills Division) (5).
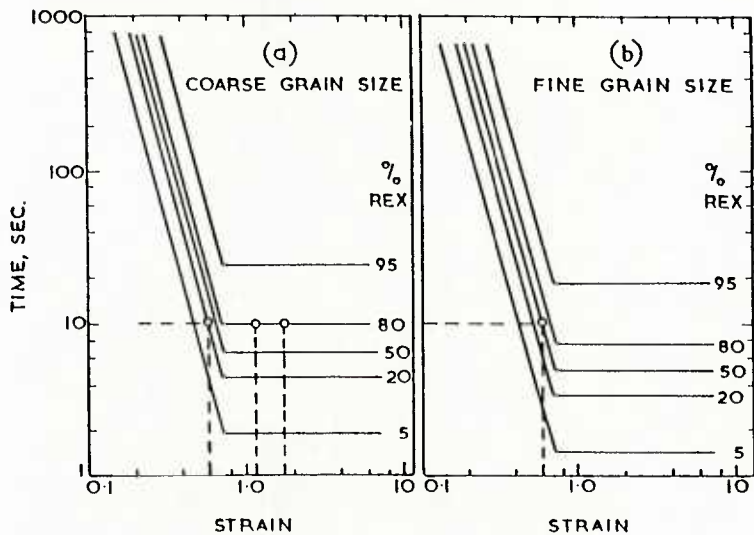
Fig. 8. Strain and grain size depend-
ence of static recrystallisation used
in the derivation of Table I.

Table I. Change in structure during
isothermal rolling schedule with
passes of 0.6 strain and constant time
intervals between passes.

After 1st Pass	100%	Def. 0.6 (coarse)
Before 2nd Pass	25%	Recrystallised (coarse)
	75%	Def. 0.6 (coarse)
After 2nd Pass	25%	Def. 0.6 (coarse)
	75%	Def. 1.2 (coarse)*
Before 3rd Pass	25%	x 25% Recryst. (coarse) = 6.3% x 75% Def. 0.6 (coarse) = 18.7%
	75%	x 80% Recryst. (fine) = 60.0% x 20% Def. 1.2 (coarse)*= 15.0%
After 3rd Pass	6.3%	Def. 0.6 (coarse)
	18.7%	Def. 1.2 (coarse)*
	60.0%	Def. 0.6 (fine)
	15.0%	Def. 1.8 (coarse)*
Before 4th Pass	6.3%	x 25% Recryst. (coarse) = 1.6% x 75% Def. 0.6 (coarse) = 4.7%
	18.7%	x 80% Recryst. (fine) = 15.0% x 20% Def. 1.2 (coarse)*= 3.7%
	60.0%	x 50% Recryst. (coarse) = 30.0% x 50% Def. 0.6 (fine) = 30.0%
	15.0%	x 80% Recryst. (fine) = 12.0% x 20% Def. 1.8 (coarse)*= 3.0%

*In materials in which dynamic recryst-
allisation can occur, the "coarse"
structure after deformation to strains
of 1.2 or more may be partially or com-
pletely replaced by a much finer dynam-
ically recrystallised grain structure.
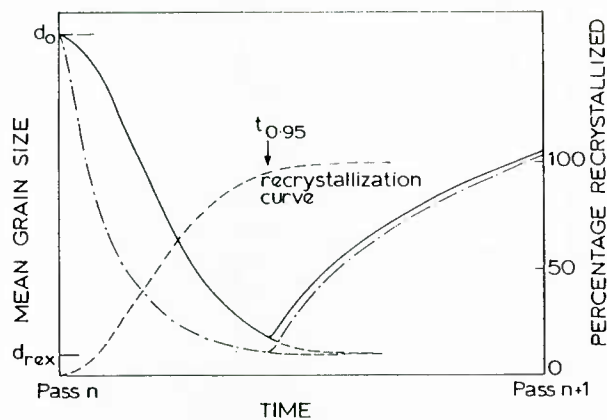
Fig. 9. Change in mean grain size with recrystallisation and grain growth between passes, showing effect of method of averaging during recrystallisation (3).
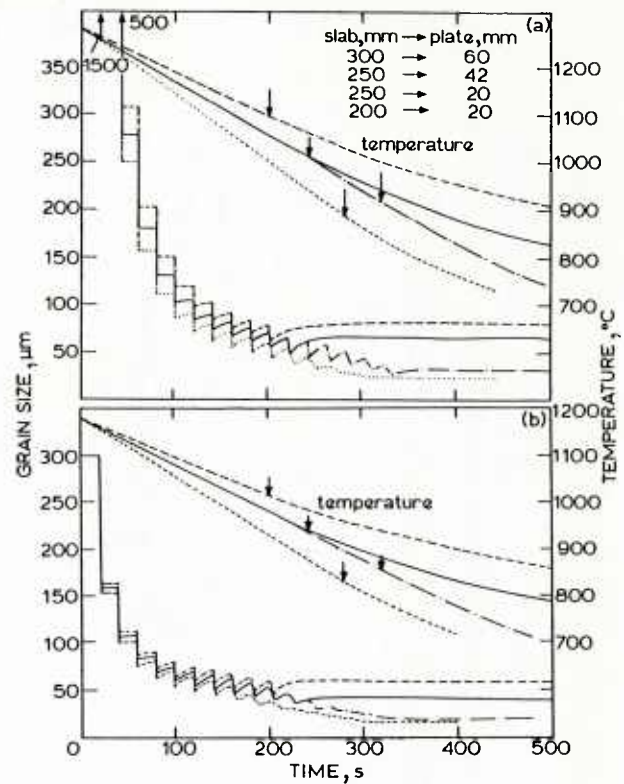
Fig. 10. Plate-rolling schedules used for computations of microstructural evolution (3).
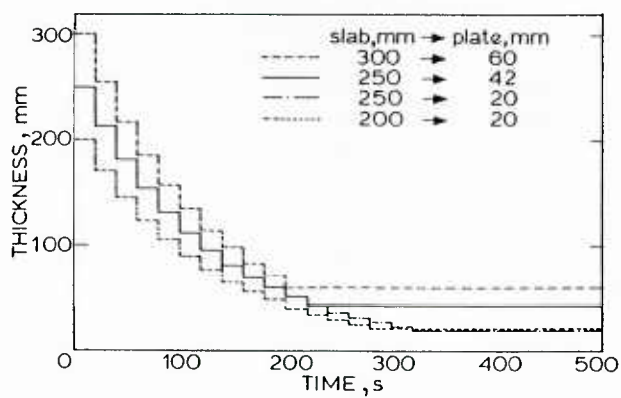
Fig. 11. Dependence of grain size evolution on rolling schedule for slabs reheated to (a) 1280°C and (b) 1180°C and rolled with constant 15% reduction per pass (3).
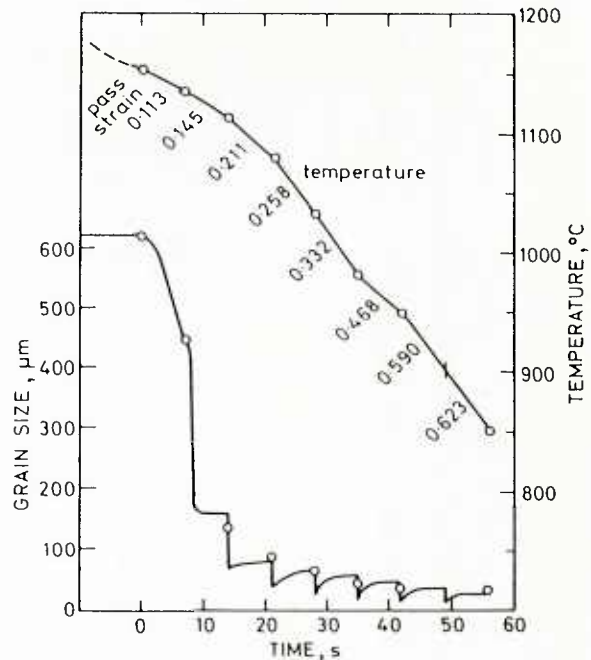
Fig. 12. Comparison of predicted structural changes with those observed by Sekine and Maruyama during experimental plate rolling schedule on vacuum-melted C-Mn steel (observations shown as points) (4).
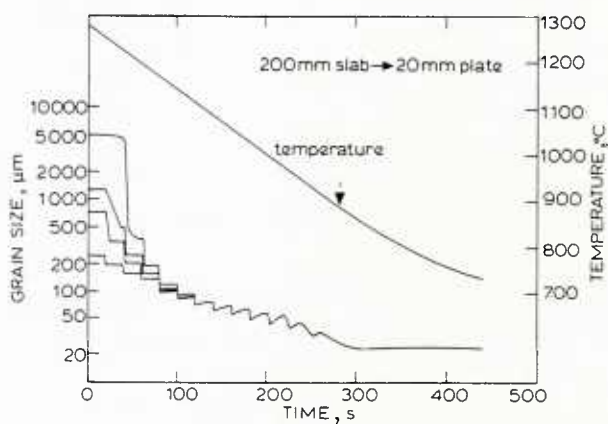
Fig. 13. Influence of initial grain size on evolution of grain size during rolling of 20 mm plate from 200 mm slab reheated to 1280°C (3).
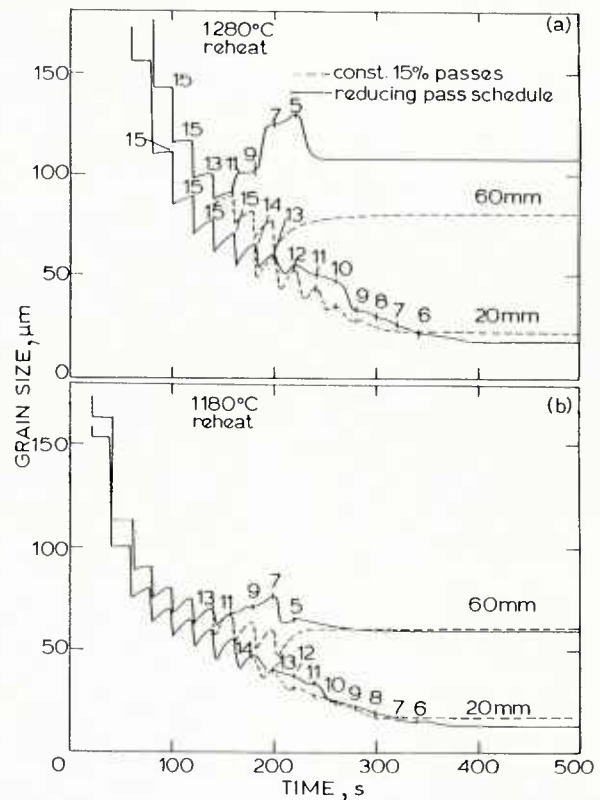
Fig. 14. Effect of reducing pass schedules on grain size evolution during rolling of plates from slabs reheated to (a) 1280°C and (b) 1180°C. Numbers beside curves indicate percentage reduction per pass (3).
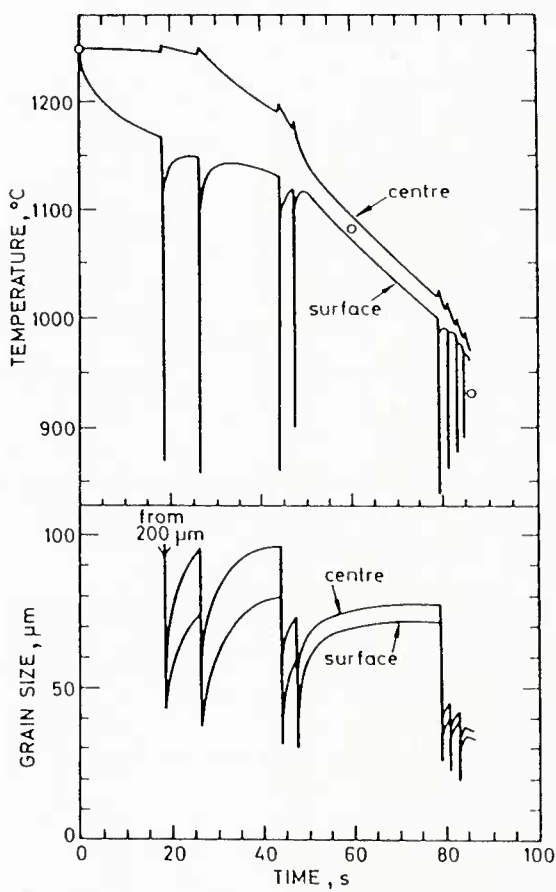
Fig. 15. Changes in temperature and in austenite grain size at the surface and at the centre of the stock during rolling of 6mm strip of C-Mn steel. Points indicate measured surface temperatures (4).
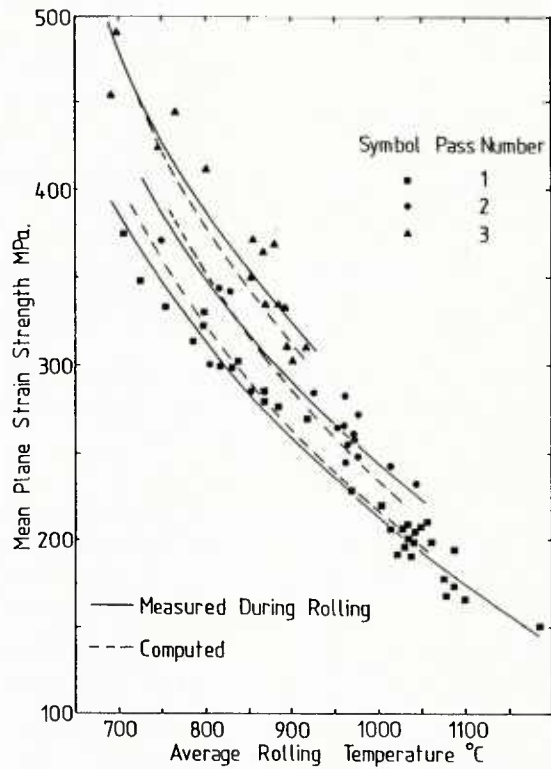
Fig. 16. Comparison of computed and measured mean plane strain flow stress as a function of mean pass temperature during experimental rolling of type 316 stainless steel in 3 passes of 25% reduction (7).

AGARD Lecture Series No.137 Advisory Group for Aerospace Research and Development, NATO PROCESS MODELING APPLIED TO METAL FORMING AND THERMOMECHANICAL PROCESSING Published September 1984 164 Pages This Lecture Series considers process modeling which provides a new perspective to advance metal forming and thermo-mechanical processing. Working and forming processes are viewed as systems which integrate component behaviour such as workpiece flow, heat flow and friction at the workpiece — tooling P.T.O.	AGARD-LS-137 Metal working Mathematical models	AGARD Lecture Series No.137 Advisory Group for Aerospace Research and Development, NATO PROCESS MODELING APPLIED TO METAL FORMING AND THERMOMECHANICAL PROCESSING Published September 1984 164 Pages This Lecture Series considers process modeling which provides a new perspective to advance metal forming and thermo-mechanical processing. Working and forming processes are viewed as systems which integrate component behaviour such as workpiece flow, heat flow and friction at the workpiece — tooling P.T.O.	AGARD-LS-137 Metal working Mathematical models
AGARD Lecture Series No.137 Advisory Group for Aerospace Research and Development, NATO PROCESS MODELING APPLIED TO METAL FORMING AND THERMOMECHANICAL PROCESSING Published September 1984 164 Pages This Lecture Series considers process modeling which provides a new perspective to advance metal forming and thermo-mechanical processing. Working and forming processes are viewed as systems which integrate component behaviour such as workpiece flow, heat flow and friction at the workpiece — tooling P.T.O.	AGARD-LS-137 Metal working Mathematical models	AGARD Lecture Series No.137 Advisory Group for Aerospace Research and Development, NATO PROCESS MODELING APPLIED TO METAL FORMING AND THERMOMECHANICAL PROCESSING Published September 1984 164 Pages This Lecture Series considers process modeling which provides a new perspective to advance metal forming and thermo-mechanical processing. Working and forming processes are viewed as systems which integrate component behaviour such as workpiece flow, heat flow and friction at the workpiece — tooling P.T.O.	AGARD-LS-137 Metal working Mathematical models

interface, and microstructural evolution. These are combined to form a system process model using deformation mechanics.

The Lecture Series covers extrusion, forging, rolling, and sheet forming processes. It will provide specific results for light metals, steels and superalloys and introduce finite element methods and related aspects of computer-aided process design.

The Lecture Series was sponsored by the Structures and Materials Panel and organized by the Consultant and Exchange Program of AGARD.

ISBN 92-835-1477-7

U216704

AGARD

NATO ⊕ OTAN

7 RUE ANCELLE · 92200 NEUILLY-SUR-SEINE

FRANCE

Telephone 745.08.10 · Telex 610176

DISTRIBUTION OF UNCLASSIFIED AGARD PUBLICATIONS

AGARD does NOT hold stocks of AGARD publications at the above address for general distribution. Initial distribution of AGARD publications is made to AGARD Member Nations through the following National Distribution Centres. Further copies are sometimes available from these Centres, but if not may be purchased in Microfiche or Photocopy form from the Purchase Agencies listed below.

NATIONAL DISTRIBUTION CENTRES

BELGIUM
Coordonnateur AGARD — VSL
Etat-Major de la Force Aérienne
Quartier Reine Elisabeth
Rue d'Evere, 1140 Bruxelles

ITALY
Aeronautica Militare
Ufficio del Delegato Nazionale all'AGARD
3 Piazzale Adenauer
00144 Roma/EUR

CANADA
Def
Dep
Ott

LUXEMBOURG

DENMA
Dar
Vec
210

RD
NLR

tablishment

FRANCE
O.N
29 /
923

GERMA
Fac
Phy
Ker
D-7:

to AGARD

GREECE
Hell
Rese
Hola

elopment (ARGE)
cara

ICELAND
Director of Aviation
c/o Flugrad
Reyjavik

UNITED KINGDOM
Defence Research Information Centre
Station Square House
St Mary Cray
Orpington, Kent BR5 3RE

UNITED STATES
National Aeronautics and Space Administration (NASA)
Langley Field, Virginia 23365
Attn: Report Distribution and Storage Unit

THE UNITED STATES NATIONAL DISTRIBUTION CENTRE (NASA) DOES NOT HOLD
STOCKS OF AGARD PUBLICATIONS, AND APPLICATIONS FOR COPIES SHOULD BE MADE
DIRECT TO THE NATIONAL TECHNICAL INFORMATION SERVICE (NTIS) AT THE ADDRESS BELOW.

PURCHASE AGENCIES

Microfiche or Photocopy

National Technical
Information Service (NTIS)
5285 Port Royal Road
Springfield
Virginia 22161, USA

Microfiche

ESA/Information Retrieval Service
European Space Agency
10, rue Mario Nikis
75015 Paris, France

Microfiche or Photocopy

British Library Lending
Division
Boston Spa, Wetherby
West Yorkshire LS23 7BQ
England

Requests for microfiche or photocopies of AGARD documents should include the AGARD serial number, title, author or editor, and publication date. Requests to NTIS should include the NASA accession report number. Full bibliographical references and abstracts of AGARD publications are given in the following journals:

Scientific and Technical Aerospace Reports (STAR)
published by NASA Scientific and Technical
Information Branch
NASA Headquarters (NIT-40)
Washington D.C. 20546, USA

Government Reports Announcements (GRA)
published by the National Technical
Information Services, Springfield
Virginia 22161, USA

SPS

Printed by Specialised Printing Services Limited
40 Chigwell Lane, Loughton, Essex IG10 3TZ

ISBN 92-835-1477-7